University of Reading

Methane's Solar Radiative Forcing

A thesis submitted for the degree of Doctor of Philosophy

Department of Meteorology

Rachael Emily Byrom

June 2021

Declaration

I confirm that this is my own work and the use of all material from other sources has been properly and fully acknowledged.

Rachael Emily Byrom

Abstract

Methane (CH_4) is a potent greenhouse gas with a global-mean surface mixing ratio that has more than doubled in the past century. Its ability to alter thermal infrared irradiances has been well studied. CH_4 also absorbs incoming shortwave (SW) radiation, predominantly at near-infrared wavelengths (0.7 – 4 μm). However, this effect is not included in many climate models, or in the Intergovernmental Panel on Climate Change 5th assessment estimate of CH_4 radiative forcing (RF).

Recent studies indicate that this SW effect enhances total CH_4 RF and related emission metrics, but estimates are sensitive to the specification of clouds and spectral overlap with water vapour. These studies did not examine the impact of CH_4 SW forcing on the spatial or seasonal variation of CH_4 stratospheric temperature-adjusted RF, nor did they quantify in detail the sensitivity of the SW effect to surface albedo or vertical profile specification.

This thesis provides the most comprehensive quantification of the CH_4 SW effect to date using a narrow-band radiative transfer model. It investigates key sensitivities, including vertical profile representation, spectrally-resolved surface albedo specification and the effect of SW absorption at mid-infrared wavelengths between 5 – 10 μm. Recent satellite measurements are exploited to derive a best estimate of CH_4 global-mean SW forcing and its impact on total CH_4 forcing from seasonally and spatially-resolved calculations, including the impact of SW absorption on CH_4 longwave forcing via stratospheric temperature change.

All-sky CH_4 SW tropopause instantaneous RF is found to be significantly smaller than previous estimates at 0.002 W m^{-2} with an uncertainty of ±25%. This is caused by a combination of factors which alter the magnitude of the downward and upward SW tropopause forcing components. In total, the CH_4 SW radiative effect is found to enhance the CH_4 longwave-only RF by 7% from 0.574 W m^{-2} to 0.613 W m^{-2}.

Acknowledgements

First and foremost, I'd like to thank my supervisor Professor Keith Shine for sharing his wisdom, insight and time throughout this project. It has been a privilege to work with Keith and to learn so much about climate change science under his supervision, his contribution to the field is nothing short of inspirational. I'd also like to thank him for his kindness, compassion and constant patience whilst I've worked towards submitting my thesis during the Covid-19 pandemic.

I'd also like to thank Dr Jonathan Elsey for his support over the years, especially for his help with coding issues and model errors. Thank you for always being so willing to help even when you were writing up your own thesis! Additional thanks must also go to my co-supervisor Professor William Collins for his expertise and advice, and also to my monitoring committee, Dr Michaela Hegglin and Professor Ellie Highwood, who have provided much appreciated insight, encouragement and guidance over the years.

Thank you to Professor William D. Collins at Lawrence Berkeley National Lab for his willingness to discuss and compare my work with his own research. I am especially grateful to him for sharing data with me, this was extremely useful and helped to advance my own understanding of methane's solar radiative forcing, in particular regarding the sensitivity to surface albedo specification.

Thank you also to those who have helped along the way, my flatmate Sally, David, Flavia, Josh and friends throughout the department. I'd especially like to thank Sophia Moreton and Kaja Milczewska, I'm very grateful to have had their support and encouragement throughout this final year.

Contents

1. Introduction 1
1.1 Motivation and background 1
1.2 Aim of thesis 4
1.3 Thesis structure 5
2. Scientific Background 6
2.1 Methane 6
2.1.1 Spectral characteristics 6
2.1.2 Atmospheric methane 8
2.2 Earth's energy balance 11
2.2.1 Incoming solar radiation 14
2.2.2 Atmospheric absorption of solar radiation 19
2.3 Radiative Forcing 22
2.3.1. CH_4 radiative forcing 29
2.3.2 Current estimates of CH_4 SW radiative forcing 32
2.4 Radiative Transfer 39
2.4.1 Fundamentals of radiative transfer 40
2.4.2 Radiative transfer in the terrestrial atmosphere 41
2.4.3 Methods for calculating radiative transfer 43
3. Methods, Models and Data 46
3.1 Radiative transfer codes 46
3.1.2 The Reference Forward Model (RFM) 47
3.1.3 RFMDISORT 49
3.1.4 The Suite Of Community RAdiative Transfer codes (SOCRATES) 50
3.1.5 SOCRATES-RF 52
3.2 Fixed dynamical heating 55
3.3 Data 57
3.3.1 HITRAN 57
3.3.2 MIPAS CH_4 climatology 59
3.3.3 ECOSTRESS Fine-snow spectral surface albedo 64
3.3.4 Rangeland spectral surface albedo 64
3.3.5 SCIAMACHY LER database 65

4. A comparison of shortwave radiation codes - is SOCRATES fit for purpose? 66
4.1 Introduction 66
4.2 Experimental setup 68
4.3 Is SOCRATES fit for purpose? 72
4.3.1 Case 1 74
4.3.2. Case 2 79
4.3.3 Case 3 83
4.4 Chapter conclusions 85
5. Sensitivities of Methane's Shortwave Radiative Forcing 87
5.1 Introduction 87
5.2 The representation of methane's vertical profile 88
5.2.1 The impact of profile representation on radiative forcing calculations 92
5.3 The effect of CH_4 absorption at solar mid-infrared wavelengths between 5 – 10 µm 96
5.3.1 Incoming solar irradiance between 5 – 10 µm 98
5.3.2 CH_4 SW absorption between 5 – 10 µm 100
5.4 The impact of surface albedo specification on methane's SW RF 102
5.4.1 The dependence of methane's SW forcing on spectrally-resolved surface albedo 108
5.4.2 The impact of SCIAMACHY-SSA in calculations of methane's SW forcing 115
5.5 Chapter conclusions 125
6. Best estimate of methane's shortwave radiative forcing 126
6.1 Introduction 126
6.2 Clear-sky and All-sky SW RF 129
6.3 The impact of SW absorption on stratospheric temperature adjustment 133
6.4 Sources of uncertainty 140
6.5 Chapter conclusions 146
7. Conclusions and Future Work 147
7.1 Introduction 147
7.2 Conclusions 147
7.2.1 Chapter 4: The ability of SOCRATES 147
7.2.2 Chapter 5: Sensitivities of methane's SW RF 148
7.2.3 Chapter 6: Best estimate of the impact of methane's SW bands on RF 149
7.3 Future work 150
Bibliography 153

Chapter 1

Introduction

1.1 Motivation and background

Radiative forcing (RF) is a fundamental metric for quantitatively comparing natural and anthropogenic drivers of climate change. It measures the net change in the Earth's energy balance due to an imposed perturbation, for example, following variations in solar activity or a change in the atmospheric concentration of radiatively active constituents, such as carbon dioxide (CO_2), or a change in surface characteristics.

RF theory evolved from early studies that investigated the response of the climate system to changes in solar output, a doubling of CO_2 and variations in water vapour (H_2O) and ozone (O_3) with the use of simple radiative-convective models (e.g. Manabe and Strickler 1964; Manabe and Wetherald 1967). These studies formed the basis of present-day calculations, demonstrating how radiative perturbations could affect atmospheric and surface temperatures. Rapid developments in the modelling of the global climate system advanced scientific understanding beyond this pioneering research, eventually demonstrating the mathematical link between perturbations in the Earth's energy balance and global-mean surface temperature (GMST) change, culminating in the development of a physical framework relating climate forcing and climate response (e.g. Ramanathan 1975; Ramanathan *et al.* 1979; Hansen *et al.* 1981, see Section 2.3). Notably, this work demonstrated the radiative impact of greenhouse gases (GHGs) and established the significance of

CO_2 as a major forcing mechanism, leading to increasing recognition of the impact of human activity on climate. RF emerged as a key concept in climate change science and the principal method for quantifying the relative impact of different forcing mechanisms on the climate system. RF has been used extensively by major international scientific bodies such as the Intergovernmental Panel on Climate Change (IPCC), which provides policymakers with regular assessments of advances in the scientific understanding of climate change, its predicted future impact and options for adaptation and mitigation strategies.

RF calculations have developed significantly over the past few decades to more accurately characterise the radiative impact of a variety of forcing mechanisms in addition to CO_2, such as methane (CH_4), nitrous oxide (N_2O), chlorofluorocarbons (CFCs), solar irradiance changes, land-use change and aerosols (Myhre *et al.* 2013a). In relation to GHGs in particular, such developments were possible due to advances in spectroscopic theory, measurements and observations which quantified the key spectral parameters that characterise molecular absorption and the transmission and emission of radiation through the Earth's atmosphere, such as absorption line position, intensity and width. Importantly, these properties were compiled and published in regularly updated databases and made available to the climate modelling community (e.g. the HIgh Resolution TRANsmission (HITRAN) spectroscopic database e.g. Gordon *et al.* 2017). Such comprehensive tabulations allowed for high spectral resolution calculations of RF by so-called line-by-line (LBL) models, which compute atmospheric radiative transfer for each individual absorption line of a radiatively active constituent. These models provided a much more exact treatment of radiative transfer through the atmosphere and subsequently served as a vital benchmark from which simplified parameterisations of radiative transfer could be assessed. Considerable effort is still being made today to address inconsistencies in the parameterisation of radiative transfer between different climate models (which lead to a large spread in climate projections of CO_2 RF, e.g. see Soden *et al.* 2018) and discrepancies in the parameterisation of other key absorbers, such as H_2O and CH_4 (e.g. Collins *et al.* 2006b; Forster *et al.* 2011). RF remains an active area of research.

Human-induced changes in the concentration of GHGs are, collectively, the most important driver of current climate change (Myhre *et al.* 2013a). An increase in the abundance of these gases contributes to the enhanced thermal infrared (TIR) 'longwave' (LW) greenhouse effect (see Section 2.2). However, many GHGs also absorb incoming solar 'shortwave' (SW) radiation at near-infrared (NIR) wavelengths (0.7 – 4 μm). This absorption has long been included in assessments of the climate impact of the most important anthropogenic GHG, i.e. CO_2 (for example it was included in Manabe and Wetherald 1967). However for CH_4, which contributes the second largest RF to total anthropogenic GHG RF since the pre-industrial era (Myhre *et al.* 2013a), this SW contribution

remains relatively unexplored. Early studies by Wang *et al.* (1976) and Donner and Ramanathan (1980) demonstrated the significance of CH_4 on the climate system and the necessity of incorporating the radiative effects of CH_4 in climate models. However, these (and subsequent) studies focussed on the absorption of LW radiation by the 7.7 μm absorption band of CH_4, which exerts a significant effect on the upward emission of TIR radiation from the Earth's surface and troposphere due to its position in a relatively transparent region of spectral absorption (see Section 2.1 and Section 2.2). Despite spectroscopic knowledge of NIR CH_4 absorption (e.g. Moorhead 1932; Migeotte 1948; Rothman *et al.* 1987), the predominance of methane's absorption of LW radiation resulted in the climate impact of its SW absorption being comparatively overlooked.

Several studies (e.g. Collins *et al.* 2006a; Li *et al.* 2010) have indicated the potential importance of CH_4 NIR absorption bands but a detailed quantification of their importance for RF is still lacking. Etminan *et al.* (2016) and Collins *et al.* (2018) offer significant progress in addressing this research gap, presenting new calculations of CH_4 SW RF. Both studies indicate that the NIR effect serves to enhance the overall CH_4 RF and related emission metrics, but the magnitude is dependent on the specification of clouds and the spectral overlap with H_2O. These studies did not examine the impact of SW absorption on the spatial or seasonal variation of stratospheric temperature-adjusted CH_4 LW RF, nor did they quantify in detail the sensitivity of the CH_4 SW effect to surface albedo or vertical profile specification – both are potentially important factors controlling the amount of reflected SW radiation absorbed by CH_4. Given methane's substantial contribution to GHG RF, and the recent rapid increase in global atmospheric CH_4 concentrations at rates last observed during the 1980s (1988:~11 parts per billion by volume (ppbv)/year, 2005:~0.3 ppbv/year, 2018:~10 ppbv/year, see Nisbet *et al.* 2019), a timely and thorough assessment of the full climate impact of CH_4 is necessary.

1.2 Aim of thesis

This thesis aims to provide the most comprehensive quantification of methane's SW effect to date, by presenting results from seasonally and spatially-resolved RF calculations, including the impact of SW absorption on LW forcing via changes in stratospheric temperature. This research will examine key sensitivities of methane's SW RF measured at the top of the atmosphere (TOA), tropopause and surface using a narrow-band radiative transfer model, focussing particularly on the following factors:

1. the representation of the vertical profile of CH_4 mixing ratios used in RF calculations.

2. the effect of CH_4 absorption at solar mid-infrared wavelengths between 5 – 10 μm. CH_4 absorption across this solar mid-infrared wavelength range was neglected by both Etminan *et al.* (2016) and Collins *et al.* (2018).

3. the impact of surface albedo specification (and particularly its spectral variation) on CH_4 SW RF.

Each of these factors are addressed throughout Chapter 5, using recent satellite-derived analyses, with the objective of identifying which 'conditions' are essential in deriving the best estimate of impact of CH_4 SW absorption bands on tropopause RF (Chapter 6).

1.3 Thesis structure

The remainder of this thesis is structured as follows:

Chapter 2: Scientific background

This chapter reviews theory and literature relevant to CH_4 SW RF. It covers the spectral and atmospheric characteristics of CH_4, the Earth's energy balance, the concept of RF, the fundamentals of radiative transfer and methods of calculating radiative transfer in the terrestrial atmosphere.

Chapter 3: Methods, models and data

This chapter details each radiative transfer code used in this thesis along with the associated methods used to calculate RF. Significant datasets are also detailed to provide the reader with a background of their origin and utility.

Chapter 4: A comparison of SW radiation codes – is SOCRATES fit for purpose?

This chapter presents a detailed model intercomparison between the narrow-band SOCRATES radiative transfer code (Manners *et al.* 2015) and the line-by-line Reference Forward Model (Dudhia 2017) to determine if SOCRATES' parameterisation of radiative transfer is suitable to calculate the SW forcings required in this thesis.

Chapter 5: Sensitivities of methane's SW radiative forcing

This chapter investigates key sensitivities of CH_4 SW absorption bands, including the vertical representation of CH_4 mixing ratios, the effect of CH_4 absorption at solar mid-infrared wavelengths between 5 – 10 μm and the dependence of CH_4 SW forcing on the specification of surface albedo.

Chapter 6: Best estimate of methane's SW radiative forcing

This chapter exploits recent satellite measurements to derive a best estimate of the global-mean CH_4 SW effect and its impact on the total CH_4 RF, including the impact of SW absorption on CH_4 LW forcing via stratospheric temperature change. It also discusses sources of uncertainty related to the calculation of RF and estimates the total uncertainty associated with the calculation of CH_4 SW, LW and net RF presented in this thesis.

Chapter 7: Conclusions and future work

Finally, this chapter presents the main conclusions from Chapters 4, 5 and 6 and explores possible avenues of future work that could extend the findings of this thesis.

Chapter 2

Scientific Background

2.1 Methane

2.1.1 Spectral characteristics

Methane is a spherical top molecule with five atoms and four distinct modes of vibration: ν_1, ν_2, ν_3 and ν_4. Table 2.1 details the stretching movements and approximate wavenumber associated with each fundamental vibrational transition. The most important of these modes (because of the variation in the electric dipole moment associated with the vibration) are the ν_3 and ν_4 bands at 3019 cm^{-1} (3.3 μm) and 1311 cm^{-1} (7.7 μm), respectively. The strong ν_4 band exerts a significant impact on TIR fluxes due to its position in a relatively transparent region of spectral absorption and its proximity to the peak of the blackbody distribution for the effective emitting temperature of the Earth (see Section 2.2.1). In contrast, both $\nu_1$and ν_2 are only weakly infrared active. However, CH_4 possesses a number of overtone bands, which result from energy transitions from the ground state (i.e. the lowest energy state) to a state with twice (or e.g. three or four) times the frequency of the fundamental vibrational transition, and combination bands, which arise when two or more fundamental vibrations are excited simultaneously. There is a roughly linear approximation between the wavenumber transition of each of methane's bands such that $\nu_1 \approx \nu_3 \approx 2\nu_2 \approx 2\nu_4$. This results in many transitions coinciding at similar wavenumbers, giving rise to a banded structure of

absorption across the mid-infrared and NIR. Figure 2.1 shows this banded structure and the intensity of CH_4 spectral lines. The most radiatively-important fundamental ν_3 and ν_4 bands are annotated on this figure to highlight their location and intensity. The use of a logarithmic axis reveals the location and intensity of weaker combination bands across the NIR, notably around 4300 cm^{-1} (2.3 µm) and 5900 cm^{-1} (1.7 µm), which both play an important role in determining CH_4 SW IRF (see Section 2.3.2).

	Wavenumber (cm^{-1})	**Stretching movement**
$\boldsymbol{\nu_1}$	2916	Symmetric stretch
$\boldsymbol{\nu_2}$	1533	Bending mode
$\boldsymbol{\nu_3}$	3019	Anti-symmetric C-H stretch
$\boldsymbol{\nu_4}$	1311	Bending mode

Table 2.1: Wavelength and type of movement associated with methane's four fundamental modes of vibration due to interaction with electromagnetic waves.

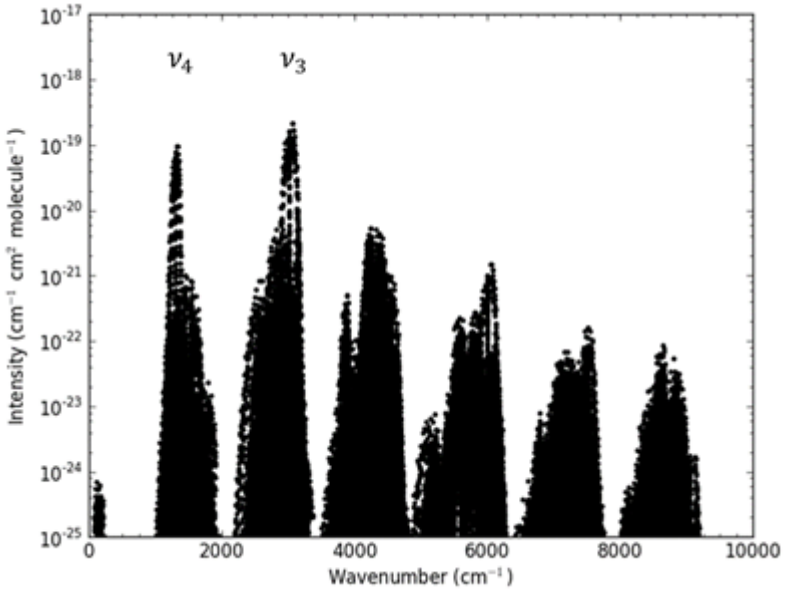

Figure 2.1: Intensity of CH_4 spectral lines in the mid-infrared and NIR region plotted using data from the HITRAN2016 database, where each dot represents a single spectral line. The location of the most radiatively important fundamental ν_4 and ν_3 bands are annotated at 1311 cm^{-1} and 3019 cm^{-1}, respectively. Source: K. Shine (2021), personal communication.

The most recently released HITRAN2016 database (Gordon *et al.* 2017) provides an updated assessment of the vibrational-rotational bands contributing to CH_4 line intensity in the NIR spectral region. Table 2.2 displays the top ten bands contributing to CH_4 total NIR line intensity in the 2500 cm^{-1} – 14,000 cm^{-1} spectral region. Around 98.8% of the total line intensity can be attributed to these bands alone. The ν_3 band for the $^{12}CH_4$ isotopologue is by far the strongest band in the NIR accounting for around 87% of the total line intensity in this spectral region. As explained in Section 2.3.2, this band has a net negative NIR IRF, due to strength of absorption in the stratosphere and the impact of spectral overlap with H_2O in the troposphere.

Band	Isotopologue	Band Range (cm^{-1})	Sum of Line Intensities	Contribution to Total NIR Line Intensity (%)
ν_3	$^{12}CH_4$	2731.264 – 3254.245	1.082×10^{-17}	87.24
$\nu_1 + \nu_4$	$^{12}CH_4$	3940.891 – 4600.165	3.800×10^{-19}	3.066
$\nu_2 + \nu_4$	$^{12}CH_4$	2466.926 – 3242.320	3.714×10^{-19}	2.996
$\nu_3 + \nu_4$	$^{12}CH_4$	3829.130 – 4725.245	2.927×10^{-19}	2.361
ν_3	$^{13}CH_4$	2742.358 - 3232.826	1.191×10^{-19}	9.604×10^{-1}
$\nu_2 + \nu_3$	$^{12}CH_4$	4308.526 – 4824.449	7.194×10^{-20}	5.803×10^{-1}
$\nu_1 + \nu_2$	$^{12}CH_4$	4043.607 – 4624.895	5.741×10^{-20}	4.631×10^{-1}
$2\nu_4$	$^{12}CH_4$	2097.799 – 3198.314	5.496×10^{-20}	4.434×10^{-1}
$\nu_3 + \nu_4$	$^{12}CH_4$	2828.821 – 3274.337	5.250×10^{-20}	4.235×10^{-1}
$3\nu_4$	$^{12}CH_4$	3322.184 – 4445.332	3.250×10^{-20}	2.622×10^{-1}

Table 2.2: Top ten bands contributing to methane's total line intensity (cm^{-1} / (molecule cm^{-2})) in the 2500 cm^{-1} - 14,000 cm^{-1} spectral region using data from HITRAN2016. Isotopologue abundances for $^{12}CH_4$ are around 98.8% and for $^{13}CH_4$ around 1.11%. All data are sourced from HITRAN2016 (Gordon et al. 2017).

2.1.2 Atmospheric methane

CH_4 is emitted into the atmosphere from a variety of anthropogenic and natural sources. Anthropogenic emissions originate from the use of natural gas and oil, coal mines, livestock, landfill, wastewater management and rice cultivation. Natural emissions occur due to wildfires, terrestrial permafrost, seepages from geological sources (such as geothermal vents and mud volcanoes) and the degradation of organic matter in anaerobic conditions (such as natural wetlands and lakes). Figure 2.2 shows global CH_4 emissions from both anthropogenic and natural sources for the 2008 - 2017 decade. Across this period, top-down estimates (based on atmospheric observations used

within an inverse-modelling framework) attribute around 60% of total emissions to anthropogenic activity, with the remaining 40% attributed to natural emissions (Saunois *et al.* 2020). Bottom-up estimates are also shown, calculated from inventories of anthropogenic emissions and process-based models that estimate contributions from land-surface emissions and atmospheric chemistry. The bottom-up approach estimates global emissions to be almost 30% larger than the top-down inversion approach, highlighting the need for further research on emission factors to constrain the global CH_4 budget (Saunois *et al.* 2020).

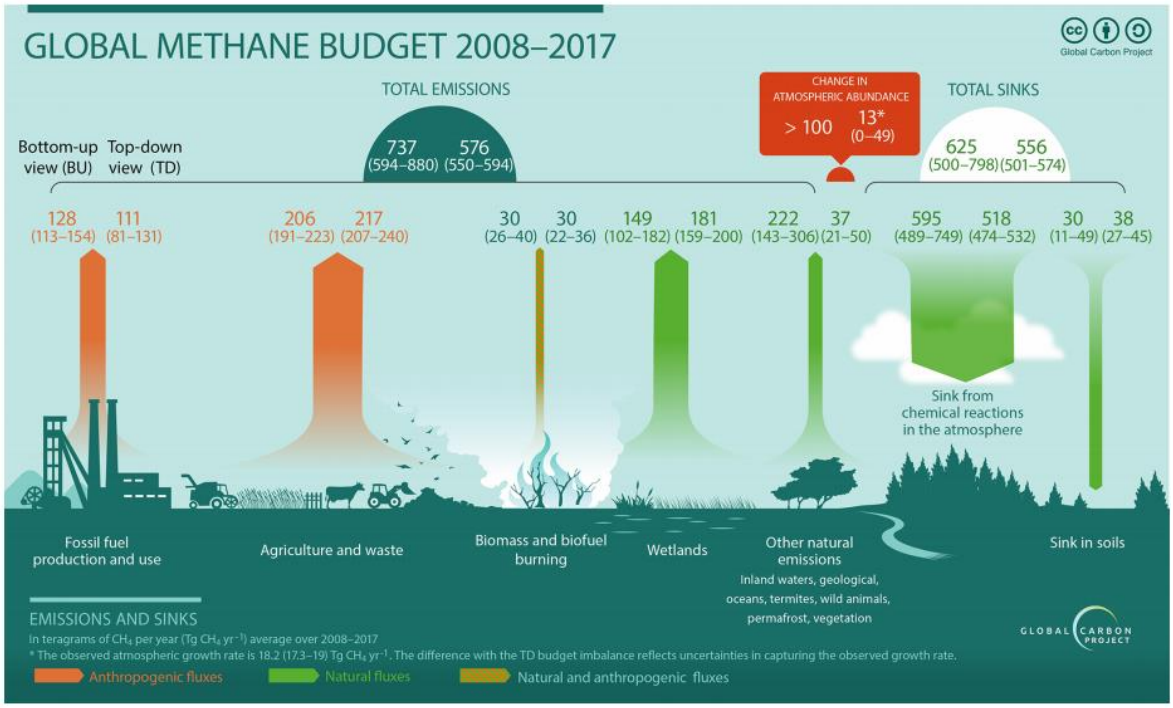

Figure 2.2: Global CH_4 budget for the 2008 to 2017 decade, showing bottom-up estimates (left-hand side) and top-down estimates (right-hand side) in Tg CH_4 yr^{-1} for each source and sink category depicted, along with total emissions and total sinks. Biomass and biofuel burning are shown as both natural and anthropogenic fluxes. Taken from Saunois et al. (2020).

The atmospheric concentration of CH_4 has risen substantially since the pre-industrial era, from 722 ± 25 ppbv in 1750 (Etheridge *et al.* 1998; Dlugokencky *et al.* 2005) to 1857 ppbv in 2018 (Saunois *et al.* 2020). Prolonged periods of increasing atmospheric CH_4 have been measured over the past three decades, albeit with a reduced rate in the 1990s (Dlugokencky *et al.* 2011) and a near constant rate from 1999 to 2006. However, as shown in Figure 2.3, atmospheric CH_4 increased rapidly in 2007 with strong yearly global-average growth resuming resulting in a total rise of around 75 ppbv across the

2007 – 2017 period (Nisbet *et al.* 2019). The cause of this observed change is poorly understood and may be due to several factors (or a combination of these), including increased emissions from biogenic sources (Nisbet *et al.* 2016), increased emissions from the use of natural gas and oil (e.g Hausmann *et al.* 2016) or a reduction in the oxidative capacity of the atmosphere, whereby the rate at which CH_4 is removed by chemical reaction has declined (e.g. Rigby *et al.* 2017).

CH_4 has an atmospheric lifetime of around 8 years (Lelieveld *et al.* 1998) defined by its atmospheric burden and rate of removal by chemical interactions in the troposphere and stratosphere. The main sink of CH_4 is oxidation by hydroxyl radicals (OH) in the troposphere (e.g. Prather *et al.* 2012) and stratosphere, which removes 9% of the total CH_4 burden in the atmosphere each year (Ciais *et al.* 2013). Further sinks include the reaction of CH_4 with chlorine (Cl) radicals and atomic oxygen O(1D) in the stratosphere (Neef *et al.* 2010), the reaction with Cl in the marine boundary layer (Allan et al. 2007) and oxidation by methanotrophic bacteria in soils (Ito and Inatomi 2012).

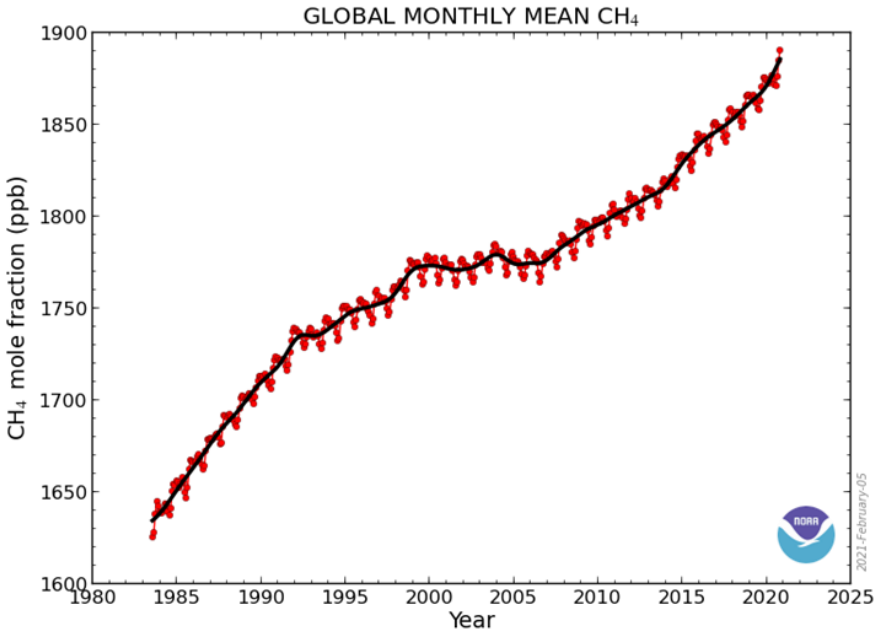

Figure 2.3: Globally-averaged monthly-mean atmospheric CH_4 abundance from 1983 to 2021 measured by The Global Monitoring Division of NOAA's Earth System Research Laboratory. Values for the last year are preliminary pending quality control steps. Figure taken from www.esrl.noaa.gov/gmd/ccgg/trends_ch4/ by Ed Dlugokencky, NOAA/Global Monitoring Laboratory.

CH_4 mixing ratios decrease with height throughout the atmosphere due to reaction with OH, which results in the production of CO_2 and H_2O. CH_4 has a marked interhemispheric gradient in surface mixing ratios, owing to stronger emission sources in the northern hemisphere, and a distinct seasonal cycle in atmospheric abundance. The stratospheric distribution of CH_4 characterises the effects of the dynamically forced Brewer-Dobson circulation cell, whereby the upward component transports high-CH_4 air from the tropical troposphere to the tropical stratosphere and the downward component transports low-CH_4 air to the extratropical latitudes, north and south of the equator (Remsberg 2015). CH_4 mixing ratios show higher concentrations in Arctic winter in comparison to Antarctic winter, owing to stronger downward circulation and wave activity in the northern hemisphere, which subsequently results in greater meridional mixing of high-CH_4 air from lower latitudes into the Arctic (Remsberg 2015).

2.2 Earth's energy balance

The Earth's energy balance is determined by the flux of incoming and outgoing radiation measured at the TOA. In an equilibrium state, incoming solar radiation balances the outgoing flux of reflected solar radiation (RSR) and outgoing longwave radiation (OLR) emitted by the Earth system.

Figure 2.4 details the different components of the Earth's energy balance, along with the current estimate of the global annual-mean magnitude of each flux at the beginning of the 21st century (from Wild *et al.* 2019). At the mean distance from the Sun, the Earth receives around 1361 W m^{-2} of incident solar irradiance (Kopp and Lean 2011). When averaged across the Earth's surface area this amounts to around 340 W m^{-2} of solar energy arriving at the TOA. About 30% of this incident energy is reflected back to space due to bright surfaces such as clouds, snow, ice and deserts. About 240 W m^{-2} is left available to the climate system, where around 80 W m^{-2} is absorbed by the atmosphere and 160 W m^{-2} by the surface. The surface also receives a downward flux of thermal radiation emitted by the atmosphere (around 342 W m^{-2}), due to emission by GHGs and clouds.

The outgoing flow of energy leaving the surface is partitioned into sensible and latent heat fluxes and, most predominantly, the upward emission of thermal radiation at 398 W m^{-2}. The magnitude of thermal radiation leaving the surface is substantially larger than the magnitude of thermal radiation emitted to space at the TOA (239 W m^{-2}). Around 159 W m^{-2} is absorbed in the intervening

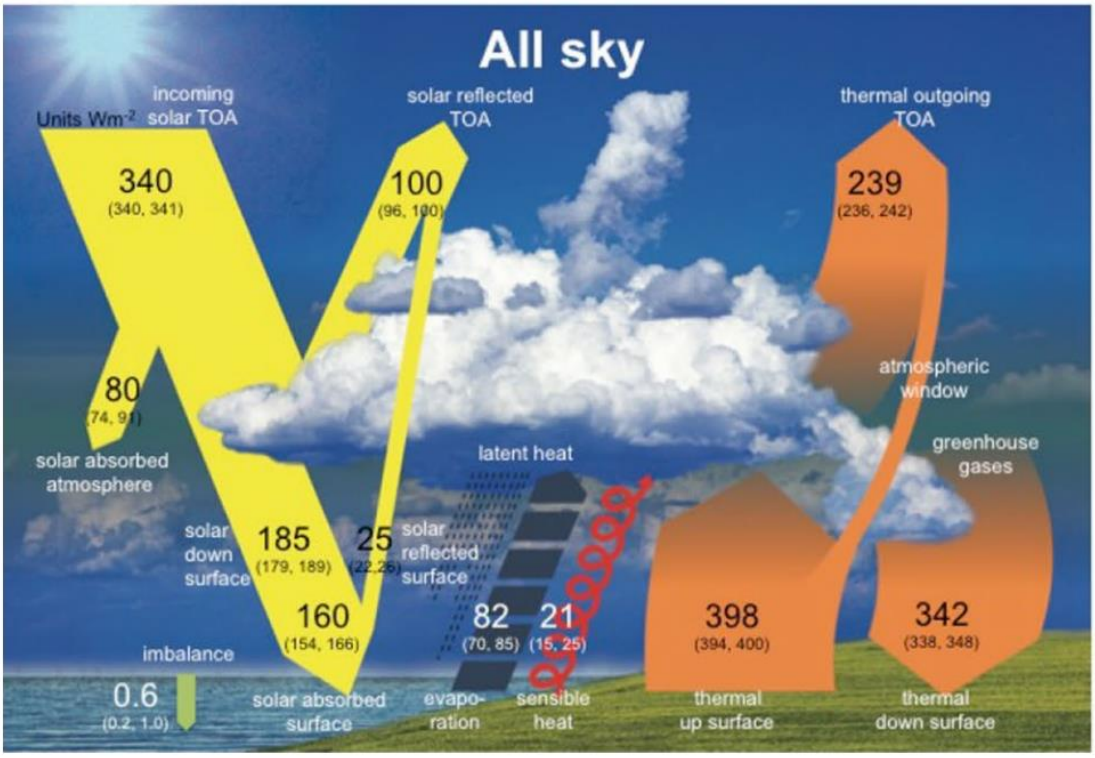

Figure 2.4: Diagram of the global annual-mean energy balance under all-sky conditions for present day climate at the start of the 21st century. Each number represents the best estimate of the magnitude of each component of the Earth's energy balance (in W m^{-2}). Uncertainty ranges correspond to those given in Wild et al. 2013b. Taken from Wild et al. 2019, adapted from Wild et al. 2015.

atmosphere by the presence of GHGs, which act to reduce the outgoing flow of thermal radiation to space. This so-called 'greenhouse effect' is a natural phenomenon driven largely by H_2O and CO_2 and is essential for making Earth habitable.

Since the start of the industrial revolution (around 1750) human activities have released increasing quantities of GHGs into the atmosphere. This further reduces the flux of outgoing thermal radiation leading to a radiative imbalance at the TOA. This perturbation to the radiation budget (with more energy entering the system than leaving) is termed the Earth's Energy Imbalance (EEI; Hansen *et al.* 2011). Since Figure 2.4 represents the magnitude of fluxes at the start of the 21st century, the impact of anthropogenic GHG emissions on the energy balance is implicit. Here, the estimated value of EEI is 0.6 W m^{-2} (Hansen *et al.* 2011; Loeb *et al.* 2012; Wild *et al.* 2013a).

EEI is the fundamental metric defining the rate and magnitude of climate change, which occurs as the system adjusts to re-establish radiative equilibrium. This manifests as a change in ocean heat content (most predominantly) (Lyman *et al.* 2010; Levitus *et al.* 2012), increased global-mean surface temperature, sea-level rise and changes in the global hydrological cycle (Dunn *et al.* 2020).

Accurately quantifying EEI is essential in monitoring the extent and predicting the evolution of climate change. Definitively, this relies on the accurate quantification of the energy fluxes flowing into, within and out of the Earth system.

Considerable progress in constraining the Earth's energy balance has been made since the start of the satellite era in the 1970s. In particular, measurements from missions such as the Earth Radiation Budget Experiment (ERBE; Barkstrom 1984), and the more recent Clouds and Earth's Radiant Energy System (CERES; Wielicki *et al.* 1996) and the Solar Radiation and Climate Experiment (SORCE; Anderson and Cahalan 2005) have allowed for significant improvement of the quantification of TOA radiative fluxes (Loeb *et al.* 2012, 2018). These missions provide essential daily observations of variations in energy fluxes at the regional and global scale. All recent studies of energy balance components derive TOA fluxes from either the CERES energy balanced and filled (EBAF) data set (Loeb *et al.* 2009) or SORCE, resulting in estimates that converge within a couple of W m^{-2} (Trenberth *et al.* 2009; Stephens *et al.* 2012; L'Ecuyer *et al.* 2015; Wild *et al.* 2015 for further discussion see Wild 2017). The incoming solar TOA flux of 340 W m^{-2} in Figure 2.4 is based on SORCE (Kopp and Lean 2011) and has a small uncertainty of ± 0.1 W m^{-2} (presented here with a rounded uncertainty range from 340 to 341 W m^{-2}). Both the RSR and OLR fluxes are estimated from CERES-EBAF with a 2-sigma uncertainty range, from 96 - 100 W m^{-2} and 236 - 242 W m^{-2}, respectively (see Wild *et al.* 2013b). Notably, these ranges are both orders of magnitude larger than EEI itself (0.6 W m^{-2}). Consequently, EEI cannot be accurately resolved through TOA satellite measurements alone. EEI must be constrained by in-situ measurements of ocean heat content, where over 90% of the positive energy imbalance is stored due to the large mass and high heat capacity of the global oceans (Lyman *et al.* 2010; Levitus *et al.* 2012; Rhein *et al.* 2013). Despite the progress provided by space-borne instruments in measuring TOA fluxes, greater uncertainty is attributed to RSR and OLR estimates due to the more limited global coverage afforded by networks of ground-based instruments (especially over the oceans). Subsequently, the estimation of fluxes within the Earth system, *particularly at the surface*, remains the most uncertain. Thus, these components are inferred from a combination of satellite measurements, physical models and ground-based observations. Deriving accurate surface estimates remains a challenge and large discrepancies of up to 15 W m^{-2} are evident in independent estimates of the net surface radiation budget (Trenberth *et al.* 2009; Stephens *et al.* 2012; L'Ecuyer *et al.* 2015; Wild *et al.* 2015; Wild 2017). Such disagreements have further implications for the accurate representation of the global energy balance in climate models - a fundamental pre-requisite for reliable simulations. The latest generation of state-of-the-art Earth system models (ESMs) participating in the 6th phase of the Coupled Model Intercomparison Project (CMIP6; Eyring *et al.* 2016) exhibit an inter-model spread of global energy balance components on

the order of 10-20 W m^{-2} (Wild 2020). Accurately quantifying and representing each component of the Earth's energy balance in ESMs remains an active area of research.

In order to fully understand the implications of the absorption of SW radiation by CH_4, it is necessary to review the energy balance components of particular interest to this thesis in further detail. The flux of incoming solar radiation and the atmospheric absorption of solar radiation are discussed in the following sections.

2.2.1 Incoming solar radiation

The Sun emits radiation approximately as a blackbody of temperature ≈5800 K (e.g. Petty 2006). The irradiance (E) emitted by a blackbody is given by Stefan's Law:

$$E = \sigma T^4 \quad (W\ m^{-2}) \tag{2.1}$$

where σ is the Stefan-Boltzmann constant (5.67 x 10^{-8} W m^{-2} K^{-4}) and T is temperature (in K). Considering the surface area of the Sun ($4\pi r_{Sun}^2$), and the mean distance across which the Sun's energy radiates before being intercepted by the Earth ($4\pi r_d^2$), if the Sun is assumed to emit as a blackbody the total solar irradiance (TSI) arriving at the TOA is given by:

$$TSI = \sigma {T_{Sun}}^4 \frac{r_{Sun}^2}{r_d^2} \quad (W\ m^{-2}) \tag{2.2}$$

where T_{Sun} is the Sun's temperature, r_{Sun} is the radius of the Sun (6.96 x 10^5 km) and r_d is the mean Sun-Earth distance (1.496 x 10^8 km).

TSI has been measured continuously since 1978 by a number of satellite instruments. Figure 2.5a presents the variation in TSI estimates with time, and notably, the successive decline in its measured value. Whilst TSI does naturally vary (Figure 2.5b), early estimates of around 1365 W m^{-2} have now been proven to be erroneously high due to the effects of uncorrected scattering and diffraction in instrument design (Kopp and Lean 2011). Despite this, these estimates remain vital for the construction of a continuous record of solar irradiance (Figure 2.5b). Reanalysis of early TSI datasets can be adjusted to account for instrument bias to form a composite record from which natural

variability in solar output can be monitored (Kopp *et al.* 2007; Kopp *et al.* 2016; Dudok de Wit *et al.* 2017).

The current TSI value of 1361 ± 0.5 W m^{-2}, measured by the Total Irradiance Monitor (TIM) onboard SORCE, is now widely acknowledged to be the most accurate estimate of current irradiance to date (Kopp and Lean 2011; Kopp 2016; Coddington *et al.* 2016; Dudok de Wit *et al.* 2017). This value represents the amount of average solar energy incident on a unit area of Earth at the TOA. Therefore, the average energy incident across the entire surface area of Earth's sphere is given by:

$$\frac{TSI\ \pi r_e^2}{4\pi r_e^2} = \frac{TSI}{4}\ \ (W\ m^{-2}) \tag{2.3}$$

where r_e is the Earth's radius (6373 km).

Thus, the average solar irradiance incident on the Earth is 340 ±0.1 W m^{-2} (L'Ecuyer *et al.* 2015; Loeb *et al.* 2018; Wild *et al.* 2015, 2019). As the primary flux of energy into the Earth system the known accuracy of this value is of vital importance. Consequently, it is well specified in ESMs, with a CMIP6 multi-model mean of 340.2 W m^{-2} (Wild 2020).

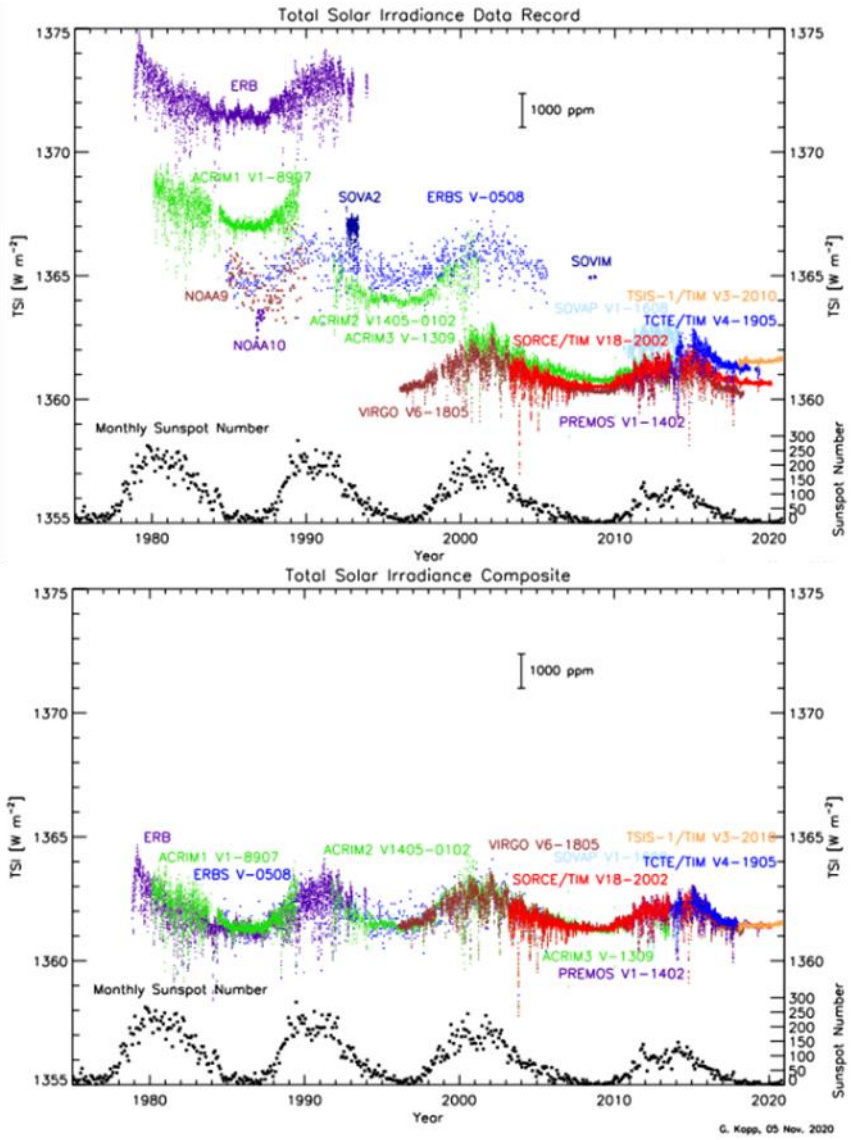

Figure 2.5: a) TSI measurements from 1978 to present as observed by overlapping satellite missions showing the decreasing trend in estimated TSI with time (originally published in Kopp et al. 2016). b) composite TSI climate record following the adjustment of TSI datasets to account for instrument error. Note that fluctuations in measured TSI (of around 0.1%) are in phase with the natural variability of the 11-year solar cycle indicated by the monthly sunspot number. Both figures are updated to November 2020 by G.Kopp via https://spot.colorado.edu/~koppg/TSI/index.html.

Solar irradiance is emitted across different wavelengths in the electromagnetic spectrum. The spectral variation of irradiance with wavelength, known as solar spectral irradiance (SSI), is approximated by the Planck Function $B_\lambda(T)$ (shown in Figure 2.6) where:

$$B_\lambda(T) = \frac{2hc^2}{\lambda^5 \left(e^{hc/(k_B \lambda T)} - 1\right)} \; (W\, m^{-2}\, m^{-1}) \tag{2.4}$$

where λ is wavelength (in metres), c is the speed of light (2.998 x 10^8 m s^{-1}), h is Planck's constant (6.626 x 10^{-34} J s) and k_B is Boltzmann's constant (1.381 x 10^{-23} J K^{-1}). Figure 2.6 shows the spectral distribution of blackbody radiation of T ≈5800 K as a function of wavelength. The maximum intensity of this distribution occurs in the visible part of the electromagnetic spectrum (0.4 – 0.7 µm).

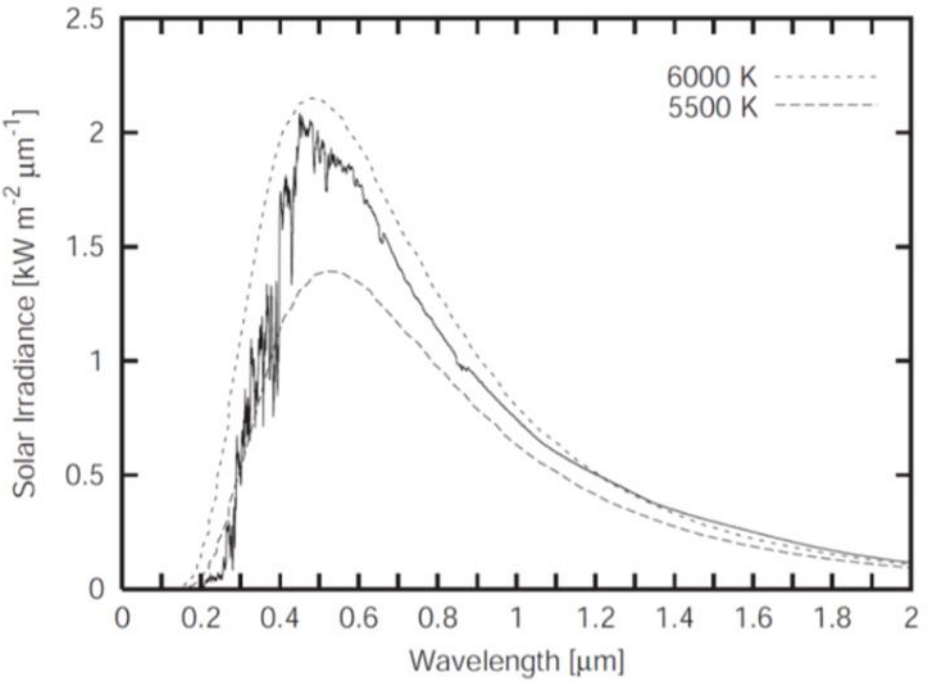

Figure 2.6: Spectral variation of energy emitted by the Sun (T = ≈5800 K) at the Earth's TOA (solid black curve) in kW m^{-2} μm^{-1}. Dashed curves represent the spectrum of blackbody emission at temperatures 6000 K and 5500 K. From Petty 2006.

Understanding and quantifying the spectral variation of solar irradiance is essential in climate research since GHGs, aerosols and clouds scatter and absorb solar radiation across particular wavelength regions depending on their spectral characteristics and physical properties. About 8% of solar irradiance lies in the ultraviolet (UV) region from 0.01 – 0.4 μm (e.g. Petty 2006). UV radiation is strongly absorbed by molecular oxygen (O_2) and ozone (O_3) in the mesosphere and stratosphere, respectively. This alters the chemical composition of the middle-atmosphere through photochemical reactions and causes heating, which in turn influences dynamics (Zhong *et al.* 2008). Consequently, changes in TOA UV radiation over the course of the 11-year solar cycle affect these mechanisms and impact atmospheric heating rates (Haigh 1994). 39% of the Sun's energy is emitted in the visible (VIS) region across 0.4 – 0.7 μm (e.g. Petty 2006), which the Earth's atmosphere absorbs relatively little of in cloud-free (clear-sky) conditions, and hence, most of this radiation is transmitted to the surface. Around 53% of SSI is emitted at solar infrared wavelengths (0.7 – 1000 μm; Petty 2006), namely at NIR wavelengths from 0.7 – 4 μm, i.e. the region of specific focus in this thesis. Unlike the visible, the atmosphere is not homogenously transparent to NIR radiation and this region displays significant atmospheric absorption, principally by H_2O. However, CO_2, CH_4 (*of special interest to this thesis*) and N_2O also exhibit important NIR absorption features. The amount of solar irradiance at wavelengths greater than 4 μm (0.9%; Petty 2006) is considerably less than the NIR. Nevertheless, as demonstrated in Section 5.3, this region also exhibits important absorption features for CH_4 that play a significant role in determining the magnitude of methane's SW RF.

It is essential to quantify the distribution of SSI arriving at the TOA in order to accurately model the attenuation of solar radiation through the atmosphere. SSI has been observed from the ground (e.g. Burlov Vasiljev *et al.* 1995; Menang *et al.* 2013), the atmosphere (Arvesen *et al.* 1969) and from space (Thuillier *et al.* 2003; Thuillier *et al.* 2014; Richard *et al.* 2016, 2018) over the last 5 decades. However, constructing a reliable SSI composite record remains challenging. Many satellite-based measurements concentrate on observing the UV and VIS (e.g. Fligge *et al.* 2001) resulting in a lack of high-resolution observations of the NIR. Many ESMs therefore use SSI data derived from semi-empirical models (which derive variations in SSI from models of the solar photospheric magnetic field with a radiative transfer code and observed spectra, e.g. Kurucz and Bell 1995; Fontenla *et al.* 2006; Ball *et al.* 2014) or composite records, which combine multiple datasets of observed SSI to construct a more reliable spectrum (Coddington *et al.* 2016).

The lack of observed NIR data was primarily addressed by the development of the ATLAS3 (ATmospheric Laboratory for Applications and Science) spectrum from Thuillier *et al.* (2003), updated by Thuillier *et al.* (2014), which measured SSI out to 2.4 μm from the SOLSPEC (SOLar SPECtrum) space-based instrument. However, a lack of consensus between ATLAS3 and

independent ground-based measurements across 1.4 – 2.5 µm (Bolsée *et al.* 2014; Elsey *et al.* 2017; Pereira *et al.* 2018) have challenged the reliability of this dataset. More recent measurements from the SOLSPEC instrument and the Total and Spectral solar Irradiance Sensor (TSIS-1) mission, both flown onboard the International Space Station (ISS), have provided new reference spectra covering the NIR region, known as the SOLAR-ISS (Meftah *et al.* 2020) and TSIS-1 Hybrid Solar Reference Spectrum (HSRS; Coddington *et al. submitted manuscript 2021*), respectively. Meftah *et al.* (2020) demonstrate good agreement between TSIS measurements and SOLAR-ISS (V2.0) for most wavelengths above 1.5 µm and report further consistency with ground-based measurements from the Continuum Absorption in the Visible and Infrared and Atmospheric Relevance (CAVIAR 2) project (Elsey *et al.* 2017) and the PYR-ILIOS SSI NIR campaign made at the Mauna Loa observatory (Pereira *et al.* 2018).

2.2.2 Atmospheric absorption of solar radiation

Atmospheric absorption of solar radiation is dependent on several factors such as, cloud height and type, the presence of aerosols, the reflectivity of the Earth's surface, and crucially, the vertical distribution and concentration of GHGs.

Figure 2.7 shows the vertical transmittance of the clear-sky atmosphere as a function of wavelength for a range of gaseous absorbers along with the total combined effect of all constituents (lower panel). Where atmospheric absorption is strong at a given wavelength, the transmittance of solar irradiance is small or reduced to zero. Strong UV absorption due to stratospheric O_3 is evident at wavelengths less than 0.35 µm. Crucially, this ensures that little of the damaging UV energy emitted by the Sun reaches ground-level, where it would otherwise be harmful to living organisms. Across the NIR, considerable absorption occurs by H_2O in particular. This results in a distinctive spectral structure of absorption 'bands', where no solar irradiance reaches the surface, and atmospheric 'windows', where absorption is significantly weaker, and the majority of solar irradiance is transmitted to the surface. This banded structure arises due to water vapour's three modes of vibration that determine the position of absorption bands in this spectral region. On interaction with solar NIR radiation, H_2O undergoes many transitions in its rotational-vibrational energy levels resulting in thousands of spectral lines of absorption attributed to various combinations of vibrational modes superimposed on the many possible rotational transitions. In addition to these sharp spectral features, H_2O possesses a continuum of absorption across both the band and window regions throughout the entire spectrum from the VIS (albeit weakly) to the infrared and microwave

regions. The physical cause of this feature may have its origins in the far-wing lines shapes of H_2O transitions and/or the spectral features due to short-lived water dimers and bound complexes of water vapour and other molecules, such as nitrogen (N_2) and O_2 (for further discussion see Shine *et al.* 2012).

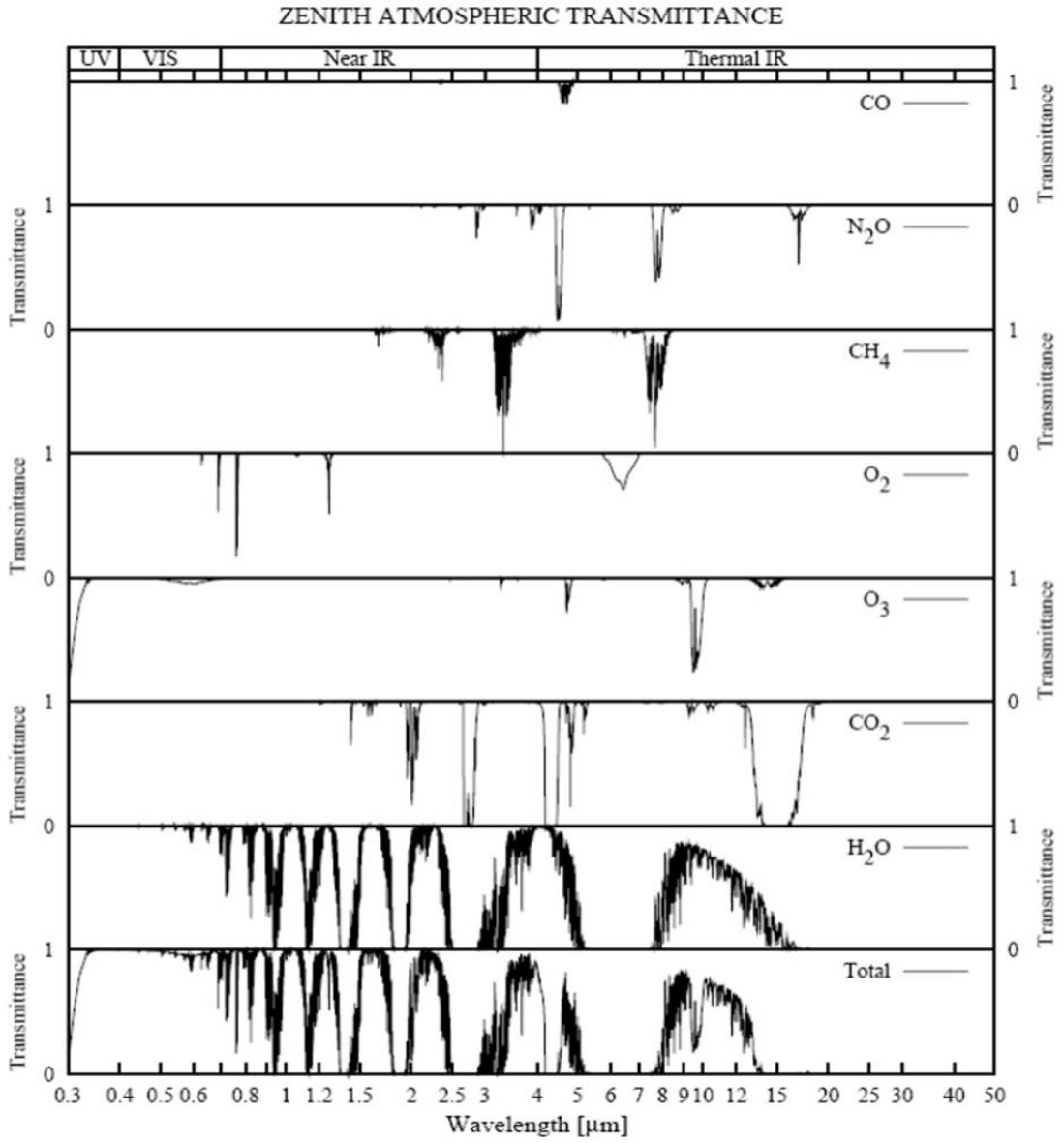

Figure 2.7: Zenith transmittance spectrum of a clear-sky (aerosol free) mid-latitude summer atmosphere. Upper panels depict absorption features of individual gases as if they were the only absorber present in the atmosphere. The lowest panel depicts the combined effect of all gases. Note that the effects of molecular scattering are not included in this figure and this depiction is highly smoothed. Taken from Petty 2006.

In total, H_2O is responsible for around 60% of the atmospheric absorption of solar irradiance (Kiehl and Trenberth 1997). This is largely attributed to spectral lines within the NIR band regions (e.g. Collins *et al.* 2006a) where absorption is *much* stronger than the H_2O continuum. As a result, the continuum plays a secondary role in absorption at these wavelengths, and consequently, has more significance to the energy balance across the window regions, particularly under clear-sky conditions (Ptashnik *et al.* 2012; Rädel *et al.* 2015). This significance is enhanced in a warming climate in the context of the water vapour feedback where atmospheric concentrations of H_2O increase in response to increased atmospheric temperatures (Held and Soden 2000; Allen and Ingram 2002; Rädel *et al.* 2015).

In addition to the effects of H_2O, gases such as CO_2, CH_4, N_2O and O_3 also exhibit absorption bands across the NIR (see Figure 2.7). The strength of these bands is determined by their individual spectroscopic characteristics and the degree of spectral overlap with coinciding absorbers, particularly H_2O. As explained in more detail in Section 2.3.2, in the case of CH_4, the strong band at 3.3 μm is located within a region of comparatively strong H_2O absorption, this weakens its effect on SW radiative fluxes at heights in the atmosphere where concentrations of H_2O are high, such as the tropical troposphere (e.g. Etminan *et al.* 2016). However, the spectroscopically weaker bands positioned at 1.6 and 2.3 μm lie towards the window regions of the H_2O spectrum. Their strength is not as muted by the spectral overlap with H_2O. As shown by Etminan *et al.* (2016), this increases the significance of their role in SW absorption and ultimately, methane's impact as a climate forcer.

Detailed studies of the atmospheric absorption of solar radiation are important. Under anthropogenic climate change the amount of solar radiation absorbed throughout the atmosphere will evolve with increasing concentrations of GHGs. In addition to altering the total amount of SW radiation absorbed by the atmosphere, this will crucially alter the amount of solar irradiance incident on the surface (Trenberth *et al.* 2009). This has important implications for the surface energy budget and the partitioning of sensible and latent heat fluxes, which ultimately drive the global hydrological cycle (Collins *et al.* 2006a; Takahashi 2009; O'Gorman *et al.* 2012; DeAngelis *et al.* 2015; Myhre *et al.* 2018). The current best estimate of atmospheric SW absorption (80 W m^{-2}) is obtained as a residual from differencing the current estimate of TOA (240 W m^{-2}) and surface absorbed (160 W m^{-2}) solar radiation (Wild *et al.* 2015, 2019; Wild 2020). This estimate is therefore derived from both satellite measurements (e.g. Loeb *et al.* 2009) and ground-based observations of downwelling surface radiation, from initiatives such as the Baseline Surface Radiation Network (BSRN; Ohmura *et al.* 1998) and the Global Energy Balance Archive (GEBA; Gilgen *et al.* 1998). An independent estimate from Kim and Ramanathan (2008) of 79 W m^{-2} shows closes agreement to

the value given by Wild (2020), and therefore quantitatively supports the magnitude of this component of the energy balance.

2.3 Radiative Forcing

RF refers to the change in net (downward minus upward) radiative flux (W m^{-2}) at the tropopause or TOA following a perturbation to the energy balance (Myhre *et al.* 2013a). In this chapter RF will be assumed to refer to the global-annual mean unless specified otherwise.

RF is used extensively to quantitatively compare the strength of anthropogenic and natural drivers of climate change, and to a first order, is a useful predictor of the GMST response to climate change (Forster *et al.* 2007; Myhre *et al.* 2013a).

RF can be linearly related to the equilibrium GMST change (ΔT_S) by:

$$\Delta T_S \approx SRF \tag{2.5}$$

where S is the climate sensitivity parameter (K (W m^{-2})$^{-1}$) and is defined as the change in equilibrium annual GMST in response to a unit change in RF. The magnitude of S is an important component in assessing the scale of climate change. However, the absolute value of S itself remains uncertain. This is attributed to the complex nature of the climate system and the interdependence of internal feedback mechanisms that respond to changes in the energy balance, such as changes in cloud cover, surface albedo and lapse rate. S may also evolve with the time-dependent response of the climate system to an imposed forcing, especially for example, with respect to the ocean (e.g. Senior and Mitchell 2000; Williams *et al.* 2008; Andrews *et al.* 2015). Thus, calculating S is a complex matter. ESMs are a useful tool for estimating S given their global resolution and ability to approximate the physical processes that are sensitive to radiative perturbations. Yet differences in the parameterisation of such processes, in particular cloud feedbacks, has led to a wide range of S estimates across different ESMs (Flato *et al.* 2013) and different forcing agents (Forster *et al.* 2007). Calculation of the closely related quantity 'effective climate sensitivity' (ECS; diagnosed from quadrupling CO_2 experiments) shows that this divergence persists in models participating in CMIP6, with ECS values ranging from 1.8 – 5.6 K across 27 ESMs (Zelinka *et al.* 2020). Whilst recent efforts

to constrain climate sensitivity appear encouraging (by combining of multiple lines of evidence from ESMs, process-resolving models, observations and theory (see Sherwood *et al.* 2020; Stevens *et al.* 2016), it remains the case that differences in projections of ΔT_S among ESMs can arise from differences in S and/or RF. Consequently, this establishes RF as a more useful metric than ΔT_S in quantifying the relative importance of drivers of climate change.

Several definitions of the RF concept have been published by successive iterations of IPCC reports following the development of scientific knowledge. Figure 2.8 shows this evolution (from left to right) and depicts the key components involved in the calculation methodology of each definition.

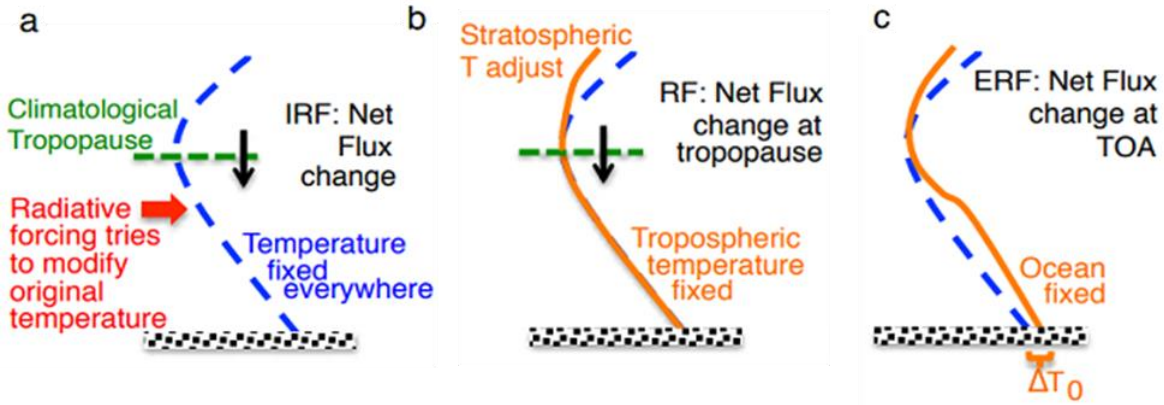

Figure 2.8: RF definitions: a) instantaneous RF (IRF) calculated online or offline as the difference between two sets of radiative transfer calculations whereby all variables are identical except the imposed forcing agent. b) stratospheric temperature-adjusted RF (SARF) calculated as the difference between two offline radiative transfer calculations with surface and tropospheric temperatures held fixed at unperturbed values. c) effective RF (ERF) calculated using dedicated ESM simulations where all rapid adjustments are included (including land-surface temperature) with SST and ice-cover fixed at climatological values (where ΔT_0 represents the land temperature response). Note that the calculation of ERF does not require the definition of a tropopause, which can be ambiguous to define in both the calculation of IRF and RF. Adapted from Myhre et al. 2013a.

The first (and most simple) definition of RF introduced by the IPCC is termed 'instantaneous radiative forcing' (IRF). This refers to an instantaneous change in net (downwards minus upwards) radiative flux at either the TOA or tropopause, with the latter providing a better indication of ΔT_S due to the radiative-convective coupling of the surface-troposphere system. As Figure 2.8a shows, this calculation involves holding the atmospheric profile of temperature fixed to its unperturbed state. However, as several studies demonstrate (e.g. Pinnock *et al.* 1995; Hansen *et al.* 1997a; Shine and

Forster 1999), the magnitude of RF can be more accurately represented when stratospheric temperatures are allowed to re-adjust to radiative equilibrium. This process takes place on much faster timescales (months) than the slowly evolving response of the surface-troposphere system (decades), which is dictated by the thermal inertia of the global oceans (Hansen *et al.* 1997b). For climate forcers such as CO_2 and O_3 (which have large radiative impacts on the stratosphere) this adjustment is important (e.g. Shine and Forster 1999). In the third (TAR; Ramaswamy *et al.* 2001) and fourth (AR4; Forster *et al.* 2007) IPCC reports RF was re-termed the 'stratospheric temperature adjusted radiative forcing' (henceforth referred to as SARF in this thesis) and redefined as the change in net irradiance at the tropopause after allowing for stratospheric temperatures to readjust to reach global-mean radiative equilibrium, while holding surface and tropospheric temperatures at unperturbed values (Figure 2.8b; Myhre *et al.* 2013a). Because stratospheric temperatures are allowed to adjust, this approach yields an identical net forcing at both the TOA and tropopause. The method for calculating SARF is discussed in more detail in Section 3.2.

The concept of RF has since been further refined to encompass the radiative effects of other processes that occur on faster timescales than the GMST response to a climate forcing. These processes, often termed 'rapid adjustments' typically occur over periods of weeks/month and include, for example, tropospheric temperature, albedo, H_2O and clouds. Due to their additional impact on the energy budget these adjustments are commonly considered a part of the initial climate forcing (Gregory *et al.* 2004). Including such processes in forcing calculations has been shown to improve the utility of RF in predicting ΔT_S due to more uniform S estimates across different forcing agents (Boucher *et al.* 2013; Myhre *et al.* 2013a; Marvel *et al.* 2016 Richardson *et al.* 2019). Two main modelling methods are used to compute this so-called 'effective radiative forcing' (ERF): (1) the 'linear regression' approach, which involves regressing the net change in TOA irradiance against the transient global mean surface temperature response following an abrupt increase in forcing agent, with ERF diagnosed when ΔT_S = 0 (Gregory *et al.* 2004) or (2) the 'fixed-SST' approach, which specifies sea-surface temperature (SST) and sea-ice cover at fixed climatological values and calculates ERF as the change in net radiative flux at the TOA after allowing all other system components to respond to an imposed perturbation (Hansen *et al.* 2005). An important advantage of the fixed-SST approach is better characterisation of uncertainty. Forster *et al.* (2016) show that 30 years of model simulation are sufficient to diagnose ERF to better than 0.1 W m^{-2} at the 95% confidence level; attaining a similar level of uncertainty with the linear-regression approach requires more than 45 ESM ensemble members of 20 year simulations. The fixed-SST approach can also be used to estimate transient ERF from a simulation with time-varying perturbations (Andrews and Ringer 2014), this diagnostic is particularly useful in assessing the

contribution of different forcing mechanisms to the historical evolution of climate. However, as land-surface temperature responses are permitted in the estimation of fixed-SST ERF (which affects ΔT_S), a clean separation of adjustments from global temperature change is not fully satisfied without accounting for the related changes associated with the land-surface response (Sherwood *et al.* 2015; Tang *et al.* 2019). More recently, ESM calculations of ERF fixing both land and SSTs have been reported for CO_2 and solar forcings (Andrews *et al.* 2021). The linear regression approach includes both land and SST responses in estimating the ERF for a zero-surface temperature change.

Figure 2.8c depicts the fixed-SST approach used by the IPCC fifth assessment report (AR5; Myhre *et al.* 2013a), defined specifically in this report as the change in net radiative flux at the TOA after allowing for atmospheric temperature, H_2O and clouds to adjust to an imposed perturbation, whilst SST and sea-ice cover remain fixed. Note that the calculation of ERF does not require the definition of a tropopause, which can be ambiguous to define. As stated in IPCC AR5, diagnosing ERF using the fixed-SST method was available for a wider variety of forcing agents in models participating in the 5th phase of CMIP experiments (CMIP5; Taylor *et al.* 2012) in comparison to the linear-regression method. Practically, this established the fixed-SST approach as the method of choice in IPCC AR5.

Figure 2.9 shows the IPCC AR5 estimate of the sign and magnitude of natural and anthropogenic forcers of climate due to their change in atmospheric concentration between 1750 and 2011. Such a comparison provides an indication of the significance of different forcing mechanisms across the pre-industrial to present day period. ERF estimates are given as solid bars (with uncertainties denoted by solid lines) and SARF estimates are given as hatched bars (with uncertainties denoted by dotted lines). The estimate of ERF and SARF are identical for CO_2 and well-mixed GHGs (WMGHGs, i.e. GHGs that have lifetimes long enough to be homogeneously mixed throughout the troposphere, including CH_4, N_2O and many halocarbons). This is owing to a lack of studies available at the time to assess rapid adjustments related to ERF. The 4 x CO_2 experiments of Vial *et al.* (2013) provide the main information from which CO_2 ERF is assessed in AR5; analysis from 11 CMIP5 models demonstrate that land-surface temperature adjustment contributes a negative component to CO_2 ERF, which is counterbalanced by positive components from a combination of lapse rate, H_2O, albedo and cloud adjustments (Myhre *et al.* 2013a). However, IPCC AR5 concluded that there was not enough information to evaluate if CO_2 ERF is greater than or less than CO_2 RF, resulting in an assessment of the ERF/RF ratio being equal to 1.0, with a larger uncertainty attributed to ERF. No studies of WMGHG ERF were available. Consequently, WMGHG ERF was assessed to be approximately equal to WMGHG SARF, albeit with a larger uncertainty.

The increase in atmospheric concentration of CO_2 (from 278 ppmv to 390.5 ppmv) leads to the largest forcing with a SARF of 1.82 (1.63 to 2.01) W m^{-2}. CH_4 contributes the second largest forcing due to an increase in concentration from 722 ppbv to 1803 ppbv, with a SARF of 0.48 ± 0.05 W m^{-2}; however, this estimate omits the effects of CH_4 SW absorption, as well as methane's indirect impacts on ozone and stratospheric water vapour. These are discussed further in Section 2.3.1. Total anthropogenic forcing is estimated at 2.3 (1.1 to 3.3) W m^{-2} under the assumption that different forcing mechanisms can be treated additively (Boucher and Haywood 2001; Forster *et al.* 2007). The large uncertainty attributed to total anthropogenic ERF is mainly caused by large uncertainty in aerosol forcing.

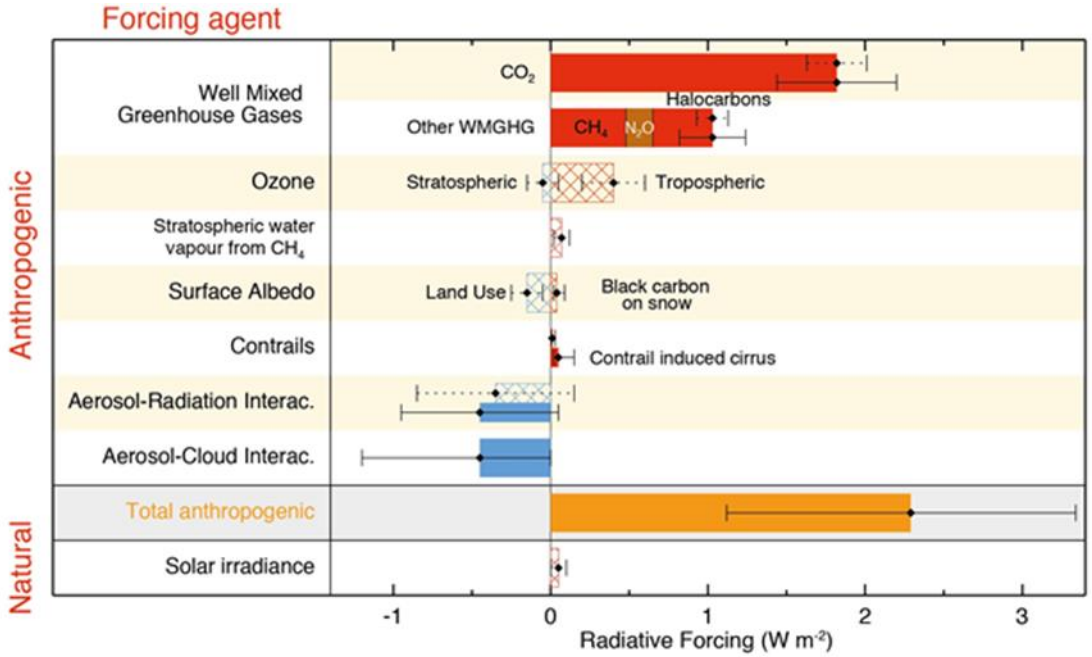

Figure 2.9: Bar chart showing estimates of SARF (hatched) and ERF (solid) for the period 1750 – 2011 for natural and anthropogenic forcers. Uncertainties are given at the 5 to 95% confidence range for SARF (dotted lines) and ERF (solid lines), adapted from Myhre et al. (2013a).

Since IPCC AR5 (Myhre *et al.* 2013a) there has been a focussed effort to further constrain ERF estimates. This has involved: comparing and evaluating diagnosis methods (e.g. Chung and Soden 2015b; Forster *et al.* 2016; Richardson *et al.* 2019; Tang *et al.* 2019), computing ERF for additional forcing mechanisms (Zelinka *et al.* 2014; Chung and Soden 2015a; Smith *et al.* 2018; Hodnebrog *et*

al. 2020; Andrews *et al.* 2021) and developing knowledge of the response of the climate system to an imposed forcing (e.g. Marvel *et al.* 2016; Sherwood *et al.* 2015). Furthermore, the Radiative Forcing Model Intercomparison Project (RFMIP; Pincus *et al.* 2016) has established protocols to ensure that ERF is consistently and routinely diagnosed by models participating in CMIP6. Previously, the lack of an agreed standard for diagnosing forcings made it challenging to compare ERF between different models (Forster *et al.* 2013) and attribute inter-model spread to a specific cause (Chung and Soden 2015b). CMIP6 modelling groups are asked to adopt the fixed-SST approach using at least a 30-year monthly-averaged climatology of SST and sea-ice distributions based on a model's specific preindustrial control simulation. This aims to limit unforced variability and improve the calculation of small ERF estimates (Pincus *et al.* 2016). RFMIP seeks to characterise global and regional ERF under present day, historical and future scenarios for the major RF groups including CO_2, GHGs, all anthropogenic forcers, land use, and combined changes in ozone and aerosol. The adjustments and ERF of different forcing agents can be isolated from fixed-SST simulations with the aid of offline radiative transfer models and the use of radiative kernels (e.g. Smith *et al.* 2018, 2020; Richardson *et al.* 2019; Tang *et al.* 2019), which approximate the change in TOA irradiance to a unit change in feedback variables (that change in response to global temperature change) such as atmospheric temperature, H_2O, surface albedo and clouds (for further detail see Chung and Soden 2015a). Such analyses aim to provide a more comprehensive quantification of ERF for the upcoming IPCC sixth assessment report (AR6) and address a key motivation of CMIP6: "How does the Earth system respond to forcing?"

Adjustments relating to a tripling of CH_4 concentrations have been calculated by Smith *et al.* (2018) in 11 ESMs using radiative kernels and the fixed-SST approach specified by RFMIP. However, only four models participating in this study include CH_4 SW absorption bands. Figure 2.10 demonstrates that the inclusion or omission of these bands dictates the magnitude of H_2O adjustment and whether stratospheric-temperature and cloud adjustments have a negative or positive effect on CH_4 forcing. Although uncertainties are large (see uncertainty bars on Figure 2.10) there is an indication that the total rapid adjustment (black bars) is negative when SW absorption is included and positive when it is not. These adjustments, of around +/-0.2 W m^{-2} can be compared with a multi-model mean IRF of 1 W m^{-2} for a 3 x CH_4 perturbation. Whilst this study progresses understanding of the nature of rapid adjustments related to CH_4, it highlights the need for modelling groups to ensure that SW absorption is explicitly treated within ESM radiative transfer codes, and importantly, that such codes are validated against more sophisticated radiative transfer models.

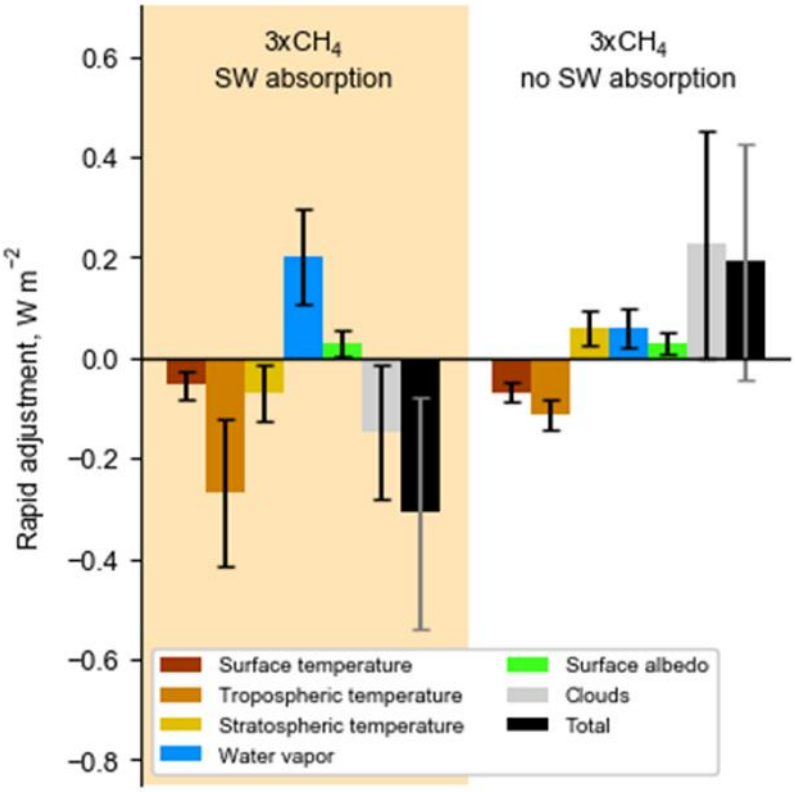

Figure 2.10: Individual CH_4 rapid adjustments for models that include and omit an explicit treatment of CH_4 SW absorption bands. ESMs that include such bands are: CanESM2, MIROC-SPRINTARS, MPI-ESM and NCAR-CESM1-CAM5, see Section 2.1 in Smith et al. (2018) for a full list of models participating in the study. Taken from Smith et al. (2018).

Despite ERF providing a better indication of the surface temperature response, calculation of IRF and SARF remain important and useful diagnostics of forcing mechanisms. Both IRF and SARF are much easier to isolate from two sets of offline (i.e. double-call) radiative transfer simulations and can be calculated at a higher spectral resolution than the current configuration of many ESMs. Section 4.3 demonstrates that the current 6-band version of the SOCRATES radiative transfer scheme (used in the Met Office's Unified Model (UM; Walters *et al.* 2019), is too coarse to fully capture the effect of CH_4 SW IRF, giving much lower values than benchmark calculations. The calculation of ERF also requires the use of computationally expensive ESMs to capture the effects of

rapid adjustments, with many years of simulation needed to reduce the influence of unforced variability, which makes the calculation of forcings of order 0.1 W m^{-2} or smaller difficult (Myhre *et al.* 2013a; Forster *et al.* 2016). Because of this, ERF calculations are often performed for larger perturbations (e.g. the 3 x CH_4 experiments in Smith *et al.* 2018) than have occurred in the recent past, or seem likely to occur in coming decades. This adds further uncertainty to their applicability to recent changes in climate. In order to quantify the effect of CH_4 SW absorption bands on RF and investigate related sensitivities in detail, it is necessary to perform RF calculations in the IRF and SARF framework. This thesis therefore focusses solely on diagnosing IRF and SARF. The CH_4 rapid adjustments of Smith *et al.* (2018) are not referenced further in Chapter 2.

2.3.1. CH_4 radiative forcing

IPCC AR5 (Myhre *et al.* 2013a) assess CH_4 SARF to be 0.48 (± 0.05) W m^{-2} due to an increase in atmospheric concentration from 722 ppbv to 1803 ppbv across 1750 to 2011. This headline value is calculated using the simplified expression of Myhre *et al.* (1998), given as:

$$\text{RF} = a\left(\sqrt{M} - \sqrt{M_0}\right) - \left(f\left(M, N_0\right) - f\left(M_0, N_0\right)\right) \tag{2.6}$$

where a is the constant 0.036, M is CH_4 in ppbv and N is N_2O in ppbv and $f(M, N)$ is the overlapping term from Hansen *et al.* (1988), which accounts for the effect of present day N_2O concentrations on CH_4 forcing:

$$f(M, N) = 0.47 \ln[1 + 2.01 \times 10^{-5} (MN) 0.75 + 5.31 \times 10^{-5} M (MN)^{1.52}] \tag{2.7}$$

Such expressions are commonly used for CH_4, CO_2 and N_2O and are derived from polynomial fitting of complex radiative transfer code calculations to express the relationship between RF and concentration over a range of pre-industrial and future concentration scenarios. For a weakly absorbing gas with low atmospheric concentrations, this relationship is found to be linear. For CH_4,

which exhibits significant TIR absorption at 7.7 μm (e.g. see Figure 2.7 and Section 2.1.1) and significant natural atmospheric concentrations, the forcing is found to be approximately proportional to the square root of its concentration. Simplified expressions show good agreement with LBL radiative transfer calculations (Myhre *et al.* 1998) and allow for a large number of WMGHG forcings to be calculated more easily in simple climate models.

CH_4 SARF can also be calculated with respect to its change in total emission since 1750. Figure 2.11 shows SARF over the industrial era by emitted species for well-mixed and short-lived gases. Calculating CH_4 SARF by emission leads to a forcing (0.97 W m^{-2}) almost double the magnitude of the forcing calculated from the concentration change (0.48 W m^{-2}; Myhre *et al.* 2013a – see Figure 2.9). This is because CH_4 emissions have an indirect effect on the energy balance through the production of CO_2, O_3 and stratospheric H_2O. Further indirect effects are related to emissions of carbon monoxide (CO) and non-methane volatile organic compounds (NMVOC), which influence the lifetime and increase the abundance of CH_4, and the emission of nitrogen oxides (NO_x) which reduce the lifetime and abundance of CH_4. This method of calculating SARF is much more complex to compute than the forcing derived from a change in atmospheric concentration because of such interactions between compounds (Myhre *et al.* 2013a). Whilst this method incorporates the full impact of CH_4 emissions on the Earth's energy balance, this thesis discusses and calculates CH_4 forcings solely with respect to concentration changes.

Both IPCC AR5 (Myhre *et al.* 2013a) estimates of CH_4 SARF are based entirely on CH_4 absorption of TIR radiation emitted by the Earth's surface and atmosphere. The role of CH_4 SW absorption bands and their impact on the forcing of climate are not considered. Recent studies by Etminan *et al.* (2016) and Collins *et al.* (2018) offer significant progress in addressing this research gap and demonstrate that omission of these bands lead to an underestimation of total CH_4 RF. This research highlights the need for a revised IPCC estimate that accounts for methane's SW effect. However, there is still significant uncertainty in the magnitude of this effect, driven by a lack of detailed sensitivity tests and disparity between the experimental approach of Etminan *et al.* (2016) and Collins *et al.* (2018). This is discussed further in Section 2.3.2. To the author's knowledge a detailed quantification of methane's SW radiative effect has not yet been conducted. This thesis provides such a detailed quantification by investigating key sensitivities such as CH_4 absorption of solar mid-infrared radiation between 5 – 10 μm, the vertical representation of CH_4 mixing ratios and the specification of surface albedo (see Section 1.2 and Chapter 5). Furthermore, it examines the impact of the SW effect on the spatial and seasonal variation of CH_4 SARF (see Section 6.3).

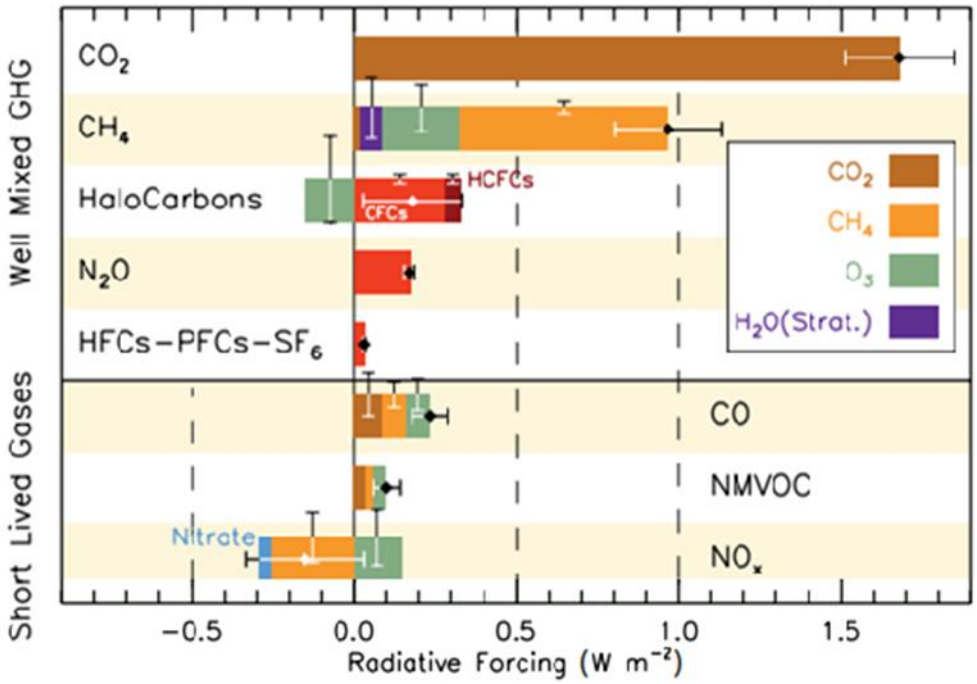

Figure 2.11: SARF bar chart for the period 1750 – 2011 based on emitted compounds for WMGHGs and short-lived gases. Several colours are used to indicate the emitted components that affect many other compounds (see inset), red (positive RF) and blue (negative RF) are used for components that affect few forcing agents. Vertical bars show relative uncertainty of RF caused by each component, whereby the length is proportional to bar thickness (i.e. for a ±50% uncertainty the full length is equal to the bar thickness). The net impact of individual contributions is given by the diamond symbol and its uncertainty (at the 95% confidence level) is given by the horizontal error bar. Adapted from Figure 8.17, Myhre et al. 2013a.

2.3.2 Current estimates of CH_4 SW radiative forcing

Etminan *et al.* (2016)

Etminan *et al.* (2016) demonstrate the significance of CH_4 SW absorption bands across the 0.2 – 5 µm spectral range using radiative transfer calculations performed by the Oslo LBL code (OLBL; Myhre *et al.* 2006). This study adopts the Myhre *et al.* (2006) two atmosphere (tropical/extratropical) approach to generate global-mean tropopause SW and LW IRF and LW SARF, calculated using the standard fixed dynamical heating (FDH) method (see Section 3.2). LW SARF calculations are performed with and without the inclusion of CH_4 SW absorption bands to demonstrate their role in stratospheric adjustment. Etminan *et al.* (2016) use spectroscopic data from the HITRAN2008 database (Rothman *et al.* 2009), include present-day natural and anthropogenic aerosols and represent surface albedo with broadband values taken from OsloCTM2 simulations (See Myhre *et al.* 2013b).

This study reports a positive CH_4 SW IRF of 0.03 W m^{-2} following a perturbation in idealised vertically-varying CH_4 from 750 ppbv to 1800 ppbv. This is a notable result in the context of previous studies. The idealised clear-sky LBL calculations conducted by Collins *et al.* (2006b) and Forster *et al.* (2011) indicate a negative, as opposed to positive, shortwave forcing for CH_4. Etminan *et al.* (2016) demonstrate that this switch in sign can be explained by the addition of clouds to the OLBL code, whereby the upward scattering of SW radiation acts to enhance CH_4 tropospheric absorption. They find that this mechanism causes the SW IRF to change from -0.045 W m^{-2}, under clear-sky conditions, to 0.03 W m^{-2}, under all-sky conditions. Figure 2.12 demonstrates the spectral nature of this positive forcing. The upper left-hand panel shows the variation of CH_4 SW tropopause IRF with wavelength. The upper right-hand and lower right-hand panels show the upwelling and downwelling components of this forcing, respectively. As shown, the sign of the SW forcing varies strongly with wavelength across the 1.7 µm, 2.3 µm and 3.3 µm absorption bands. The net forcing of each band depends on the strength of the negative downwelling forcing (due to increased absorption in the stratosphere) relative to the positive upwelling forcing (due to increased absorption in the troposphere). A net positive forcing at 1.7 µm and 2.3 µm dominates over a net negative forcing at 3.3 µm. As explained by Etminan *et al.* (2016), this contrasting behaviour is driven by the stratospheric opacity of CH_4 and the degree of overlap with H_2O absorption bands in the troposphere. The lower left-hand panel of Figure 2.12 shows the sum of absorption line strengths for CH_4 (black) and H_2O (blue) across the 1 – 5 µm spectral region. Both the 1.7 µm and 2.3 µm bands lie close to the centre of the H_2O window regions. Conversely, the 3.3 µm band lies within a region

of relatively strong H_2O absorption; this spectral overlap acts to mute the impact of increases in CH_4 concentration at 3.3 μm.

In total, Etminan *et al.* (2016) report a 25% increase in CH_4 1750 - 2011 SARF (from 0.48 W m^{-2} to 0.61 W m^{-2}) compared to the IPCC AR5 (Myhre *et al.* 2013a) value, of which more than half (15%) is due to the inclusion of CH_4 SW absorption bands. This substantial revision is due to methane's direct SW IRF and the warming impact of SW absorption in the stratosphere, which consequently increases the longwave CH_4 forcing (this effect is discussed in more detail in Section 5.2 and Section 6.3). However, a lack of detailed assessments of error sources for WMGHG SW forcings limits the understanding of the reliability of this estimate. The authors adopt an uncertainty of ± 25% on the SW radiative effect due to a range of factors including: the specification of surface albedo, the calculation of day-averaged forcings, and the impact of spatial and temporal averaging. Consequently, a more detailed quantification of methane's SW effect is needed.

Etminan *et al.* (2016) also update the simplified expression of Myhre *et al.* (1998) to incorporate the effect of CH_4 SW absorption and updates to the strength of the H_2O continuum (which also contributed to the 25% total increase in CH_4 SARF given above), giving the following equation:

$$\text{RF} = [a\overline{M} + b\overline{N} + 0.043]\left(\sqrt{M} - \sqrt{M_0}\right) \quad (2.8)$$

where a = -1.3 x 10^{-6} W m^{-2} $ppbv^{-1}$ and b = -8.2 x 10^{-6} W m^{-2} $ppbv^{-1}$and M is the concentration of CH_4 at the time in which the forcing is required and M_0 is the initial CH_4 concentration and $\overline{M}$ and $\overline{N}$ are the mean of the initial and final concentration of CH_4 and N_2O, respectively. This new expression is proven to calculate CH_4 forcings to within better than 5% of OLBL derived forcings across a range of concentration changes covering the lowest values of CH_4 as found in ice-core records (340 ppbv) to the highest projected amount in 2300 (3500 ppbv; Etminan *et al.* 2016).

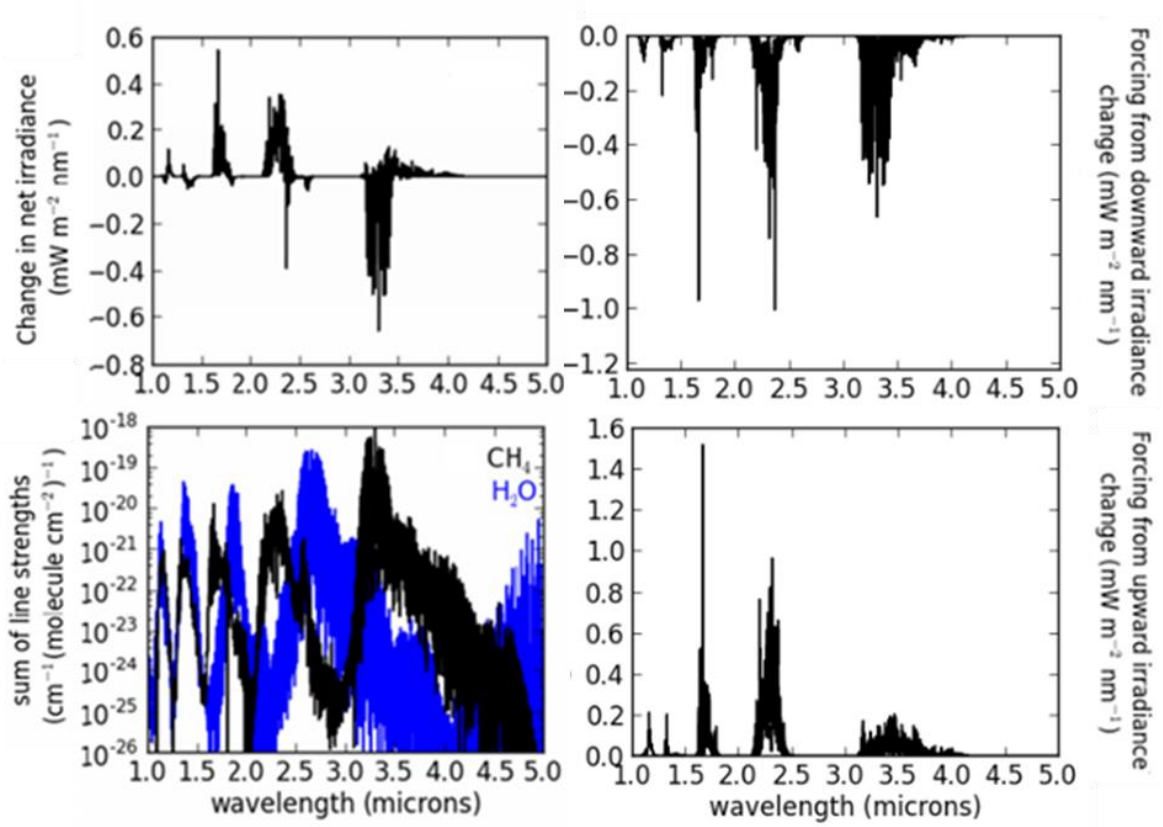

Figure 2.12: Upper left: Spectral variation of global-mean, all-sky CH_4 NIR tropopause IRF for a perturbation from 750 ppbv to 1800 ppbv. Also shown is the spectral variation of the downwelling (upper right) and upwelling (lower right) components of the global-mean all-sky CH_4 NIR tropopause IRF. Lower left: The sum of the absorption line strengths in 1 nm intervals for CH_4 (black) and H_20 (blue). Adapted from Etminan et al. (2016).

Collins *et al.* (2018)

Collins *et al.* (2018) calculate monthly-mean, spatially-resolved CH_4 SW tropopause IRF using the MODerate resolution atmospheric TRANsmission (MODTRAN) radiative transfer code (eight streams at 15 cm^{-1} resolution) with atmospheric information averaged across 2006 to 2010 from two different ESMs: CSIRO Mk3-6-0 (Rotstayn *et al.* 2012) and INMCM4 (Volodin *et al.* 2010). Forcings are derived following a perturbation in CH_4 from 806 ppbv to 1760 ppbv across the 0.84 – 5 µm spectral range, using HITRAN2008 data under clear-sky and all-sky (aerosol-free) conditions with spectral surface albedos inferred from satellite observations.

Table 2.3 shows their resulting global-annual mean estimates and associated uncertainty ranges (attributed to interannual variability in atmospheric and surface conditions).

	CH_4 SW IRF (W m^{-2})	
	All-sky	**Clear-sky**
CSIRO Mk3-6-0	0.025 ± (1 x 10^{-4})	0.011 ± (3 x 10^{-5})
INMCM4	0.026 ± (4 x 10^{-4})	0.008 ± (2 x 10^{-4})

Table 2.3: Collins et al. (2018) estimate of global, annual-mean tropopause SW CH_4 IRF following a perturbation from 806 ppbv to 1760 ppbv, calculated under clear-sky and all-sky (aerosol-free) conditions using the MODTRAN radiative transfer code and atmospheric information from CSIRO Mk3-6-0 and INMCM4 ESMs averaged over 2006 – 2010. Uncertainties signify interannual variability in forcing estimates.

The authors infer that the global annual mean all-sky IRF of approximately 0.026 W m^{-2} agrees with the all-sky estimate of 0.03 W m^{-2} reported by Etminan *et al.* (2016). However, disagreement in the size and sign of the clear-sky tropopause CH_4 SW IRF suggests that this apparent agreement is coincidental, resulting from a different combination of the clear-sky forcing and cloud radiative effect (CRE). Collins *et al.* (2018) estimate a positive, rather than negative, clear-sky CH_4 SW IRF of 0.008 W m^{-2} and 0.011 W m^{-2}, given atmospheric state information from INMCM4 and CSIRO Mk3-6-0, respectively. These are notable results that are in marked contrast to Etminan *et al.* (2016), where it is demonstrated that it is the inclusion of clouds that causes the sign of the SW IRF to be positive, increasing by 0.075 W m^{-2} from -0.045 W m^{-2} (clear-sky) to 0.03 W m^{-2} (all-sky). Conversely, Collins *et al.* (2018) attribute their positive clear-sky forcings to the use of realistic surface conditions; the effect of clouds enhances the SW IRF by just 0.014 W m^{-2} (from 0.008 W m^{-2} to 0.026 W m^{-2}; INMCM4) and 0.018 W m^{-2} (from 0.011 W m^{-2} to 0.025 W m^{-2}; CSIRO Mk3-6-0). This hints that the SW forcing is sensitive to the specification of surface albedo and background climatology, given that CRE deviates by 30% between INMCM4 and CSIRO Mk3-6-0.

Figure 2.13a shows the annual-mean all-sky CH_4 SW tropopause IRF calculated using atmospheric state information from the CSIRO Mk3-6-0 ESM. Collins *et al.* (2018) report that local annual-mean IRF is positive over 90% of the Earth's surface and note that large spatial gradients in the SW IRF are driven by corresponding gradients in NIR surface albedo. Figure 2.13b shows the corresponding clear-sky TOA NIR reflected flux, which is strongly dependent on surface albedo. Bright desert surfaces across the Sahara and Arabian Peninsula reflect the downwelling NIR flux upward, increasing photon path length and CH_4 NIR absorption. The authors report a localised maximum forcing of 0.25 W m^{-2} in this region, around 10 times the size of their global annual-mean all-sky SW IRF of approximately 0.026 W m^{-2} (See Table 2.3).

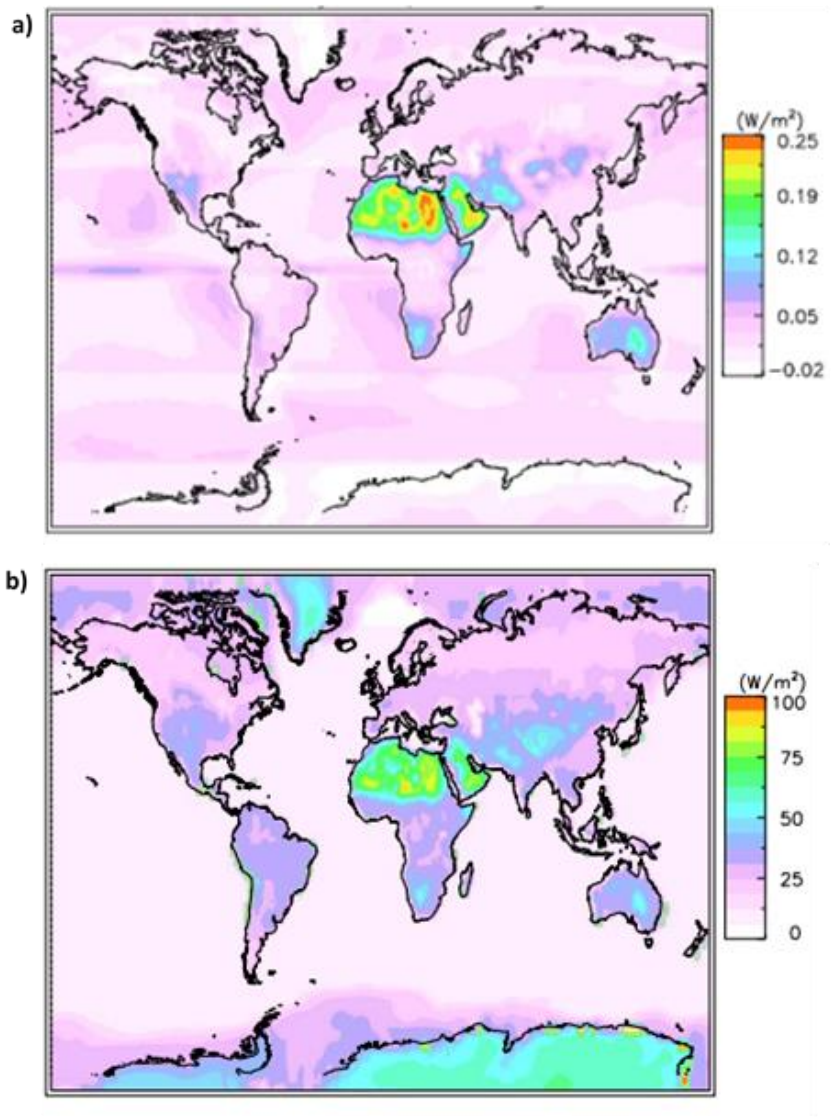

Figure 2.13: a). Collins et al. (2018) annual-mean CH_4 SW tropopause IRF calculated by the CSIRO Mk3-6-0 ESM under all-sky aerosol-free conditions following a perturbation in CH_4 from 806 ppb to 1760 ppb. b) TOA NIR reflected flux under clear-sky, aerosol-free conditions from the CSIRO Mk3-6-0 ESM.

Figure 2.14a shows the spatial distribution of the annual-mean enhancement to CH_4 SW IRF by CRE from the CSIRO Mk3-6-0 ESM. Localised enhancement from the effects of clouds reaches a maximum of 0.068 W m^{-2} associated with oceanic stratocumulus cloud decks west of Southern Africa, North and South America and cloud components of the Intertropical Convergence Zone (ITCZ). Figure 2.14b shows the area-weighted cumulative probability distribution of CRE. Over 12% of the Earth's surface, CRE reduces CH_4 SW IRF relative to clear-sky conditions. As Collins *et al.* (2018) explain, high-altitude clouds can reduce the flux of downward solar irradiance incident on the lower troposphere, hence, resulting in a reduction of CH_4 absorption. However, over 88% of the Earth's surface CRE is positive, which enhances CH_4 SW IRF by up to 2.75 times the global, annual-mean forcing (0.025 W m^{-2}; See Table 2.3).

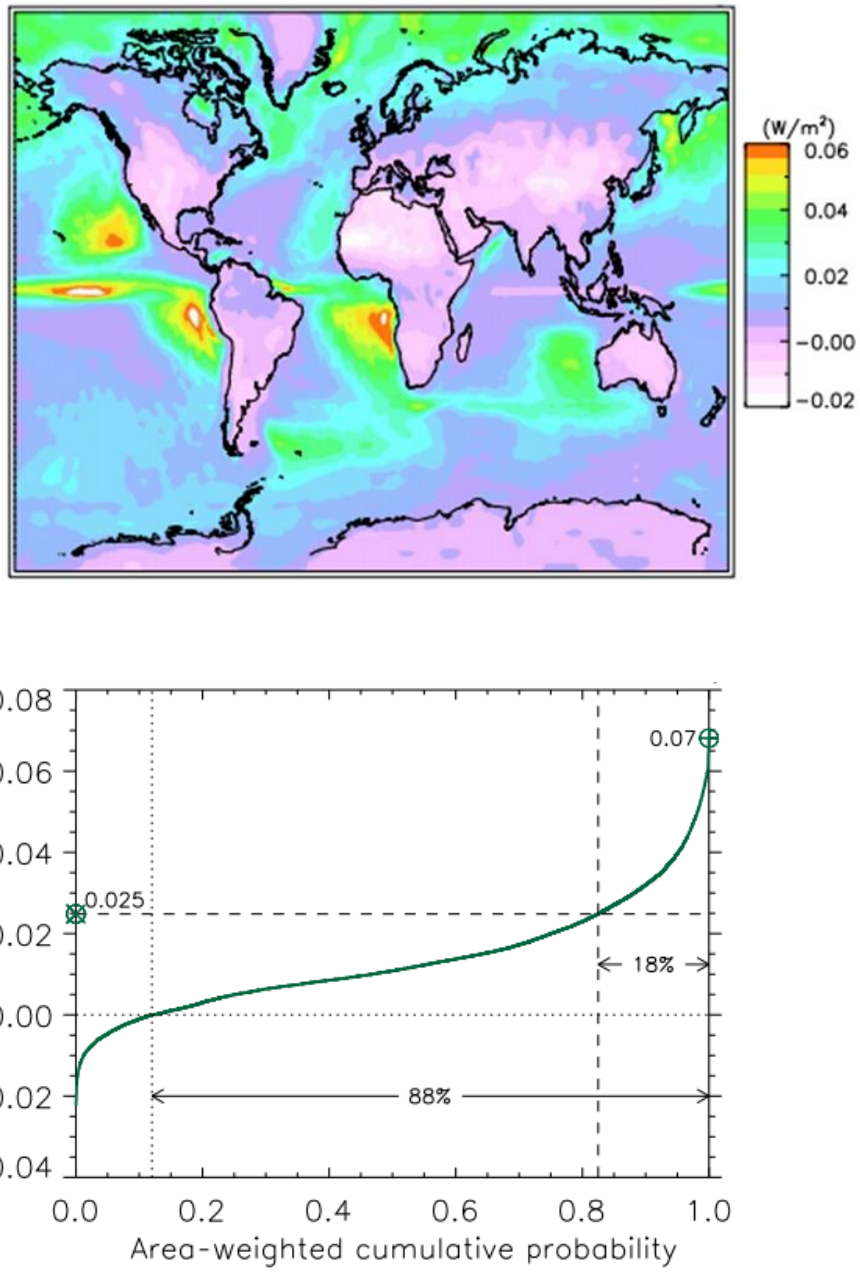

Figure 2.14: a). Collins et al. (2018) annual-mean enhancement to CH_4 SW tropopause IRF from clouds in the CSIRO Mk3-6-0 ESM. Derived as the difference between all-sky and clear-sky CH_4 IRF at the tropopause. b). Area-weighted cumulative probability distribution of CRE. Dotted lines signify where the IRF exceeds zero, dashed lines signify where the IRF equals the global, annual-mean all-sky IRF (marked by circle and cross symbol) and the circle and plus symbol labels the maximum IRF value.

2.4 Radiative Transfer

Radiative transfer theory describes the propagation of electromagnetic radiation within the terrestrial atmosphere. It defines the modification of radiation by the presence of atmospheric gases and particles, which, depending on size, shape and chemical composition, act to alter the radiation field through absorption, emission and scattering.

Following the assumption of blackbody distribution for the effective emitting temperature of the Sun (T_{Sun} ≈ 5800 K) and Earth (T_{Earth} ≈ 255 K), radiative fluxes within the atmosphere can be represented by two separate spectra: solar (SW) radiation and terrestrial (LW) radiation. Figure 2.15 shows normalised blackbody curves for the Sun and the Earth and the wavelength range of photons emitted by each source. Here, the solar curve is scaled so that the area under each curve represents approximately equal irradiance, demonstrating that the amount of SW energy absorbed by the Earth-atmosphere system is equal to the amount of LW energy emitted at the TOA. This scaling of the solar spectrum is achieved by accounting for the Sun-Earth distance, Earth's planetary albedo (α_p) and the distribution of solar energy per unit area of the Earth's surface (see Equation 2.3).

The transmission of both SW and LW radiation through the atmosphere plays a vital role in defining the Earth's radiative balance and the distribution of energy around the planet. Differences in temperature initiate pressure gradients and drive atmospheric circulations. Radiative transfer is therefore central in observing, understanding and predicting the evolution of weather and climate. As such, radiative transfer calculations form the core of numerical weather prediction (NWP) models and ESMs.

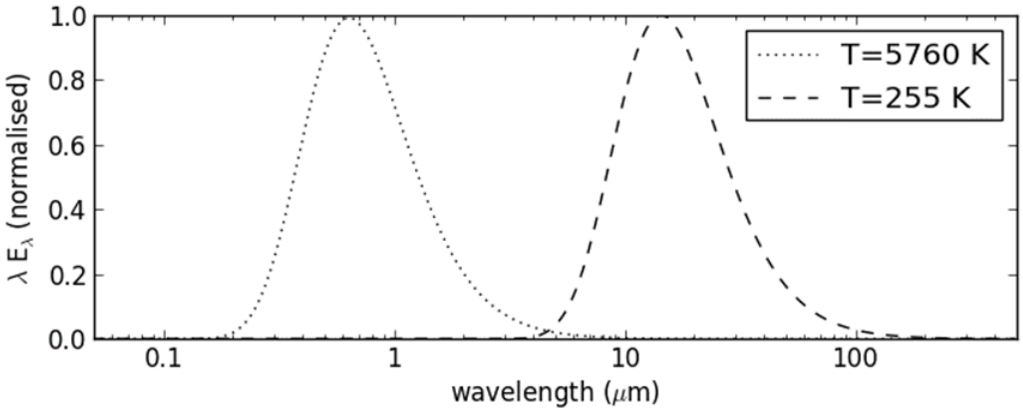

Figure 2.15: Normalised blackbody emission curves at the effective emitting temperature of the Sun (5800 K; dotted line) and Earth (255 K; dashed line). The solar curve is scaled by the Sun-Earth distance and multiplication by $(1-\alpha_p)/4$ to account for *the distribution of irradiance across the Earth's surface area (see Equation 2.3) and the fraction of solar irradiance reflected back to Space by* α_p*, so that the area under each curve represents approximately equal irradiance. Source: Keith Shine 2021, personal communication.*

A brief overview of radiative transfer theory relevant to this thesis is given in the following sections. A more detailed account is provided by e.g. Liou (2002) and Petty (2006).

2.4.1 Fundamentals of radiative transfer

A beam of monochromatic radiation, at wavenumber ν, travelling through a path in the atmosphere is attenuated by matter such as molecules, aerosols, ice crystals and water droplets. The change in intensity of radiation after travelling this path, of length (ds), is given by (e.g. Liou 2002):

$$dI_\nu = -k_\nu^e \rho I_\nu ds \tag{2.9}$$

where I_ν is the intensity of the incident beam of radiation, ρ is the density of matter and k_ν^e is the extinction cross-section, which is a measure of the amount of radiation removed from the incident beam on interaction with a particle of matter. k_ν^e is the sum of the absorption cross section k_ν^a and scattering cross section k_ν^s, which denote extinction due to absorption and scattering, respectively.

Conversely, the intensity of I_ν along ds may increase due to emission and scattering of radiation into the beam at the same wavelength. The source function coefficient, j_ν, represents this process and is given by:

$$dI_\nu = j_\nu \rho ds \tag{2.10}$$

Combining Equation 2.9 and Equation 2.10 yields the total change in I_ν due to both a reduction in and strengthening of the beam's intensity:

$$dI_\nu = -k_\nu^e \rho I_\nu ds + j_\nu \rho ds \tag{2.11}$$

Since the physical meaning of j_ν and k_ν^e are analogous, it is practical to define the source term, J_ν, as:

$$J_\nu \equiv \frac{j_\nu}{k_\nu^e} \tag{2.12}$$

Following this, Equation 2.11 can be rearranged to give the most fundamental description of radiative transfer in the atmosphere:

$$\frac{dI_\nu}{k_\nu^e \rho ds} = J_\nu - I_\nu \tag{2.13}$$

2.4.2 Radiative transfer in the terrestrial atmosphere

Radiative transfer in the terrestrial atmosphere is often treated using the plane-parallel approximation. This neglects the effect of the curvature of the Earth on level heights in the atmosphere. It also considers that, locally, variations in properties such as temperature, pressure, density and composition vary only in the vertical direction (z). Since such parameters vary more rapidly over vertical distances, horizontal variations are ignored, and radiative transfer is calculated solely with respect to the vertical distance (dz) travelled through the atmosphere.

The path length, ds, may now be expressed in terms of dz as follows:

$$ds = \frac{dz}{\mu} \tag{2.14}$$

where $\mu = \cos(\theta)$, whereby θ denotes the zenith angle of the incident beam relative to the local normal.

The extinction of the incident beam, I_ν, along ds may now be evaluated at any level (z) in the atmosphere. The change in intensity of I_ν observed at level z is given by integrating Equation 2.15 from infinity (i.e. the TOA) to z:

$$I_\nu = I_{0,\nu} \exp\left(-\int_z^\infty k_\nu^e \rho dz\right) \tag{2.15}$$

This equation is the Bouguer-Lambert law. It states that the intensity of an incident beam of monochromatic radiation travelling through the atmosphere falls off at an exponential rate proportional to the product of the extinction cross-section, the density of matter and the vertical distance travelled. Here it is practical to introduce the term *optical depth* (τ) which is defined as follows:

$$\tau(z,\infty) \equiv \int_z^\infty k_\nu^e \rho dz \tag{2.16}$$

Hence, the Bouguer-Lambert law may now be expressed as a function of τ as a vertical coordinate:

$$I_\nu = I_{0,\nu} \exp(-\tau) \tag{2.17}$$

From Equation 2.17, the fraction of radiation that is transmitted through the atmosphere without being absorbed or scattered is given by:

$$T_r = \frac{I_\nu}{I_{0,\nu}} = \exp(-\tau) \tag{2.18}$$

where T_r is the transmittance, a dimensionless quantity that ranges from near zero, for $\tau \longrightarrow \infty$, to one, when τ = 0.

2.4.3 Methods for calculating radiative transfer

Line-by-line models

LBL models are widely considered to provide the best estimate of radiative transfer solutions due to their ability to accurately calculate transmittance functions for each spectral line associated with radiatively active atmospheric constituents. Numerous studies have proven that agreement between LBL codes is strong and differ by only a few percent (e.g. Clough and Iacono 1995; Zhang *et al.* 2005, Collins *et al.* 2006b, Iacono *et al.* 2008, Forster *et al.* 2011; Pincus *et al.* 2020) with calculations comparing well to radiative fluxes measured in controlled conditions (Tjemkes *et al.* 2003, Oreopoulos *et al.* 2012). Thus, LBL calculations are widely considered as the 'truth' and serve as a benchmark against which less accurate, but more computationally-efficient, banded radiative transfer codes are evaluated.

LBL calculations are performed throughout Chapter 4 by the Reference Forward Model (RFM; Dudhia 2017). As described in Section 3.1.2, the RFM is used to calculate molecular absorption cross sections for each line transition in the 0.87 - 10 μm spectral range.

Essentially, this process involves summing the contribution from all absorption lines at all altitudes to the monochromatic radiance at a given height (z) in the atmosphere, whereby the total absorption coefficient is given by (e.g. Petty 2006):

$$k_{\nu\rho}^{\alpha}(z) = \sum_{i=1}^{N} \rho_i(z) \left[k_{cont,i}(\bar{\nu}; z) + \sum_{j=1}^{M_i} S_{ij}(z) f_{ij}(\tilde{\nu} - \tilde{\nu}_{ij}; z) \right] \tag{2.19}$$

where $\rho_i(z)$ is the local density of the number of constituents N, M_i is the number of absorption lines, S_{ij}, f_{ij}, $\tilde{\nu}_{ij}$ are the strength, shape and position of the j_{th} line of the i_{th} constituent, with $k_{cont,i}$ representing the continuum absorption component.

Effectively this approach means that calculations would need to be repeated for every wavelength in the spectral region of interest, at every height in the atmosphere. However due to the

computational expense of this approach, LBL models don't explicitly calculate the contribution from each individual spectral line, but instead employ the use of a spectral sampling step ($\Delta\nu$) which represents the wavelength interval across which line parameters are sampled. The size of $\Delta\nu$ is an important consideration and ultimately determines how many spectral lines contribute to radiative transfer calculations. Efforts must be taken to ensure that a suitable $\Delta\nu$ resolution is specified. If $\Delta\nu$ is too large, then calculations may omit the contributions of a particular line to irradiance, leading to erroneous results. Ideally the value of $\Delta\nu$ needs to be smaller than the width of spectral lines included in calculations (Maycock and Shine 2012). As demonstrated in Section 3.1.2, a $\Delta\nu$ of 0.01 cm^{-1} (which can be compared with a typical collision-broadened halfwidth of 0.05 cm^{-1} at STP) is found to be sufficient to provide a robust set of benchmark calculations.

The accuracy of the spectral line parameters is another important factor to consider when using LBL models. For calculations in this thesis these are provided by the HITRAN spectroscopic database (Gordon *et al.* 2017). This database is widely used in radiative transfer models and supplies spectroscopic parameters such as line strength, position and width for all the main atmospheric absorbers.

HITRAN has undergone several updates since the release of the first edition in the early 1990s (Rothman *et al.* 1992) owing to advances in experimental and theoretical spectroscopy. This has led to the modification of line parameters of some atmospheric gases. Such updates could cause differences in calculations if different versions of the HITRAN database are employed in radiative transfer models. However, as demonstrated in Section 3.3.1, no significant difference is found between the HITRAN2012 (Rothman *et al.* 2013) and HITRAN2016 (Gordon *et al.* 2017) editions in the calculation of CH_4 SW IRF. This thesis uses both HITRAN2012 and HITRAN2016 data (see Section 3.3.1).

Narrow and broad-band models

Band models provide a more computationally-efficient method for calculating radiative transfer through the atmosphere. These models make use of parameterisations that simplify the fundamental equations of radiative transfer for each spectral line of a radiatively active constituent by calculating irradiances across a specified spectral band, as opposed to an individual line-by-line basis. This is achieved by making assumptions about the behaviour of radiative transfer across the spectral interval ($\Delta\nu$), such that the band-averaged transmittance is (e.g. Petty 2006):

$$\overline{T_r} = \Delta\nu^{-1} \int_{\Delta\nu} T_{r,\nu}(z)\, d\nu \tag{2.20}$$

Whilst these assumptions significantly enhance computational efficiency, the use of approximations can induce error, thus, it is essential to assess banded radiation codes against LBL models to evaluate their accuracy. This thesis uses a narrow-band configuration of The Suite Of Community RAdiative Transfer codes (SOCRATES) to calculate CH_4 RF (see Section 3.1.4 and 3.1.5). This narrow-band configuration is evaluated against benchmark calculations performed by the RFM in Chapter 4. A broad-band configuration of SOCRATES is used in Section 4.3 to demonstrate that the spectral resolution of this code is too coarse to capture the effect of CH_4 SW RF.

Both configurations of SOCRATES use the correlated-k distribution (CKD) method to treat gaseous absorption and calculate $\overline{T_r}$. This method is a widely-used technique based on the principle that a given gaseous absorption coefficient (k) value is likely to be applicable to many different wavenumbers (e.g. Petty 2006). Across a given spectral interval, a range of k values can be ordered according to their strength, resulting in a k-distribution of gaseous absorption coefficients, whereby the resulting function $k(g)$ ranges from g = 0, for the least absorbing value of k present, to g = 1, for the most absorbing value of k. The smooth, monotonically increasing function, $k(g)$, can be discretized using a significantly smaller quantity of quadrature points to represent spectral absorption than LBL models. In its entirety, the SW and LW spectrum can be characterized by order 10^2 independent pseudo-monochromatic calculations, typically referred to as k-terms (Hogan and Matricardi 2020). An increased number of k-terms increases the accuracy of calculations; however, this subsequently results in a reduction in computational efficiency.

Using the CKD method, transmittance is calculated by (e.g. Petty 2006):

$$\overline{T_r}\,(u) = \int_0^1 \exp\left[-\int_0^u k\,(g,u')du'\right] dg \tag{2.21}$$

where for each value of g, transmittance is calculated over the atmospheric path (u) between the location u' = 0 and u' = u.

Chapter 3

Methods, Models and Data

3.1 Radiative transfer codes

This thesis uses a combination of offline radiative transfer codes to understand the impact of methane's SW absorption on radiative forcing. LBL calculations, performed by RFM and RFMDISORT, provide high spectral-resolution analysis of CH_4 SW optical depth and IRF, respectively. The narrow-band model (NBM), SOCRATES-RF, utilises the radiance core of the Suite of Community Radiative Transfer codes (SOCRATES) to calculate IRF and stratospherically-adjusted RF using the FDH methodology (see Section 3.2).

The RFM is used extensively in Chapter 4 to evaluate the performance of SOCRATES in calculating CH_4 SW IRF. Additional calculations in Chapter 4 are conducted by RFMISORT, namely to compare calculations of CH_4 SW IRF against previously published estimates. RFMDISORT is used predominantly in Chapter 5 to assess the dependence of CH_4 SW RF on spectrally-varying surface albedo. SOCRATES-RF performs the main calculations of this thesis in Chapters 5 and 6. It provides global-annual mean and spatially-resolved calculations of CH_4 SW IRF and RF (including the effect of SW forcing on the longwave forcing, following stratospheric temperature adjustment).

Each of these radiative transfer codes are described in further detail below.

3.1.2 The Reference Forward Model (RFM)

The RFM (Dudhia 2017) is a LBL radiative transfer model based on the GENLN2 (Edwards 1992) suite of radiative transfer codes. The model ingests spectroscopic data, either from the HITRAN database or from direct tabulations of spectral absorption coefficients, along with a user defined viewing geometry and atmospheric profile. The viewing geometry depends the representation of the atmosphere, either: homogeneous, plane-parallel or circular. The atmospheric profile must contain parameters of temperature, pressure and volume mixing ratios (VMRs) specified on common altitude levels; n pressure levels, defining $n-1$ atmospheric layers. As desired, the RFM outputs optical depth, transmittance, and radiance spectra (as a result of atmospheric emission and absorption). These quantities can be converted to useful additional measures, such as absorption or brightness temperature. An overview of the LBL method for calculating transmittance functions is provided in Section 2.4.3.

The RFM can perform a variety of different spectroscopic calculations for a range of radiative transfer applications (mainly across the microwave and infrared) in wavenumber space. As the RFM does not include any scattering processes its usefulness for calculations at shorter wavelengths is more limited. However, it can still be used to effectively model molecular absorption (up to UV wavelengths) using HITRAN (see Section 3.3.1) spectral line data.

This thesis uses RFM version 5.0 to calculate clear-sky molecular optical depths in a plane-parallel atmosphere across the solar spectral range of 1000 – 11494 cm^{-1} (i.e. 0.87 – 10 μm). All calculations use a zenith viewing geometry whereby spectra are computed viewing upwards into horizontally-uniform atmospheric layers. Spectroscopic data are taken from the HITRAN2012 database (Rothman *et al.* 2013) for the following molecules: CH_4, H_2O, CO_2 and N_2O. When H_2O absorption is specified (as per the experiment design given in Section 4.2), version 2.5 of the MT_CKD model (Mlawer *et al.* 2012) is used to represent the effects of H_2O continuum absorption.

For calculations in this thesis an important post-processing step involves converting RFM optical depth values into the quantity of irradiance. Ultimately, this allows for the calculation of wavenumber-integrated fluxes of irradiance at the surface, tropopause and TOA due to the presence of varying concentrations of absorbing molecules throughout the atmosphere. Only molecular absorption is considered in RFM experiments and no scattering is assumed. Since the RFM contains no solar term to model surface solar reflectance, all calculations therefore also assume a surface albedo of zero. A description of the laws governing the atmospheric transmission of radiation were given in Section 2.4.2. Specifically in this post-processing stage, the Bouguer-Lambert

law (see Equation 2.17) is applied to RFM optical depths to derive spectral irradiances using the Kurucz extra-terrestrial solar spectrum (Chance and Kurucz 2010).

RFM Spectral Sampling Resolution

For reasons outlined in Section 2.4.3, the size of the user-defined spectral sampling resolution ($\Delta\nu$) is an important consideration when running the RFM. Ultimately this determines how many spectral lines contribute to the calculation of optical depth, and thus, efforts must be taken to ensure that a suitable $\Delta\nu$ is specified.

Table 3.1 shows the effect of using three different sizes of $\Delta\nu$ in the RFM: at 1 cm^{-1}, 0.01 cm^{-1} and 0.001 cm^{-1}. Each spectral sampling step is used to calculate methane's wavenumber integrated irradiance at 806 ppbv and 1760 ppbv across the 1000 – 11494 cm^{-1} spectral range at the tropopause (13 km) and surface (0 km) of a control mid-latitude summer (MLS) profile.

	E_{net} (806 ppb)			E_{net} (1760 ppb)		
	1	**0.01**	**0.001**	**1**	**0.01**	**0.001**
13 km	313.933	313.811	313.811	313.722	313.591	313.590
0 km	312.820	312.660	312.660	311.796	311.597	311.597

Table 3.1: RFM calculations across the 1000 – 11494 cm^{-1} spectral range of net irradiance (E_{net}; W m^{-2}) using three different spectral sampling step sizes (1 cm^{-1}, 0.01 cm^{-1} and 0.001 cm^{-1}) for a clear-sky CH_4-only MLS atmosphere at the tropopause (13 km) and surface (0 km) using CH_4 concentrations of 806 ppbv and 1760 ppbv.

	ΔE_{net}		
	1	**0.01**	**0.001**
13 km	-0.210	-0.221	-0.221
0 km	-1.025	-1.063	-1.063

Table 3.2: Change in net irradiance (ΔE_{net}; W m^{-2}) that results from an increase in CH_4 concentrations from 806 ppbv to 1760 ppbv for a clear-sky CH_4-only MLS atmosphere at the tropopause (13 km) and surface (0 km) calculated using three different spectral sampling step sizes (1 cm^{-1}, 0.01 cm^{-1} and 0.001 cm^{-1}). A negative ΔE_{net} indicates a decrease in downwelling irradiance, and hence, a negative RF.

Firstly, this reveals that the difference in wavenumber integrated irradiance (from here on denoted net irradiance; E_{net}) between $\Delta\nu$ of 0.01 cm^{-1} and 0.001 cm^{-1} is indistinguishable at the precision of 6 significant figures. Secondly, at $\Delta\nu$ of 1 cm^{-1} and 0.01 cm^{-1}, only a small difference in E_{net} (< 0.1%) is discernible at the tropopause and surface at both 806 ppbv and 1760 ppbv. However, when considering the change in net irradiance (ΔE_{net}), as shown in Table 3.3, this difference increases by two orders of magnitude (≈5%).

Since the aim of this thesis is to calculate ΔE_{net}, i.e. radiative forcings, a difference of ≈5% is significant, especially in the context of the RFM serving as a benchmark model from which the NBM, SOCRATES, will be compared against in Chapter 4. Thus, this demonstrates that a $\Delta\nu$ of 1 cm^{-1} is not sufficient to fully capture the large variation in methane's spectral forcing across the SW. Instead, a $\Delta\nu$ of 0.01 cm^{-1} (which can be compared with a typical collision-broadened halfwidth of 0.05 cm^{-1} at STP) will be required. Hence, unless otherwise stated, all RFM calculations presented throughout the remainder of this thesis will sample HITRAN2012 data at a spectral resolution of 0.01 cm^{-1}.

3.1.3 RFMDISORT

RFMDISORT is a combination of two major radiative transfer codes, the RFM and a general-purpose Fortran programme for DIScrete Ordinate Radiative Transfer (DISORT; Stamnes *et al.* 2000) for scattering calculations, with a collection of minor codes written in Fortran and Korn-shell scripts (Bharmal 2009). Given a user-specified atmospheric profile, containing parameters of temperature, pressure and VMRs on common altitude levels, RFMDISORT is able to calculate both SW and LW optical depths, radiative fluxes and heating rates due to scattering and absorption throughout the atmosphere. Recently this code has undergone several important updates by Dr Jonathan Elsey at the University of Reading. As a result, the user is now able to run RFMDISORT at an increased spectral resolution (tested up to 0.01 cm^{-1}) and include the absorbing and scattering effects of clouds. Furthermore, and of particular interest to this thesis (see Chapter 5), the user may also specify a spectrally-varying surface albedo and therefore include the effects of spectral surface reflectance in model calculations. Thus, RFMDISORT is used in this thesis to perform vital, additional high spectral-resolution LBL experiments that are beyond the capability of the RFM.

This thesis uses version 05-12-18 of RFMDISORT to calculate clear-sky and all-sky SW radiative fluxes across the spectral range of 1000 – 10000 cm^{-1} (i.e. 1 – 10 μm) at $\Delta\nu$ a of 0.01 cm^{-1}. These calculations use the 'lean_12' solar spectrum (taken as a mean spectral data from 2000-2011 as recommended by the SPARC/SOLARIS group; http://solarisheppa.geomar.de/ccmi) interpolated onto a 1 cm^{-1}

regular grid. Spectroscopic data are taken from the HITRAN2016 database (Gordon *et al.* 2017) for the following molecules: CH_4, H_2O, CO_2 and N_2O. When H_2O absorption is specified (as per the experiment design given in Section 5.4.1), version 3.2 of the MT_CKD (Mlawer *et al.* 2019) is used to represent continuum absorption by H_2O. As RFMDISORT is predominantly used to assess the dependence of methane's SW forcing on surface albedo (see Chapter 5) the exact specification of albedo in RFMDISORT calculations will be given in all relevant chapter sections of this thesis.

3.1.4 The Suite Of Community RAdiative Transfer codes (SOCRATES)

SOCRATES is the radiative transfer scheme (based on Edwards and Slingo 1996; Manners *et al.* 2015) currently used in Global Atmosphere 7.0 (GA7) configuration of the UK's Met Office Unified Model (UM; Walters *et al.* 2019). SOCRATES uses a two-stream approximation (whereby the angular variation of radiance is characterized by an upward and downward diffuse irradiance, along with a direct SW solar irradiance) to perform a number of quasi-monochromatic calculations to compute radiative fluxes, radiances or heating rates (see Manners *et al.* 2015 for further detail). SOCRATES is a versatile code that has the capability to represent scattering by water droplets, ice crystals and aerosols, in addition to representing the effects of gaseous absorption. The model uses the CKD method to derive absorption coefficients based on HITRAN2012 data (Rothman *et al.* 2013) to calculate atmospheric transmittance. A description of this procedure was given in Section 2.4.3.

A core feature of SOCRATES involves the use of spectral files which contain the major spectral information needed to run the code. As shown in Table 3.3, the spectral files currently used in the GA7 configuration of the UM divide solar radiation (from 0.18 – 10 μm) into 6 spectral bands and thermal radiation (from 3.34 – 10000 μm) into 9 spectral bands, named sp_sw_ga7 and sp_lw_ga7, respectively. However, for purposes of validation, higher-resolution reference versions of both the SW and LW spectral files have been generated to aid offline UM diagnostics. These reference spectral files contain 260 bands in the SW and 300 bands in the LW, named sp_sw_260_jm2 and sp_lw_300_jm2 respectively, and have each been validated against independent LBL models (Walters *et al.* 2019). Both versions of the SW spectral file use data from the 'lean_12' solar spectrum (http://solarisheppa.geomar.de/ccmi last accessed 12/03/2021) taken as the mean of spectral data from 2000-2011, as recommended by the SPARC/SOLARIS (Solar Influences for SPARC: Stratospheric Processes and their Role in Climate) group (Manners *et al.* 2015).

LW Bands	Wavelength range (μm)	SW Bands	Wavelength range (μm)
1	25 - 10000	1	0.18 – 0.32
2	18.18 - 25	2	0.32 – 0.505
3	12.5 - 18.18	3	0.505 – 0.69
4	13.33 - 16.95	4	0.69 – 1.19
5	8.33 - 12.5	5	1.19 – 2.38
6	8.93 - 10.10	6	2.38 - 10
7	7.52 - 8.33	-	-
8	6.67 - 7.52	-	-
9	3.34 - 6.67	-	-

Table 3.3: Wavelength range of each spectral band in the LW (sp_lw_ga7) and SW (sp_sw_ga7) spectral files used in the GA7 configuration of the UM to treat outgoing TIR radiation and incoming solar radiation. Taken from Manners et al. 2015.

This thesis uses version 1504 of SOCRATES to calculate the net downward flux of irradiance, and hence, change in irradiance (i.e. IRF) due to perturbations in CH_4 concentrations. When additional absorbers are specified, namely H_2O, CO_2 and N_2O (as per the experimental setup stated in the relevant sections of this thesis), random gaseous overlap is assumed within the CKD method. Furthermore, when H_2O is specified, continuum absorption is based on the MT_CKD 2.5 (Mlawer *et al.* 2012) model with modifications in the NIR window regions using CAVIAR data (Ptashnik *et al.* 2011, 2012).

As this thesis aims to deliver a detailed quantification of the impact of CH_4 SW absorption on RF, it is necessary to use the highest possible resolution available in SOCRATES to most accurately characterise the spectral variation of CH_4 irradiance and the complex spectral overlap with other gaseous absorbers. Therefore, this thesis predominantly employs the sp_sw_260_jm2 (260-band) version of SOCRATES. Chapter 4 presents a detailed evaluation of the performance of this spectral file against benchmark calculations of the RFM, specifically in the context of assessing SOCRATES' ability in accurately resolving CH_4 SW spectral characteristics. To aid the discussion given in Chapter 4, the 6-band version of SOCRATES is also used to provide an example of CH_4 IRF estimates as calculated by a broad-band model with a much lower SW spectral resolution.

3.1.5 SOCRATES-RF

SOCRATES-RF (Checa-Garcia *et al.* 2018) is an offline radiative transfer model developed at the University of Reading. SOCRATES-RF utilises the radiance core of SOCRATES to calculate IRF and SARF using the FDH methodology, as described by Forster *et al.* (1997) (see Section 3.2). SOCRATES-RF has the capability to represent scattering by water droplets, ice crystals and aerosols, in addition to representing the effects of gaseous absorption and continuum absorption as per the method of SOCRATES. Furthermore, SOCRATES-RF also allows for the calculation of spatially-resolved forcings. All SOCRATES-RF simulations in this thesis are run at a 5° x 5° spatial resolution, chosen to balance out the computational costs of running spatially-resolved calculations with the need for a reasonable grid-box resolution.

This thesis uses SOCRATES-RF to calculate IRF and SARF following perturbations in CH_4 mixing ratios (as per the experimental setup stated in the relevant sections of this thesis). Calculations are run using ERA-interim reanalysis (Dee *et al.* 2011) monthly-mean atmospheric data averaged across the period 2000-2009, with a hybrid sigma-pressure vertical coordinate using 60 model layers with the TOA located at 0.1 hPa. Vertically-constant mixing ratios of CO_2 and N_2O are included at the pre-industrial values for 1850 taken from IPCC AR5 (Myhre *et al.* 2013a), at 278 ppmv and 258 ppbv respectively. Three-dimensional fields of O_3 mixing ratios are also included, taken from the International Global Atmospheric Chemistry (IGAC)/SPARC Chemistry-Climate Model Initiative (CCMI) O_3 data set, as designed for CMIP6 (Hegglin *et al.* 2016).

Experiments are conducted for both clear-sky and all-sky atmospheres. Ice and water clouds are treated separately under all-sky conditions and 'random overlap in a mixed column' is assumed for the handling of vertical overlap between different cloud layers. The effects of aerosols are absent from all calculations. Crucially, the sp_sw_260_jm2 (260-band) SW spectral file is used in all calculations to most accurately represent CH_4 SW absorption across the 0.18 - 10 µm spectral range. SW spectral gaseous overlap is treated using the equivalent extinction with correlated scaling method, as recommended for computational efficiency (for further detail see Section 1.1.8 of Manners *et al.* 2015). The sp_lw_ga7 (9-band) LW spectral file is used to characterise thermal absorption and emission by atmospheric constituents when stratospheric temperature-adjusted forcings are computed. In comparison to the sp_lw_300_jm2 (300-band) LW spectral file, experiments reveal that sp_lw_ga7 is able to adequately simulate methane's LW IRF at sufficient accuracy when gaseous overlap is treated using the more accurate 'random overlap' assumption. Table 3.4 compares the magnitude of methane's LW all-sky tropopause IRF for January calculated using both sp_lw_ga7 and sp_lw_300_jm2, each with gaseous absorption treated using both the

random overlap and equivalent extinction with correlated scaling method. As shown, the use of random gaseous overlap in calculations conducted using sp_lw_ga7 and sp_lw_300_jm2 yields LW IRFs that differ by less than 2% (comparing 0.577 W m^{-2} and 0.568 W m^{-2}). Treating gaseous overlap with the alternative equivalent extinction approximation (that is recommended for faster runs) results in a 7% difference (comparing 0.472 W m^{-2} with 0.506 W m^{-2}). Thus, to balance the need for computational efficiency and accurate results, the lower spectral resolution sp_lw_ga7 is suitable to use for the calculations conducted in this thesis if the more accurate method of random gaseous overlap is assumed.

	January all-sky LW IRF (W m^{-2})	
	Random	***Equivalent extinction***
sp_lw_ga7 (9 band)	0.577	0.472
sp_lw_300_jm2 (300 band)	0.568	0.506

Table 3.4: Comparison of January all-sky LW tropopause IRF calculated using the 9-band and 300-band LW spectral files, each with random gaseous overlap (most accurate but slow) and the equivalent extinction method with correlated scaling (recommended for fast runs).

To account for the diurnal variation in solar zenith angle (θ), daily average absorption ($\bar{F}_{abs}$) is calculated by integrating absorption over half of the day length as follows (e.g. see Paynter 2008):

$$\bar{F}_{abs} = \left(\frac{2}{86400}\right)\int_0^{D/2} F_{abs}\left(\lambda, \theta(t)\right)dt \tag{3.1}$$

where D is the day length (i.e. the number of seconds in which the Sun is above the horizon), F_{abs} is total SW radiation absorbed by the atmosphere, and t is time (in seconds). The integration is performed over half of the day length following the assumption that absorption in the first and second halves of the day are equal.

This integral is approximated using a three-point Gaussian quadrature method which uses weighted values of F_{abs} from three points in the half-day to calculate daily average absorption as follows:

$$\bar{F}_{abs} = \left(\frac{2D}{86400}\right)\sum_{i=1}^{3} W_i F_{abs}(\lambda, \theta(t_i)) \quad (3.2)$$

where W_i is the weighted value of F_{abs} for θ at time t_i. This calculation requires knowledge of how the solar zenith angle varies with latitude, time of day and time of year (e.g. see Petty 2006).

SOCRATES-RF models the tropopause pressure (p_{trop}) based on the following parametric equation of Checa-Garcia *et al.* (2018), which describes a symmetrical tropopause between both hemispheres as:

$$p_{trop} = \delta \tanh[\beta^{-1}(|\phi| - \alpha)] + \gamma \quad (3.3)$$

where ϕ is latitude, γ is the average of p_{trop} at 90° and 0°, δ defines the decrease in pressure between 90° and 0°, α defines the latitude at the centre of the transition from the 90° and 0° tropopause level (i.e. where $\tanh[\beta^{-1}(|\phi| - \alpha)] = 0$) and β defines the characteristic latitudinal width of the transition between the 90° and 0° tropopause. These parameters describe a tropopause without any seasonal dependence following the estimation of a climatological tropopause by Hansen *et al.* (2005). As described by Checa-Garcia *et al.* (2018), a seasonally-evolving tropopause may be characterised by introducing a time-dependence on several of the above parameters. All SOCRATES-RF calculations throughout this thesis use the combination of parameter values given in Table 3.5 to define p_{trop}. This yields an equatorial (0°) tropopause at 100 hPa and a polar (90°) tropopause at 230 hPa, resulting in a γ of 165 hPa (i.e. the average of 100 hPa and 230 hPa) and a δ of 65 hPa (which is defined as the difference between the tropopause at 90° and 0° divided by two i.e. δ = (230 hPa – 100 hPa)/2). At the latitude specified by α (i.e. 35°), p_{trop} equals γ; at latitudes either side of α, the tropopause varies according to Equation 3.3. Figure 3.1 shows the variation in p_{trop} with latitude as based on the parameters defined in Table 3.5.

δ	β	γ	α
65 hPa	10	165 hPa	35°

Table 3.5: Climatological tropopause parameters used to determine tropopause pressure in all SOCRATES-RF calculations. See Checa-Garcia et al. 2018.

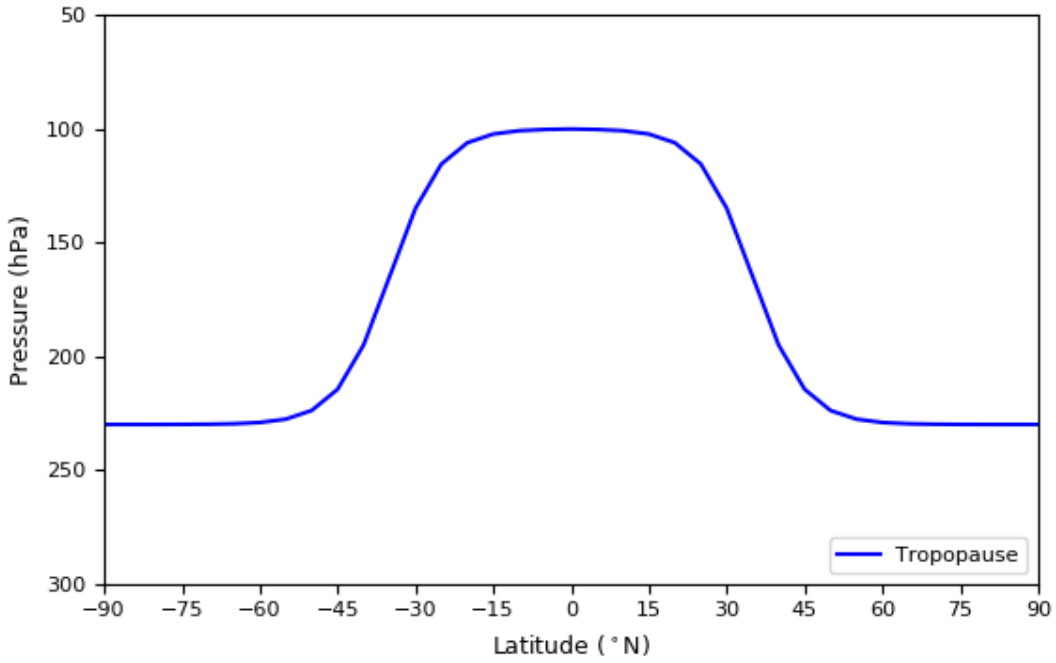

Figure 3.1: Variation in tropopause pressure with latitude as defined by Equation 3.3 and the parameters specified in Table 3.5. All SOCRATES-RF tropopause RFs are calculated using this definition of tropopause height.

Several studies highlight the sensitivity of RF calculations to the specification of tropopause height and demonstrate a spread in the estimation of global-mean forcings by up to 10%, depending on the definition used (e.g. Myhre and Stordal 1997; Freckleton *et al.* 1998; Forster *et al.* 2005). Checa-Garcia *et al.* (2018) investigate the sensitivity of O_3 tropopause RF to a range of parameter values used in Equation 3.3 and find that all-sky SW IRF, LW SARF and net RF varies by around 10%, 17% and 7%, respectively, depending on the combination of parameter values used (see supplementary material of Checa-Garcia *et al.* 2018). It is acknowledged that the specification of tropopause height contributes to uncertainty in the RF estimates calculated in this thesis. This source of uncertainty is quantified and discussed alongside other factors that influence RF estimates in Section 6.4.

3.2 Fixed dynamical heating

As described in Section 2.3, the magnitude of a forcing can be more accurately characterised by the calculation of SARF i.e. the change in net irradiance at the tropopause after allowing for stratospheric temperatures to readjust to radiative equilibrium, while holding surface and tropospheric temperatures at unperturbed values. All SARFs in this thesis are calculated using the widely used FDH approximation (originally developed by Ramanathan and Dickinson 1979 and Fels

et al. 1980). This approximation follows the assumption that stratospheric temperatures adjust via radiative processes alone following a perturbation in radiative heating. It is a widely used methodology (e.g. see Ramaswamy *et al.* 2018) for calculating a first-order estimate of the global-mean stratospheric temperature response to an imposed perturbation, and has been shown to produce estimates of stratospheric temperature change that are reasonably comparable to ESM simulations, in terms of the magnitude and structure of the temperature response (e.g. Fels *et al.* 1980; Kiehl and Boville 1988; Forster and Shine 2002; Maycock *et al.* 2013). The following description of the FDH process is a summary of the methodology outlined by Forster *et al.* (1997).

The stratosphere is both heated and cooled by dynamic and radiative processes. Thus, the rate of change of temperature in the stratosphere can be described by the following equation:

$$\frac{dT}{dt} = Q_{dyn} + Q_{SW} + Q_{LW}(T) \tag{3.4}$$

where Q_{dyn} is the dynamical heating rate and Q_{SW} and $Q_{LW}(T)$ are the SW and LW radiative heating rates, respectively. In an equilibrium state, the sum of each of these heating rate components equals zero throughout the stratosphere:

$$Q_{dyn} + Q_{SW} + Q_{LW}(T) = 0. \tag{3.5}$$

However, if the radiative balance of the atmosphere is perturbed, for example following a change in concentration of a radiatively active gas, then both Q_{SW} and $Q_{LW}(T)$ will be altered accordingly. The FDH methodology assumes that in such a case Q_{dyn} remains unchanged following the perturbation to each radiative heating rate term, and furthermore, that the stratosphere itself readjusts to radiative equilibrium on a faster timescale than the perturbation causing radiative imbalance. Such assumptions result in stratospheric temperatures being calculated following:

$$Q_{dyn} + Q'_{SW} + Q'_{lW}(T') = 0 \tag{3.6}$$

where Q'_{SW} and $Q'_{LW}(T')$ is the radiative heating in the perturbed atmosphere and Q_{dyn} is defined as:

$$Q_{dyn} = -(Q_{SW} + Q_{LW}(T)) \quad (3.7)$$

In SOCRATES-RF stratospheric temperatures are calculated following this process, whereby the left-hand term in Equation 3.4 is calculated using climatological data defined by the model user. Both the SW and LW terms of the radiative heating rate are also calculated using climatological data, with the dynamical heating rate estimated as a residual. This estimate of the dynamical heating rate is then kept constant, as stratospheric temperatures adjust using the following equation:

$$\frac{dT(t)}{dt} = Q_{dyn} + Q'_{SW}(t) + Q'_{LW}(T'(t)) \quad (3.8)$$

Stratospheric temperatures are estimated in SOCRATES-RF using Equation 3.8, with $Q'_{SW}(t)$ and $Q'_{LW}(T(t))$ being calculated at each time-step. This is iterated until $\frac{dT(t)}{dt} = 0$ at which $T(t) = T'$.

At this point SARF is calculated as the change in net irradiance at the tropopause (but note that the forcing is constant with height throughout the stratosphere, yielding an identical net forcing at both the TOA and tropopause). In this thesis, SOCRATES-RF is set to run assuming a 200-day adjustment time. This value is found to be a sufficient time scale over which stratospheric temperatures at the TOA and tropopause converge, indicating that stratospheric temperature adjustment has been achieved.

3.3 Data

3.3.1 HITRAN

The HITRAN database is widely used in radiative transfer models. As described in Section 2.4.3, It supplies spectroscopic parameters such as line intensity, position and width for all the main atmospheric absorbers. Due to improvements in experimental and theoretical spectroscopy, HITRAN has undergone regular updates over the past few decades leading to modifications to the

line parameters of some gases (Rothman *et al.* 1992, 1998, 2005, 2009, 2013); Gordon *et al.* 2017). The most recent HITRAN release, (Gordon *et al.* 2017) (widely referred to as HITRAN2016), report new measurements and analyses in the 3750 - 4700 cm^{-1} range for the $^{13}CH_4$ isotopologue and updates to the $^{12}CH_4$ line position, shape and intensities. Such updates could ultimately lead to significant differences in radiative transfer calculations if different versions of the HITRAN database are used.

To test the importance of HITRAN updates, RFM calculations of methane's NIR forcing across the 1 µm - 4 µm spectral range are compared using data from both HITRAN2012 (Rothman *et al.* 2013) and HITRAN2016 (Gordon *et al.* 2017). Table 3.6 details these experiments, calculated at the surface and tropopause, for a perturbation in CH_4 from 722 ppbv to 1720 ppbv and from 1720 ppbv to 3440 ppbv, using a global mean atmospheric profile. In all cases the percentage difference remains below 1%.

CH_4 perturbation (ppb)	**Surface IRF (W m^{-2})**		**% difference[a]**	**Tropopause IRF (W m^{-2})**		**% difference**
	HITRAN 2012	**HITRAN 2016**		**HITRAN 2012**	**HITRAN 2016**	
1720 -722	-1.15	-1.16	0.39	-0.166	-0.168	0.75
3440 - 1720	-1.60	-1.61	0.50	-0.22	-0.22	0.77

[a] *Percentage difference given by:* $\frac{HITRAN2012-HITRAN2016}{\frac{1}{2}(HITRAN2012+HITRAN2016)} \times 100$

Table 3.6: RFM calculations of surface (0 km) and tropopause (16 km) IRF for perturbations in a constant vertical profile of CH_4, in a CH_4-only atmosphere, from 722 ppbv - 1720 ppbv and 1720 ppbv - 3440 ppbv using a global mean atmospheric profile and different versions of the HITRAN database. Calculations are derived using a solar zenith angle of 0^o and the Kurucz extra-terrestrial solar spectrum, with $\Delta\nu$ = 1 cm^{-1}.

Further to this, updates to the H_2O spectrum could equally be significant due to the importance of CH_4 overlap with H_2O across the NIR (see Section 2.3.2). Table 3.7 shows the wavelength-integrated reduction in spectral irradiance at the surface and tropopause due to the presence of CH_4 at 1720 ppb (row 1) and its overlap with H_2O (row 2). Calculations are conducted using the RFM across the 1 µm - 4 µm spectral range using data from both HITRAN2012 and HITRAN2016. Again, the percentage difference remains below 1% and in most cases is much smaller than this.

These experiments demonstrate that the use of HITRAN2012 does not produce significant differences in CH_4 IRF and CH_4 and H_2O spectral irradiance calculations in comparison to the more

recent HITRAN2016 database. Furthermore, the reported differences (of below 1%) are likely small in comparison to other sources of error, such as the formulation of the radiation code and the specification of atmospheric parameters. As previously stated in Section 3.1.4, HITRAN2012 is used in all SOCRATES (and hence SOCRATES-RF) calculations. This is because HITRAN2012 is already built into the spectral files that drive this model. Given this, HITRAN2012 is also employed in all RFM calculations (which predominantly feature in Chapter 4) to make the intercomparison of IRF estimates conducted by the RFM and SOCRATES more comparable. Since RFMDISORT calculations are not compared to SOCRATES (or SOCRATES-RF) forcing estimates, HITRAN2016 is used in all RFMDISORT model simulations presented in Section 5.4.1.

Absorber	Wavelength-integrated reduction in spectral irradiance (W m^{-2}) Surface			Wavelength-integrated reduction in spectral irradiance (W m^{-2}) Tropopause		
	HITRAN 2012	HITRAN 2016	% difference	HITRAN 2012	HITRAN 2016	% difference
CH_4	2.505	2.513	0.31	0.365	0.367	0.64
$(CH_4 + H_2O) - (H_2O)$	1.580	1.582	0.14	0.364	0.366	0.63

Table 3.7: RFM calculations of surface (0 km) and tropopause (16 km) wavelength-integrated reduction in spectral irradiance due to a CH_4 only atmosphere (1720 ppbv, row 1) and its overlap with H_2O (held fixed at the values specified in the global mean atmospheric profile, row 2) for each version of the HITRAN database. Percentage differences highlight the difference in result when each version of HITRAN is used to provide spectroscopic parameters to the RFM. Calculations are derived using a solar zenith angle of 0^o and the Kurucz extra-terrestrial solar spectrum, with $\Delta v = 1$ cm $^{-1}$.

3.3.2 MIPAS CH_4 climatology

All SOCRATES-RF calculations presented in Chapter 6 use vertically-varying CH_4 mixing ratios derived from Michelson Interferometer for Passive Atmospheric Sounding (MIPAS) CH_4 climatology (Hegglin *et al.* 2021) created by the SPARC Data Initiative (SPARC 2017). This dataset is comprised of monthly zonal-mean CH_4 VMRs on a common latitude-pressure grid covering the upper troposphere to lower mesosphere (from 300 hPa to 0.1 hPa) with a latitudinal resolution of 5° from 87.5° north to 87.5° south.

MIPAS was a mid-infrared Fourier transform spectrometer, flown onboard the Sun-synchronous, polar-orbiting European Space Agency Environmental satellite (Envisat). MIPAS used the limb emission technique to observe aerosol, trace gas and atmospheric temperature in the 4.3 – 15 µm wavelength region during the day and night with global coverage. Table 3.8 provides further information on the dataset version, measurement period, vertical resolution and vertical range of CH_4 measurements included in the MIPAS CH_4 climatology used in this thesis. As detailed, this dataset consists exclusively of measurements taken after 2004 during the second MIPAS observation period (henceforth referred to as MIPAS-2), where the instrument operated with a reduced spectral resolution (but a higher vertical resolution) compared to its earlier 2002 – 2004 measurement mode (Plieninger *et al.* 2016).

Dataset version	**Measurement period**	**Vertical resolution**	**Vertical range**	**Reference**
MIPAS-2 (v224)	2005 - 2012	2 – 3.7 km	6 km/cloud top - 70 km	Plieninger *et al.* (2016)

Table 3.8: MIPAS CH_4 2005 – 2012 climatology measurement information. Obtained from Hegglin et al. (2021). Also see Plieninger et al. (2016) for further information on CH_4 measurements by the MIPAS instrument.

As reported by Hegglin *et al.* (2021), MIPAS-2 captures the extent and timing of high-latitude minima in CH_4 VMRs during the summer months (caused by photochemical reactions) and the semi-annual oscillation in CH_4 VMR maxima in the tropical upper-stratosphere (caused by the upwelling of less depleted CH_4 air by the equatorial semi-annual oscillation; e.g. Choi and Holton 1991). Such spatio-temporal features are shown in Figure 3.1, which depicts the time-latitude progression of MIPAS-2 CH_4 VMRs at 2 hPa averaged between 2005 – 2008.

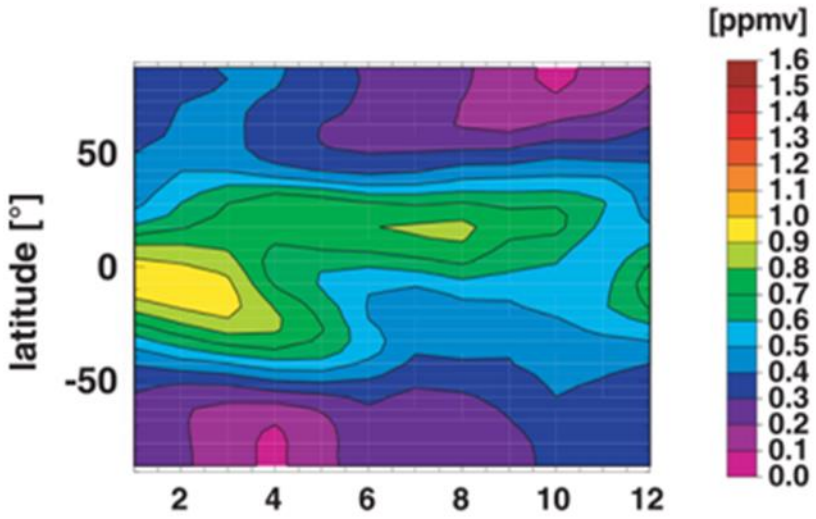

Figure 3.1: Latitude-time evolution of zonal, monthly-mean MIPAS-2 CH_4 VMRs at 2 hPa averaged over 2005 – 2008. From Hegglin et al. (2021).

Data preparation

Monthly-mean CH_4 VMRs are constructed by averaging individual months across the eight years in the 2005 – 2012 climatology period. Any remaining missing data points[1] at a given pressure level are filled in using the VMR from the same pressure level at the neighbouring latitude grid-point. Given that the majority of such missing data points occur (at several consecutive pressure levels) at the highest latitude grid-point of 87.5° south, an interpolation on the same pressure level between neighbouring grid-points was not consistently possible; however, it is appreciated that this option would provide a better solution for retaining horizontal gradients in CH_4 VMRs.

Interestingly, exploration of MIPAS CH_4 climatology reveals that VMRs in regions of the tropical upper troposphere are higher than those at lower pressure levels close to 300 hPa (where the highest VMRs are typically expected to be found). Figure 3.2 displays this feature in zonal-mean, monthly-mean CH_4 VMRs for July. As shown, VMR maxima with values greater than 1.75 ppmv (yellow filled contour) are evident across the equatorial region up to around 50 hPa.

[1] Remaining missing data points occur in April, July, August and September predominantly at 87.5° south between 300 hPa – 150 hPa.

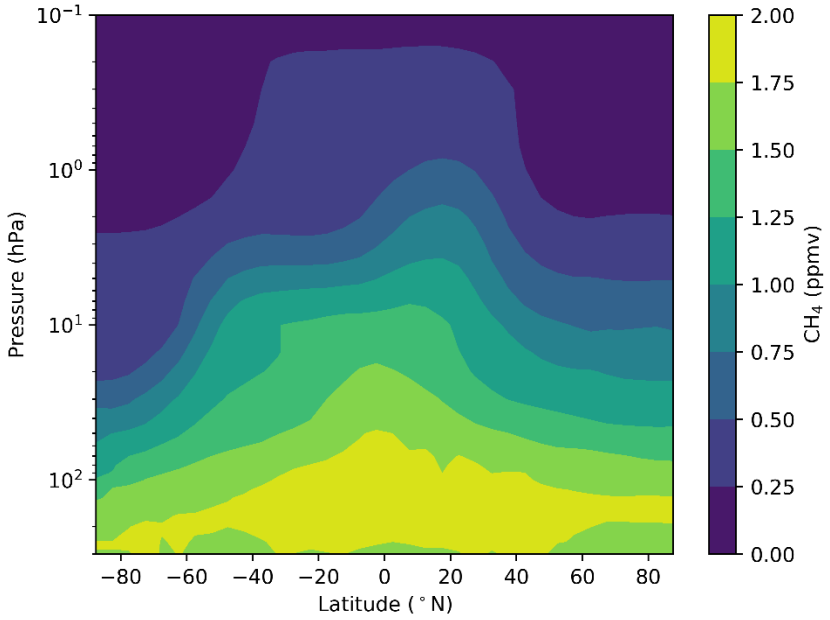

Figure 3.2: Zonal-mean, monthly-mean CH_4 VMRs (in ppmv) for July averaged over 2005 – 2012 showing maximum values high in the tropical upper troposphere.

SPARC (2017) note that MIPAS measurements exhibit a maximum in CH_4 VMRs in upper troposphere lower stratosphere (UTLS) region that is not present in other vertically-resolved satellite climatologies created by the SPARC Data Initiative, such as the Atmospheric Chemistry Experiment-Fourier Transform Spectrometer (ACE-FTS) and the Halogen Occultation Experiment (HALOE) datasets. This high bias is a known feature reported by several studies (e.g. von Clarmann *et al.* 2009; Laeng *et al.* 2015; Errera *et al.* 2016). Explanations as to why this occurs may be linked to instrument bias or the resulting impact of deep convection associated with the Asian monsoon region, which uplifts and traps high concentrations of CH_4 in the upper troposphere (Ricaud *et al.* 2014). Indeed, satellite retrievals from the Atmospheric Infrared Sounder (AIRS) from 2003 – 2007 confirm the presence of strong CH_4 enhancement during the monsoon season in the middle to upper troposphere during July, August and September over South Asia (Xiong *et al.* 2009). The noted maxima in MIPAS-2 data may therefore occur as a result of such dynamical processes, which is missing from both ACE-FTS and HALOE due to sparser sampling of the tropics by their solar occultation retrieval technique. However, it is unlikely that such an enhancement in CH_4 VMRs would have been present during pre-industrial times. Given that MIPAS CH_4 climatology is used to create pre-industrial fields of CH_4 in SOCRATES-RF calculations, it is therefore necessary to remove

this localised maximum before data are assimilated into SOCRATES-RF input files (see Section 6.1). Thus, this feature is removed as follows:

1. At each latitude, pre-industrial CH_4 profiles are constructed using the fall-off rate of MIPAS CH_4 VMRs, with a value of 750 ppbv at 300 hPa.

2. All data points higher than 750 ppbv above 300 hPa are masked and set to a value of 750 ppbv.

This ensures that CH_4 VMRs do not exceed 750 ppbv at altitudes higher than 300 hPa. Figure 3.3 shows the resulting zonal-mean, monthly-mean pre-industrial CH_4 VMRs for July. The experimental setup detailed in Section 6.1 provides further information on how MIPAS CH_4 fields are assimilated into SOCRATES-RF calculations.

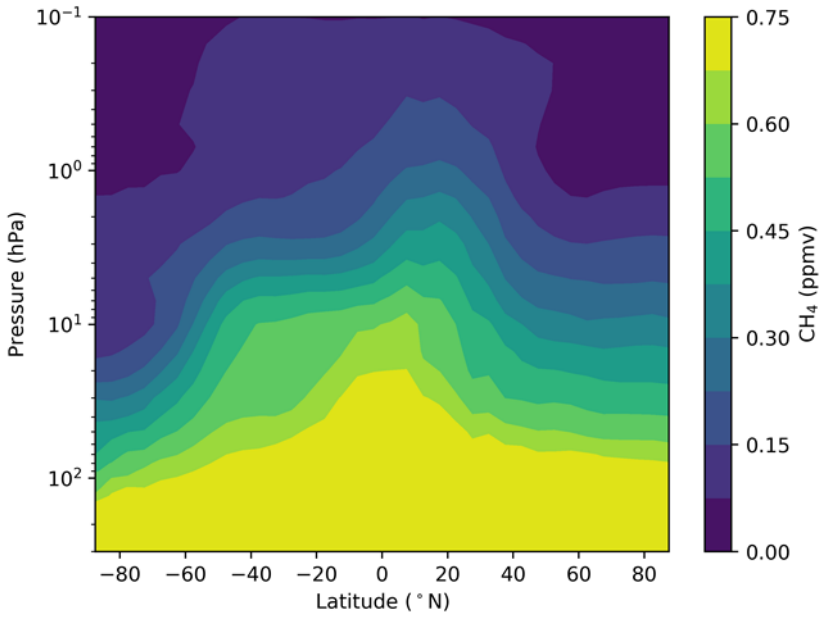

Figure 3.2: Pre-industrial zonal-mean, monthly-mean CH_4 VMRs for July (averaged over 2005 – 2012). Constructed using the fall-off rate of MIPAS CH_4 VMRs with a value of 0.75 ppmv at 300 hPa. The localised maxima in the tropical upper-troposphere in MIPAS CH_4 VMRs (see text) has been removed by masking all data points higher than 0.75 ppmv above 300 hPa to a value of 0.75 ppmv.

3.3.3 ECOSTRESS Fine-snow spectral surface albedo

The ECOSTRESS spectral library (Baldridge *et al.* 2009; Meerdink *et al.* 2019) provides a comprehensive selection of over 3000 spectra of natural and man-made surfaces, such as lunar and terrestrial soils, minerals, rocks, vegetation and water/snow/ice, covering the 0.35 µm – 15.4 µm wavelength range. Designed to support research related to the ECOsystem Spaceborne Thermal Radiometer Experiment on Space Station (ECOSTRESS) mission (deployed on the ISS), this library also includes contributions from three other spectral libraries: John Hopkins University, Jet Propulsion Laboratory (JPL) and the United States Geological Survey.

The ECOSTRESS 'Fine-snow' spectra is used in RFMDISORT experiments in Section 5.4.1 to investigate the dependence of methane's SW forcing on spectrally-resolved surface albedo related to snow-covered land surface type. The Fine-snow spectra were collected at the John Hopkins University Infrared Spectroscopy Laboratory and covers the 0.3 µm - 14 µm spectral range, based on model data from 0.3 µm to 2.08 µm and laboratory measurements from 2.08 µm to 14 µm. As stated in Section 5.4.1, this thesis utilises data across the 1 µm – 10 µm (1000 – 10000 cm^{-1}) spectral range.

3.3.4 Rangeland spectral surface albedo

To further investigate the dependence of methane's SW forcing on spectrally-resolved surface albedo, RFMDISORT experiments in Section 5.4.1 utilise the spectrally-varying 'Rangeland' (i.e. land occupied by native grasses/shrubs) surface albedo spectra measured at the Atmospheric Radiation Measurement (ARM) Climate Research Facility at the Southern Great Plains (SGP) observatory in Lamont, Oklahoma, United States. This site provides high quality data measurements from a range of instrument platforms for observational analysis, model simulations and process studies.

The Rangeland spectra were obtained from irradiance measurements taken by the upward-viewing Multi-Filter Rotating Shadowband Radiomenter (MFRSR) and the downward-viewing Multi-filter Radiometer (MFR) instruments collocated on 10 m and 25 m towers at the SGP site (https://circ.gsfc.nasa.gov/CIRC_input.html, last accessed 17 March 2021). The ratio of upward to downward irradiance measured across six measurement channels are used alongside published spectral albedos to produce a continuous spectral albedo function with a 1 cm^{-1} resolution. The surface albedo function related to each tower are averaged to create the Rangeland spectral surface

albedo, available from 0.2 µm to 12.2 µm. As stated in Section 5.4.1., this thesis uses Rangeland data across the 1 µm – 10 µm (1000 – 10000 cm^{-1}) spectral range.

3.3.5 SCIAMACHY LER database

The Scanning Imaging Absorption Spectrometer for Atmospheric Chartography (SCIAMACHY) flew on board the European Space Agency's Envisat satellite in a near-polar Sun-synchronous orbit. SCIAMACHY provided observations of the Earth's spectral surface reflectance between the 0.328 and 2.314 µm wavelength range from 2002 – 2012.

The SCIAMACHY surface LER database (Tilstra *et al.* 2017) provides the Lambertian-equivalent reflectivity (LER) of the Earth's surface across 34 one-nm wavelength bands between 0.328 and 2.314 µm for each month of the year at a 0.5° x 0.5° spatial resolution. LER is defined as the reflectance of an isotropic surface required to match observed TOA reflectance in a clear-sky, aerosol-free Rayleigh scattering atmosphere (e.g. see Kleipool *et al.* 2008). LER values were derived from SCIAMACHY observations using the Doubling-Adding KNMI polarised radiative transfer code (Stammes *et al.* 2012), consisting of an O_3 absorbing and Rayleigh scattering atmosphere with a Lambertian surface (i.e. where surface reflectivity is assumed to be isotropic). Henceforth, LER values are referred to as surface albedo values.

This thesis uses SCIAMACHY surface albedo data between 0.355 and 2.314 µm. Data at 0.328 µm were not included due to the small contribution of surface reflectivity to TOA reflectance at this wavelength (Tilstra *et al.* 2017). Initial handling of the database revealed that surface albedo values above one occur multiple times in each month in several different wavebands (mostly in the VIS), predominantly across the high-latitude and polar regions. It is not known why this occurs and inspection of the accompanying metadata did not provide an explanation. To handle this, all surface albedo values above one were replaced with a value of 0.95 (Huang *et al.* 2018). Further handling of the database revealed low spectral surface albedo values (around 0.001 to 0.008) across the NIR region over the global oceans. Based on a review of literature (e.g. Briegleb and Ramanathan 1982; Roesch *et al.* 2002; Séférian *et al.* 2018), these values are judged to inadequately represent the spectral reflectance of sea-surfaces which depend on a variety of complex factors, such as wind-induced variations in surface roughness, salinity, the effect of ocean whitecaps and marine biogeochemistry. Therefore, all open-ocean SCIAMACHY grid-points are masked and replaced with spectrally-varying sea-surface albedo values calculated using a SOCRATES internal subroutine, which is described further in the experimental setup detailed in Section 5.4.2.

Chapter 4

A comparison of shortwave radiation codes - is SOCRATES fit for purpose?

4.1 Introduction

In order to quantify methane's global mean SW radiative effect, there must be confidence in the ability of the employed radiative transfer code to produce accurate results. It is vital for the code to be able to fully simulate methane's effect on irradiance in the SW and accurately represent its complex spectral overlap with H_2O. As demonstrated by Etminan *et al.* (2016), both methane's band strength and overlap with H_2O play a key role in determining the sign and magnitude of its SW RF. Thus, the accurate representation of these characteristics will be crucial to meet the aims of this thesis.

Due to the high computational cost of calculating spatially and temporally-resolved, global-mean IRFs and SARFs, it is impractical to use a LBL model to perform the RF calculations required in this thesis. It is therefore necessary to employ a band model, which makes use of parameterisations that simplify the fundamental equations of radiative transfer for each spectral line of a radiatively active atmospheric constituent (see Section 2.4.3). These parameterisations essentially calculate

irradiances across a specified spectral band (rather than on an individual line-by-line basis) by making assumptions about the behaviour of radiative transfer across the spectral interval (e.g. Chapter 10, Petty 2006). Whilst such assumptions greatly increase computational efficiency, the use of approximations can inherently lead to errors in results. It is therefore vital to evaluate banded radiation codes against LBL models to assess the accuracy of their performance.

Several intercomparison studies of SW radiative transfer models now exist (e.g. Ellingson and Fouquart 1991; Fouquart *et al.* 1991; Halthore *et al.* 2005; Collins *et al.* 2006b; Forster *et al.* 2011). Most of these studies focus on quantifying differences in the calculation of clear-sky SW IRF between models in an effort to understand how well they perform given a simplified case, without the added complication of clouds and scattering. However, even under such constrained conditions, several studies report large discrepancies between banded radiation codes (used in ESMs) and LBL calculations (e.g. Fouquart *et al.* 1991; Collins *et al.* 2006b, Forster *et al.* 2011). Reasons for differences include diversity in the choice of parameterisations and the use of different spectral databases. Collins *et al.* (2006b) also report that such discrepancies are partly due to the omission of the NIR effects of CH_4 and N_2O in ESM radiation codes. Collins *et al.* (2006b) compared results from several LBL models against the majority of ESM codes included in IPCC AR4 and found that ESM codes systematically underestimate the magnitude of SW forcings at the surface, tropopause and TOA because CH_4 absorption (and to a lesser extent N_2O) were not included in parameterisations. Figure 4.1 demonstrates the extent to which CH_4 produces forcings across the SW for the corresponding LBL calculations from Collins *et al.* (2006b) for a CH_4 perturbation from 806 ppbv to 1760 ppbv (with the horizontal bar indicating the LBL model spread). Good agreement between the five LBL models is evident, and it is clear to see how the omission of SW CH_4 absorption in ESMs will lead to erroneous results.

Considering the results of Collins *et al.* (2006b) there is serious uncertainty surrounding the current ability of ESM codes to accurately resolve methane's SW forcing. Whilst some ESM codes do now include CH_4 SW absorption in parameterisations (e.g. see Smith *et al.* 2018), the low spectral resolution of their SW spectrum is unlikely to fully capture the effect of CH_4. For instance, in the current setup of the Met Office's UM (Walters *et al.* 2019), SW radiation is sampled across just 6-bands in the SOCRATES radiation scheme. This chapter will demonstrate that use of only 6 bands in SOCRATES (as they are currently parameterised) across the entire SW spectrum (0.17 - 10 μm) is inadequate for experiments in this thesis. Instead, a narrow-band configuration of SOCRATES is considered with a high k-distribution resolution in the SW, namely, with 260 bands across the 0.17 – 10 μm wavelength range (see Section 3.1.4).

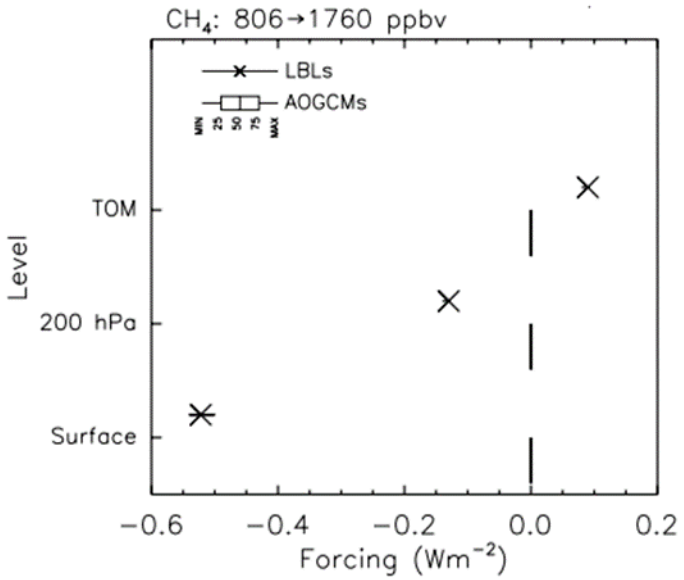

Figure 4.1: Clear-sky SW IRF at the surface, 200 hPa and TOA for a CH_4 perturbation from 806 ppbv to 1760 ppbv using a mid-latitude summer atmospheric profile with a solar zenith angle of 53^o and a surface albedo of 0.1, taken from Collins et al. (2006b).

This chapter presents a comparison of the 260-band version of SOCRATES against a benchmark LBL code, the RFM (Dudhia 2017). Calculations conducted using SOCRATES will be evaluated against the RFM for a range of clear-sky cases to assess the ability of this NBM in accurately simulating CH_4 SW IRF. The results presented in this chapter are therefore an essential precursor to the experiments presented throughout the rest of this thesis.

4.2 Experimental setup

The experiments in this chapter are computed using the RFM (described in Section 3.1.2) and SOCRATES (described in Section 3.1.4). SOCRATES calculations are predominantly carried out using the 260-band SW spectral file (sp_sw_260_jm2), henceforth referred to as SOC(260). The 6-band (sp_sw_ga7) configuration of SOCRATES, henceforth referred to as SOC(6), is used exclusively in Section 4.3 to demonstrate the inability of this broad-band code in calculating CH_4 SW IRF. Whilst

Etminan *et al.* (2016) demonstrate the importance of methane's NIR effect on stratospheric temperature adjustment, the experiments here omit the effects of this process as it is currently not possible to perform stratospheric temperature adjusted calculations using the RFM.

This radiation code intercomparison is based upon calculations of CH_4 SW tropopause and surface IRF. All calculations in this chapter are performed using the spectral range of 0.87 - 10 μm. To make results more closely comparable to the intercomparison of Collins *et al.* (2006b), these experiments utilise the same CH_4 perturbation in forcing calculations, from 806 ppbv to 1760 ppbv. Calculations are performed using profiles for mid-latitude summer (MLS), tropical (TROP) and sub-arctic winter (SAW) atmospheres which have been widely used in radiation code intercomparison studies (e.g. Ellingson *et al.* 1991). The tropopause is specified at 179 hPa, 93.7 hPa and 282.9 hPa in the MLS, TRO and SAW profiles, respectively, as based on the conventional definition of the thermal tropopause defined by the World Meteorological Organization (WMO 1986). As each model has a different approach to specifying the vertical grid of gaseous absorbers, model input files have been carefully constructed to ensure comparability between the calculation of IRF by SOC(260) and the RFM. For example, SOC(260) requires CH_4 VMRs to be specified at the *pressure midpoint* of the atmospheric layer between each pressure level, whilst the RFM specifies CH_4 VMRs at each pressure level. However, both models specify output at each pressure level (i.e. for SOC(260) this is the net downward flux of irradiance and for the RFM this is optical depth, see Section 3.1.4 and Section 3.1.2, respectively). Therefore, to ensure consistency between the vertical grid of CH_4 VMRs and the level at which IRFs are subsequently derived, SOC(260) calculations utilise a vertical grid of 61 pressure levels and hence 60 pressure layer midpoints and 60 CH_4 VMRs; RFM calculations utilise the same vertical grid of 60 pressure layer midpoints (as specified in SOC(260)) but instead specified as pressure levels, along with 60 CH_4 VMRs. In addition, surface pressure (from the lowest model level in SOC(260)) and surface CH_4 VMRs are added to the RFM vertical grid resulting in 61 pressure levels and 61 CH_4 VMRs. This set-up ensures that CH_4 VMRs are specified at the same pressure in each model. This is an important consideration, particularly with regards to investigating how the vertical variation of CH_4 VMRs impacts the calculation of CH_4 SW IRF (see Section 4.3.3). To calculate tropopause SW IRFs, model output is linearly interpolated onto the tropopause pressure levels stated above for each MLS, TROP and SAW experiment. Surface SW IRFs are calculated at the lowest model level. All calculations are carried out under clear-sky conditions in the absence of aerosols and scattering with zero a surface albedo assumed for simplicity. Four solar zenith angles (θ) are used (0^o, 30^o, 53^o, and 75^o) to test the ability of SOCRATES in handling both small and large air masses and to analyse the effect of long path lengths on atmospheric absorption.

The following cases are used to compare SOCRATES against the RFM:

Case 1: IRF due to a perturbation in CH_4 with CO_2, H_2O and N_2O held at fixed values.

Case 2: IRF due to a perturbation in CH_4 with no other gases present.

Case 3: IRF due to a perturbation in a vertically varying profile of CH_4 with no other gases present.

Table 4.1 details the concentration of atmospheric constituents specified in each case. Constant vertical profiles of CH_4, CO_2 and N_2O are used in Case 1, with a H_2O profile held fixed at the values specified in each given atmosphere (see Figure 4.2a). CO_2, N_2O and H_2O are included due to the significance of their spectral overlap with CH_4 absorption across the 0.87 – 10 μm region. As Case 2 represents a CH_4 only atmosphere, no other absorbers are prescribed in this calculation. Case 3 employs vertically-varying mixing ratios of CH_4 corresponding to MLS, TROP and SAW atmospheres (Anderson *et al.* 1986) with surface values corresponding to concentrations in 1860 and 2000 (See Figure 4.2b). Wavelength-integrated SW IRFs are calculated in all three cases along with spectrally-resolved SW IRFs for Cases 1 and 2, since agreement in the former does not always guarantee agreement in the latter.

Case	CH_4 (ppbv)	CO_2 (ppmv)	N_2O (ppbv)	H_2O[a]
1	806 → 1760	369	316	1
2	806 → 1760	0	0	-
3	806[b] → 1760[c]	0	0	-

[a] *Multiplier applied to atmospheric profile H_2O mixing ratio.*
[b,c] *Surface values only of vertically varying profile.*

Table 4.1: Mixing ratios of atmospheric constituents used in each case of the RFM - SOCRATES comparison. Mixing ratios of CH_4 in Cases 1, 2 and 3 all increase from 806 ppbv to 1760 ppbv and correspond to levels from 1860 and 2000 respectively (IPCC 2001). Mixing ratios of CH_4 in Case 3 vary with height throughout the atmosphere.

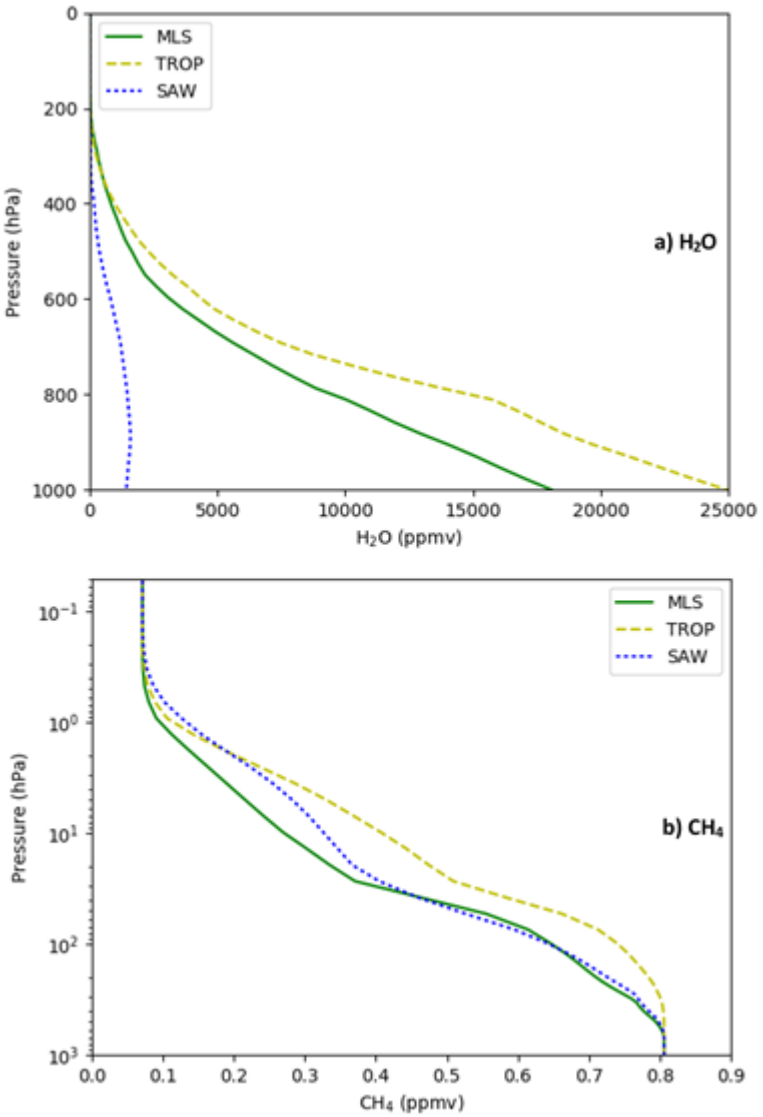

Figure 4.2:
a) H_2O mixing ratios as specified in Case 1 for each MLS, TROP and SAW atmospheric profile.

b) Vertically varying CH_4 mixing ratios as specified in Case 3 for each MLS, TROP and SAW atmospheric profile. Derived from Anderson et al. (1986).

4.3 Is SOCRATES fit for purpose?

The importance of evaluating the performance of banded radiation codes against LBL models is demonstrated in Figure 4.3, which compares methane's SW IRF calculated by the RFM, SOC(260) and SOC(6) at the surface and tropopause using the MLS atmospheric profile and Case 1 conditions with $\theta = 53°$.

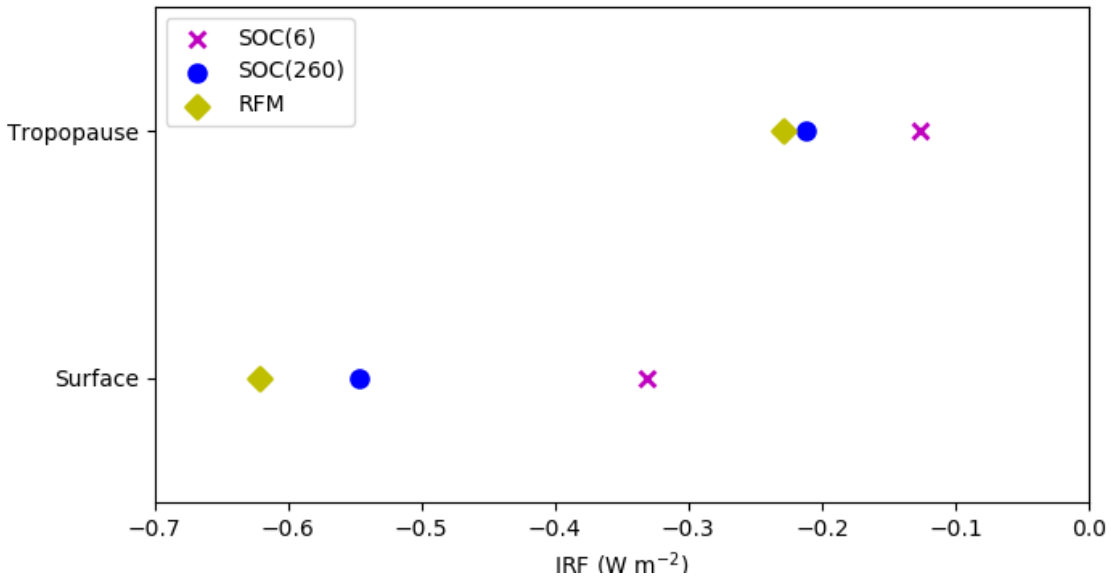

Figure 4.3: Clear-sky CH_4 SW IRF calculated at the surface and tropopause following a perturbation from 806 ppbv to 1760 ppbv using MLS atmospheric profile and conditions as stated in Case 1 in Table 4.1 with θ = 53°. Calculations have been run using the RFM, SOC(260) and SOC(6) to explore the difference in IRF estimates between each radiative transfer model.

Whilst SOC(6) does show capability in calculating CH_4 SW IRF (unlike some ESM radiation codes, as discussed in Section 4.1) it is clear that this configuration's spectral resolution is too coarse to fully capture the effect of methane's SW IRF, giving much lower values than both SOC(260) and the RFM at both model levels. Table 4.2 quantifies the extent of this poor performance showing the percentage error between SOC(6) and the RFM. Both the surface and tropopause SOC(6) SW IRFs are inaccurate (and underestimated) by about 45%. An explanation for this poor behaviour is evident on inspection of the sp_sw_ga7 spectral file used to drive SOC(6). CH_4 absorption across the entire SW spectrum in this configuration is represented by just two bands, from 1.19 - 2.38 µm and 2.38 - 10 µm. CH_4 transmittance in each of these bands is characterised by just one and four k-terms, respectively. Given that the magnitude and sign of CH_4 SW IRF varies strongly with wavelength, and

is highly dependent on the spectral overlap with H_2O (Etminan *et al.* 2016), it is clear that more bands (with an increased number of k-terms) are needed to accurately model CH_4 absorption. As SOC(6) is currently used in the Met Office's UM (Walters *et al.* 2019), it is evident that the spectral resolution of this configuration will render this ESM unreliable at calculating methane's SW RF. SOC(6) will therefore play no further role in this intercomparison.

	CH_4 SW IRF (W m^{-2})			**% Error[a] SOC(6) – RFM**	**% Error SOC(260) – RFM**
	SOC(6)	**SOC(260)**	**RFM**		
Tropopause	-0.126	-0.212	-0.229	-44.98	-7.42
Surface	-0.331	-0.547	-0.622	-46.78	-12.06

[a]*Percentage error is given by:* $\frac{SOC-RFM}{RFM} \times 100$

Table 4.2: Clear-sky CH_4 SW IRF calculated the RFM, SOC(260) and SOC(6) at the surface and tropopause following a perturbation from 806 ppbv to 1760 ppbv using MLS atmospheric profile and conditions as stated in Case 1 in Table 4.1 with θ = 53°. The percentage error between SOC(6) and RFM IRFs are shown in column 5. The percentage error between SOC(260) and RFM IRFs are shown in column 6.

SOC(260), however, does show better skill in calculating methane's SW IRF in comparison to the RFM. At both the tropopause and surface the magnitude of error is much smaller, at around 7% and 12% respectively (see Table 4.2). Whilst the SOC(260) surface SW IRF deviates more from the RFM (a potential concern), this is an encouraging initial result that indicates the use of a 260-band SW spectrum may be fit for purpose in calculating global-mean estimates of methane's SW radiative effect. However, it is important to test the capability of SOC(260) further using the range of cases listed in Section 4.2 and to examine if spectrally resolved forcings agree.

Collins *et al.* (2006b) report LBL multi-model mean clear-sky CH_4 SW IRF of -0.53 W m^{-2} and -0.13 W m^{-2} at the surface and tropopause, respectively, using conditions equivalent to Case 1 but with a surface albedo of 0.1 and a tropopause height of 200 hPa (see Figure 4.1). Whilst the forcings given in Table 4.2 are not directly comparable to Collins *et al.* (2006b), it is interesting to note that the RFM surface IRF (which accounting for a surface albedo of 0.1 would result in an IRF[2] of -0.56 W m^{-2}) agrees well with the multi-model LBL mean reported in that study. However, the RFM tropopause

[2] -0.622 x 0.9 = -0.56 W m^{-2}

IRF (which accounting for a surface albedo of 0.1 would result in a very much approximated IRF[3] of – 0.21 W m^{-2}) is around 1.5 times larger than Collins *et al.* (2006b). Given that Collins *et al.* (2006b) report good agreement amongst LBL codes participating in this intercomparison (which includes the RFM), this difference is disconcerting. Possible reasons for this disparity include the use of a slightly different version of the MLS atmosphere and tropopause height, possible different versions of SSI and TSI, and the spectral range across which forcings are calculated. Collins *et al.* (2006b) use a SW spectral range from 0.2 – 5 µm, which therefore omits the effect of solar absorption by methane's mid-infrared 7.7 µm band (see Figure 2.1). As demonstrated in Section 5.3, absorption at this wavelength plays a significant role in determining the magnitude of CH_4 SW IRF. With regard to SOC(260), accounting for a surface albedo of 0.1 would result in an IRF[4] of -0.49 W m^{-2} and -0.19 W m^{-2} at the surface and tropopause, respectively. Like the RFM, SOC(260) shows better agreement with Collins *et al.* (2006b) at the surface and a stronger disparity at the tropopause.

4.3.1 Case 1

Table 4.3 compares surface and tropopause SW IRFs calculated by SOC(260) and the RFM due to a perturbation in CH_4 with CO_2, H_2O and N_2O held at fixed values, using a range of different solar zenith angles. This allows for an evaluation of how well SOC(260) can calculate CH_4 SW IRF in the presence of spectrally overlapping gases for both small (1) and large (3.86) air masses. The percentage error and absolute error between each SOC(260) and RFM estimate are also shown.

SOC(260) produces the most accurate forcings at both the surface and tropopause under SAW atmospheric conditions. Here the percentage error for all SW IRFs remains below 7% at the tropopause and below 5% at the surface. This performance is likely due to low H_2O concentrations throughout the SAW profile (see Figure 4.2a) reducing the degree of H_2O spectral overlap with CH_4, allowing for SOC(260) to better simulate the change in irradiance due to a CH_4 perturbation. In contrast, much higher percentage errors are found (and with increasing air mass) in the TROP profile at the surface (~12 - 26%), and to a slightly lesser extent in the MLS profile at the surface (~10 - 19%). This is likely due to the presence of higher amounts of H_2O with increased path length through the troposphere. To test if this is the cause, comparisons can be made against Case 2 (CH_4-only atmosphere, see Section 4.3.2) to investigate if the absence of H_2O improves both the TROP and MLS surface forcings.

[3] -0.229 x 0.9 = -0.21 W m^{-2}

[4] -0.547 x 0.9 = -0.49 W m^{-2} (surface) and -0.212 x 0.9 = -0.19 W m^{-2} (tropopause)

Profile	θ (°)	Tropopause SW IRF (W m^{-2})			
		SOC(260)	RFM	% Error	Absolute Error
MLS	0	-0.248	-0.268	-7.46	2.00×10^{-2}
	30	-0.237	-0.256	-7.42	1.90×10^{-2}
	53	-0.212	-0.229	-7.42	1.70×10^{-2}
	75	-0.164	-0.175	-6.29	1.10×10^{-2}
TROP	0	-0.138	-0.153	-9.80	1.50×10^{-2}
	30	-0.132	-0.146	-9.59	1.40×10^{-2}
	53	-0.120	-0.132	-9.09	1.20×10^{-2}
	75	-0.093	-0.102	-8.82	9.00×10^{-3}
SAW	0	-0.366	-0.393	-6.87	2.70×10^{-2}
	30	-0.351	-0.376	-6.65	2.50×10^{-2}
	53	-0.314	-0.337	-6.82	2.30×10^{-2}
	75	-0.242	-0.256	-5.47	1.40×10^{-2}
Profile	θ (°)	Surface SW IRF (W m^{-2})			
		SOC(260)	RFM	% Error	Absolute Error
MLS	0	-0.707	-0.781	-9.48	7.40×10^{-2}
	30	-0.660	-0.733	-9.96	7.30×10^{-2}
	53	-0.547	-0.622	-12.06	7.50×10^{-2}
	75	-0.318	-0.393	-19.08	7.50×10^{-2}
TROP	0	-0.636	-0.723	-12.03	8.70×10^{-2}
	30	-0.590	-0.676	-12.72	8.60×10^{-2}
	53	-0.478	-0.568	-15.85	9.00×10^{-2}
	75	-0.259	-0.350	-26.00	9.10×10^{-2}
SAW	0	-0.951	-1.001	-5.00	5.00×10^{-2}
	30	-0.903	-0.947	-4.65	4.40×10^{-2}
	53	-0.786	-0.825	-4.73	3.90×10^{-2}
	75	-0.543	-0.567	-4.23	2.40×10^{-2}

Table 4.3: Case 1 surface and tropopause SW IRFs following a perturbation in CH_4 from 806 ppbv to 1760 ppbv with CO_2, H_2O and N_2O held at fixed values (see Table 4.1) using four different solar zenith angles for each MLS, TROP and SAW atmospheric profile. The percentage error (as defined in Table 4.2) and absolute error between SOC(260) and the RFM are shown for each solar zenith angle at both the tropopause and the surface.

Despite the TROP and MLS surface SW IRF errors (where θ = 53° and 75°), it is evident that SOC(260) does perform well compared to the RFM (i.e. with a mean error of around 8%). Interestingly, in every case the sign of the percentage error is negative. This indicates that SOC(260) is consistently underestimating CH_4 SW IRF in comparison to the RFM. However, this may be due to a compensation of errors across the 260 bands, with some spectral regions overestimating and others underestimating the forcing. It is therefore important to conduct a spectral analysis of the SW IRF

calculated by SOC(260). This is achieved by calculating the IRF per 'spectral region' within the 0.87 - 10 μm range, whereby a spectral region is defined as sets of SOC(260) bands which exhibit CH_4 absorption.

Table 4.4 compares the SW IRF calculated per spectral region in SOC(260) against the corresponding SW IRF per spectral region in the RFM for the MLS atmosphere at θ = 53°. The percentage error and absolute error between each SOC(260) and RFM estimate are also shown. As evident by the sign of the percentage error for each spectral region, SOC(260) both overestimates and underestimates tropopause and surface forcings. This demonstrates that a compensation of errors takes place to generate the wavelength-integrated SW IRFs for the MLS atmosphere given in Table 4.3. The greatest percentage error occurs at the surface in the 5.5 - 10 μm region (∼23%) and at the tropopause in the 1.6 - 2.02 μm region (∼-16%). However, comparison of the magnitude of the IRF of each spectral region reveals that the main contributors to methane's surface and tropopause SW IRF are the 1.6 - 2.02 μm, 2.1 - 2.9 μm and 3.0 - 4.8 μm spectral regions (see Figure 4.4). Consequently, despite the fact that the percentage error is large for the 5.5 – 10 μm region at the surface, its contribution to the total surface SW IRF is not the most significant (see Figure 4.4b). The magnitude of the absolute error between SOC(260) and the RFM (6.80×10^{-4}, see Table 4.4) further demonstrates that the impact of a ∼23% error in this spectral region is not significantly detrimental to the overall 0.87 - 10 μm surface SW IRF. However, this is not the case for the 1.6 - 2.02 μm spectral region at the tropopause (see Figure 4.4a). Here, the absolute error between SOC(260) and the RFM is more significant at 4.46×10^{-3} (see Table 4.4) and therefore the ∼-16% error in SW IRF across this spectral region contributes more to the total error in SW IRF across the full 0.87 – 10 μm for the MLS atmosphere at θ = 53° (i.e. -7.42%, see Table 4.3). Etminan *et al.* (2016) identify that a positive forcing at 1.6 μm plays a key role in determining the sign and magnitude of the global-mean all-sky CH_4 SW IRF. It is therefore vital to explore possible causes of this error to determine the significance of this result. Reasons as to why some spectral regions in SOC(260) miscalculate the SW IRF could likely include the complex overlap of CH_4 with other absorbers (particularly H_2O) and the parameterised approximations of radiative transfer processes employed in the model. Further analysis on this matter is given in Case 2 (see Section 4.3.2), whereby the corresponding spectral analysis of a CH_4-only atmosphere can provide more clarity in determining the exact nature (and significance of) these errors.

Spectral region (μm)	Tropopause SW IRF (W m^{-2})			
	SOC(260)	**RFM**	**% Error**	**Absolute Error**
0.87 – 0.91	-0.00050	-0.00047	6.38	3.00×10^{-5}
1.09 – 1.24	-0.00585	-0.00584	0.17	1.00×10^{-5}
1.3 – 1.52	-0.00911	-0.00971	-6.18	6.00×10^{-4}
1.6 - 2.02	-0.02354	-0.02800	-15.93	4.46×10^{-3}
2.1 - 2.9	-0.08258	-0.09095	-9.20	8.37×10^{-3}
3.0 - 4.8	-0.07901	-0.08286	-4.65	3.85×10^{-3}
5.5 – 10	-0.01125	-0.01161	-3.10	3.60×10^{-4}
Spectral region (μm)	**Surface SW IRF (W m^{-2})**			
	SOC(260)	**RFM**	**% Error**	**Absolute Error**
0.87 – 0.91	-0.00220	-0.00216	1.85	4.00×10^{-5}
1.09 – 1.24	-0.01440	-0.01436	0.28	4.00×10^{-5}
1.3 – 1.52	-0.00510	-0.00440	15.91	7.00×10^{-4}
1.6 - 2.02	-0.10960	-0.11517	-4.84	5.57×10^{-3}
2.1 - 2.9	-0.29300	-0.34621	-15.37	5.32×10^{-2}
3.0 - 4.8	-0.11840	-0.13640	-13.20	1.80×10^{-2}
5.5 – 10	-0.00360	-0.00292	23.29	6.80×10^{-4}

Table 4.4: Case 1 MLS summer surface and tropopause SW IRF per 'spectral region' for a perturbation in CH_4 from 806 ppbv to 1760 ppbv with CO_2, H_2O and N_2O held at fixed values (see Table 4.1) using a solar zenith angle of 53°. The percentage error (as defined in Table 4.2) and absolute error between SOC(260) and the RFM are shown for each spectral region at both the tropopause and the surface.

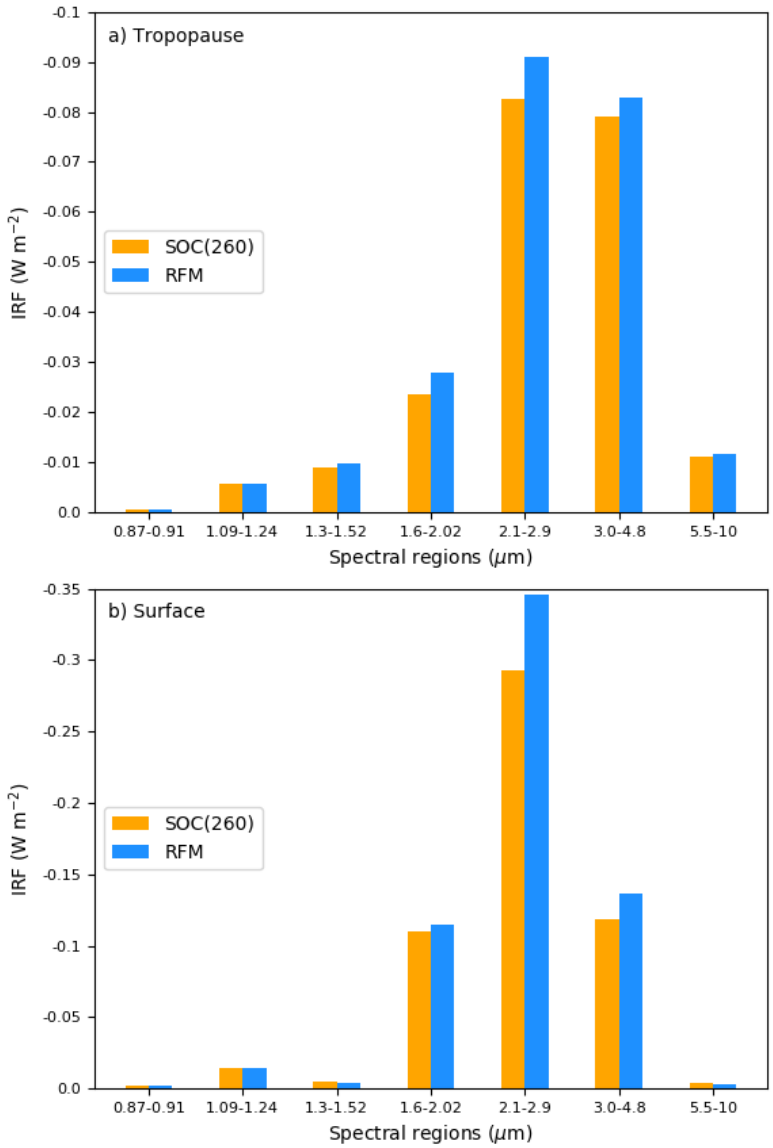

Figure 4.4: MLS SW IRF per spectral region for SOC(260) and the RFM at a) the tropopause and b) the surface for a perturbation in CH_4 from 806 ppbv to 1760 ppbv with CO_2, H_2O and N_2O held at fixed values (see Table 4.1) using a solar zenith angle of 53^o. Note that Table 4.4 provides the best comparison of forcings for the 0.87 - 0.91 µm region as the small size of the IRFs here render these results difficult to see in this figure.

4.3.2. Case 2

Table 4.5 compares CH_4 SW IRF calculated by SOC(260) and the RFM at the surface and tropopause due to a perturbation in a CH_4-only atmosphere from 806 ppbv to 1760 ppbv. This provides an evaluation of how well SOC(260) can calculate CH_4 SW IRF without the influence of the spectrally overlapping gases as used in Case 1. The percentage error and absolute error between each SOC(260) and RFM estimate are also shown.

Profile	θ (°)	Tropopause SW IRF (W m^{-2})			
		SOC(260)	RFM	% Error	Absolute Error
MLS	0	-0.249	-0.269	-7.43	2.00×10^{-2}
	30	-0.238	-0.257	-7.39	1.90×10^{-2}
	53	-0.214	-0.231	-7.36	1.70×10^{-2}
	75	-0.164	-0.178	-7.87	1.40×10^{-2}
TROP	0	-0.139	-0.153	-9.15	1.40×10^{-2}
	30	-0.133	-0.146	-8.90	1.30×10^{-2}
	53	-0.120	-0.132	-9.09	1.20×10^{-2}
	75	-0.094	-0.102	-7.84	8.00×10^{-3}
SAW	0	-0.370	-0.398	-7.04	2.80×10^{-2}
	30	-0.354	-0.380	-6.84	2.60×10^{-2}
	53	-0.319	-0.342	-6.73	2.30×10^{-2}
	75	-0.248	-0.262	-5.34	1.40×10^{-2}
Profile	θ (°)	Surface SW IRF (W m^{-2})			
		SOC(260)	RFM	% Error	Absolute Error
MLS	0	-1.186	-1.240	-4.35	5.40×10^{-2}
	30	-1.137	-1.185	-4.05	4.80×10^{-2}
	53	-1.022	-1.063	-3.86	4.10×10^{-2}
	75	-0.779	-0.796	-2.14	1.70×10^{-2}
TROP	0	-1.186	-1.240	-4.35	5.40×10^{-2}
	30	-1.138	-1.185	-3.97	4.70×10^{-2}
	53	-1.022	-1.063	-3.86	4.10×10^{-2}
	75	-0.779	-0.796	-2.14	1.70×10^{-2}
SAW	0	-1.173	-1.228	-4.48	5.50×10^{-2}
	30	-1.126	-1.173	-4.01	4.70×10^{-2}
	53	-1.01	-1.052	-3.99	4.20×10^{-2}
	75	-0.769	-0.787	-2.29	1.80×10^{-2}

Table 4.5: Case 2 surface and tropopause SW IRF for a perturbation in a CH_4-only atmosphere from 806 ppbv to 1760 ppbv (see Table 4.1) using four different solar zenith angles for each MLS, TROP and SAW atmospheric profile. The percentage error (as defined in Table 4.2) and absolute error between SOC(260) and the RFM are shown for each zenith angle at both the tropopause and the surface.

As shown, SOC(260) is able to calculate forcings at the surface and tropopause within 9% of the RFM in all cases. The absence of H_2O, CO_2 and N_2O results in much smaller percentage errors (< ~4%) in both the TROP and MLS profiles at the surface; this reinforces the hypothesis that SOC(260) struggles to fully resolve surface CH_4 SW IRF when conditions of high H_2O concentrations are present. Arguably this could also be due to the presence of increased spectral overlap with CO_2 and N_2O. However, initial testing (not shown) of the impact of GHG overlap with CH_4 shows definitively that H_2O has the greatest effect on CH_4 SW IRF. The calculation of daily-average forcings should reduce the impact of the errors found at higher solar zenith angles for calculations including H_2O.

As previously explained, it is important to evaluate whether or not the performance of SOC(260) (now under Case 2 conditions) is due to a compensation of errors across the 260 bands. Table 4.6 compares the SW IRF calculated per spectral region in SOC(260) against the corresponding SW IRF per spectral region in the RFM for the MLS atmosphere for θ = 53°. The percentage error and absolute error between each SOC(260) and RFM estimate are also shown.

Spectral region (μm)	**Tropopause SW IRF (W m^{-2})**			
	SOC(260)	**RFM**	**% Error**	**Absolute Error**
0.87 – 0.91	-0.00040	-0.00047	-14.89	7.00×10^{-5}
1.09 – 1.24	-0.00584	-0.00585	-0.17	1.00×10^{-5}
1.3 – 1.52	-0.00931	-0.00993	-6.24	6.20×10^{-4}
1.6 - 2.02	-0.02355	-0.02804	-16.01	4.49×10^{-3}
2.1 - 2.9	-0.08287	-0.09145	-9.38	8.58×10^{-3}
3.0 - 4.8	-0.07939	-0.08325	-4.64	3.86×10^{-3}
5.5 – 10	-0.01201	-0.01248	-3.77	4.70×10^{-4}
Spectral region (μm)	**Surface SW IRF (W m^{-2})**			
	SOC(260)	**RFM**	**% Error**	**Absolute Error**
0.87 – 0.91	-0.00240	-0.00238	0.84	2.00×10^{-5}
1.09 – 1.24	-0.03560	-0.03533	0.76	2.70×10^{-4}
1.3 – 1.52	-0.05450	-0.05620	-3.02	1.70×10^{-3}
1.6 - 2.02	-0.13600	-0.14343	-5.18	7.43×10^{-3}
2.1 - 2.9	-0.43010	-0.45115	-4.67	2.11×10^{-2}
3.0 - 4.8	-0.31640	-0.32708	-3.27	1.07×10^{-2}
5.5 – 10	-0.04625	-0.04702	-1.64	7.70×10^{-4}

Table 4.6: MLS surface and tropopause SW IRF per 'spectral region' for a perturbation in a CH_4-only atmosphere from 806 ppbv to 1760 ppbv using a solar zenith angle of 53^o. The percentage error (as defined in Table 4.2) and absolute error between SOC(260) and the RFM are shown for each spectral region at both the tropopause and the surface.

The majority of Case 2 surface forcings have a lower percentage error compared to Case 1. This indicates that the presence of H_2O, CO_2 or N_2O spectral overlap was the cause of a major portion of the inaccuracy in the surface SW IRFs under Case 1 conditions. This is particularly evident in the 5.5 - 10 μm spectral region where the percentage error is reduced by around 20%. Improvement in surface SW IRFs is expected to be more pronounced than tropopause SW IRFs when other gases (in particular H_2O) are removed, as the influence of spectrally overlapping gases on tropopause forcings is expected to be small since stratospheric concentrations of H_2O are low. Consequently, at the tropopause the percentage errors remain largely the same compared to Case 1, apart from the 0.87 - 0.91 μm spectral region which exhibits an increased error of around 9%. However, the largest tropopause percentage error remains in the 1.6 – 2.02 μm region (-16.01%). Here the error value is marginally higher than in Case 1 (-15.93%, see Table 4.4) indicating that the cause of inaccuracy in this region must be attributed to CH_4. Further analysis (not shown) of the 1.6 – 2.02 μm region indicates that the majority of the percentage error in this spectral range occurs between 1.6 - 1.7 μm. Analysis of spectral irradiance across this region reveals that this wavelength range exhibits a large variation in the strength of CH_4 absorption. Examination of the spectral file used to drive SOC(260) reveals that CH_4 absorption across the 1.6 - 1.7 μm region is represented by just 5 bands which each have 1, 1, 3, 4 and 5 k-terms respectively. It is evident that an increased number of k-terms are needed here to more accurately characterise CH_4 absorption and the change in irradiance due to a perturbation in gas concentration. These findings have been reported to the SOCRATES radiative transfer parameterisation team at the U.K Met Office.

As shown in Case 1, comparison of the magnitude of the IRF of each spectral region reveals that the main contributors to methane's surface and tropopause SW IRF are the 1.6 - 2.02 μm, 2.1 - 2.9 μm and 3.0 - 4.8 μm spectral regions (see Figure 4.5). Consequently, the ∼15% error at the tropopause in the 0.87 - 0.91 μm spectral region is not detrimental to the total 0.87 - 10 μm SW IRF (See Figure 4.5b). The magnitude of the absolute error between SOC(260) and the RFM across this region is small at just 7.00×10^{-5} (see Table 4.6). Since the 1.6 - 2.02 μm spectral region plays a key role in determining methane's all-sky tropopause SW IRF (Etminan *et al.* 2016), the percentage error across this wavelength range at the tropopause (under both Case 1 and Case 2 conditions) is a more serious discrepancy. However, it must be considered that the *wavelength-integrated* tropopause SW IRF for the MLS profile at $\theta = 53^{o}$ exhibits an error of less than 8% in both Case 1 and Case 2, and additionally, that SOC(260) offers a much more detailed representation of CH_4 compared to ESM radiation codes (e.g. SOC(6), see also Collins *et al.* 2006b). Furthermore, to calculate geographically and seasonally resolved RFs (which include stratospheric temperature adjustment), compromises between computational speed and accuracy are necessary.

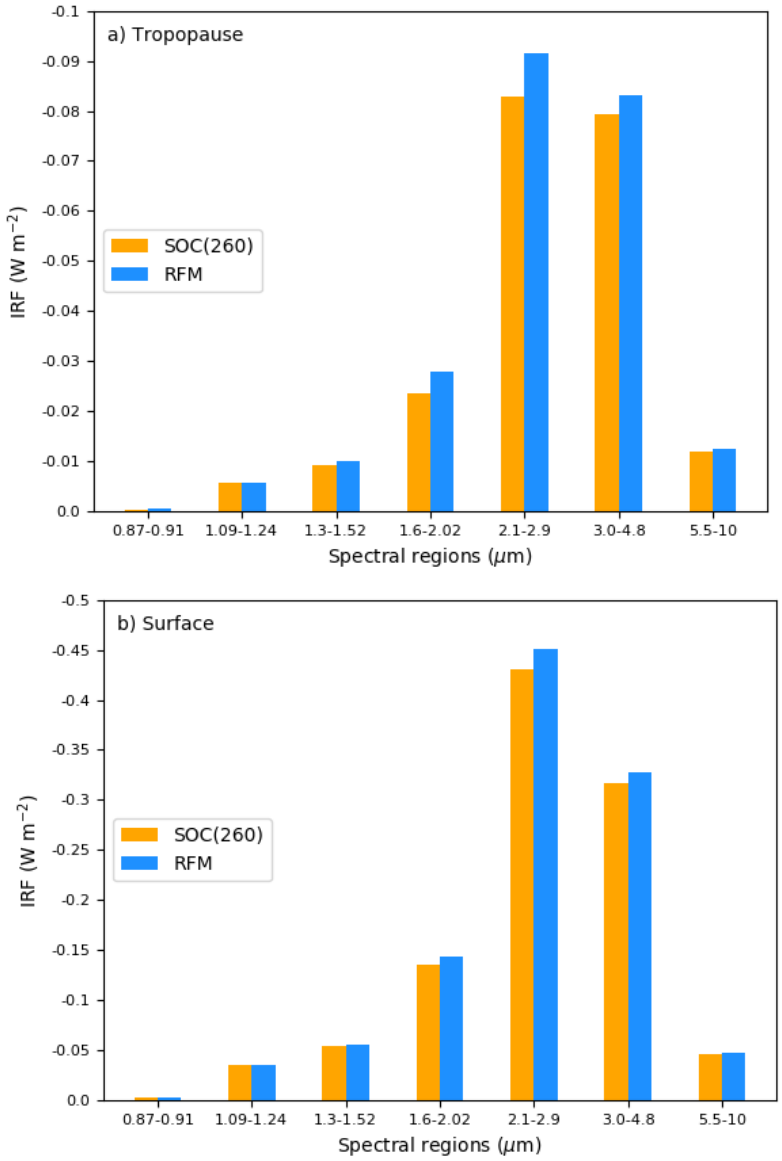

Figure 4.5: Case 2 MLS SW IRF per spectral region for SOC(260) and the RFM at a) the tropopause and b) the surface for a perturbation in a CH_4-only atmosphere from 806 ppbv to 1760v ppb (see Table 4.1) using a solar zenith angle of 53^o. Note that Table 4.6 provides the best comparison of forcings for the 0.87 - 0.91 µm region as the small size of the IRFs here render these results difficult to see in this figure.

4.3.3 Case 3

All forcings presented in Case 1 and Case 2 utilise constant vertical profiles of CH_4. However, observational studies show that CH_4 decreases with height above the tropopause (e.g. Koo *et al.* 2017). A realistic representation of methane's atmospheric profile could be of potential importance to forcing calculations since stratospheric CH_4 SW absorption contributes significantly to the sign and magnitude of its SW IRF (Etminan *et al.* 2016). Freckleton *et al.* (1998) consider the effect of vertically-varying profiles on TIR calculations of GHG RFs, and report that the use of a realistic profile reduces forcings by around 2%. However, initial clear-sky tests conducted using the RFM reveal that the impact of a realistic profile is more significant in the SW for CH_4, causing a reduction in tropopause SW IRF by around 20% (analysis not shown). It is therefore essential to analyse this further. Firstly, by comparing Case 3 SW IRFs against Case 2 SW IRFs, which are calculated using vertically-varying CH_4 mixing ratios and constant vertical CH_4 mixing ratios, respectively (in CH_4-only atmospheres, see Table 4.1). Secondly, to determine if SOC(260) is capable of capturing the effect of vertically-varying mixing ratios on SW IRF in comparison to the RFM.

Table 4.7 compares Case 3 surface and tropopause CH_4 SW IRFs calculated by SOC(260) and the RFM following a perturbation from 806 ppbv to 1760 ppbv. These results can be directly compared to Table 4.5, which shows equivalent Case 2 calculations conducted using constant vertical profiles of CH_4 mixing ratios. In comparison to Case 2, the use of vertically-varying profiles reduces the magnitude of both SOC(260) and RFM tropopause SW IRFs by around 20% in MLS and TROP atmospheres, and by around 14% in SAW. This reduction occurs because vertically-varying mixing ratios result in less stratospheric SW CH_4 absorption, at both pre-industrial and present-day levels (as shown in Figure 4.2b, CH_4 decreases significantly with height above the troposphere). Hence, following a perturbation in CH_4, the change in downward SW irradiance at the tropopause is reduced. The difference between Case 3 and Case 2 is less pronounced at the surface. Here, SW IRFs differ by around 3-4% in MLS and SAW atmospheres and by 1.5% in TROP. The effect of decreasing CH_4 mixing ratios above the tropopause has a smaller effect on the downward SW irradiance at the surface, at both pre-industrial and present day concentrations. However, a reduction in the tropopause SW IRF by 14-20% is significant. This demonstrates the importance of profile specification in CH_4 SW forcing calculations. Further analysis presented in Section 5.2 quantifies the impact of CH_4 profile specification on all-sky SW IRFs and SARFs.

Table 4.7 also shows the percentage error and absolute error between SOC(260) and the RFM for forcings calculated using a vertically varying profile of CH_4. The percentage error never exceeds 9% and in most cases is lower than this, especially at the surface. For each profile and solar zenith angle

the percentage error is greatest at the tropopause. However, all percentage errors are slightly improved in comparison to Case 2 (Table 4.5). This shows that the use of a vertically-varying profile improves SOC(260)'s calculation of methane's SW IRF.

Profile	θ (°)	Tropopause SW IRF (W m^{-2})			
		SOC(260)	RFM	% Error	Absolute Error
MLS	0	-0.200	-0.215	-6.98	1.50×10^{-2}
	30	-0.192	-0.206	-6.80	1.40×10^{-2}
	53	-0.172	-0.185	-7.03	1.30×10^{-2}
	75	-0.133	-0.144	-7.64	1.10×10^{-2}
TROP	0	-0.114	-0.125	-8.80	1.10×10^{-2}
	30	-0.109	-0.119	-8.40	1.00×10^{-2}
	53	-0.098	-0.107	-8.41	9.00×10^{-3}
	75	-0.077	-0.084	-8.33	7.00×10^{-3}
SAW	0	-0.321	-0.344	-6.69	2.30×10^{-2}
	30	-0.309	-0.328	-5.79	1.90×10^{-2}
	53	-0.277	-0.296	-6.42	1.90×10^{-2}
	75	-0.216	-0.229	-5.68	1.30×10^{-2}
Profile	θ (°)	Surface SW IRF (W m^{-2})			
		SOC(260)	RFM	% Error	Absolute Error
MLS	0	-1.145	-1.193	-4.02	4.80×10^{-2}
	30	-1.099	-1.141	-3.68	4.20×10^{-2}
	53	-0.989	-1.025	-3.51	3.60×10^{-2}
	75	-0.756	-0.772	-2.07	1.60×10^{-2}
TROP	0	-1.171	-1.221	-4.10	5.00×10^{-2}
	30	-1.123	-1.167	-3.77	4.40×10^{-2}
	53	-1.009	-1.048	-3.72	3.90×10^{-2}
	75	-0.770	-0.787	-2.16	1.70×10^{-2}
SAW	0	-1.136	-1.18	-3.73	4.40×10^{-2}
	30	-1.092	-1.134	-3.70	4.20×10^{-2}
	53	-0.981	-1.019	-3.73	3.80×10^{-2}
	75	-0.748	-0.765	-2.22	1.70×10^{-2}

Table 4.7: Case 3 surface and tropopause SW IRF for a perturbation in a vertically varying profile of CH_4 from 806 ppbv to 1760 ppbv (See Table 4.1 and Figure 4.2b) using four different solar zenith angles for each MLS, TROP and SAW atmospheric profile. The percentage error (as defined in Table 4.2) and absolute error between SOC(260) and the RFM are shown for each zenith angle at both the tropopause and the surface.

4.4 Chapter conclusions

This chapter has investigated if the 6-band and 260-band configurations of the SOCRATES radiative transfer scheme can accurately calculate CH_4 forcings in the SW. SOCRATES has been compared against the reference LBL model, the RFM, to evaluate if its parameterisations of radiative transfer can simulate tropopause and surface SW IRFs under MLS, TROP and SAW atmospheric conditions following a perturbation in CH_4.

The results in this chapter have shown:

- that SOC(6) significantly underestimates CH_4 SW IRF by about 45% at the surface and tropopause, and hence, an ESM using this radiation code would not fully capture the climate impact of changes in the atmospheric concentration of CH_4. This low spectral resolution version of SOCRATES is not suitable for the purposes of this thesis and is not considered further.

- for a CH_4 perturbation from 806 ppbv to 1760 ppbv, and in the presence of CO_2, H_2O and N_2O (Case 1), SOC(260) can calculate CH_4 SW IRF with a mean error of around 8% at the tropopause. However, surface errors are much higher (12 to 26%) for higher solar zenith angles in the relatively moist MLS and TROP atmospheres. However, the calculation of daily-average forcings should reduce the impact of the errors found at higher solar zenith angles for calculations including H_2O.

- in the case of a CH_4-only atmosphere, and for a perturbation from 806 ppbv to 1760 ppbv (Case 2), SOC(260) can calculate CH_4 SW IRF at the surface and tropopause with an error of less than 10% compared to the RFM. In most cases (especially at the surface) the percentage error is much lower than this. Even the large surface errors found in Case 1 TROP and MLS profiles (where $\theta = 53^o$ and 75^o) are greatly reduced. The vast improvement of these results under CH_4-only atmospheric conditions suggests that SOC(260) cannot fully resolve the spectral overlap between CH_4 and H_2O when high concentrations of H_2O are present.

- that a compensation of errors takes place across 0.87 - 10 µm for SOC(260) to achieve forcings that have an error of less than 10% compared to the RFM in Case 1 and Case 2, whereby some spectral regions overestimate or underestimate CH_4 SW IRF. The significance of the overestimation or underestimation of SW IRF of each spectral region depends on the

corresponding magnitude of the absolute error between SOC(260) and the RFM and how much a given spectral region contributes to the total wavelength-integrated SW IRF.

- In Case 1, the underestimation of tropopause SW IRF by around 16% across the 1.6 - 2.02 μm spectral range is a notable error which is not diminished when H_2O is excluded from calculations in Case 2. Since this spectral region plays a key role in determining the size and sign of CH_4 SW IRF this error is potentially significant. However, it must be considered that the *wavelength-integrated* tropopause SW IRF across 0.87 - 10 μm for the MLS profile at θ = 53^o has a percentage error of less than 8% for both Case 1 and Case 2.

- SOC(260) is able to calculate CH_4 SW IRF with an error of less than 9% compared to the RFM when vertically-varying profiles of CH_4 are used. All percentage errors are slightly improved in comparison to Case 2 where CH_4-only atmospheres are used to calculate SW IRFs using constant vertical profiles. This shows that the use of a vertically-varying profile improves SOC(260)'s calculation of CH_4 SW IRF.

This thesis aims to derive the best estimate of the impact of CH_4 SW absorption bands on tropopause RF. Given the conclusions of this SW radiative transfer model intercomparison, SOC(260) is judged to be suitable to calculate the tropopause forcings required in this thesis given the computational constraints of a requirement to produce geographically and seasonally resolved forcings, including the impact of stratospheric temperature adjustment.

Chapter 5

Sensitivities of Methane's Shortwave Radiative Forcing

5.1 Introduction

A detailed quantification of the sensitivity of methane's SW RF has not yet been published (to the author's knowledge). This chapter aims to address this research gap, focussing specifically on the following factors:

1. the representation of the vertical profile of CH_4 mixing ratios used in RF calculations.

2. the effect of CH_4 absorption at solar mid-infrared wavelengths between 5 – 10 µm.

3. the impact of surface albedo specification on CH_4 SW IRF.

Each of these factors are addressed with the objective of identifying which 'conditions' are essential in deriving the most accurate estimate of methane's SW RF. This work offers a significant update to the sensitivity tests performed by Etminan *et al.* (2016) and provides an important discussion of the estimates of methane's tropopause SW IRF given by Etminan *et al.* (2016) and Collins *et al.* (2018). In Sections 5.2 and 5.3, the focus will be mostly on the global-annual mean forcing. The geographical distribution of the forcing, and in particular its dependence on surface albedo specification, will be discussed in Section 5.4.

5.2 The representation of methane's vertical profile

It was shown in Section 4.3.3 that methane's clear-sky tropopause SW IRF is sensitive to the representation of the vertical profile of CH_4 mixing ratios. In comparison to constant vertical profiles, the use of vertically varying profiles reduced forcings by around 20% in MLS and TROP atmospheres, and by around 14% in SAW. The use of vertically-varying mixing ratios, at both pre-industrial and present-day levels, results in less stratospheric SW CH_4 absorption. Hence, following a perturbation in CH_4, the change in downward SW irradiance at the tropopause is reduced. This result is significant in the context of clear-sky conditions (with a zero surface albedo); without the upward scatter of tropospheric SW radiation, the magnitude of the tropopause IRF is dependent solely on the amount of SW irradiance absorbed from above.

An important next step involves expanding this analysis to global-mean calculations conducted under both clear-sky and all-sky conditions. To make results more closely comparable to the global-mean calculations of Collins *et al.* (2018), this analysis utilises the same CH_4 mixing ratio scale heights obtained from the National Center for Atmospheric Research (NCAR) Community Atmosphere Model 3.0 (CAM 3.0; Collins *et al.* 2004). These are idealised vertically-varying profiles of CH_4. Satellite-derived CH_4 fields are used in Chapter 6.

Experimental Set-up

The experiments in this section are carried out using SOCRATES-RF, configured with sp_sw_260_jm2 (260-band SW spectral file) and sp_lw_ga7 (9-band LW spectral file), as described in Section 3.1.5. Global-mean CH_4 IRFs and SARFs are calculated under clear-sky and all-sky conditions for the four mid-season months (January, April, July and October). Analysis demonstrates that the average of these months (referred to here as the quasi-annual mean) serves as a good representation of the

full 12-month annual mean; for a doubling of CH_4, from 722 ppbv to 1444 ppbv, the percentage error between quasi-annual and full-annual all-sky SW IRFs at the TOA, tropopause and surface is -0.9%, 0% and -0.07% respectively. Consequently, all quasi-annual results discussed here (and in the following sections of Chapter 5) are assumed to be characteristic of full-annual mean forcings. As described in Section 3.1.5, all experiments are run at a 5° x 5° spatial resolution using monthly-mean climatological fields of ERA-interim reanalysis data. Mixing ratios of CO_2, N_2O and O_3 are also included as specified in Section 3.1.5.

Forcings derived with constant vertical profiles of CH_4 use globally-uniform mixing ratios of 750 ppbv and 1800 ppbv to simulate preindustrial and present-day (2011) concentrations respectively (Myhre *et al.* 2013a). This perturbation is used throughout all Chapter 5 experiments to make results comparable to Etminan *et al.* (2016). Vertically-varying profiles of CH_4 are obtained from NCAR CAM 3.0 (Collins *et al.* 2004). The following description, taken from Collins *et al.* (2004)[5], outlines how CAM 3.0 CH_4 mixing ratios are derived:

Globally, tropospheric mixing ratios are assumed to be well mixed and are prescribed in units of mass mixing ratio as follows:

$$\mu^0_{\mathrm{CH_4}} = 0.554 w_{CH_4} \tag{5.1}$$

where w_{CH_4} denotes the volume mixing ratio of methane. Above the tropopause CH_4 mass mixing ratios are specified as zonally-averaged quantities that vary with latitude to imitate the effect of stratospheric circulation and chemistry on CH_4. The pressure level of the tropopause (in hPa) is defined by:

$$p_{trop} = 250.0 - 150.0\, cos^2\phi \tag{5.2}$$

where ϕ denotes latitude.

[5] Two errors were found in this description of CH_4 mixing ratio scale-heights. Both related to Equation 5.5, reported originally by Collins *et al.* (2004) as: $X_{CH_4} = 0.2353 + 0.22549(\phi)$. See Equation 5.5 for corrections.

Following this, for $p \leq p_{trop}$, stratospheric CH_4 mass mixing ratios are defined as:

$$\mu_{CH_4} = \mu^0_{CH_4} \left(\frac{p}{p_{trop}} \right)^{X_{CH_4}} \tag{5.3}$$

where X_{CH_4} denotes the mixing ratio scale heights. For $|\phi| \leq 45°$,

$$X_{CH_4} = 0.2353 \tag{5.4}$$

and for $|\phi| > 45°$,

$$X_{CH_4} = 0.2353 + 0.022549(\phi - 45) \tag{5.5}$$

Figure 5.1 shows CAM 3.0 CH_4 profiles (in units of VMR) at a sample of four latitudes: 0°, 30°, 60° and 90°. Since CAM 3.0 zonal-mean mixing ratio scale height does not account for hemispherical or seasonal variations in CH_4 mixing ratios, these profiles are representative of both the northern and southern hemispheres, for every month in the year.

As shown, CH_4 mixing ratios remain well-mixed throughout the troposphere at each latitude and decrease exponentially above a latitudinally-dependent tropopause at the rate given by Equation 5.3. As stated in Collins *et al.* (2004): "the exact latitude dependence of the mixing ratio scale height was based on information from a two dimensional chemical model (S. Solomon, personal communication)" but no further details are given. It is recognised that this representation is highly idealised in comparison to recent developments in the modelling of atmospheric CH_4 in chemistry transport models and chemistry climate models, some of which now prescribe, for example, the hemispheric asymmetry in CH_4 surface mixing ratios and a seasonal cycle (see Morgenstern *et al.* 2017). However, for the sensitivity tests conducted in this chapter, CAM 3.0 mixing ratio scale

heights are judged to provide an adequate representation of methane's fall-off rate in the stratosphere and also allow for a direct comparison with Collins *et al.* (2018). As shown in Figure 5.1, the profile variation from 0° to 90° crudely represents the effect of stratospheric circulation on mixing ratio abundance and the rate of decrease with height characterises the loss of CH_4 due to photochemical reactions with OH (most predominantly), Cl and $O(^1D)$ in the stratosphere (Ciais *et al.* 2013).

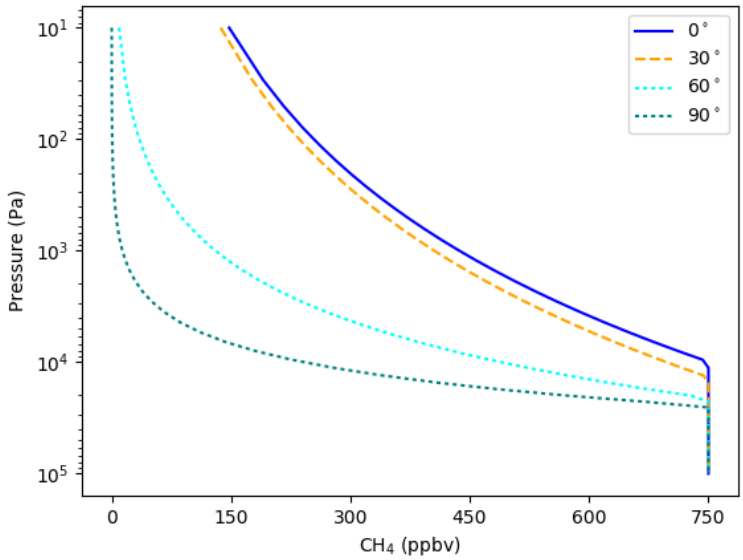

Figure 5.1: Zonal-mean vertically-varying CH_4 profiles (in units of VMR) at 0°, 30°, 60° and 90° latitude. CH_4 is well-mixed throughout the troposphere at 750 ppbv and decreases exponentially above the tropopause as per the CAM 3.0 latitude-dependent mixing ratio scale height given by Equation 5.3. Note that the profile at 90° does not drop to zero completely, however it reaches a minimum of 0.04 ppbv at 10 Pa. Also note that this equation does not model hemispherical and seasonal differences in mixing ratio scale heights. The profiles at the four latitudes shown here are therefore representative of both the northern and southern hemispheres for each month of the year.

5.2.1 The impact of profile representation on radiative forcing calculations

Table 5.1 compares the effect of profile representation on methane's quasi-annual, global-mean clear-sky SW IRF at the TOA, tropopause and surface. Consistent with the results presented in Section 4.3.3, this effect is greatest at the tropopause. Here, the 'CAM 3.0' SW IRF (-0.018 W m^{-2}) is almost two times smaller than the 'Constant' IRF (-0.032 W m^{-2}). In the context of a global-mean, quasi-annual calculation, this confirms that the use of vertically-varying CH_4 mixing ratios substantially reduces the negative forcing at the tropopause under clear-sky conditions.

In comparison, both the surface and TOA forcings remain relatively unaffected by the specification of methane's profile. At the surface, this result is consistent with the experiments presented in Section 4.4.3. As previously explained, the magnitude of the clear-sky surface SW IRF is more sensitive to a perturbation in CH_4 mixing ratios throughout the troposphere. The effect of exponentially decreasing CH_4 in the stratosphere has a negligible effect on the downward SW flux at the surface, at both pre-industrial and present day levels. Since both Constant and CAM 3.0 calculations are performed using globally-uniform, well-mixed tropospheric CH_4 mixing ratios, the resulting surface SW IRFs differ by only around 1%. The difference between Constant and CAM 3.0 forcings at the TOA is comparable at around 2%. The sign and magnitude of the TOA forcing is driven by enhanced absorption of reflected SW radiation between the surface and TOA, following an increase in CH_4 concentration. Considering these results are derived under clear-sky conditions, the TOA forcings here are attributed to the absorption of SW radiation reflected (predominantly) by the land surface. The similarity between Constant and CAM 3.0 calculations at the TOA indicates that this forcing is *very* slightly driven by increased absorption of surface-reflected radiation in the stratosphere, regardless of profile specification.

	Clear-sky SW IRF		
	Constant	**CAM 3.0**	**% difference**
TOA	0.052	0.051	-1.9
Tropopause	-0.032	-0.018	-44
Surface	-0.226	-0.223	-1.3

Table 5.1: Quasi-annual, global-mean clear-sky SW IRF (W m^{-2}) at the TOA, tropopause and surface following a perturbation in CH_4 from 750 ppbv to 1800 ppbv calculated using a globally-uniform constant vertical profile of CH_4 (Constant) and CAM 3.0 latitudinally-dependent vertically-varying CH_4 mixing ratios in the stratosphere (CAM 3.0). The percentage difference (i.e. (CAM 3.0-Constant)/Constant) is given in the third column.

	All-sky SW IRF		
	Constant	**CAM 3.0**	% difference
TOA	0.090	0.087	-3.3
Tropopause	0.003	0.016	433
Surface	-0.157	-0.155	-1.3

Table 5.2: Quasi-annual, global-mean all-sky SW IRF (W m^{-2}) at the TOA, tropopause and surface following a perturbation in CH_4 from 750 ppbv to 1800 ppbv. Calculated using a globally-uniform constant vertical profile of CH_4 (Constant) and CAM 3.0 latitudinally-dependent vertically-varying CH_4 mixing ratios in the stratosphere (CAM 3.0). The percentage difference (i.e. (CAM 3.0-Constant)/Constant) is given in the third column.

Table 5.2 compares the impact of profile representation for the all-sky case. As expected at the TOA, both Constant and CAM 3.0 forcings increase in magnitude following the inclusion of clouds, and hence, an increase in the amount of reflected SW radiation available for absorption with increased CH_4 concentration. However, with less stratospheric CH_4 in CAM 3.0 compared to Constant, it follows that the TOA forcing will be consequently smaller. This yields a greater percentage difference in SW IRF at the TOA compared to the clear-sky calculation. Interestingly, the effect of all-sky conditions on the surface SW IRF percentage difference is imperceptible (when reported at two significant figures). Given that prescribed all-sky conditions are identical in both calculations, and that tropospheric CH_4 is well-mixed, this shows again that stratospheric CH_4 absorption has a negligible effect on CH_4 SW surface forcing.

At the tropopause, the inclusion of clouds *significantly* enhances the difference between Constant and CAM 3.0 SW IRF. Here, CAM 3.0 SW IRF (0.016 W m^{-2}) is over five times greater than Constant SW IRF (0.003 W m^{-2}). The cause of this difference is explained by the mechanism proposed by Etminan *et al.* (2016), which describes how the sign of methane's SW IRF switches from negative in clear-sky conditions, to positive in all-sky conditions. As discussed in Section 2.3.2, Etminan *et al.* (2016) report that tropospheric CH_4 absorption is significantly enhanced when clouds are included. At the tropopause, the positive upward forcing component dominates over the negative downward forcing component (from increased CH_4 absorption in the stratosphere). Both Constant and CAM 3.0 estimates demonstrate this switch from negative to positive following the inclusion of clouds (comparing Table 5.1 and Table 5.2 at the tropopause). The 433% difference in the all-sky Constant and CAM 3.0 SW IRF originates from the size of the downward forcing component. In the Constant case, the downward forcing component is more negative than CAM 3.0, since more CH_4 is present in the stratosphere. As a result, the positive upward forcing component due to clouds makes the

CAM3 forcing decisively positive but only weakly positive for the Constant case. The difference between the clear and all-sky cases is almost identical for Constant and CAM3 (about 0.034 W m^{-2}) indicating that clouds have a similar influence in both cases. Given that the RF of GHGs are more usefully assessed under all-sky conditions, this result strengthens the conclusion that vertically-varying CH_4 mixing ratios are essential in achieving an accurate quantification of methane's SW IRF. This motivates the more detailed representation of CH_4 mixing ratios that are presented in Chapter 6.

In contrast, it is found that the representation of methane's vertical profile is not important at TIR wavelengths. Table 5.3 shows the effect of profile specification on CH_4 all-sky LW IRF. The surface forcing is unaffected by vertically-varying stratospheric CH_4. Similarly, the impact at the TOA is negligible. Like the SW, the greatest difference occurs at the tropopause. However, at three orders of magnitude smaller than the all-sky SW IRF (-1% compared to 433%), this result is not significant. For IRF calculations at TIR wavelengths it is appropriate to specify CH_4 with a globally constant, well-mixed profile.

	All-sky LW IRF		
	Constant	**CAM 3.0**	% difference
TOA	0.548	0.549	0.2
Tropopause	0.580	0.575	-0.9
Surface	0.179	0.179	0.0

Table 5.3: Quasi-annual, global-mean all-sky LW IRF (W m^{-2}) at the TOA, tropopause and surface following a perturbation in CH_4 from 750 ppbv to 1800 ppbv. Calculated using a globally-uniform constant vertical profile of CH_4 (Constant) and CAM 3.0 latitudinally-dependent vertically-varying CH_4 mixing ratios in the stratosphere (CAM 3.0). The percentage difference (i.e. (CAM 3.0-Constant)/Constant) is given in the third column.

	LW-only			*FULL*		
	Constant	**CAM 3.0**	**% difference**	**Constant**	**CAM 3.0**	**% difference**
Net RF	0.576	0.570	-1.0	0.617	0.619	0.3
LW SARF	0.576	0.570	-1.0	0.614	0.603	-1.8
SW IRF	-	-	-	0.003	0.016	433

Table 5.4: Quasi-annual, global-mean all-sky net TOA RF, tropopause LW SARF and SW IRF - calculated without (LW-only) and with (FULL) SW heating rates included in the FDH approximation. All forcings are given in W m^{-2} and are calculated following a perturbation in CH_4 from 750 ppbv to 1800 ppbv using a globally-uniform constant vertical profile of CH_4 (Constant) and CAM 3.0 latitudinally-dependent vertically-varying CH_4 mixing ratios in the stratosphere (CAM 3.0). The percentage difference (i.e. (CAM 3.0-Constant)/Constant) between 'Constant' and 'CAM 3.0' IRFs are also shown.

Table 5.4 extends this analysis to CH_4 all-sky LW SARF and compares the impact of profile representation on CH_4 'LW-only' SARF (whereby SW absorption is *excluded* from the FDH approximation) against CH_4 'FULL' LW SARF (whereby SW absorption is *included* in the FDH approximation). The corresponding tropopause SW IRF and net RF estimates are also given.

In the LW-only case, methane's SARF is only slightly affected by profile specification; Constant and CAM 3.0 forcings differ by about 1%. This result agrees with Freckleton *et al.* (1998) and Jain *et al.* (2000). Following a similar experiment design, both studies consider the effect of the vertical distribution of CH_4 on the LW SARF (without SW absorption) and report an impact of 2% and 1% respectively. This finding appears to be consistent in the FULL LW SARF case. Despite the inclusion of SW absorption, Constant and CAM 3.0 SARF differ by around just 2%. This shows that even when SW heating rates are included in the FDH process, the LW SARF is not significantly dependent on the vertical representation of CH_4 mixing ratios. Section 6.3 examines the inclusion of SW heating rates in the FDH approximation in more detail.

However, Etminan *et al.* (2016) demonstrate the importance of including stratospheric absorption of SW radiation in the calculation of methane's LW SARF; they found that for a perturbation in CH_4 from 750 ppbv to 1800 ppbv (with vertically-varying mixing ratios), the SW forcing enhances the LW-only SARF by 15%. The results presented in Table 5.4 support this finding, albeit to a lesser extent (reasons for this disparity are addressed in Section 5.1.2, Section 5.1.3 and Chapter 6). In total, the CAM 3.0 SW effect increases methane's forcing by around 9%, from the LW-only SARF (0.570 W m^{-2}) to the net RF of 0.619 W m^{-2}. Thus, the inclusion of SW absorption in methane's SARF is important, and the impact of the SW forcing in the LW SARF is larger (0.033 W m^{-2}) than the SW forcing itself

(0.016 W m^{-2}); this emphasizes Etminan *et al.*'s finding that the impact of SW absorption on CH_4 LW SARF is important in quantifying the overall CH_4 SW impact.

Table 5.4 shows that the net RF is almost identical between the FULL Constant and CAM 3.0 cases. This is partly because the LW SARF dominates the net RF (over 90%) and partly because the impact of profile representation on the LW SARF goes in the opposite direction to the SW IRF. However, the use of vertically-varying mixing ratios notably enhances the impact of the SW IRF relative to the LW-only net RF. The FULL Constant net RF is 0.041 W m^{-2} greater than the LW-only net RF (0.617 W m^{-2} versus 0.576 W m^{-2}), whereas in the FULL CAM 3.0 case, the net RF is 0.049 W m^{-2} greater than the LW-only net RF (0.619 W m^{-2} versus 0.570 W m^{-2}). Considering a realistic representation of methane's vertical profile is essential in achieving an accurate quantification of the global-mean SW IRF and it is subsequently essential in the calculation of methane's global-mean net RF.

5.3 The effect of CH_4 absorption at solar mid-infrared wavelengths between 5 – 10 µm

This section explores the effect of solar absorption by methane's mid-infrared 7.7 µm band (see Figure 2.1). This effect is not considered by Etminan *et al.* (2016) or Collins *et al.* (2018); whereby the upper wavelength limit is constrained to 5 µm in each study. This section investigates the importance of CH_4 solar absorption between 5 – 10 µm on methane's clear-sky and all-sky SW IRFs and LW SARF. This spectral region was implicitly included in the calculations presented in the previous sub-section.

Experimental Set-up

All experiments are carried out using SOCRATES-RF. Quasi-annual, global-mean CH_4 IRFs and SARFs are calculated under clear-sky and all-sky conditions at a 5° x 5° spatial resolution using monthly-mean climatological fields of ERA-interim reanalysis data. Forcings are derived using CAM 3.0 mixing ratios of CH_4 following a perturbation from 750 ppbv to 1800 ppbv. Mixing ratios of CO_2, N_2O and O_3 are also included as specified in Section 3.1.5. SW calculations are performed across three solar spectral ranges in sp_sw_260_jm2 to determine the importance of CH_4 absorption between 5 – 10 µm. Table 5.5 shows the wavelength bounds of each spectral range alongside the corresponding band number range in the sp_sw_260_jm2 spectral file. As specified in Section 3.1.5, all LW calculations are performed across 3.3 – 10000 µm.

Wavelength range (μm)	Band number range
0.87 – 10	123 – 260
0.87 – 5	123 – 248
5 – 10	248 – 260

Table 5.5: Wavelength range of SW calculations across which CH_4 SW IRFs are performed. Also shown are the corresponding band number range in the sp_sw_260_jm2 260-band SW spectral file.

As stated in SOCRATES Technical Guide (Manners *et al.* 2015), sp_sw_260_jm2 uses SSI data from the 'lean_12' spectrum, described as a "new solar spectrum taken as the mean of spectral data from 2000-2011 from the recommendation of the SPARC/SOLARIS [i.e. Solar Influences for SPARC: Stratospheric Processes and their Role in Climate] group". The source of lean_12 is attributed to the following webpage: http://solarisheppa.geomar.de/ccmi (last accessed 12/03/2021). On inspection, this credits the origin of SSI data to the Naval Research Laboratory Solar Spectral Irradiance model version 1 (NRLSSI; Lean *et al.* 2005).

Table 5.6 details additional SSI datasets used to evaluate the distribution of solar irradiance in sp_sw_260_jm2. This is achieved by integrating SSI across individual 'spectral regions' in the 0.87 - 10 μm range of each dataset and comparing the total SSI of each spectral region against the corresponding spectral region in sp_sw_260_jm2 (as stated in Chapter 4 a spectral region is defined as sets of sp_sw_260_jm2 bands which include CH_4 absorption). Kurucz_95 provides a high spectral resolution comparison of SSI with a spectral resolution that is variable across whole spectrum. Derived theoretically from quiet-Sun solar atmosphere and spectral line models, Kurucz_95 has been widely used in LBL and narrow-band models, such as the LBL-Radiative Transfer Model (LBLRTM; Clough et al. 2005) and the MODerate spectral resolution atmospheric TRANsmittance code (MODTRAN; Bark et al. 2003). NRLSSI2 is a newly formulated version of NRLSSI, comprised of both modelled SSI, from the Solar Irradiance Climate Data Record algorithm (Coddington and Lean 2015), and observed SSI from SORCE (Harder et al. 2005) and SOLSPEC (Thuillier et al. 1998) measurements (see Coddington *et al.* 2016). NRLSSI2 spectra are available at monthly-averaged resolution from 1882 to present. Here, NRLSSI2 is taken as the mean of spectral data from 2000 – 2011 to match the sampled time-period of the lean_12 spectrum.

Name	Source	Spectral Range	Reference
Kurucz_95	Theoretical	0.2 – 196 µm	Kurucz (1995)
NRLSSI2	Empirical	0.115 – 100 µm	Coddington *et al.* (2016)

Table 5.6: Solar spectral irradiance datasets used for comparison against SOCRATES-RF's sp_sw_260_jm2 260-band SW spectral file.

5.3.1 Incoming solar irradiance between 5 – 10 µm

Table 5.7 compares total SSI per spectral region in sp_sw_260_jm2 against lean_12, Kurucz_95 and NRLSSI2. Whilst lean_12 does not provide an independent comparison against sp_sw_260_jm2, it is useful to include in this analysis to evaluate the nature of banded solar flux in each spectral region of sp_sw_260_jm2. Although the total SSI in the 5 – 10 µm is a seemingly small proportion of the TSI (< 0.5%), this spectral region contains methane's second strongest absorption band (see Figure 2.1), hence SW absorption across this spectral region could play an important role in CH_4 SW RF.

Calculation of the percentage difference between sp_sw_260_jm2 and each dataset (not shown) reveals that total SSI in most spectral regions of sp_sw_260_jm2 differ by less than 1%. Between 0.87 – 0.91 µm, 1.3 – 1.52 µm and 1.6 – 2.02 µm the percentage difference between sp_sw_260_jm2 and NRLSSI2 increases to around 2%, 1% and 1% respectively. However, between 5 – 10 µm the percentage difference between sp_sw_260_jm2, Kurucz_92 and NRLSSI2 increases significantly to 13% and 14% respectively. It is interesting to note that a 14% difference also occurs with lean_12; here the total SSI differ by 0.82 W m^{-2}. Such a discrepancy is of note considering sp_sw_260_jm2 uses data from the lean_12 spectrum. To investigate this further, Table 5.8 compares the total SSI in each CH_4 absorbing band within the 5 – 10 µm spectral range of sp_sw_260_jm2 and lean_12. As shown, each band exhibits almost identical total SSI apart from band 260, between 9.5 – 10 µm. Here sp_sw_260_jm2 contains 0.82 W m^{-2} more irradiance than lean_12.

Spectral region (μm / band number)		Total SSI (W m^{-2})			
		sp_sw_260_jm2	lean_12	Kurucz_95	NRLSSI2
0.87 – 0.91	*123 - 126*	37.37	37.32	37.62	36.58
1.09 – 1.24	*145 - 157*	79.86	79.71	80.42	79.32
1.3 – 1.52	*161 -171*	74.96	74.81	75.54	75.78
1.6 – 2.02	*176 - 196*	71.36	71.22	71.93	72.16
2.1 – 2.9	*201 - 225*	43.76	43.68	44.08	44.00
3.0 – 4.8	*228 - 248*	20.15	20.12	20.31	20.12
5.0 – 10	*251 - 260*	6.24	5.42	5.47	5.41

Table 5.7: Comparison of total SSI per 'spectral region' in each solar spectrum. Spectral regions are defined as sets of bands within sp_sw_260_jm2 which include CH_4 absorption, the corresponding band number range of each spectral region is also given alongside the wavelength range of each spectral region in the first column.

Spectral region (μm/Band number)	Total SSI (W m^{-2})	
	sp_sw_260_jm2	lean_12
5.0 – 5.5 (251)	1.49	1.48
5.5 – 6.0 (252)	1.06	1.03
6.0 – 6.5 (253)	0.77	0.75
6.5 – 7.0 (254)	0.57	0.56
7.0 – 7.5 (255)	0.43	0.42
7.5 – 8.0 (256)	0.33	0.33
8.0 – 8.5 (257)	0.26	0.25
8.5 – 9.0 (258)	0.21	0.20
9.0 – 9.5 (259)	0.17	0.16
9.5 – 10 (260)	0.96	0.14

Table 5.8: Comparison of TSI per band within the 5 – 10 μm range in sp_sw_260_jm2 and lean_12 spectra.

Table 5.9 shows that this discrepancy is by design. The TSI across the entire 0.2 – 100 µm range of lean_12 amounts to 1368.62 W m^{-2}, with 0.81 W m^{-2} lying between 10 – 100 µm. Given that the upper spectral limit of sp_sw_260_jm2 occurs at 10 µm, an additional 0.81 W m^{-2} of irradiance has been placed in band 260 to conserve TSI. Analysis (not shown) reveals that this 'additional' irradiance does not affect methane's SW forcing because absorption between 9.5 – 10 µm is negligible; excluding band 260 from CH_4 forcing experiments has no impact on the results presented here. However, the impact could be larger for SW absorption by other gases.

Spectral region (µm)	Total SSI lean_12 (W m^{-2})
0.12 - 100	1368.62
10 - 100	0.81

Table 5.9: TSI across the entire 0.2 – 100 µm lean_12 spectrum and the 10 – 100 µm subrange.

5.3.2 CH_4 SW absorption between 5 – 10 µm

Table 5.10 shows the magnitude of CH_4 SW IRF across 5 – 10 µm at the TOA, tropopause and surface under clear-sky conditions. Also shown is the percentage contribution that the 5 – 10 µm SW IRF makes to the total 0.87 – 10 µm SW IRF.

	Clear-sky SW IRF (W m^{-2})		5 – 10 µm IRF as % of total 0.87 – 10 µm IRF
	0.87 – 10 µm	5 – 10 µm	
TOA	0.051	0	-
Tropopause	-0.018	-0.004	22
Surface	-0.223	-0.002	0.9

Table 5.10: Quasi-annual, global-mean clear-sky SW IRF at the TOA, tropopause and surface following a perturbation in vertically-varying CAM 3.0 CH_4 from 750 ppbv – 1800 ppbv across the 0.87 – 10 µm spectral region and the 5 – 10 µm spectral region. Also shown is the percentage contribution that the 5 – 10 µm IRF makes to the total 0.87 – 10 µm IRF.

Methane's forcing across the solar mid-infrared is the largest at the tropopause; the IRF between 5 – 10 µm is negative in sign and accounts for 22% of the total SW IRF. Given that the total IRF is also negative in sign, CH_4 absorption across 5 – 10 µm acts to increase the magnitude of the clear-sky SW IRF. At the surface, this impact is significantly reduced to around 1%. As the 5 – 10 µm surface SW IRF is smaller than the tropopause SW IRF, it is evident that an increase in CH_4 concentrations results in greater absorption across the solar mid-infrared between the TOA and the tropopause in comparison to between the tropopause and the surface. It is also evident that any surface reflectance across 5 – 10 µm does not yield a forcing at the TOA.

Table 5.11 shows equivalent experiments conducted under all-sky conditions. As previously shown, the inclusion of clouds switches the sign of methane's tropopause SW IRF to 0.016 W m^{-2}. In consequence, the negative forcing across 5 – 10 µm acts to *reduce* the total 0.87 – 10 µm forcing, as shown here, by 25%. The fact that the 5 - 10 µm tropopause SW IRF is identical in Tables 5.10 and 5.11 further emphasizes that this spectral region mainly impacts absorption in the stratosphere. This is a significant result and highlights the importance of including solar mid-infrared absorption in calculations of CH_4 SW IRF.

	All-sky SW IRF (W m^{-2})		**5 – 10 µm IRF as % of total 0.87 – 10 µm IRF**
	0.87 – 10 µm	**5 – 10 µm**	
TOA	0.087	0	-
Tropopause	0.016	-0.004	-25
Surface	-0.155	-0.001	0.6

Table 5.11: Quasi-annual, global-mean all-sky SW IRF at the TOA, tropopause and surface following a perturbation in vertically-varying CAM 3.0 CH_4 from 750 ppbv – 1800 ppbv across the 0.87 – 10 µm spectral region and the 5 – 10 µm spectral region. Also shown is the percentage contribution that the 5 – 10 µm IRF makes to the total 0.87 – 10 µm IRF.

Table 5.12 shows the magnitude of methane's tropopause SW IRF calculated across the reduced 0.87 – 5 µm spectral range along with the LW SARF (whereby SW absorption across 0.87 – 5 µm is *included* in the FDH approximation) and net RF. These values can be directly compared to the FULL CAM 3.0 results presented in Table 5.4, whereby SW calculations use the entire 0.87 – 10 µm spectral range.

As shown, excluding CH_4 SW absorption across 5 – 10 µm in forcing calculations results in a larger SW IRF (0.019 W m^{-2}). However, as a result, the LW SARF is slightly smaller (comparing 0.601 W m^{-2} shown in Table 5.12 and 0.603 W m^{-2} shown in Table 5.4). This opposing effect results in a very similar net RF (comparing 0.620 W m^{-2} shown in Table 5.12 and 0.619 W m^{-2} shown in Table 5.4). This demonstrates that stratospheric SW absorption across 5 – 10 µm does not significantly alter the impact of CH_4 SW heating rates on stratospheric temperature adjustment.

	All-sky (W m^{-2})		
	SW IRF	**LW SARF**	**Net RF**
Tropopause	0.019	0.601	0.620

Table 5.12: Quasi-annual, global-mean all-sky SW IRF, LW SARF and Net RF following a perturbation in vertically-varying CAM 3.0 CH_4 from 750 ppbv – 1800 ppbv across the reduced 0.87 – 5 µm spectral region.

5.4 The impact of surface albedo specification on methane's SW RF

The specification of surface albedo (α_s) is an important factor controlling the amount of reflected SW radiation absorbed by methane. Both Etminan *et al.* (2016) and Collins *et al.* (2018) highlight the potential sensitivity of methane's SW forcing to α_s specification. Etminan *et al.* (2016) found that increasing the global-mean α_s value by 1 percentage point (from 12.3% to 13.3%) enhanced methane's shortwave forcing by 6.7%. As previously mentioned, Collins *et al.* (2018) attribute NIR α_s as the key driver of strong spatial gradients in their estimate of methane's SW forcing.

To demonstrate the impact of α_s on the SW forcing, Figure 5.2 presents methane's zonal-mean tropopause SW IRF for July under clear-sky (upper panel) and all-sky (lower panel) conditions calculated by SOCRATES-RF using globally-uniform, spectrally-constant α_s varied in turn from 0 to 1. These calculations use the vertically-varying CAM 3.0 CH_4 mixing ratios. Note that SW IRFs are absent from around -65°S to -90°S due to polar night.

Surface albedo plays an important role in determining the size and sign of CH_4 SW forcing under clear-sky conditions. When $\alpha_s = 0$ the forcing is negative at all latitudes, with a magnitude dependent solely on the amount of downward solar irradiance absorbed by CH_4 between the TOA

and tropopause. When α_s = 0.2 the magnitude of the forcing is reduced at all latitudes; the negative downward forcing component is counterbalanced by the positive upward forcing component due to absorption of surface reflected SW radiation in the troposphere. As a result, the sign of the forcing switches to positive at most latitudes between -30° and 30°, albeit marginally. When α_s = 0.4 the forcing is positive everywhere. Successively increasing α_s in increments of 0.2 has a near linear effect on the magnitude of the forcing at all latitudes. When α_s = 1 the forcing is around 0.55 W m^{-2} at 90°N, compared to around -0.12 W m^{-2} when α_s = 0.

The influence of α_s is dampened under all-sky conditions (Figure 5.2, lower panel), particularly across polar latitudes due to high cloud amounts during July; here, the forcing remains positive regardless of the value of α_s. However, α_s continues to exert a significant impact on the forcing magnitude. This is most marked at around 30° where the forcing varies by over 0.3 W m^{-2} across the 0 to 1 α_s range.

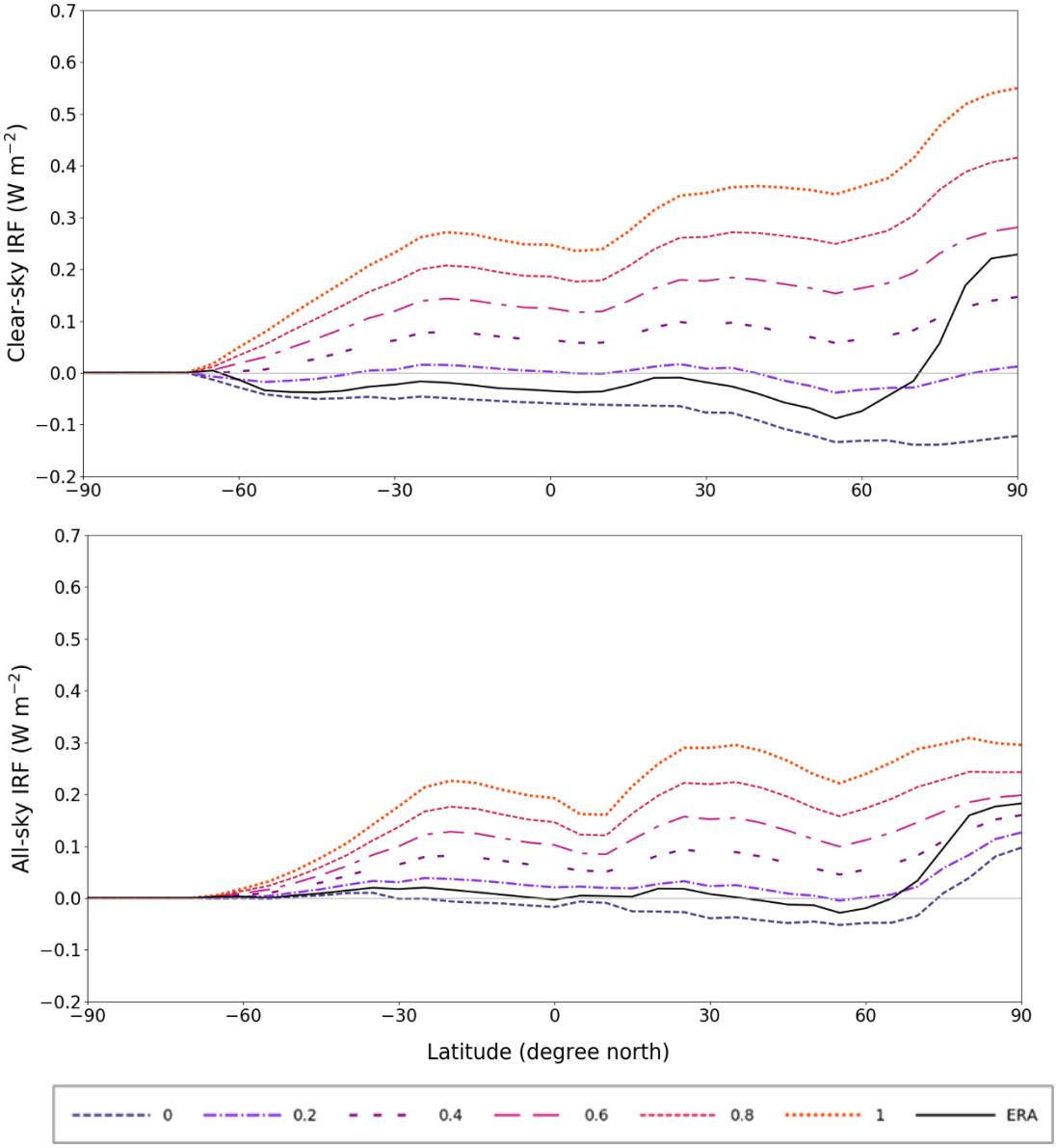

Figure 5.2: CH_4 SW July zonal-mean tropopause IRF under clear-sky (top panel) and all-sky (lower panel) conditions calculated by SOCRATES-RF (configured with sp_sw_260_jm2) with globally-uniform, spectrally-constant surface albedo varied in turn from 0 to 1. Also shown (black line) is the zonal-mean forcing calculated using ERA-interim globally-varying, spectrally-constant surface albedo values. All forcings are calculated following a perturbation in CH_4 from 750 ppbv to 1800 ppbv using CAM 3.0 vertically-varying CH_4 mixing ratios.

Figure 5.2 also shows methane's July clear-sky and all-sky zonal-mean tropopause SW IRF calculated by SOCRATES-RF, using monthly-mean ERA-interim reanalysis α_s data (Dee *et al.* (2011); black lines). These values vary regionally, to represent the variation in reflectance with land surface type, and are spectrally-constant, weighted with respect to the spectral distribution of incoming solar irradiance as follows:

$$\bar{\alpha}\,(\phi,\omega)\;=\;\int S(\lambda,\phi,\omega)\;\alpha_s(\lambda,\phi,\omega)\;d\lambda \tag{5.6}$$

where $\bar{\alpha}\;(\phi,\omega)$ is termed 'effective albedo' at a given latitude, ϕ, and longitude, ω. $S(\lambda,\phi,\omega)$ denotes downward surface irradiance and $\alpha_s(\lambda,\phi,\omega)$ is spectral surface albedo. For brevity, both ϕ and ω will be dropped from all terms relating to Equation 5.6 for the remainder of this thesis. As shown in both panels, ERA-interim $\bar{\alpha}$ significantly effects the magnitude of the forcing across the northern polar latitudes, where highly reflective snow and ice-covered surfaces strongly enhance tropospheric CH_4 absorption.

All SOCRATES-RF calculations presented throughout this thesis so far use monthly-mean ERA-interim $\bar{\alpha}$ fields. Figure 5.3 shows the spatial distribution of methane's quasi-annual all-sky SW tropopause IRF following a perturbation from 750 ppbv to 1800 ppbv, derived using such ERA-interim $\bar{\alpha}$ values. As reported in Section 5.2.1 and Section 5.3.2, this equates to a global-mean SW IRF of 0.016 W m^{-2}.

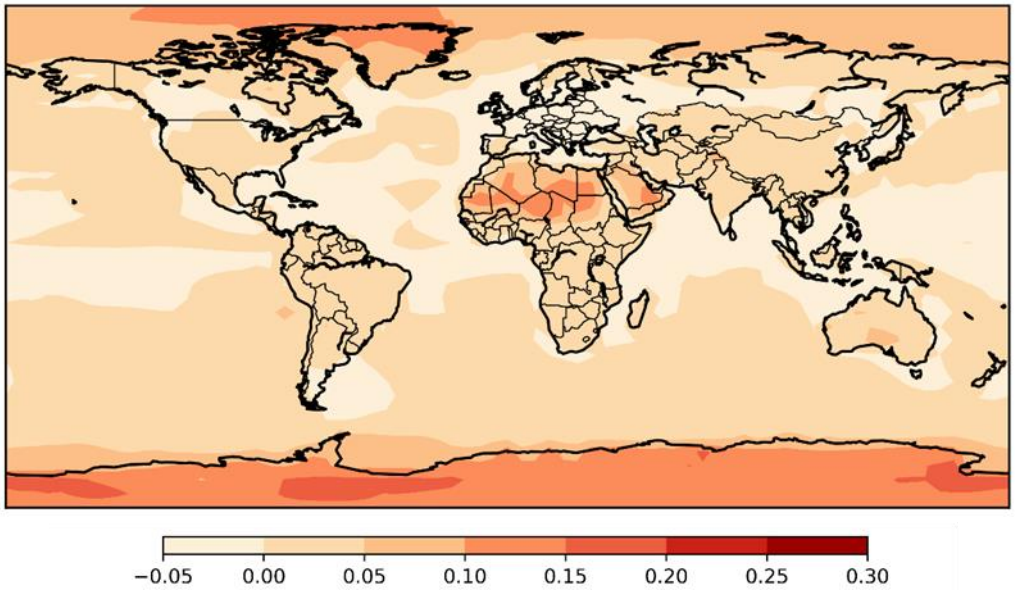

Figure 5.3: Quasi-annual all-sky CH_4 SW tropopause IRF (W m^{-2}) following a perturbation from 750 ppbv to 1800 ppbv, derived using CAM 3.0 mixing ratios of CH_4 and monthly-mean fields of ERA-interim surface albedo.

As shown, the distribution of the SW forcing exhibits large spatial gradients. Areas of maxima are located over the Sahara and Arabian Peninsula where bright desert surfaces (with a high albedo) increase the reflection of downwelling SW irradiance upwards through the atmosphere. This significantly enhances the magnitude of tropospheric CH_4 SW absorption, leading to a stronger localised positive forcing. Similarly, this is also found across both polar regions whereby highly reflective snow and ice-covered land surfaces increase photon path length. Collins *et al.* (2018) show comparable regions of maxima across the Sahara and Arabian Peninsula, however, the poleward amplification of the SW forcing is notably absent (see Figure 2.13a, note that forcings are plotted on a different scale). Such a marked spatial discrepancy between both estimates hints that surface albedo specification may be the main causal factor driving this difference. This is addressed further in Section 5.4.2

Datasets such as ERA-interim provide a useful description of lower boundary conditions in radiation codes that do not support the specification of spectrally-varying α_s. However, the radiative properties of surface features are highly wavelength-dependent. Vegetation and soils typically tend to reflect much more strongly in the NIR than in the visible region of the solar spectrum, whilst snow surfaces reflect much more strongly in the visible than in the NIR (see e.g. Roesch *et al.* 2002). Considering methane's main solar-absorbing bands lie in the NIR region, it is likely that the SW

forcing will be further sensitive to spectrally-resolved reflectance. Thus, an assessment of the interdependence between methane's SW forcing and spectral surface albedo is necessary.

Section 5.4.1 investigates the dependence of methane's SW forcing on spectrally-resolved α_s for two different land surface types: snow-covered and vegetated rangeland. The aims of this analysis are:

- to examine the spectral variation of the SW forcing with spectrally-resolved α_s.

- to compare the wavenumber-integrated IRF calculated using spectrally-resolved α_s to the wavenumber integrated IRF calculated using $\overline{\alpha}$ (Equation 5.6).

- compare the wavenumber integrated IRF calculated using spectrally-resolved α_s to the wavenumber integrated IRF calculated using $\bar{\alpha}_{\mathrm{CH_4}}$, defined as:

$$\bar{\alpha}_{CH_4} = \int \Delta S(\lambda)\ \alpha_s(\lambda)\, d\lambda \tag{5.7}$$

where $\bar{\alpha}_{CH_4}$ is the effective albedo for a perturbation in CH_4, $\Delta S(\lambda)$ denotes the change in downward surface irradiance following a perturbation in CH_4 and $\alpha_s(\lambda)$ is spectral surface albedo. In terms of calculating radiative forcing for methane, this is a more physically robust method for calculating solar-weighted surface effective albedo.

Section 5.4.2 presents the implementation of spectrally-varying SCIAMACHY α_s data in SOCRATES-RF and subsequently presents updated calculations of methane's global-mean and spatially-resolved SW forcing.

5.4.1 The dependence of methane's SW forcing on spectrally-resolved surface albedo

Experimental set up

RFMDISORT is used to calculate clear-sky and all-sky radiative fluxes at five solar zenith angles (0°, 20°, 40°, 60°, 80°) across the spectral range 1000 – 10000 cm^{-1} at a $\Delta\nu$ of 0.01 cm^{-1} As stated in Section 3.1.3, this code has recently been updated to include the effects of spectral surface reflectance in model calculations. Accordingly, the user may specify α_s either as a spectrum, where reflectance varies as a function of wavelength (i.e. spectrally-varying) or as a single value, to represent reflectance across all wavelengths (i.e. spectrally-constant). Both specifications are utilised to accommodate spectrally-varying fine-snow and rangeland α_s , along with $\overline{\alpha}$ and $\bar{\alpha}_{\mathrm{CH_4}}$values.

Atmospheric profiles of pressure, temperature, H_2O, CO_2, N_2O and CH_4 are taken from Phase I of the Continual Intercomparison of Radiation Codes (CIRC) experiments, namely Case 4 and Case 6 (Oreopoulos *et al.* 2012). Respectively, these consist of observational data measured by the ARM Climate Research Facility at the North Slope of Alaska, Utqiaġvik, (NSA) and the Southern Great Plains, Oklahoma (SGP) observatories in the United States. Data from each case provides the relevant atmospheric information for snow-covered (Case 4-NSA) and rangeland (Case 6-SGP) land surface types. Pre-industrial CH_4 mixing ratios are constructed using the fall-off rate of 'present day' CH_4 given in Case 4-NSA and Case 6-SGP. Subsequently, SW forcings are derived from radiative flux model output at the TOA, tropopause and surface for a perturbation in CH_4 from 850 ppbv to 1700 ppbv. The tropopause is defined at the point where the lapse rate changes sign, i.e. the temperature minimum, at 192.71 hPa in Case 4-NSA and 45.91 hPa in Case 6-SGP. Surface forcings are calculated at the lowest model level. Case 4-NSA experiments employ the 'Fine-snow' spectrally-varying α_s dataset taken from the ECOSTRESS spectral library (Baldridge *et al.* 2009; Meerdink *et al.* 2019), as described in Section 3.3.3. Case 6-SGP experiments utilise spectrally-varying 'Rangeland' α_s measurements taken at the SGP ARM research facility, as described in Section 3.3.4. Both α_s datasets are interpolated onto a 0.01 cm^{-1} spectral grid within RFMDSIORT.

Figure 5.4 shows the spectral variation of the Fine-snow and Rangeland α_s across the 1000 – 10000 cm^{-1} spectral range. Both datasets exhibit very different variations in α_s with wavenumber. The Fine-snow spectra displays low α_s values (< 0.1) in regions where CH_4 absorption bands are located (e.g. at around 1300 cm^{-1}, 3000 cm^{-1} and 4300 cm^{-1}). At some NIR wavenumbers, Rangeland α_s values exceed those of the Fine-snow spectra.

Table 5.13 shows the value of $\overline{\alpha}$ and $\overline{\alpha}_{CH_4}$ at each solar zenith angle for Case 4-NSA and Case 6-SGP. $\overline{\alpha}$ values are derived following Equation 5.6 and $\overline{\alpha}_{CH_4}$ values are derived following Equation 5.7, using the same CH_4 perturbation in Case 4-NSA and Case 6-SGP forcing calculations. Because $S(\lambda)$ and $\Delta S(\lambda)$ in Equations 5.6 and 5.7 vary with θ, so too do the derived α_s. Note that the θ range is used for illustrative purposes, not all θ are relevant to the conditions in which the Fine-snow and Rangeland α_s were derived.

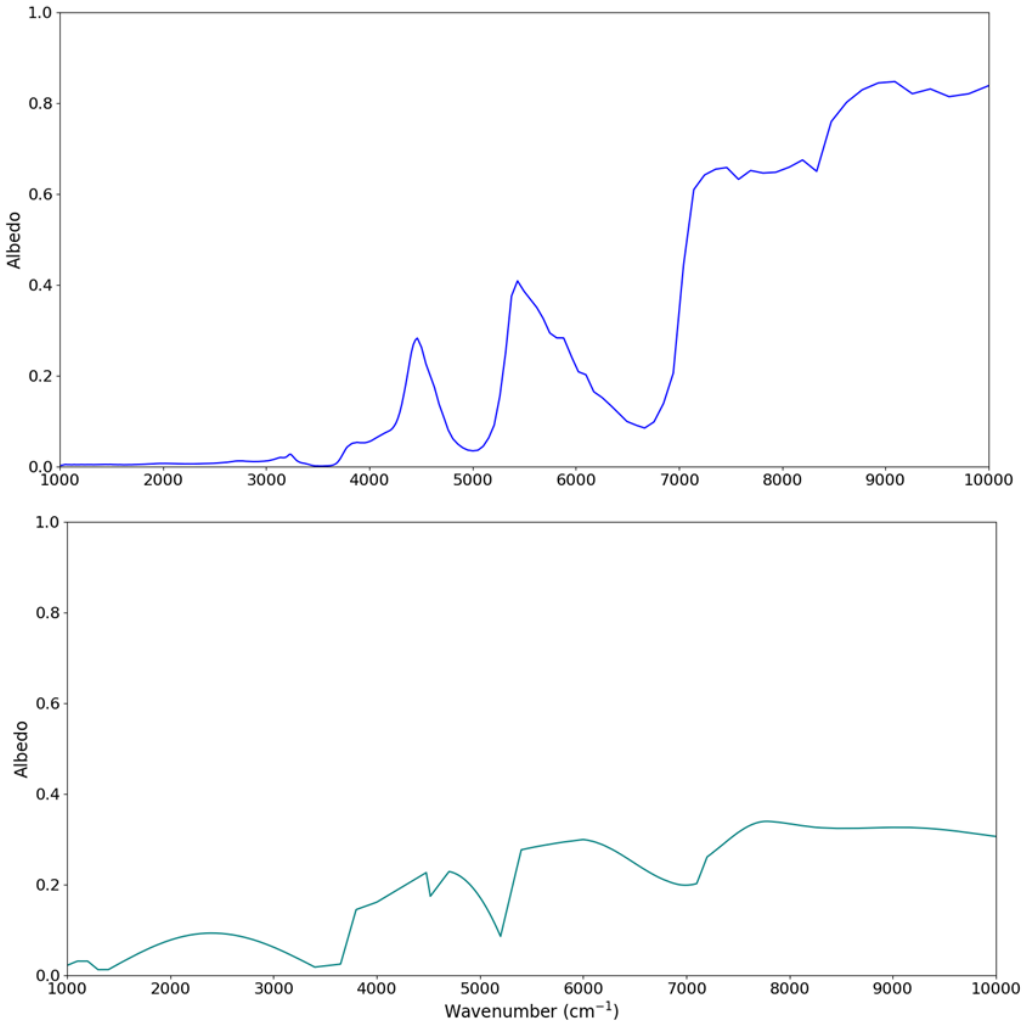

Figure 5.4: Spectral variation of Case 4-NSA fine-snow albedo (top panel) and Case 6-SGP rangeland surface albedo across 1000 – 10000 cm^{-1} (1 – 10 µm) plotted at a resolution of 1 cm^{-1}.

It is of particular note that Case 6-SGP $\bar{\alpha}_{\mathrm{CH_4}}$ values are higher than Case 4-NSA $\bar{\alpha}_{\mathrm{CH_4}}$ values. As shown in Figure 5.4, Rangeland α_s values are higher than those of the Fine-snow spectra in regions where CH_4 absorption bands are located (e.g. at around 1300 cm^{-1}, 3000 cm^{-1}, 4300 cm^{-1} and 6000 cm^{-1}). Given that $\bar{\alpha}_{\mathrm{CH_4}}$ is weighted with respect to $\Delta S(\lambda)$ following a perturbation in CH_4, it follows that Case 6-SGP $\bar{\alpha}_{\mathrm{CH_4}}$ are subsequently higher than Case 4-NSA.

θ	Case 4-NSA		Case 6-SGP	
	$\bar{\alpha}$	$\bar{\alpha}_{\mathrm{CH_4}}$	$\bar{\alpha}$	$\bar{\alpha}_{\mathrm{CH_4}}$
0°	0.486	0.147	0.284	0.182
20°	0.486	0.148	0.285	0.183
40°	0.489	0.153	0.286	0.187
60°	0.494	0.162	0.288	0.194
80°	0.510	0.187	0.293	0.210

Table 5.13: Case 4-NSA and Case 6-SGP $\bar{\alpha}$ and $\bar{\alpha}_{CH_4}$ values calculated at each solar zenith angle. $\bar{\alpha}$ values are derived following Equation 5.6. $\bar{\alpha}_{CH_4}$ values are derived following Equation 5.7 using the same CH_4 perturbation employed in Case 4-NSA and Case 6-SGP forcing calculations.

Results

Table 5.14 compares methane's wavenumber-integrated clear-sky SW IRF for Case 4-NSA at the TOA, tropopause and surface calculated using spectrally-resolved fine-snow α_s, $\bar{\alpha}$ and $\bar{\alpha}_{\mathrm{CH_4}}$ at a solar zenith angle of 0°. Table 5.15 shows the equivalent calculations for Case 6-SGP.

	Case 4-NSA SW IRF ($W\ m^{-2}$)		
	Fine-snow	$\bar{\alpha}_{\mathrm{CH_4}}$	$\bar{\alpha}$
TOA	0.27	0.24	0.78
Tropopause	0.06	0.03	0.55
Surface	-0.71	-0.71	-0.43

Table 5.14: Case 4-NSA clear-sky CH_4 SW IRF at the TOA, tropopause and surface for a perturbation from 750 ppbv to 1800 ppbv, calculated using spectrally-varying Case 4-NSA fine-snow α_s (first column) and spectrally-constant $\bar{\alpha}$ (with a value of 0.486) and $\bar{\alpha}_{CH_4}$ (with a value of 0.147) at θ = 0°.

	Case 6-SGP SW IRF (W m^{-2})		
	Rangeland	$\bar{\alpha}_{\mathrm{CH_4}}$	$\bar{\alpha}$
TOA	0.25	0.23	0.35
Tropopause	0.19	0.17	0.30
Surface	-0.58	-0.58	-0.51

Table 5.15: Case 6-SGP clear-sky CH_4 SW IRF at the TOA, tropopause and surface for a perturbation from 750 ppbv to 1800 ppbv, calculated using spectrally-varying Case 6-SGP rangeland α_s (first column) and spectrally-constant $\bar{\alpha}$ (with a value of 0.284) and $\bar{\alpha}_{CH_4}$(with a value of 0.182) at θ = 0°.

In comparison to forcings calculated using spectrally-resolved α_s, the use of $\bar{\alpha}$ leads to an overestimation of the IRF at the TOA and tropopause and a more negative forcing at the surface. This is evident in both Case 4-NSA and Case 6-SGP; however, the bias is most marked in Case 4-NSA, in particular at the tropopause, where the IRF calculated using $\bar{\alpha}$ (0.55 W m^{-2}) is around 9 times larger than the corresponding Fine-snow derived IRF (0.06 W m^{-2}). As shown in Figure 5.4, the Fine-snow spectrum exhibits high α_s values across 7000 – 10,000 cm^{-1} (from around 0.6 to 0.8), as expected for a snow-covered surface. Conversely, the Rangeland spectral albedos are much lower across 7000 – 10,000 cm^{-1} (from around 0.2 to 0.3) and indeed across the entire 1000 – 10,000 cm^{-1} range. Given that $\bar{\alpha}$ is weighted with respect to the spectral distribution of incoming solar irradiance (which is considerably stronger at such higher wavenumbers), it follows that $\bar{\alpha}$ is larger for Case 4-NSA than Case 6-SGP. As shown in Table 5.13, at every θ, Case 4-NSA $\bar{\alpha}$ are around 1.7 times larger than Case 6-SGP. Hence, the use of $\bar{\alpha}$ in Case 4-NSA calculations results in a more prominent overestimation of the IRF at the TOA and tropopause, with greater CH_4 absorption of surface reflected SW radiation, and subsequently a larger underestimation of the IRF at the surface. Nonetheless, both Case 4-NSA and Case 6-SGP demonstrate that $\bar{\alpha}$ is an inadequate proxy of spectral surface reflectance when calculating methane's SW forcing at θ = 0°. This is also demonstrated in calculations where θ = 20°, 40°, 60° and 80°, and under all-sky conditions (not shown). Thus, the use of $\bar{\alpha}$ in forcing calculations is analysed no further.

By definition $\bar{\alpha}_{\mathrm{CH_4}}$ provides a better characterisation of spectral surface reflectance following a perturbation in CH_4. Identical surface forcings demonstrate the utility of this approach; in Case 4-NSA both the Fine-snow and $\bar{\alpha}_{\mathrm{CH_4}}$ derived calculations produce an IRF of -0.71 W m^{-2}, in Case 6-SGP

both the Rangeland and $\bar{\alpha}_{\mathrm{CH_4}}$ derived calculations produce an IRF of -0.58 W m^{-2}. However, at the TOA and tropopause the use of $\bar{\alpha}_{\mathrm{CH_4}}$ leads to an underestimation of the IRF in both cases. Again, this bias is most marked in Case 4-NSA at the tropopause where the $\bar{\alpha}_{\mathrm{CH_4}}$ derived forcing (0.03 W m^{-2}) is half the magnitude of the Fine-snow derived forcing (0.06 W m^{-2}). The error induced by $\bar{\alpha}_{\mathrm{CH_4}}$ can be understood with reference to the spectral variation of the SW forcing. Figure 5.5 shows the spectral variation of Case 4-NSA tropopause IRF calculated using Fine-snow α_s (top panel) and $\bar{\alpha}_{\mathrm{CH_4}}$ (middle panel). Also shown is the difference between the Fine-snow derived IRF and $\bar{\alpha}_{\mathrm{CH_4}}$ derived IRF (lower panel). Figure 5.6 shows the equivalent spectra for Case 6-SGP. In comparison to the Fine-snow derived IRF spectra of Case 4-NSA, the use of $\bar{\alpha}_{\mathrm{CH_4}}$ (at a value of 0.147) results in less surface reflectance, weaker CH_4 absorption and hence a smaller forcing across CH_4 bands at around 4300 cm^{-1}, 6000 cm^{-1}, 7700 cm^{-1} and 9000 cm^{-1}. This is also evident in Case 6-SGP, most notably at around 6000 cm^{-1}, where $\bar{\alpha}_{\mathrm{CH_4}}$ (with a value of 0.182) results in less surface reflectance (and hence a smaller forcing) compared to the Rangeland spectra.

Although it was useful to explore whether a simplified spectrally-constant representation of α_s could be used to accurately model the SW IRF for CH_4, these results demonstrate that it is necessary to incorporate spectrally-resolved α_s in SOCRATES-RF to derive a best estimate of methane's SW forcing.

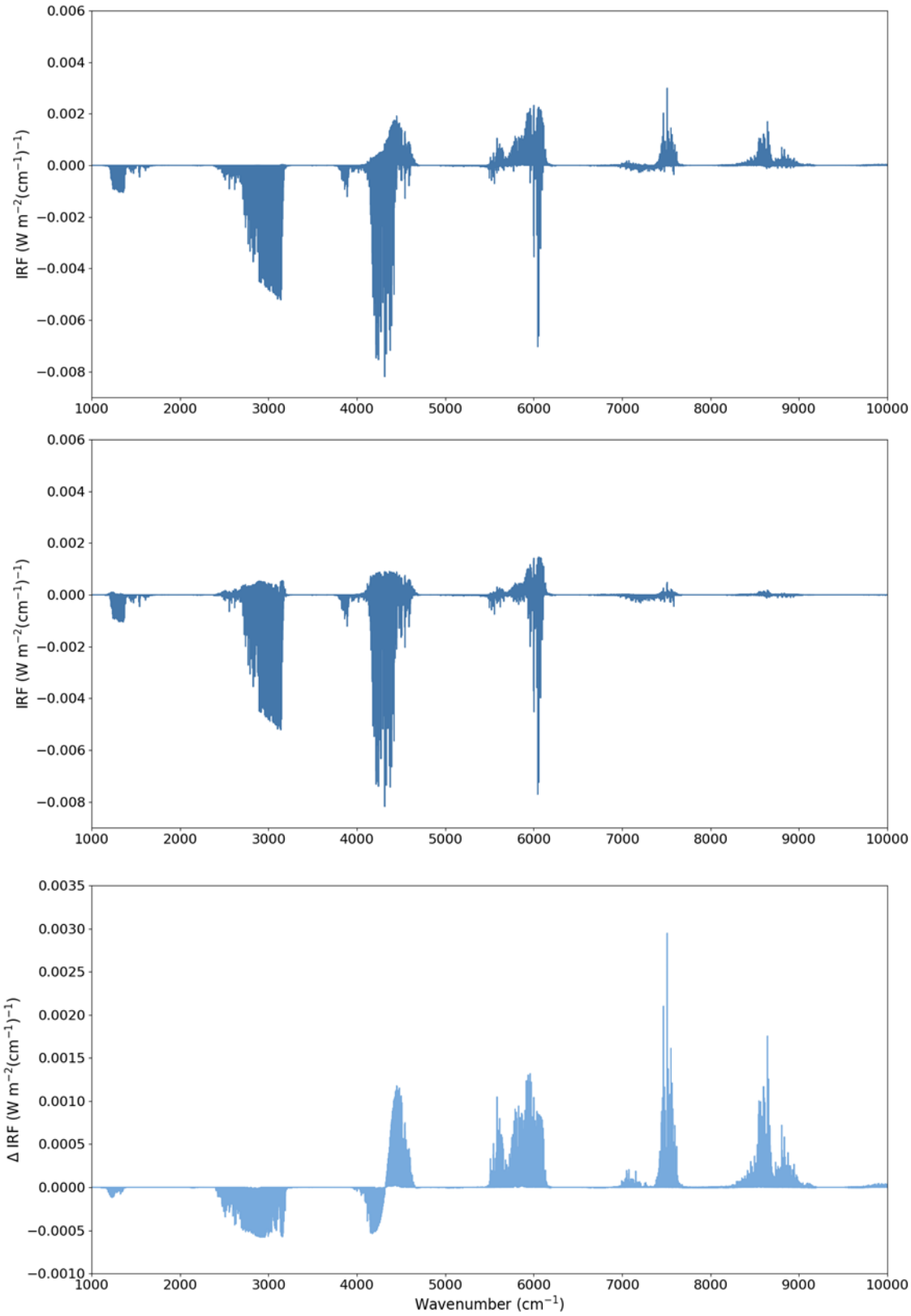

Figure 5.5: Spectral variation of Case 4-NSA clear-sky CH_4 SW tropopause IRF following a perturbation from 750 ppbv to 1800 ppbv calculated using spectrally-varying Fine-snow α_s (top panel) and $\bar{\alpha}_{CH_4}$ (middle panel). The lower panel shows the difference between the forcing calculated using the Fine-snow spectra and $\bar{\alpha}_{CH_4}$ (i.e. top panel – middle panel).

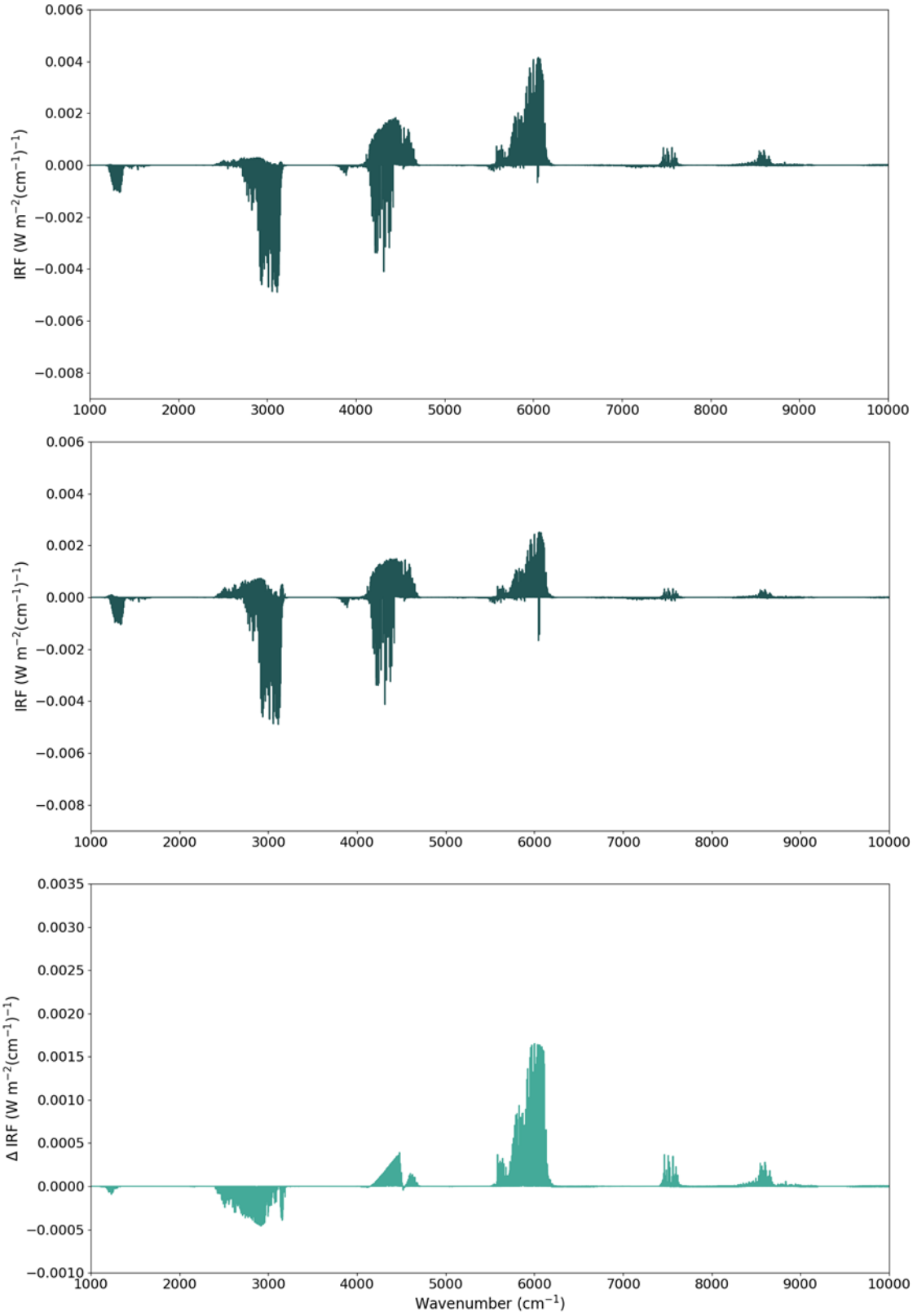

Figure 5.6: Spectral variation of Case 6-SGP clear-sky CH_4 SW tropopause IRF following a perturbation from 750 ppbv to 1800 ppbv calculated using spectrally-varying Rangeland α_s (top panel) and $\bar{\alpha}_{CH_4}$(middle panel). The lower panel shows the difference between the forcing calculated using the Rangeland spectra and $\bar{\alpha}_{CH_4}$ (i.e. top panel – middle panel).

5.4.2 The impact of SCIAMACHY-SSA in calculations of methane's SW forcing

Experimental Setup

All experiments are carried out using SOCRATES-RF. Quasi-annual, global-mean CH_4 IRFs and SARFs are calculated under clear-sky and all-sky conditions at a 5° x 5° spatial resolution using spectrally-resolved α_s retrievals from the SCIAMACHY α_s database, described in Section 3.3.5. Forcings are derived using CAM 3.0 mixing ratios of CH_4 following a perturbation from 750 ppbv to 1800 ppbv. Mixing ratios of CO_2, N_2O, and O_3 are also included as specified in Section 3.1.5.

As described in Section 3.3.5, the SCIAMACHY α_s database consists of 34 wavelength bands between 0.328 and 2.314 µm. Data are available for each month of the year at a 0.5° x 0.5° spatial resolution. For reasons outlined in Section 3.3.5, this thesis uses SCIAMACHY data between 0.355 and 2.314 µm. Figure 5.7 presents a schematic of the method used to assimilate SCIAMACHY data into SOCRATES-RF's 260-band SW spectral file, sp_sw_260_jm2. This process is carried out for each 0.5° x 0.5° grid-point in the SCIAMACHY dataset. Between 0.355 and 2.314 µm, SCIAMACHY data are linearly interpolated to the upper wavelength limit of each sp_sw_260_jm2 band in this spectral region. To extend spectral reflectance to wavelengths greater than 2.314 µm, an additional α_s datapoint is constructed at 5 µm with a value of 0.05. Huang *et al.* (2018) show that surface emissivity (ε) at wavelengths above 5 µm are around 0.95 for a range of land surface types such as water, ice, snow and desert. Therefore assuming:

$$\alpha = 1 - \varepsilon \tag{5.8}$$

it follows that the value of 0.05 is appropriate to use as stated above. To extend spectral reflectance to the upper and lower limits of sp_sw_260_jm2, data are linearly extrapolated from 5 to 10 µm and from 0.355 to 0.17 µm. Given the lack of monthly, global albedo datasets at wavelengths greater than 2.314 µm and less than 0.328 µm, this approach constructs a 'best estimate' of spectral surface reflectance across the 0.17 to 10 µm range. It is acknowledged that this method could be significantly improved if such global datasets became available.

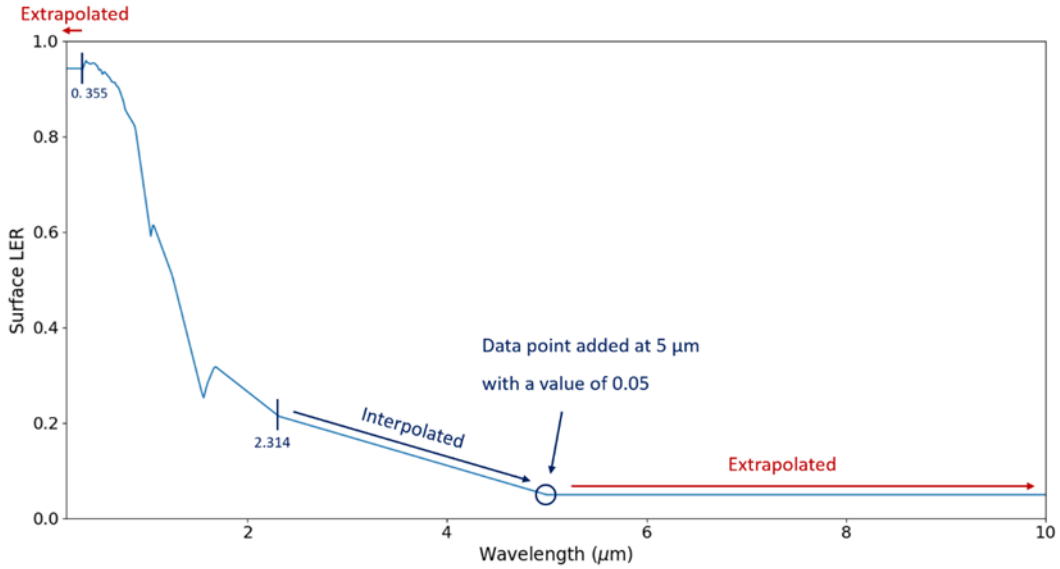

Figure 5.7: Schematic of the method used to assimilate SCIAMACHY spectral α_s data (Tilstra et al. 2017) into SOCRATES-RF's SW spectral file, sp_sw_260_jm2. This example demonstrates the process at a snow-covered grid-point located at 70°N, 155°W, Alaska for the month of May.

As stated in Section 3.3.5, SCIAMACHY α_s are judged to inadequately represent the spectral reflectance of sea-surfaces. Therefore, all open-ocean SCIAMACHY grid-points are masked and replaced based on a SOCRATES internal subroutine, extracted by Professor Keith Shine at the University of Reading. This subroutine accounts for the spectral variation of sea-surface albedo due to Fresnel reflection, modified to account for the impact of wind-induced variations in sea-surface roughness following Cox and Munk (1954), assuming nominal values for 10 metre wind speed of 7 m s^{-1}. Refractive indices of water are taken from Jerlov (1976) and Hale and Querry (1973), modified for nominal values of sea surface salinity of 35 g kg^{-1}. The effect of ocean whitecaps are also included from Whitlock *et al.* (1982); however this makes a small contribution to spectral reflectance given that whitecaps typically account for less than 2% of the sea-surface. Since sea-surface albedo is dependent on solar zenith angle, α_s is calculated assuming a daylight-average solar zenith angle at each grid-point and month. This scheme is of similar complexity to the representation of sea-surface albedo in Collins *et al.* (2018) and is more sophisticated than models such as the European Centre for Medium-range Weather Forecasts Integrated Forecasting System (ECMWF-IFS), where no spectral variation is assumed (IFS Documentation CY47R1 2020). Much more sophisticated sea-surface parameterisations are available, for example Séférian *et al.* (2018). However, these require the specification of many more parameters, such as biophysical processes that govern the

interaction of solar radiation with marine chlorophyll. Including such parameters is beyond the scope of this thesis.

Consequently, monthly α_s fields consist of an amalgamation of SCIAMACHY data and SOCRATES sea-surface albedo, henceforth referred to as SCIAMACHY-SSA. Following this data are re-gridded to a 5° x 5° spatial resolution.

Results

Table 5.16 compares methane's quasi-annual, global mean clear-sky SW IRF at the TOA, tropopause and surface following a perturbation in CH_4 from 750 ppbv to 1800ppbv, calculated using ERA-interim $\bar{\alpha}$ (first column) and SCIAMACHY-SSA α_s (second column). These calculations are identical in nature apart from the specification of surface albedo. As shown, the use of SCIAMACHY-SSA α_s causes an increase in the magnitude of the global-mean surface forcing by around 4.5%, from -0.223 W m^{-2} to -0.233 W m^{-2}. Given that the size of the downward surface forcing component is the same in both calculations, this demonstrates that SCIAMACHY-SSA α_s produces less surface reflectance than ERA-interim $\bar{\alpha}$. This is also evident at the tropopause; whereby reduced surface reflectance causes a reduction in tropospheric CH_4 absorption of surface-reflected SW radiation. Consequently, the SCIAMACHY-SSA derived IRF (-0.03 W m^{-2}) is around 67% more negative than the ERA-interim derived forcing (-0.018 W m^{-2}). Given that the sign of the TOA IRF is positive (driven by enhanced absorption of reflected SW radiation between the surface and TOA following an increase in CH_4 concentrations) it follows that reduced surface reflectance in SCIAMACHY-SSA calculations causes a decrease in the TOA IRF compared to ERA-interim. Here the SCIAMACHY-SSA IRF is around 24% smaller than the ERA-interim IRF.

	Clear-sky SW IRF (W m^{-2})	
	ERA-interim	**SCIAMACHY-SSA**
TOA	0.051	0.039
Tropopause	-0.018	-0.030
Surface	-0.223	-0.233

Table 5.16: Comparison of quasi-annual, global mean clear-sky CH_4 SW TOA, tropopause and surface IRF calculated using ERA-interim $\bar{\alpha}$ (first column) and SCIAMACHY-SSA α_s (second column). All estimates are derived following a perturbation from 750 ppbv to 1800 ppbv, using CAM 3.0 vertically-varying CH_4 mixing ratios.

Table 5.17 compares equivalent calculations conducted under all-sky conditions. The inclusion of clouds dampens the effect of reduced surface reflectance on the TOA IRF. This results in forcings that are more comparable in magnitude; the SCIAMACHY-SSA derived IRF (0.08 W m^{-2}) is 8% smaller than the ERA-interim derived IRF (0.087 W m^{-2}). However, despite the addition of clouds, both the surface and tropopause forcings exhibit a similar level of sensitivity to the specification of α_s. This is most apparent at the tropopause where the SCIAMACHY-SSA derived IRF (0.009 W m^{-2}) is 44% smaller than the ERA-interim derived IRF (0.016 W m^{-2}). This result is significant in the context of previous estimates of methane's all-sky tropopause SW IRF. Both Etminan *et al.* (2016) and Collins *et al.* (2018) estimate the tropopause forcing to be about a factor of three larger, at 0.03 W m^{-2} and 0.026 W m^{-2}, respectively. Such a disparity warrants further investigation; however, an important difference in experiment design must first be taken into account. Etminan *et al.* (2016) and Collins *et al.* (2018) derive methane's SW forcing across a narrower spectral range, from 0.2 - 5 µm and 0.84 – 5 µm, respectively. As demonstrated in Section 5.3.2, the effect of CH_4 absorption at solar mid-infrared wavelengths between 5 – 10 µm has a significant impact on the all-sky tropopause IRF; extending the SW spectral range to 10 µm acts to *reduce* the forcing by 25%.

	All-sky SW IRF (W m^{-2})	
	ERA-interim	**SCIAMACHY-SSA**
TOA	0.087	0.080
Tropopause	0.016	0.009
Surface	-0.155	-0.161

Table 5.17: Comparison of quasi-annual, global mean all-sky CH_4 SW TOA, tropopause and surface IRF calculated using ERA-interim $\bar{\alpha}$ (first column) and SCIAMACHY-SSA α_s (second column). All estimates are derived following a perturbation from 750 ppbv to 1800 ppbv, using CAM 3.0 vertically-varying CH_4 mixing ratios.

To enable a cleaner comparison with Etminan *et al.* (2016) and Collins *et al.* (2018), Table 5.18 shows methane's quasi-annual global-mean tropopause IRF calculated using a reduced SW spectral range, from 0.17 – 5 µm. Henceforth, this SOCRATES-RF calculation is referred to as the 'reduced-SW' estimate. As expected, excluding the mid-infrared wavelengths causes a reduction in the magnitude of the IRF under both clear-sky and all-sky conditions, by 13% and 44% respectively. The difference between this all-sky result and Etminan *et al.* (2016) and Collins *et al.* (2018) is reduced from a factor of 3 to a factor of 2.

	Tropopause IRF (W m^{-2})
All-sky	0.013
Clear-sky	-0.026

Table 5.18: Quasi-annual, global mean all-sky CH_4 SW tropopause IRF calculated across the reduced SW spectral range of 0.17 – 5 µm using CAM 3.0 vertically-varying CH_4 mixing ratios and SCIAMACHY-SSA α_s. Both estimates are derived following a perturbation in CH_4 from 750 ppbv to 1800 ppbv.

Spatial distribution of CH_4 SW tropopause IRF

Figure 5.8 shows the spatial distribution of methane's quasi-annual all-sky SW tropopause IRF calculated by SOCRATES-RF across the complete 0.18 – 10 µm wavelength range, derived using SCIAMACHY-SSA α_s. This distribution can be directly compared to Figure 5.3 which shows the equivalent forcing derived using ERA-interim $\bar{\alpha}$. Notably, the forcing is negative over larger areas of North America, Eurasia and the equatorial oceans. This contributes to the decrease in the global-mean IRF in comparison to the ERA-interim $\bar{\alpha}$ derived IRF (see Table 5.17) . Interestingly, the use of SCIAMACHY-SSA α_s intensifies the area of maxima over the Arabian Peninsula, and most markedly, the Sahara. Here, the forcing exceeds 0.20 W m^{-2} over a sizable region of the desert with a maximum localised value of 0.25 W m^{-2}, approximately 30 times greater than the quasi-annual global-mean forcing (0.009 W m^{-2}). This emphasizes the dependence of the SW forcing on spectrally-resolved α_s over desert land surfaces. Notably, the poleward amplification of the forcing seen in Figure 5.3 is absent here. This indicates that the use of ERA-interim $\bar{\alpha}$ yields too much surface reflectance across the 0.17 – 10 µm range, resulting in an overestimation of the SW forcing across both polar regions. Again, this underlines the importance of the dependence of the SW forcing on spectrally-resolved α_s.

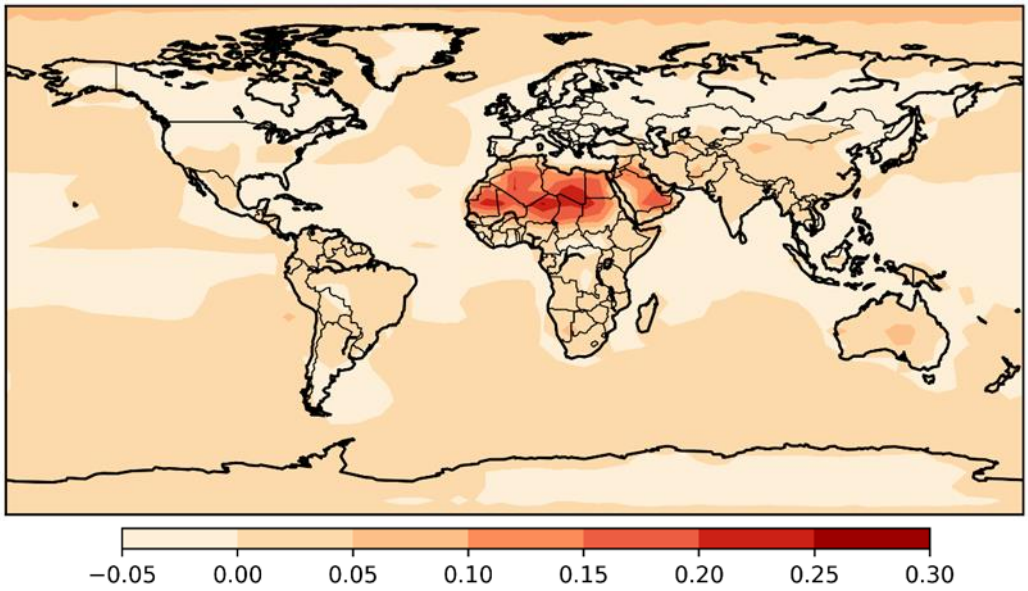

Figure 5.8: Quasi-annual all-sky CH_4 SW tropopause IRF (W m^{-2}) following a perturbation in CH_4 from 750 ppbv to 1800 ppbv, derived using CAM 3.0 mixing ratios of CH_4 and SCIAMACHY-SSA α_s. As noted in the text, this plot can be directly compared to Figure 5.3.

Figure 5.9 (upper panel) shows the spatial distribution of methane's all-sky tropopause IRF calculated by SOCRATES-RF using the reduced-SW 0.17 – 5 µm wavelength range and SCIAMACHY-SSA α_s. Also shown in Figure 5.9 (lower panel) is a replotted version of Figure 2.13a of the spatial distribution of methane's all-sky SW tropopause IRF (calculated using the background climatology from the CSIRO Mk3-6-0 ESM) from Collins *et al.* (2018). This has been produced using data kindly provided by Professor William D. Collins (personal communication, January 2021).

Given the absence of the poleward amplification as seen in Figure 5.3, the spatial distribution of Figure 5.9 (upper panel) shows closer agreement to the Collins *et al.* (2018) estimate (see Figure 5.10 lower panel). Although, as previously noted, the global annualised IRF of Collins et *al.* (2018) is remarkably larger, at around two times the size of the reduced-SW SOCRATES-RF IRF presented here (0.013 W m^{-2}, see Table 5.17).

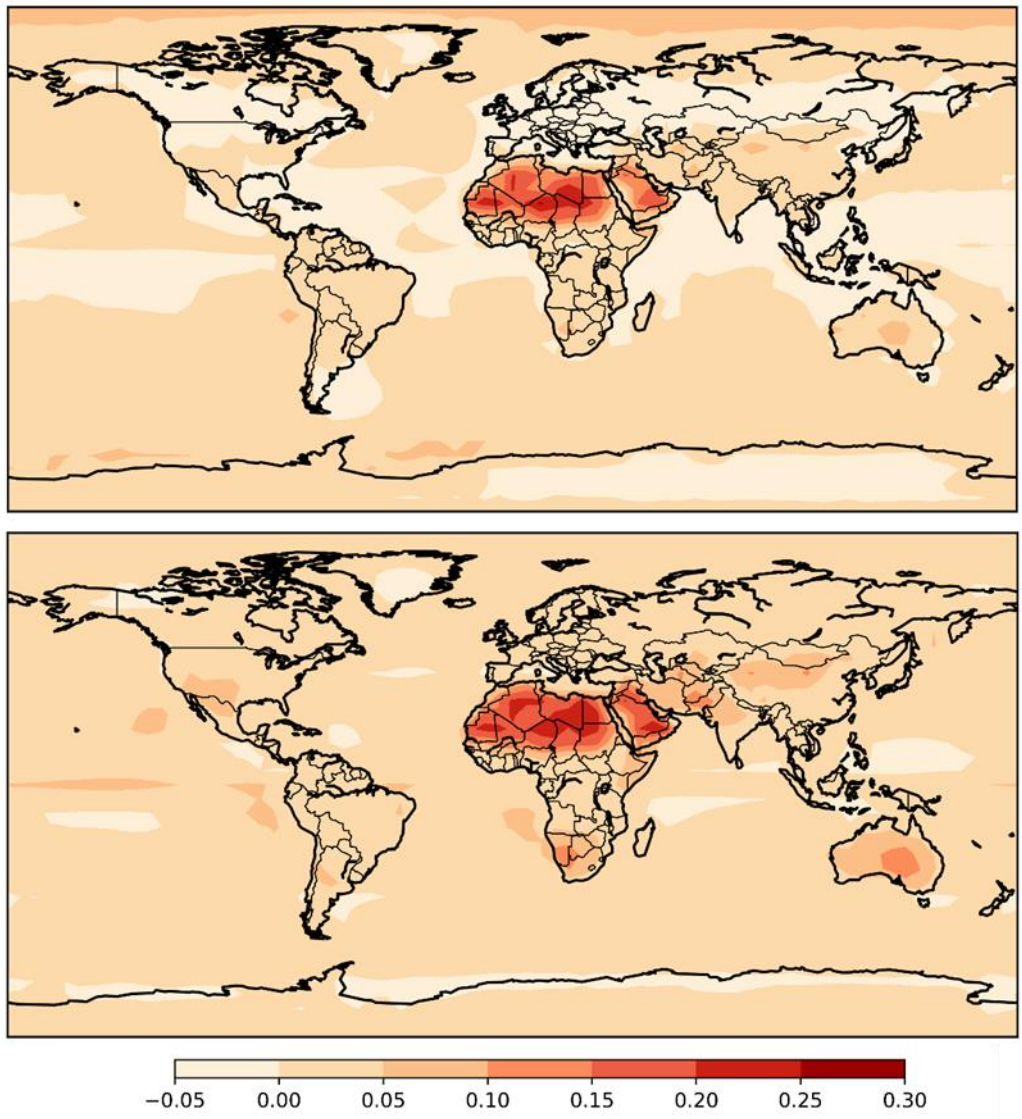

Figure 5.9: Upper panel: Quasi-annual mean all-sky CH_4 SW tropopause IRF (W m^{-2}) calculated across the reduced-SW spectral range from 0.17 – 5 µm following a perturbation in CH_4 from 750 ppbv to 1800 ppbv, derived using CAM 3.0 mixing ratios of CH_4 and SCIAMACHY-SSA α_s.

Lower panel: Replotted version of Figure 2.13a from Collins et al. (2018) showing annual-mean all-sky CH_4 SW tropopause IRF (W m^{-2}) calculated across from 0.84 – 5 µm following a perturbation in CH_4 from 806 ppbv to 1760 ppbv using the background climatology from the CSIRO Mk3-6-0 Earth System Model.

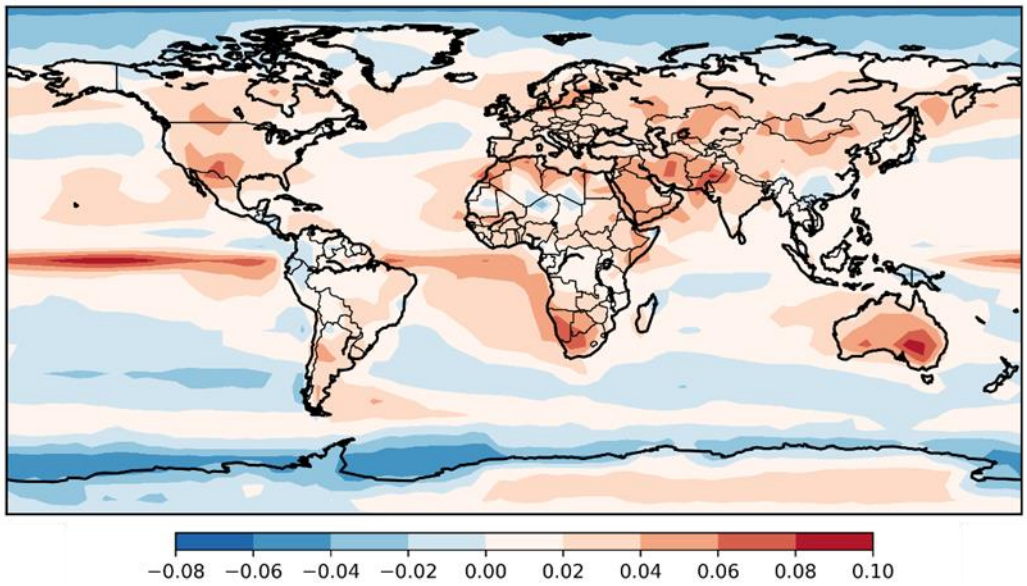

Figure 5.10: Difference (in W m^{-2}) between the lower panel and upper panel of Figure 5.9 (i.e. Collins et al. (2018) – SOCRATES-RF) to show the spatial disparity between methane's SW tropopause IRF produced by each estimate. Regions where the difference is above zero denote where the Collins et al. (2018) IRF is larger than the reduced SW SOCRATES-RF IRF, the blue regions denote the opposite. Note that Collins et al. (2018) derive their estimate of CH_4 SW IRF using a smaller perturbation in CH_4 from 806 ppbv to 1760 ppbv (compared to 750 ppbv to 1800 ppbv as used in the SOCRATES-RF calculation).

Figure 5.10 shows the corresponding difference between the Collins et *al.* (2018) estimate and the reduced-SW SOCRATES-RF estimate (i.e. Figure 5.9 lower panel – Figure 5.9 upper panel). This demonstrates that the Collins *et al.* (2018) estimate of methane's all-sky SW tropopause IRF is larger over most of the world's land mass. The forcing is between 0.02 – 0.04 W m^{-2} greater than SOCRATES-RF over large regions of North America, Eurasia, and Western Antarctica. This increases to 0.04 – 0.10 W m^{-2} over regions such as Namibia, South Africa, Pakistan and Australia. This indicates that the discrepancy in methane's global mean forcing can be partially explained by the different specification of α_s in each estimate. Collins *et al.* (2018) state that land surface and snow α_s values are "obtained from climate model grid spectral seven-band Moderate Resolution Imaging Spectroradiometer (MODIS) bi-directional reflectance distribution functions" (BDRFs; Shuai *et al.* 2008). Inspection of the instrument specification of MODIS shows that these seven bands cover the 0.620 - 2.155 µm wavelength range (https://modis.gsfc.nasa.gov/about/specifications.php, last accessed 05/04/2021). However, further detail is not provided on how MODIS observations are spectrally distributed across the 0.84 – 5 µm spectral range used in their SW forcing calculations. Such detail is needed given the importance of methane's SW bands within this spectral range (at 2.3 µm and 3.3 µm) and their dependence on the specification of spectrally-resolved α_s, as

demonstrated throughout Section 5.4.1. Arguably the use of SCIAMACHY α_s data, with 33 bands across 0.355 - 2.314 μm, provides a more highly resolved description of land surface albedo. Nevertheless, it is acknowledged that the method used to interpolate and extrapolate SCIAMACHY α_s data to the upper waveband limits in SOCRATES-RFs SW spectral file is idealised (see the Experimental setup of Section 5.4.2). Confidence in the fidelity of spectral surface reflectance at wavelengths greater than 2.314 μm would be significantly enhanced with the availability of global observational datasets.

Figure 5.10 also shows a disparity over the global oceans. Differences in the specification of α_s in each calculation are likely to contribute to this discrepancy; although as previously mentioned, the representation of sea-surface α_s in both estimates is of similar complexity, built on the methods of Cox and Munk (1954). Large areas of the Southern Ocean exhibit a lower forcing in the reduced-SW SOCRATES-RF estimate, up to -0.04 W m^{-2} in the South Pacific Ocean. Conversely, large regions of the tropical oceans exhibit a higher forcing in the Collins *et al.* (2018) estimate, particularly off the west coast of North America, Africa and across the Pacific and Atlantic equatorial region, where the forcing varies locally by around 0.1 W m^{-2}. The spatial signature of such a positive bias suggests that this discrepancy originates from SW CREs associated with oceanic stratus cloud decks and the ITCZ. Indeed, consideration of the size and sign of methane's clear-sky forcing, and how it changes under all-sky conditions, indicates that the CRE is different in each estimate.

Table 5.19 compares methane's clear-sky and all-sky tropopause SW IRF calculated by SOCRATES-RF (across both the complete and reduced-SW wavelength ranges), Etminan *et al.* (2016) and Collins *et al.* (2018; using the background climatology from the CSIRO Mk3-6-0 ESM). As stated in Section 2.3.2, it is notable that Collins *et al.* (2018) estimate a positive (0.011 W m^{-2}), rather than negative, clear-sky IRF. A positive clear-sky SW tropopause IRF is in marked contrast to the results of Etminan *et al.* (2016) (supported by the calculations presented in this thesis), where it is the inclusion of clouds that causes the sign of the SW tropopause IRF to be positive. The Etminan *et al.* (2016) tropopause IRF changes sign from -0.045 W m^{-2} under clear-sky conditions, to 0.03 W m^{-2} under all-sky conditions. Overall, the IRF increases by 0.075 W m^{-2}. Both SOCRATES-RF estimates demonstrate this switch in sign of the forcing, albeit with a less pronounced increase. The reduced-SW SOCRATES-RF tropopause IRF changes sign from -0.026 W m^{-2} under clear-sky conditions, to 0.013 W m^{-2} under all-sky conditions. Overall, the IRF increases by 0.039 W m^{-2}. This effect is similar to the case of the 'full' SW SOCRATES-RF tropopause IRF calculated across the complete 0.18 – 10 μm range. Here, the clear-sky IRF of -0.03 W m^{-2} increases by 0.039 W m^{-2} to 0.009 W m^{-2}. The inclusion of clouds in Collins *et al.* (2018) causes the forcing to increase by just 0.014 W m^{-2} to 0.025 W m^{-2}. This implies

that α_s are systematically likely higher in Collins et al. (2018), which then has the knock-on effect that the addition of clouds has a lower impact compared to the SOCRATES-RF calculations.

CRE is examined in further detail in Chapter 6, following the calculation of full 12-month annual mean CH_4 SW forcings.

	SOCRATES-RF		**Etminan *et al.* (2016)**	**Collins *et al.* (2018)**
	0.18 – 10 µm	**0.18 – 5 µm**		
Clear-sky	-0.030	-0.026	-0.045	0.011
All-sky	0.009	0.013	0.03	0.025

Table 5.19: Comparison of clear-sky and all-sky tropopause CH_4 SW IRF calculated by SOCRATES-RF across both the complete 0.18 – 10 µm wavelength range and the reduced-SW 0.18 – 5 µm wavelength range, Etminan et al. (2016) and Collins et al. (2018) using the background climatology from the CSIRO Mk3-6-0 Earth System Model. SOCRATES-RF and Etminan et al. (2016) derive forcings using a CH_4 perturbation from 750 ppbv – 1800 ppbv, Collins et al. (2018) derive forcings using a CH_4 perturbation from 806 ppbv – 1760 ppbv.

5.5 Chapter conclusions

This chapter has investigated the sensitivity of methane's SW forcing to the representation of the vertical profile of CH_4 mixing ratios, absorption of solar radiation between 5 – 10 μm and the specification of surface albedo. To summarise, the key findings are:

- A realistic representation of methane's vertical profile is essential in achieving an accurate quantification of the global-mean SW IRF. Considering the impact of SW absorption on the stratospheric-temperature adjustment process, it is also important in the calculation of methane's global-mean LW SARF and net RF.

- Methane's forcing across the solar mid-infrared is the largest at the tropopause, due to enhanced absorption in the stratosphere. Under clear-sky conditions, CH_4 absorption across 5 – 10 μm acts to increase the magnitude of the negative tropopause forcing by 22%, Under all-sky conditions CH_4 absorption across 5 – 10 μm acts to reduce the magnitude of the positive tropopause forcing by 25%. This result is significant and highlights the importance of including solar mid-infrared absorption in calculations of methane's forcing.

- Methane's SW tropopause forcing is highly sensitive to the specification of spectrally-varying surface albedo. This sensitivity is largest under clear-sky conditions; however, the effect is also significant under all-sky conditions. The use of spectrally-varying SCIAMACHY-SSA α_s causes a reduction in the all-sky tropopause SW IRF by 44% compared to the equivalent calculation conducted using spectrally-constant ERA-interim $\bar{\alpha}$ fields.

- Comparing the results presented here with previous calculations by Etminan *et al.* (2016) and Collins *et al.* (2018) shows distinct differences in methane's clear-sky SW IRF and the impact of CRE.

Chapter 6

Best estimate of methane's shortwave radiative forcing

6.1 Introduction

This chapter presents a best estimate of CH_4 global annual-mean SW IRF and its impact on the stratospheric-temperature adjusted LW forcing. This estimate includes SW absorption between 5 – 10 µm, spectrally-resolved SCIAMACHY-SSA α_s and satellite-derived stratospheric CH_4 mixing ratios to incorporate a realistic description of the spatial and temporal variability in atmospheric CH_4 in forcing calculations. This estimate therefore offers a significant update to the SW forcing reported by Etminan *et al.* (2016) and Collins *et al.* (2018). The final section presents an assessment of sources of uncertainty related to RF and estimates the total uncertainty associated with the calculation of CH_4 SW IRF, LW SARF and net RF presented in this chapter.

Experimental Setup

All experiments are carried out using SOCRATES-RF. Global-annual mean CH_4 IRFs and SARFs are calculated under clear-sky and all-sky conditions following a perturbation from 750 ppbv to 1800 ppbv. Unlike the quasi-annual mean results presented in Chapter 5, annual-mean calculations are derived using all 12 months. Experiments are run at a 5° x 5° spatial resolution using monthly-mean

climatological fields of ERA-interim reanalysis data, as described in Section 3.1.5 and SCIAMACHY-SSA α_S, as described in Section 5.4.3. Mixing ratios of CO_2, N_2O, and O_3 are also included as specified in Section 3.1.5.

Vertically-varying CH_4 profiles are derived from MIPAS CH_4 climatology (Hegglin *et al.* 2021). As detailed in Section 3.3.2, this climatology comprises monthly-mean, zonal-mean CH_4 mixing ratios from 300 hPa to 0.1 hPa averaged between 2005 – 2012. Data are available at a 5° spatial resolution from 87.5° N to 87.5° S. MIPAS CH_4 fields are incorporated into SOCRATES-RF calculations as follows:

1. At each latitude, pre-industrial CH_4 profiles are constructed using the fall-off rate of MIPAS CH_4 mixing ratios, with a value of 750 ppbv at 300 hPa. This assumes that processes determining the fall off rate (and its monthly and latitudinal variation) are unchanged relative to the present day.

2. Data are regridded to a 5° x 5° spatial resolution to match the latitudinal and longitudinal coordinates of monthly-mean ERA-interim climatological fields.

3. Data are interpolated to monthly-mean ERA-interim pressure levels, resulting in constant CH_4 mixing ratios throughout the troposphere and vertically-varying CH_4 mixing ratios in the stratosphere.

Figure 6.1 shows zonal-mean, seasonal-mean MIPAS CH_4 profiles from 300 hPa to 0.1 hPa for December, January, February (DJF; upper panel) and June, July, August (JJA; lower panel) at 30°, 60° and 90° north (left-hand side) and south (right-hand side) of the equator. As shown, CH_4 mixing ratios exhibit a variable rate of decrease with height at each latitude; notably, this does not follow the smooth exponential decrease as represented by CAM 3.0 mixing ratio scale-heights used in Chapter 5 (see Figure 5.1). It is of further note that MIPAS CH_4 mixing ratios are at least 2.5 times larger than CAM 3.0 CH_4 mixing ratios at 300 hPa at 0°. This disparity increases with distance from the equator, at 60° and 90° (north and south) MIPAS CH_4 mixing ratios are over 10 times larger than CAM 3.0 at 300 hPa. The resulting impact on methane's SW forcing is discussed in Section 6.2. Figure 6.1 also shows the marked seasonality in MIPAS CH_4 mixing ratios. Stratospheric mixing ratios are observed to be lower in the winter hemisphere than the summer hemisphere between 60° and 90°. As described in Section 2.1.2, this due to the descending branch of the Brewer-Dobson circulation carrying low-CH_4 air into the stratosphere during winter.

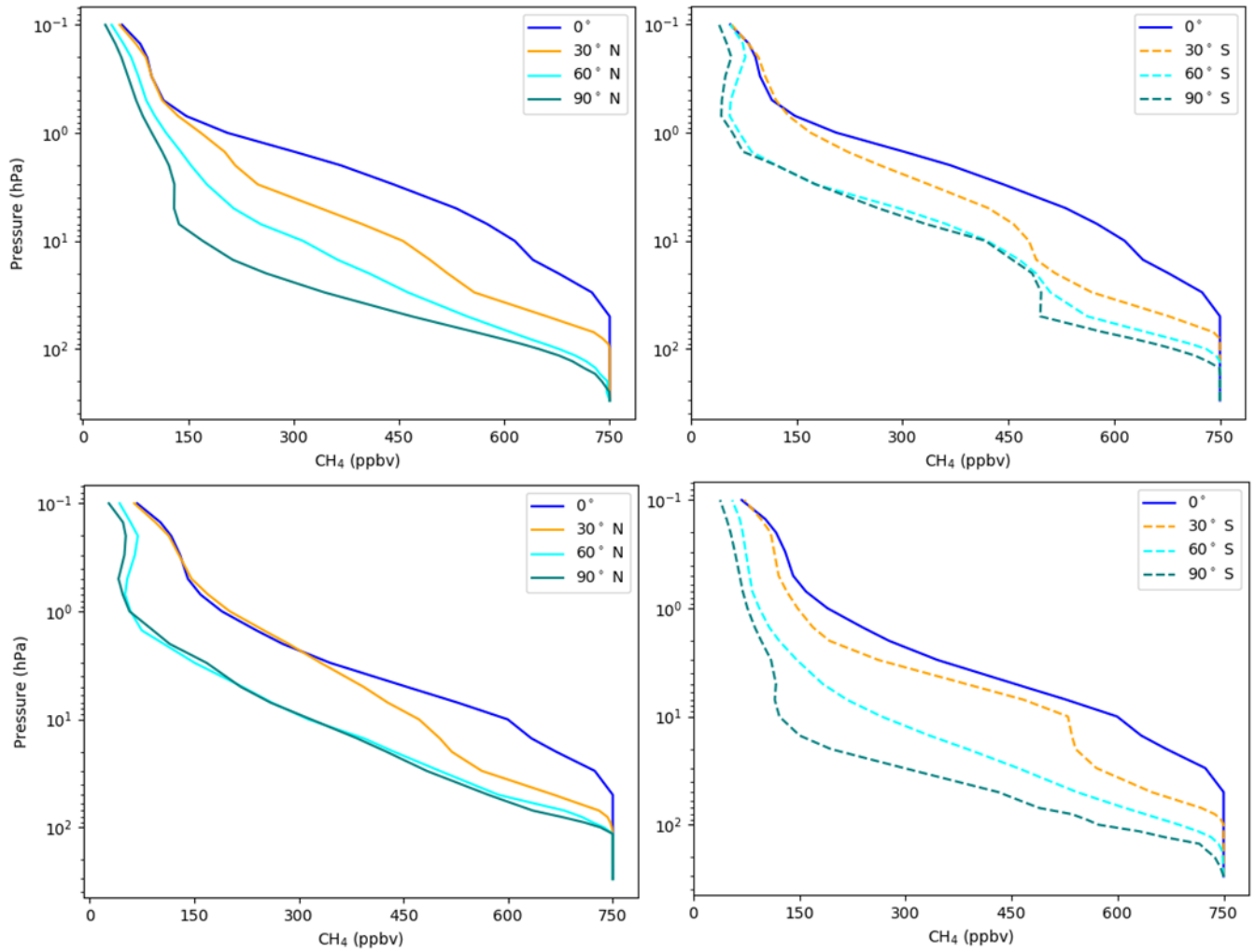

Figure 6.1: Pre-industrial (750 ppbv) zonal seasonal-mean CH_4 profiles for DJF (upper panel) and JJA (lower panel) at 0°, 30°, 60° and 90° north (left-hand side) and south (right-hand side) constructed using MIPAS zonal-mean CH_4 fall off rate as described in the main text.

6.2 Clear-sky and All-sky SW RF

Table 5.1 shows methane's global annual mean clear-sky SW IRF at the TOA, tropopause and surface following a perturbation from 750 ppbv to 1800 ppbv, calculated using MIPAS CH_4 mixing ratios. The corresponding LW and net forcings are also shown to demonstrate the impact of SW absorption on methane's total clear-sky radiative effect.

	Clear-sky IRF (W m^{-2})		
	SW	**LW**	**Net**
TOA	0.040	0.650	0.690
Tropopause	-0.038	0.674	0.636
Surface	-0.235	0.306	0.071

Table 6.1: Global-annual mean clear-sky CH_4 SW, LW and net IRF at the TOA, tropopause and surface following a perturbation in CH_4 from 750 ppbv to 1800 ppbv. Forcings are derived using MIPAS CH_4 observations and SCIAMACHY-SSA α_s.

As expected, the sign of methane's SW forcing at each level is consistent with the clear-sky SOCRATES-RF estimates presented in Chapter 5, whereby, the forcing is positive at the TOA, driven by enhanced absorption of surface-reflected SW radiation between the surface and TOA, and negative at the tropopause and surface, following a reduction in the downward SW flux after a perturbation in CH_4. In comparison to the SW forcings derived using idealised CAM 3.0 CH_4 mixing ratio scale-heights (see Table 5.16, second column), the use of MIPAS CH_4 mixing ratios results in a more positive forcing at the TOA and a more negative forcing at the tropopause and surface. As previously noted, MIPAS CH_4 mixing ratios are higher than CAM 3.0 throughout the stratosphere, which subsequently means that the *change* in CH_4 is also higher going from pre-industrial to present day levels. This results in increased stratospheric CH_4 SW absorption and a greater reduction in the downward SW flux at the tropopause and surface, and increased absorption of surface-reflected SW radiation between the tropopause and TOA. However, as demonstrated in Section 5.2.1, both the surface and TOA clear-sky forcings are less sensitive to specification of methane's stratospheric profile; the use of MIPAS CH_4 mixing ratios increases the forcing (relative to Table 5.16) by just 0.86%

(from 0.039 W m^{-2} to 0.040 W m^{-2}) and 2.6% (from -0.233 W m^{-2} to -0.235 W m^{-2}), respectively. The tropopause exhibits significantly higher sensitivity, increasing by 27% from -0.030 W m^{-2} to -0.038 W m^{-2}. Consequently, this result is in closer agreement to the clear-sky SW tropopause IRF of -0.045 W m^{-2} reported by Etminan *et al.* (2016) and a stronger disparity with the *positive* clear-sky IRF (0.011 W m^{-2} from the CSIRO Mk3-6-0 ESM) of Collins *et al.* (2018). Given that the SOCRATES-RF estimate lies between both Etminan *et al.* (2016) and Collins *et al.* (2018), the spread in methane's clear-sky SW tropopause IRF remains as reported in Section 5.4.2, at 0.056 W m^{-2}. Such a spread is significant and likely occurs due to a combination of factors associated with differences in experimental design, particularly the specification of methane's vertical profile and α_s. As previously highlighted, the SOCRATES-RF forcing is the only estimate to include solar absorption between 5 – 10 μm, which was shown in Section 5.3.2 to make the CAM 3.0-derived clear-sky tropopause forcing 22% more negative. Both SOCRATES-RF and the narrow-band MODTRAN calculations of Collins *et al.* (2018) rely on approximate treatments of radiative transfer which introduce parameterisation error in forcing estimates. Chapter 4 demonstrates that the radiance core of SOCRATES-RF can calculate methane's clear-sky SW tropopause IRF to within 10% of the benchmark RFM, which increases confidence in the SOCRATES-RF estimate presented here. Collins *et al.* (2018) report a 13% error in MODTRAN relative to benchmark LBL calculations of methane's clear-sky tropopause SW IRF, for a perturbation from 806 ppbv to 1760 ppbv using a MLS profile, α_s = 0.1 and θ = 53°. Over high albedo surfaces this 13% error may be exacerbated. A coordinated intercomparison of SOCRATES-RF and MODTRAN against the OLBL code used by Etminan *et al.* (2016), performed with a representative set of atmospheric conditions, would help determine the extent of model error.

Although it is not the focus of this chapter, it is notable that the SW surface IRF (-0.235 W m^{-2}) counterbalances the LW surface IRF (0.306 W m^{-2}), leaving a residual net forcing of just 0.071 W m^{-2} (see Table 6.1). This demonstrates the importance of accounting for methane's SW IRF at the surface. RF calculations that omit the SW effect will overestimate methane's net surface forcing.

Table 6.2 shows methane's global annual mean all-sky SW, LW and net IRF at the TOA, tropopause and surface. As expected at the TOA, the SW IRF increases in magnitude following the inclusion of clouds, which increases the amount of reflected SW radiation available for absorption with increased CH_4 concentrations. As described in Section 5.2.1, this mechanism is also responsible for the switch in sign of the SW tropopause IRF. However, the magnitude of this forcing (0.002 W m^{-2}) is significantly smaller than the CAM 3.0 derived SW tropopause IRF (0.009 W m^{-2} see Table 5.17, second column). Given that MIPAS CH_4 mixing ratios are higher than CAM 3.0 throughout the stratosphere, this results in a larger downward forcing component at the tropopause that is only marginally offset by the positive upward forcing component due to tropospheric absorption.

Consequently, the tropopause IRF is a relatively small residual of these compensating terms. Relative to the net tropopause IRF (0.58 W m^{-2}), the SW forcing accounts for just 0.3% of methane's total radiative effect. In the context of previous estimates of methane's all-sky SW tropopause IRF, this forcing is significantly smaller; Etminan *et al.* (2016) estimate the tropopause IRF to be 15 times larger, at 0.03 W m^{-2}, and 5.5% of the net tropopause IRF (0.52 W m^{-2}). Collins *et al.* (2018) estimate the tropopause IRF to almost 13 times larger at 0.025 W m^{-2}.

	All-sky IRF (W m^{-2})		
	SW	**LW**	**Net**
TOA	0.082	0.553	0.635
Tropopause	0.002	0.578	0.580
Surface	-0.163	0.180	0.017

Table 6.2: Global annual mean all-sky CH_4 SW IRF at the TOA, tropopause and surface following a perturbation in CH_4 from 750 ppbv to 1800 ppbv. Forcings are derived using MIPAS CH_4 observations and SCIAMACHY-SSA surface albedo.

MIPAS CH_4 fields provide a significantly improved representation of the spatial and temporal variation in stratospheric CH_4 in comparison to the idealised CAM 3.0 mixing ratio scale-heights used by Collins *et al.* (2018) and the limited spatial representation of the two-atmosphere (tropical/extratropical) approach used by Etminan *et al.* (2016). Furthermore, the SOCRATES-RF forcing includes a more highly spectrally-resolved description of α_s and solar CH_4 absorption between 5 – 10 µm. Thus, this estimate arguably provides a more detailed quantification of CH_4 SW all-sky tropopause forcing. As discussed in Section 5.4.2, the apparent agreement between Etminan *et al.* (2016) and Collins *et al.* (2018) appears to be a coincidence of significantly different clear-sky forcing and a significantly different impact of including clouds.

Figure 6.2 shows the spatial distribution of CH_4 annual mean all-sky SW tropopause IRF derived using MIPAS CH_4 mixing ratios. This distribution can be directly compared to Figure 5.10 which shows the equivalent forcing derived using CAM 3.0 CH_4 mixing ratio scale-heights. Notably, the forcing is negative (note the area with the lightest shading) over increased areas of North America, Eurasia, the equatorial oceans and Antarctica. The forcing still exceeds 0.20 W m^{-2} over a sizable region of the Sahara, emphasising that strong spatial gradients are driven by spectrally-resolved α_s over desert land surfaces; however, the spatial extent of this maxima is reduced.

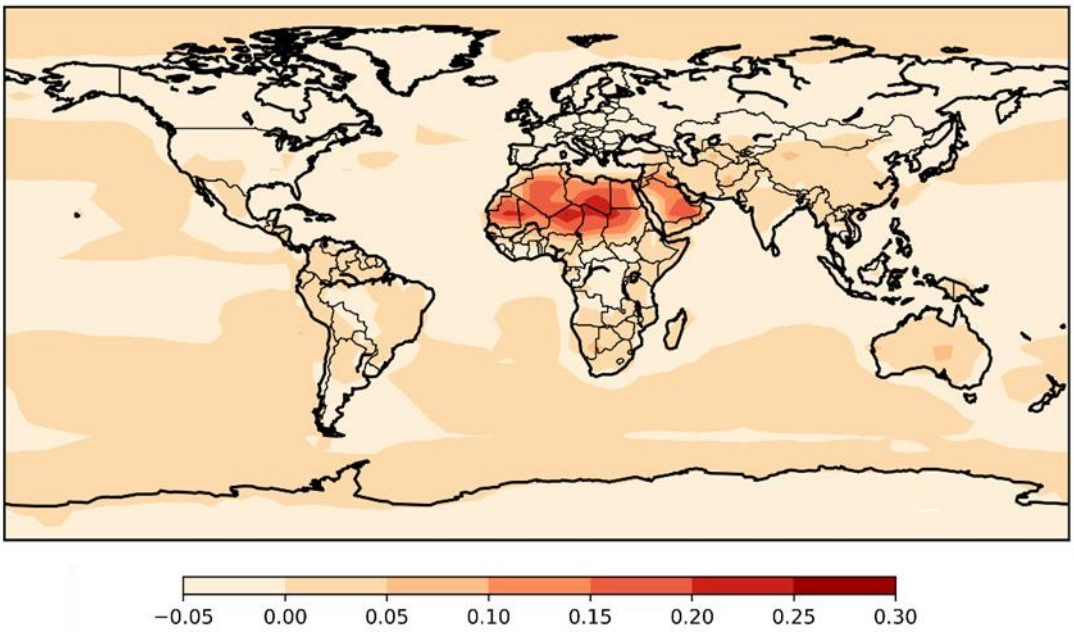

Figure 6.2: Global annual mean all-sky CH_4 SW tropopause IRF (W m^{-2}) following a perturbation in CH_4 from 750 ppbv to 1800 ppbv, derived using MIPAS CH_4 observational fields and SCIAMACHY-SSA α_s.

Figure 6.3 shows CRE on methane's all-sky SW tropopause IRF. This effect is positive over most of the Earth's surface with a local maximum as large as 0.1 W m^{-2} off the west coast of South America, associated with oceanic stratocumulus cloud decks. The presence of clouds across the Southern Ocean also contributes over 0.06 W m^{-2} to the SW forcing. This figure can be compared to Figure 2.14a, which shows CRE on the SW tropopause IRF of the Collins *et al.* (2018) using background climatology from the CSIRO Mk3-6-0 ESM. As stated in Section 2.3.2, Collins *et al.* (2018) report a maximum CRE of 0.068 W m^{-2}. Regions of maxima are more intense in the SOCRATES-RF estimate and much more marked over the southern oceans; this is consistent with the finding that clouds have a greater impact on the SW IRF compared to Collins *et al.* (2018). However, regions with low (< 0.01 W m^{-2}) or negative CRE are comparable, particularly across northern Africa, the Arabian Peninsula, Asia and Australia which exhibit relatively high NIR α_s (see Figure 2.13b).

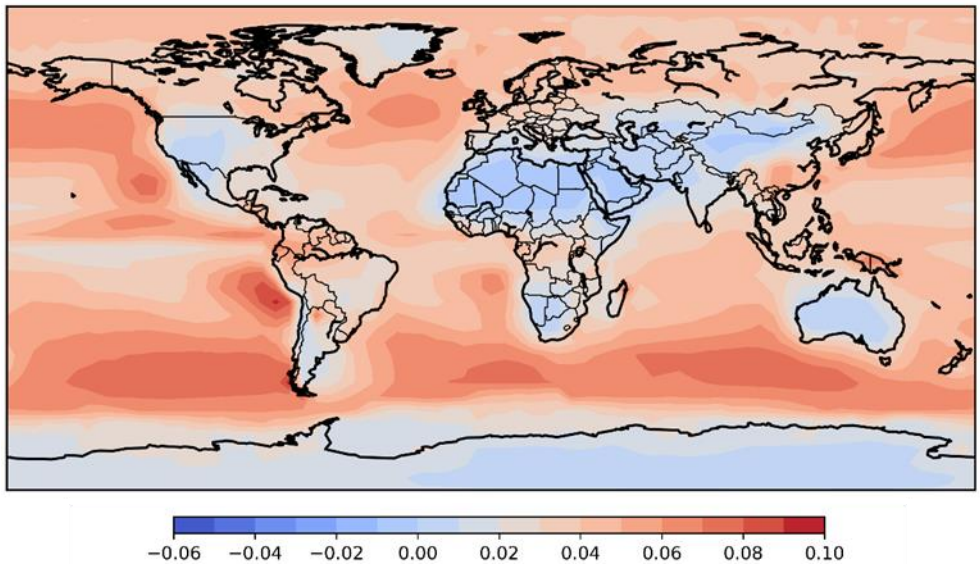

Figure 6.3: Cloud radiative effect (W m^{-2}) on CH_4 tropopause SW IRF calculated as the difference between all-sky and clear-sky conditions, following a perturbation in CH_4 from 750 ppbv to 1800 ppbv, derived using MIPAS CH_4 observational fields and SCIAMACHY-SSA α_s.

6.3 The impact of SW absorption on stratospheric temperature adjustment

As demonstrated by Etminan *et al.* (2016), and shown in Section 5.2, it is important to consider the impact of stratospheric CH_4 SW absorption in the calculation of methane's LW SARF. Methane's full SW effect can be quantified by comparing the net RF, calculated due to both SW and LW CH_4 absorption, against the net RF due to LW CH_4 absorption alone, in both cases after stratospheric temperature adjustment. Table 6.3 shows methane's all-sky tropopause SW IRF, LW SARF (whereby SW absorption is *included* in the FDH approximation), net RF (SW IRF plus LW SARF) and LW-only SARF (whereby SW absorption is *excluded* from the FDH approximation), following a perturbation from 750 ppbv to 1800 ppbv, calculated using MIPAS CH_4 mixing ratios.

	All-sky CH_4 RF (W m^{-2})			
	SW IRF	**LW SARF (incl. SW)**	**Net (SW + LW incl. SW)**	**LW-only SARF**
Tropopause	0.002	0.611	0.613	0.574

Table 6.3: Global annual mean all-sky CH_4 SW IRF, LW SARF (including SW heating rates in the FDH approximation) and LW-only SARF (excluding SW heating rates in the FDH approximation) following a perturbation in CH_4 from 750 ppbv to 1800 ppbv. Forcings are derived using MIPAS CH_4 mixing ratios and SCIAMACHY-SSA α_s

As shown, the SW IRF of 0.002 W m^{-2} accounts for only a small fraction (0.3%) of methane's net tropopause RF (0.613 W m^{-2}). However, when SW absorption is included in the calculation of stratospheric temperature adjustment, methane's SW effect increases the net forcing by 7% from the adjusted LW-only value of 0.574 W m^{-2} to 0.613 W m^{-2}. The difference between these two forcings (0.04 W m^{-2}) is 20 times larger than the SW IRF itself. This emphasises that methane's SW forcing should not be assessed by considering the impact on SW fluxes alone, especially also, considering that the tropopause forcing is a small residual of the upward and downward forcing components and is highly sensitive to the specification of CH_4 mixing ratio and α_S.

Figure 6.4 demonstrates the importance of including SW absorption in the FDH approximation. This plot compares the temperature difference (ΔT) following stratospheric temperature adjustment calculated using LW-only heating rates (upper panel) and LW plus SW heating rates (lower panel). Following a perturbation, the increase in stratospheric CH_4 concentrations leads to an increase in the emissivity of the stratosphere and increased absorptance of upwelling LW radiation from the troposphere, which act to cool and warm the stratosphere, respectively. The net effect of this depends on the effective emitting temperature of the troposphere and the vertical profile of stratospheric absorption and emission (Shine and Myhre 2020). A net cooling effect decreases emission of LW radiation downward to the troposphere, resulting in a reduction in the SARF relative to the IRF. A net warming effect increases LW emission to the troposphere, which enhances the SARF relative to the IRF. As shown in Figure 6.4 in the LW-only case (upper panel), the increase in stratospheric CH_4 concentrations leads to a cooling across most of the stratosphere, with a maximum ΔT > -0.2 K. A small warming effect is evident above the tropical tropopause; however, this does not counterbalance the increased emissivity of the stratosphere.

Thus, the adjustment process leads to a net cooling effect in the stratosphere, which has a small and negative impact on the LW IRF, decreasing by 0.7% from 0.578 W m^{-2} (Table 6.2) to 0.574 W m^{-2} (Table 6.3). When SW absorption is included in the FDH approximation, the cooling effect is reduced across the entire stratosphere and reverses the sign over much of the lower stratosphere, giving a strong warming with a maximum ΔT of 0.5 K above the tropical tropopause. As a result, the LW IRF increases by 6% from 0.578 W m^{-2} to 0.611 W m^{-2}.

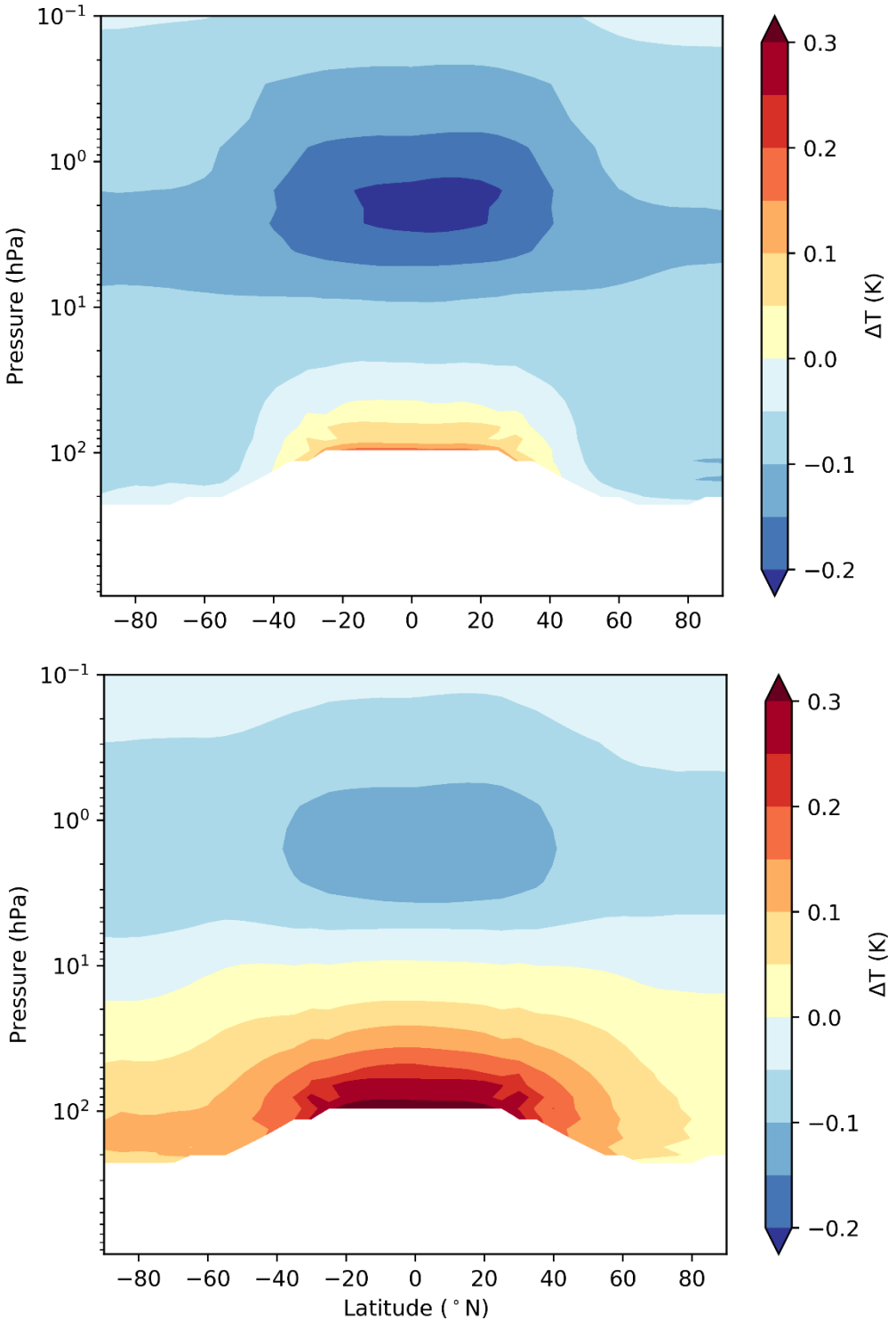

Figure 6.4: ΔT following stratospheric temperature adjustment calculated using LW-only heating rates (upper panel) and LW plus SW heating rates (lower panel) for a perturbation in CH_4 from 750 ppbv to 1800 ppbv. Small oscillations in ΔT occur near the tropopause when SW heating rates are included in stratospheric temperature adjustment, therefore data in the lower plot have been smoothed.

The ΔT reported here also shows consistency with the idealised experiments of Modak *et al.* (2018), who report that SW absorption causes stratospheric warming of around 0.8 K, peaking at 100 hPa for a 10 x increase in CH_4 surface mixing ratios (1796 ppbv). Although a ΔT of 0.5 K seems large, it must be remembered that this is the effect over more than 100 years, after perturbing CH_4 from preindustrial (1750) to present day (2011) levels. Maycock *et al.* (2018) report typical observed lower stratosphere cooling of -0.2 to -0.4 K decade^{-1} between 1979 and 2005. The warming presented here is of order 0.05 K decade^{-1} (if occurred at a constant rate), however the rate is likely larger in the more recent period of the observational record, given that increases in CH_4 have risen more sharply over the past few decades (e.g. Saunois *et al.* 2016). Considering this, the CH_4 warming effect will have counteracted a small but non-negligible amount (possibly 0.1 K decade^{-1}) of the cooling driven by other causes, such as O_3 depletion and increases in stratospheric H_2O.

As previously mentioned, methane's total SW effect increases the net forcing by 7% from the adjusted LW-only value of 0.574 W m^{-2} to 0.613 W m^{-2}. This is smaller than the total CH_4 SW effect of 15% reported by Etminan *et al.* (2016). The difference between these estimates is largely explained by the substantial difference in the magnitude of the SW tropopause IRF (0.002 W m^{-2} compared to 0.03 W m^{-2}). However, it is also dependent on the magnitude of stratospheric temperature adjustment. Etminan *et al.* (2016) find this process has a slightly larger negative effect on their estimate of methane's LW IRF, decreasing by 2% from 0.516 W m^{-2} to 0.504 W m^{-2}. Considering the total SW CH_4 effect is measured relative to adjusted LW-only SARF, this yields a larger percentage increase from their LW-only SARF (0.504 W m^{-2}) to their net RF (0.582 W m^{-2}). This shows that in addition to the sensitivities addressed in Chapter 5, the total CH_4 SW effect is also dependent on state variables that affect the LW forcing and the adjustment process, such as temperature, humidity and clouds. Uncertainties associated with the adjustment approximation are discussed in Chapter 7.

Figure 6.5 (upper panel) shows the spatial distribution of methane's net tropopause RF (i.e. the LW SARF (including SW heating rates in the FDH approximation) plus the SW IRF). As shown in Table 6.3, this equates to a global-mean net RF of 0.613 W m^{-2}. Figure 6.5 (lower panel) shows the spatial distribution of methane's LW-only SARF. As shown in Table 6.3, this equates to a global-mean SARF of 0.574 W m^{-2}. Figure 6.6 shows the corresponding difference between methane's net tropopause RF and the LW-only SARF (i.e. Figure 6.5 upper panel – Figure 6.5 lower panel). This figure presents the first spatially-resolved calculation of the total effect of the SW bands on methane's net RF (to the author's knowledge), since this reveals not only the direct impact of the SW bands but also the effect of the SW bands on stratospheric temperature adjustment.

The inclusion of SW bands increases the magnitude of the net RF largely across the entire globe. Regional enhancements to the LW-only SARF are evident over areas with low high cloud cover for example, across the southern Pacific, Atlantic and Indian Oceans. Marked increases in the net RF (between 0.15 and 0.30 W m^{-2}) are evident across the Sahara and Arabian Peninsula, collocated with areas of maxima in the SW tropopause IRF (see Figure 6.2). Further notable increases (between 0.05 and 0.10 W m^{-2}) are evident across the north Pacific and Australia, and also, across the Southern Ocean, where the presence of clouds enhances the SW IRF by over 0.06 W m^{-2} (see Figure 6.3). Regional distributions of RFs could be important for climate response (e.g. Shindell and Faluvegi 2009; Shindell *et al.* 2010), however, further investigation of this would require the use of an ESM. As discussed in Section 4.3, there is serious uncertainty surrounding the current ability of ESM codes to accurately resolve methane's SW forcing. Whilst some ESM codes do now include methane's SW absorption in parameterisations (e.g. Smith *et al.* 2018), the low spectral resolution of their SW spectrum is unlikely to fully capture the effect of CH_4.

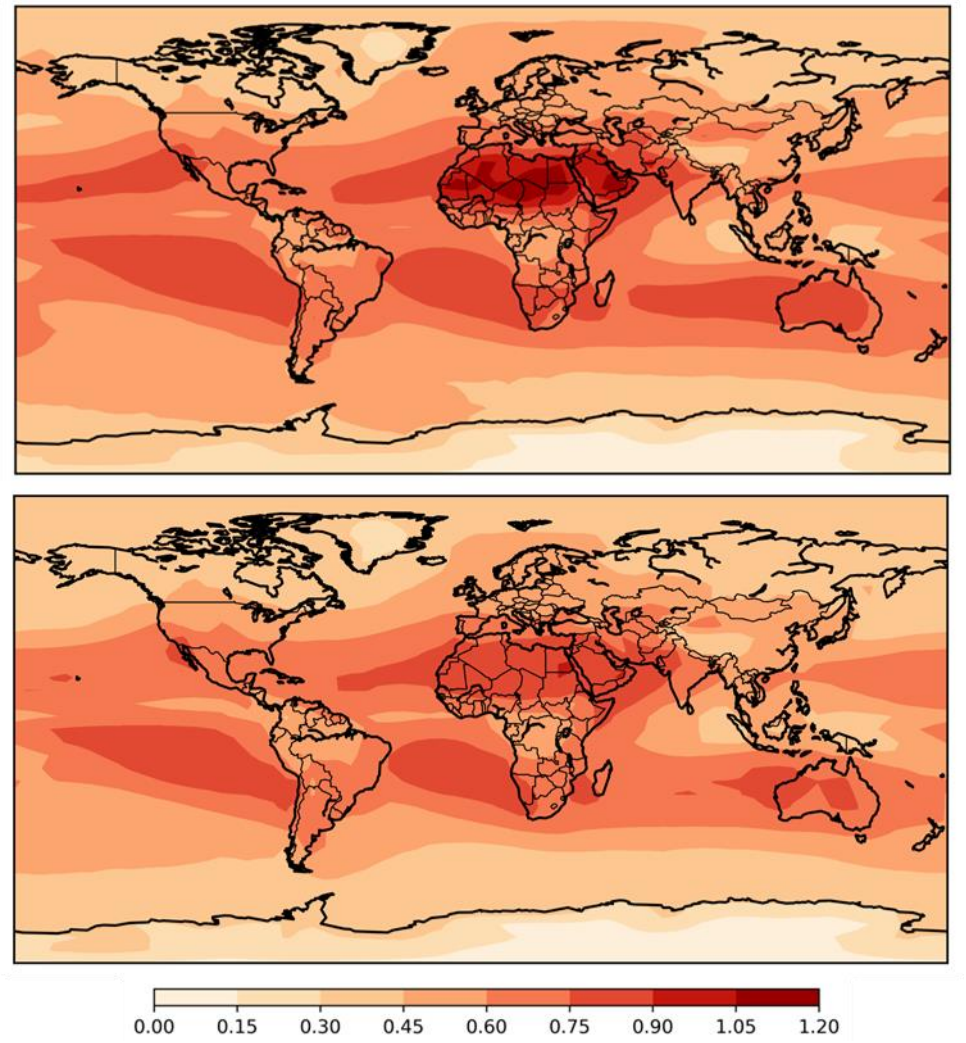

Figure 6.5: Upper panel: Global annual mean all-sky CH_4 net RF (i.e. LW SARF (including SW in FDH approximation) + SW IRF) (W m^{-2}) following a perturbation in CH_4 from 750 ppbv to 1800 ppbv, derived using MIPAS CH_4 observational fields and SCIAMACHY-SSA α_s.

Lower panel: Global annual mean all-sky CH_4 LW-only SARF (W m^{-2}) following a perturbation in CH_4 from 750 ppbv to 1800 ppbv, derived using MIPAS CH_4 observational fields and SCIAMACHY-SSA α_s.

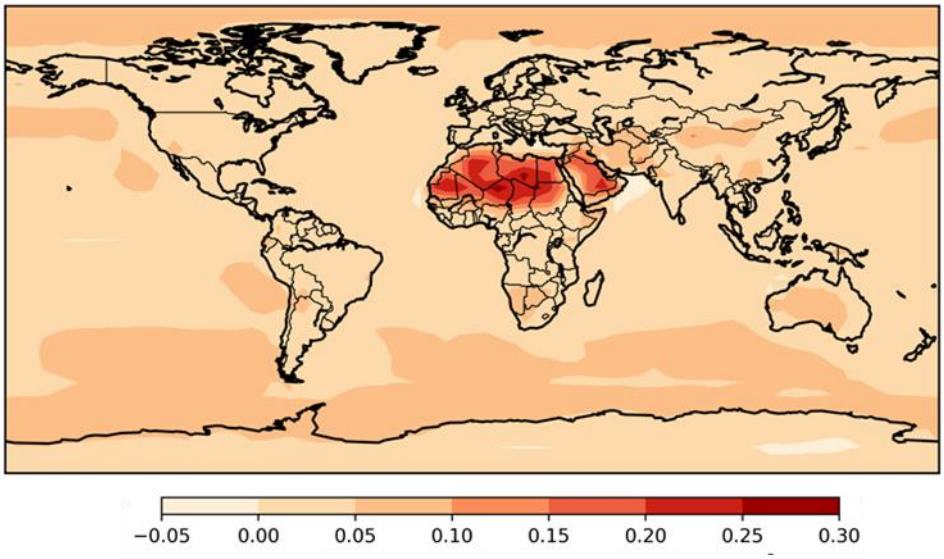

Figure 6.6: Difference (in W m^{-2}) between the lower panel and upper panel of Figure 6.5 (i.e. Net RF – LW-only SARF). This shows the total effect of methane's SW absorption bands on global annual mean all-sky CH_4 net RF following a perturbation in CH_4 from 750 ppbv to 1800 ppbv, derived using MIPAS CH_4 observational fields and SCIAMACHY-SSA α_s.

Conceptual understanding of methane's SW RF

A more robust estimation of methane's SW radiative effect is achieved by accounting for the impact of the SW absorption bands on stratospheric temperature adjustment. As stated in Section 2.3, the calculation of SARF provides a better indication of ΔT_S and, by definition, yields an identical net forcing at both the TOA and tropopause (although the partitioning of the net forcing between SW and LW differs, see Table 6.4 which shows methane's all-sky tropopause SW IRF, LW SARF and Net RF at the TOA and tropopause). It is interesting to note that a more consistent view of methane's SW radiative effect can be found using a TOA perspective; the experiments presented throughout this thesis have demonstrated that methane's SW TOA IRF displays significantly less sensitivity to the range of factors that considerably influence the magnitude of the SW tropopause IRF. For example, Table 5.2, Table 5.17 and Table 6.2 show that methane's SW tropopause IRF varies by a factor of 8 between different experiments (from 0.016 W m^{-2} to 0.002 W m^{-2}), whilst the TOA IRF varies by around only 10% (from 0.090 W m^{-2} to 0.080 W m^{-2}). Because the SW TOA IRF is larger than the SW tropopause IRF (because it is not subject to cancellation between the changes in the upward and downward irradiances), the convergence of SW radiation across the stratosphere (TOA minus

tropopause IRF), which drives the stratospheric temperature adjustment, is also relatively less sensitive (around 20% variation) than the tropopause IRF (Shine *et al. in prep.*). Thus, the TOA is a beneficial level at which to estimate methane's SW forcing, providing a more robust view of the sign and magnitude of the forcing in a more consistent perspective with the ERF framework, which does not require the definition of a tropopause at all.

	All-sky CH_4 RF (W m^{-2})		
	SW IRF	**LW SARF**	**Net RF**
TOA	0.082	0.530	0.613
Tropopause	0.002	0.611	0.613

Table 6.4: Global annual mean all-sky CH_4 SW IRF, LW SARF (including SW heating rates in the FDH approximation) and net RF following a perturbation in CH_4 from 750 ppbv to 1800 ppbv at the tropopause and TOA. Forcings are derived using MIPAS CH_4 mixing ratios and SCIAMACHY-SSA α_s

6.4 Sources of uncertainty

Given that the total radiative impact of methane's SW bands is quantified by both the direct SW IRF and the impact on LW SARF, it is essential to consider sources of error that affect both SW and LW forcings. Prior literature has predominantly focussed on assessing sources of uncertainty with respect to WMGHG LW forcings. Discussion of uncertainty related specifically to WMGHG SW forcings is more limited. Hence, the following assessment draws on a range of previous research and subjective judgement to determine a measure of uncertainty for methane's SW radiative effect calculated using the root-sum-square method.

A range of factors contribute to uncertainty in RF estimates. Largely, these are related to the robustness of spectroscopic data, the choice of radiative transfer scheme, methods of calculation, and the specification and averaging of atmospheric conditions. Assessment of the impact of HITRAN updates on LW forcings (e.g. Kratz 2008) and spectroscopic parameter uncertainty (specifically in the case of CO_2; Mlynczak *et al.* 2016) are shown to contribute a small fraction to RF uncertainty, at less than 1%. Whilst the most recent update to the HITRAN database (HITRAN2016; Gordon *et al.* 2017) provides a renewed assessment of the vibrational-rotational bands contributing to methane's NIR line intensity, Section 3.3 demonstrates that CH_4 SW IRFs differ by less than 1% when derived using HITRAN2012 and HITRAN2016 data. In line with the evidence of Kratz (2008) and Mlynczak *et*

al. (2016) spectroscopic uncertainty is therefore assessed to contribute 1% to the total uncertainty of methane's SW radiative effect.

Multi-model intercomparison studies provide a useful basis from which to assess uncertainty in the type of radiative transfer scheme used in forcing calculations (e.g. Halthore *et al.* 2005; Collins *et al.* 2006b; Forster *et al.* 2011; Oreopoulos *et al.* 2012; Pincus *et al.* 2015). Nevertheless, there is lack of research comparing the performance of broad-band radiative transfer codes against reference LBL calculations specifically for CH_4 SW forcings, largely because many ESM radiation codes have historically omitted explicit treatment of CH_4 SW absorption. Collins *et al.* (2006b) compare results from several LBL models against the majority of ESM radiation codes included in IPCC AR4 and report that ESMs systematically underestimate the magnitude of SW forcings at the TOA, tropopause and surface because CH_4 SW absorption is not included in radiative transfer parameterisations. The importance of CH_4 SW absorption has been emphasized following Etminan *et al.* (2016) and Collins *et al.* (2018), leading to increased recognition that its exclusion will result in erroneous forcing estimates and spurious assessments of the sign and magnitude of rapid adjustments related to CH_4 RF (Smith *et al*. 2018). Hogan and Matricardi (2020) also report an underestimation of CH_4 SW IRF by 25 – 45% by the Rapid Radiative Transfer Model for General Circulation Models (RRTMG) (Mlawer *et al.* 1997) code against benchmark calculations, for a range of perturbations across 350 ppbv to 3500 ppbv. However, a multi-model intercomparison of methane's SW effect has not yet been published (to the author's knowledge); such a study would deliver a much needed indication of the accuracy of ESM radiation schemes in comparison to LBL codes.

As stated in Section 3.1.4, this thesis uses a narrow-band (260 band) version of SOCRATES to calculate SW irradiances across 0.17 – 10 μm. Originally generated to aid offline UM diagnostics, Walters *et al.* (2019) report that this code has been validated against independent LBL models, however the exact nature and scope of this validation is not made clear. Thus, the radiative transfer code intercomparison presented in Chapter 4 forms the basis of the assessment of uncertainty related to SOCRATES' ability to accurately resolve CH_4 SW spectral characteristics. This work demonstrates that the 260-band version of SOCRATES can estimate methane's SW tropopause IRF with a mean error of 8% across each solar zenith angle and MLS, TROP and SAW atmospheres. Pincus *et al.* (2015) also report that this configuration agrees quite well with reference LBL models and furthermore, it serves as a benchmark model in Pincus *et al.* (2020), providing computations of clear-sky IRFs due to a perturbation in CH_4 from 722 ppbv to present day levels.

For reasons of computational cost, LW irradiances are calculated at a lower spectral resolution than the SW, using a broad-band version of SOCRATES with 9 bands across 3.34 – 10000 μm. Given that

this thesis focuses on the calculation of CH_4 SW forcings, Chapter 4 did not provide an assessment of this code against reference LBL calculations. However, as described in Section 3.1.5, this spectral file is demonstrated to calculate CH_4 LW IRF to within 2% of the 300-band reference configuration of SOCRATES' LW spectral file (which is reported to have been validated against independent LBL codes; Walters *et al.* (2019)). The intercomparison study of Collins *et al.* (2006b) and Forster *et al.* (2011) show larger differences between LW WMGHG forcings calculated by various ESM radiation codes, and between ESM codes and LBL calculations. For a CH_4 perturbation from 806 ppb to 1760 ppb under clear-sky conditions and at a solar zenith angle of 53°, Collins *et al.* (2006b) report a standard deviation of about 30% of the mean of an ensemble of ESM LW forcings, and a 6% difference between the ESM ensemble mean and LBL ensemble mean. Considering prior research and the asserted validation of both the 6-band and 300-band versions of SOCRATES LW spectral file (Walters *et al.* 2019) uncertainty associated with the LW radiation scheme is assessed to be 6%.

Hodnebrog *et al.* (2013; 2020) provide a detailed discussion of uncertainty in RF calculations based on a multitude of previous studies. The authors examine this research to assess uncertainty related specifically to halocarbon RF, however, their discussion can be used more generally to assess error in other WMGHG forcing calculations and is used here to quantify the following uncertainties: the calculation of FDH (4%), atmospheric temperature (3%) and clouds (5%) and spatial and temporal averaging (1%). Another key factor affecting the estimation of RF is the specification of tropopause height. As highlighted in Section 3.5, several studies demonstrate the impact of alternative tropopause definitions (e.g. Myhre and Stordal 1997; Freckleton *et al.* 1998; Forster *et al.* 2005). Freckleton *et al.* (1998) investigate the impact of three different tropopause definitions on CO_2 and CFC-12 SARF, namely: 1). the 'conventional' thermal tropopause, defined by the WMO (1986) as the lowest level where the temperature lapse rate between this level and all higher levels within 2 km falls to, or below, 2 K km^{-1} 2). the temperature minimum, i.e. where the temperature lapse rate changes sign, and 3). where there is a significant change in stability in the atmospheric profile occurring below the conventional thermal tropopause. The author's report that SARF (calculated using three atmospheric profiles from each hemisphere) is sensitive to tropopause definition, with forcings varying by 4% and 6% for CO_2, under clear-sky and all-sky conditions respectively, and by 8% and 9% for CFC-12. However, the author's also note that forcings are sensitive to the latitudinal resolution of atmospheric profiles as the temperature profile, and hence tropopause height, are affected by spatial averaging. Hodnebrog *et al.* (2013) assess uncertainty related to tropopause height in total halocarbon RF to be slightly lower, at around 5%. Here, this uncertainty is assessed to be 8% for CH_4 SW tropopause IRF and 5% for CH_4 LW SARF. A higher uncertainty is attributed to

SW calculations owing to the particular sensitivity of CH_4 tropopause SW IRF to the magnitude of the upward and downward SW forcing components.

As noted by Etminan *et al.* (2016), error sources for calculating SW forcings extend more specifically to the specification of α_s, aerosol concentration and the integration over the day to produce a day-averaged forcing. As discussed in Section 5.4.2, the method used to interpolate and extrapolate SCIAMACHY data to the upper waveband limits in SOCRATES-RFs SW spectral file is idealised, owing to a lack of global datasets that extend across the 0.17 – 10 μm range. It is appreciated that this introduces further uncertainty on the SW forcings calculations presented in this chapter. Subsequently, an uncertainty of 20% is attributed to the use of SCIAMACHY-SSA α_s. Furthermore, idealised tests demonstrate significant sensitivity of CH_4 SW IRF to the representation of H_2O continuum absorption, as modelled by MT_CKD version 2.5 with modifications in the NIR window regions using CAVIAR data. Running SOCRATES-RF with and without H_2O continuum absorption for an all-sky CH_4 perturbation from 750 ppbv to 1800 ppbv for January resulted in a 150% difference in methane's SW tropopause IRF (comparing 0.002 W m^{-2} when continuum absorption is included and 0.005 W m^{-2} when continuum absorption is omitted), but this was for an extreme case with complete removal of the continuum. Uncertainty in MT_CKD self-continuum in the 2.1 μm and 4 μm window regions has also been noted by J. Elsey and K. P. Shine due to increased understanding of CAVIAR-lab measurements (SOCRATES water vapour self-continuum changelog, 2020). An initial sensitivity test conducted by SOCRATES-RF using a modified version of the sp_sw_260_jm2 spectral file (with weaker H_2O continuum across the 2.1 μm window) resulted in a 5% difference in January, clear-sky CH_4 tropopause SW IRF (for a perturbation from 750 ppbv to 1800 ppbv) compared to an equivalent experiment conducted using sp_sw_260_jm2. Following this, uncertainty in the specification of H_2O continuum is assessed to contribute 5% to CH_4 SW IRF. Further experiments (particularly under all-sky conditions) would provide a better constraint on this source of error. Similarly, the specification of H_2O fields adds further uncertainty to CH_4 SW forcings. As highlighted by Etminan *et al.* (2016), the magnitude of methane's SW IRF is dependent on the degree of spectral overlap with H_2O. Chapter 4 demonstrates this is particularly important in relatively moist MLS and TROP atmospheres at the surface; here, error in the estimation of clear-sky CH_4 SW IRF by SOC(260) ranges between 12% to 26% in higher θ cases when H_2O, CO_2 and N_2O are included in forcing calculations. When these gases are omitted from calculations, errors at the surface are reduced to below 4% (see Section 4.3.1 and Section 4.3.2). Arguably, such error could be attributed to spectral overlap with CO_2 and N_2O, however, as previously mentioned, initial testing (not shown) demonstrates definitely that H_2O has the greatest effect on CH_4 SW IRF. Whilst the calculation of daily-average forcings should reduce the impact of such errors found in moist atmospheres with

high θ, these experiments demonstrate the significance of high H_2O concentrations on surface CH_4 SW IRF in particular. Tropopause CH_4 SW IRFs show less sensitivity to H_2O spectral overlap as stratospheric concentrations of H_2O are low. Omitting H_2O, CO_2 and N_2O from calculations in Chapter 4 impacts the magnitude of CH_4 SW tropopause IRF by less than 1% (comparing Table 4.3 and Table 4.5). Collins *et al.* (2018) use atmospheric fields from two different ESMs, CSIRO Mk3-6-0 and INMCM4 (see Section 2.3.2), in their MODTRAN calculations of spatially-resolved, monthly-mean CH_4 SW tropopause IRF. This provides further opportunity to assess error induced by the choice of background climatology, and hence the specification of H_2O fields. As shown in Table 2.3, the choice of atmospheric input influences the magnitude of CH_4 SW tropopause IRF, resulting in forcings that differ by 32% (under clear-sky conditions) and 4% (under all-sky conditions). As all SOCRATES-RF calculations throughout this thesis utilise monthly-mean ERA-interim reanalysis H_2O fields (see Section 3.1.5), it would be beneficial to conduct identical forcing calculations with an alternative dataset of H_2O concentrations to further constrain this source of error in SOCRATES-RF estimations. Here, uncertainty related to H_2O fields is assessed to contribute ±2% to the total uncertainty in all-sky CH_4 SW tropopause IRF and LW SARF.

Finally, considering the sensitivity of CH_4 SW IRF to the specification of a vertically-varying profile, an uncertainty of 5% is attributed to the use of MIPAS CH_4 climatology based on the standard deviation of multi-instrument spread in CH_4 measurements across the upper-troposphere, lower stratosphere and middle stratosphere regions reported by Hegglin *et al.* (2021). A lower uncertainty of 2% is attributed to the use of MIPAS CH_4 climatology in CH_4 LW SARF, as the calculation of LW SARF is not significantly dependent on the vertical representation of CH_4 mixing ratios. As demonstrated in Section 5.2.1, CH_4 LW SARF calculated using 'Constant' and 'CAM 3.0' mixing ratios differ by just 1.8% (see Table 5.4).

Table 6.5 lists each source of uncertainty and their estimated contribution to total uncertainty in the calculation of CH_4 SW tropopause IRF and CH_4 LW SARF. These estimates are based on previous literature and the discussion given above. Using the root-sum-square method, a total uncertainty of ±12% is attributed to CH_4 LW SARF and a total uncertainty of ±25% is tentatively attributed to CH_4 SW tropopause IRF. This is the same as the ±25% uncertainty estimated by Etminan *et al.* (2016) in their calculation of CH_4 SW tropopause IRF. However, given the highly sensitive nature of CH_4 SW tropopause IRF as demonstrated throughout this thesis, it is apparent that Etminan *et al.*'s estimation of uncertainty at ±25% is too low.

In total, given that the CH_4 SW effect is about 6% of the net CH_4 RF of 0.613 W m^{-2} (including its contribution to LW SARF, i.e. increasing the LW-only SARF from 0.574 W m^{-2} to 0.611 W m^{-2}, see Table 6.3), this yields a total uncertainty of around ±13% in the net CH_4 RF.

Source of Uncertainty	**Estimated Contribution to SW Uncertainty**	**Estimated Contribution to LW Uncertainty**
Spectroscopic parameters	1%	1%
SW radiation code	8%	-
LW radiation code	-	6%
H_2O continuum	5%	Not assessed
FDH calculation	4%	4%
Tropopause level	8%	5%
Atmospheric temperature	3%	3%
Clouds	5%	5%
H_2O field	2%	4%
Spatial and temporal averaging	1%	1%
MIPAS CH_4 mixing ratios	5%	2%
SCIAMACHY-SSA α_s	20%	-
Total uncertainty	**25%**	**12%**

Table 6.5: Sources of uncertainty and their estimated contribution to total uncertainty in Chapter 6 estimates of CH_4 SW tropopause IRF and CH_4 LW SARF. The total uncertainty is also shown and is calculated using the root-sum-square method. See text for references used as basis for uncertainty estimates.

6.5 Chapter conclusions

This chapter has presented a best estimate of methane's total shortwave radiative effect, which considers both the direct SW IRF and the effect of SW absorption on the stratospheric temperature adjusted LW forcing. Given the limitations of earlier studies, it is argued that this is the most advanced estimate of methane's SW effect now available.

To summarise, the key findings are:

- Methane's SW tropopause IRF is estimated to be 0.002 W m^{-2}. This is significantly smaller than previous estimates due to the combination of factors including SW CH_4 absorption between 5 – 10 µm, a more highly resolved description of α_s and satellite-derived stratospheric CH_4 mixing ratios. Each of these factors alter the size of the downward and upward shortwave forcing components at the tropopause. Consequently, the tropopause IRF is demonstrated to be a relatively small residual of these compensating terms.

- Methane's SW effect cannot be considered by the magnitude of the tropopause IRF alone. CH_4 SW absorption plays an important role in stratospheric temperature adjustment and causes the LW IRF to increase by 6% from 0.578 W m^{-2} to 0.611 W m^{-2}. In total, CH_4 SW absorption increases the net forcing by 7% from the adjusted LW-only SARF value of 0.574 W m^{-2} to 0.613 W m^{-2}.

- A total uncertainty of ±12% and ±25% is attributed to CH_4 LW SARF and CH_4 SW tropopause IRF, respectively. Conducting additional calculations with alternate fields of H_2O, vertically-varying mixing ratios, spectrally-varying α_s and alternate definitions of tropopause height would provide a better constraint on uncertainty related to CH_4 SW tropopause IRF. As the CH_4 SW effect is about 6% of the net CH_4 RF (including its contribution to LW SARF), a total uncertainty of around ±13% is attributed to net CH_4 RF.

Chapter 7

Conclusions and Future Work

7.1 Introduction

This chapter presents the main conclusions from Chapters 4, 5 and 6. The final section explores possible avenues of future research that could improve and extend the findings of this thesis.

7.2 Conclusions

7.2.1 Chapter 4: The ability of SOCRATES

Chapter 4 presents a radiative transfer code intercomparison between both a 6-band (SOC(6)) and 260-band (SOC(260)) version of SOCRATES and the reference LBL model, the RFM. This work was essential to evaluate if SOCRATES' parameterisation of radiative transfer can calculate methane's SW IRF at the tropopause and surface to within 10% error of the RFM.

It was shown that SOC(6) significantly underestimates the magnitude of methane's SW tropopause and surface IRF by around 45%, and hence, is not suitable for quantifying the effect of CH_4 SW absorption bands on RF. Subsequently, an ESM using this code (as currently parameterised) would not be able to fully resolve the radiative impact of changes in CH_4 concentrations. This low spectral resolution version of SOCRATES was not considered further in this thesis.

SOC(260) is able to calculate methane's SW IRF to within 10% at the tropopause, however, surface errors are much larger (12% to 26%) for higher solar zenith angles (53° and 75°) using MLS and TROP profiles. The magnitude of surface errors are greatly reduced (to < 5%) in experiments conducted using a CH_4-only atmosphere. This vast improvement indicates that SOC(260) struggles to handle the spectral overlap of CH_4 and H_2O in relatively moist atmospheres. Further analysis of the treatment of gaseous spectral overlap between CH_4 k-terms and H_2O k-terms is needed to identify how this code may be improved with respect to the calculation of CH_4 surface forcings. However, the calculation of daily-averaged forcings should reduce the impact of errors found at higher solar zenith angles in simulations that include relatively high mixing ratios of H_2O. Furthermore, given that the primary focus of this thesis relates to tropopause forcings, SOCRATES was judged to be suitable to perform the calculations required in this thesis.

Further analysis of SW IRF per spectral region within the 0.87 - 10 µm range demonstrates that compensation of errors takes place to achieve the forcings that are within 10% when the full 0.87 - 10 µm range is used. A notable error of around 16% is found across the 1.6 - 2.02 µm spectral range at the tropopause, which is not diminished when H_2O is excluded from calculations. Here SOC(260) underestimates the magnitude of CH_4 SW IRF in comparison to the RFM. Since this spectral region plays a key role in determining the size and sign of methane's SW forcing this error potentially significant. As explained in Section 4.4.2, increasing the number of k-terms in this spectral region would more accurately characterise CH_4 absorption and the change in irradiance due to a perturbation in gas concentration.

7.2.2 Chapter 5: Sensitivities of methane's SW RF

Chapter 5 presents the first detailed investigation into key sensitivities that effect methane's SW radiative impact, focussing specifically on the representation of methane's vertical profile, the effect of CH_4 absorption of solar mid-infrared irradiance between 5 – 10 µm and the specification of α_s. This work offers a significant update to the sensitivity tests performed by Etminan *et al.* (2016) and provides an important discussion of the estimates of methane's tropopause SW IRF given by Etminan *et al*. (2016) and Collins *et al.* (2018).

A realistic representation of methane's vertical profile is essential in achieving an accurate quantification of the global-mean SW IRF. Given the impact of SW absorption on the stratospheric-temperature adjusted forcings, it is also important in the calculation of methane's global-mean LW SARF and net RF.

Methane's forcing across the solar mid-infrared at 7.7 μm plays a significant role in determining the magnitude of the tropopause SW IRF, due to enhanced absorption in the stratosphere, and hence, a strengthening of the negative forcing component. Under all-sky conditions CH_4 absorption across 5 – 10 μm reduces the magnitude of the positive tropopause forcing by 25%. This result is significant and highlights the importance of including solar mid-infrared absorption in calculations of methane's forcing. Neither Etminan *et al.* (2016) or Collins *et al.* (2018) accounted for CH_4 absorption of solar mid-infrared irradiance, therefore their estimates of the SW forcing do not encapsulate the full spectral range of CH_4 SW radiative effects.

Methane's SW tropopause forcing is considerably sensitive to the specification of spectrally-varying α_s. This sensitivity is largest under clear-sky conditions; however, all-sky conditions also show significant sensitivity. The use of spectrally-varying SCIAMACHY-SSA α_s reduces the all-sky tropopause SW IRF by 44% compared to the equivalent calculation conducted using spectrally-constant ERA-interim albedo fields.

7.2.3 Chapter 6: Best estimate of the impact of methane's SW bands on RF

Methane's SW tropopause IRF is estimated to be 0.002 W m^{-2}. This is considerably smaller than previous estimates due to the combination of factors including SW absorption between 5 – 10 μm, a highly resolved description of α_s and satellite-derived stratospheric CH_4 mixing ratios. As demonstrated throughout Chapter 5 and Chapter 6, each of these factors alter the size of the downward and upward shortwave forcing components at the tropopause, and consequently, the tropopause IRF is demonstrated to be a relatively small residual of these compensating terms.

This work also demonstrates that methane's SW effect cannot be considered by the magnitude of the tropopause IRF alone. CH_4 SW absorption plays an important role in stratospheric temperature adjustment and causes the LW IRF to increase by increases by 6% from 0.578 W m^{-2} to 0.611 W m^{-2}. In total, CH_4 SW absorption increases the net forcing by 7% from the adjusted LW-only value of 0.574 W m^{-2} to 0.613 W m^{-2}.

7.3 Future work

- **Impact of aerosol concentrations on global-mean and spatially resolved SW forcing.** This thesis did not examine the sensitivity of methane's SW forcing to aerosol concentration and specification. However, the inclusion of aerosol would likely increase planetary albedo, and hence the amount of reflected SW radiation available for CH_4 absorption. Etminan *et al.* (2016) did include present-day and anthropogenic aerosol from the OsloCTM2 simulations for AeroCom Phase II (Myhre *et al.* 2013b) in their calculation of methane's SW radiative effect. Including such aerosol specification in SOCRATES-RF experiments (and comparing these results to those presented in this thesis) would allow for a quantification of the impact of aerosol on the CH_4 radiative effect presented here and provide a further means of comparison against Etminan *et al.* (2016).

- **Update to water vapour continua.** The current version of the H_2O continuum used in SOCRATES-RF exhibits too strong self-continuum absorption across the 2.1 μm and 4 μm window regions (SOCRATES water vapour self-continuum changelog, 2020). Implementing the improved and recently updated "Elsey-Shine" continuum into SOCRATES-RF (that incorporates weaker H_2O self-continuum absorption across the 2.1 μm window) is necessary to determine the effect of erroneous self-continuum absorption on methane's SW IRF. Considering CH_4 has an important NIR band at 2.3 μm, this effect may be non-negligible.

- **Update to Etminan *et al.* (2016) simplified expression for CH_4.** This thesis did not provide an update to methane's simplified expression based on the reduced impact of methane's SW radiative effect reported in this thesis. Updating this expression would require calculating forcings over a wider range of CH_4 concentration changes (along with N_2O to account for the effects of spectral overlap), including those relevant to palaeoclimate and future climate scenarios. Updating this expression would also allow for a re-estimation of the impact of methane's SW radiative effect on historical and future forcing estimate and crucially, emission metrics for CH_4.

- **RF calculations using a higher spectral resolution LW code.** All LW calculations in this thesis are conducted using SOCRATES-RF configured with a 9-band sp_lw_ga7 spectral file. As stated in Section 3.1.4, a higher resolution 300-band version of this spectral file is available,

generated for model validation purposes to aid offline UM diagnostics. To balance the need for computational efficiency and accurate results, experiments shown in Section 3.1.5 demonstrate that the 9-band spectral file is able to adequately simulate methane's LW IRF at sufficient accuracy when gaseous overlap is treated using the more accurate 'random overlap' assumption. However, conducting forcing calculations using the 300-band spectral file would increase confidence in SOCRATES-RF's ability to simulate CH_4 LW IRFs and SARFs.

- **The contribution of methane's SW forcing to CH_4 ERF.** This would require the use of an ESM to calculate rapid adjustments related to CH_4 SW forcing. It would be essential to validate the ESM radiation code against more sophisticated radiative transfer models to examine the accuracy of CH_4 SW treatment. Smith *et al.* (2018) demonstrate that the inclusion or omission of methane's SW bands dictates the magnitude of H_2O adjustment and whether stratospheric-temperature and cloud adjustments have a negative or positive effect on CH_4 forcing. Motivated by this result, it would therefore be interesting to examine these adjustments in further detail, to understand the extent to which each are dependent on CH_4 SW absorption and also, which of the rapid adjustments are most important for this forcing. The use of an ESM would also allow for further analysis of the impact of methane's surface SW forcing on surface energy budget components. As noted in Section 6.2, methane's global annual mean SW surface IRF (-0.235 W m^{-2}) counterbalances the LW surface IRF (0.306 W m^{-2}), leaving a residual net forcing of just 0.071 W m^{-2} (see Table 6.1). Further analysis is needed to examine how this could affect the global hydrological cycle.

- **Detecting methane's SW RF from high-spectral resolution measurements at the surface and TOA.** Various studies have attempted to use satellite observations to infer GHG forcings, so far concentrating mostly on the LW (e.g. Harries *et al.* 2001; Feldman *et al.* 2015; Feldman *et al.* 2018; Whitburn *et al.* 2020). These studies provide experimental evidence of the influence of increases in GHGs on the Earth's energy balance. Such analysis could be extended to the CH_4 SW radiative effect using satellite observational records and ground-based instrumentation to test whether the impact of increasing CH_4 concentrations on upwelling/downwelling SW radiation can be detected.

- **Assessment of how methane's SW (and also LW) RF might change in the future.** Climate change induced alterations to the background state of the atmosphere and surface (e.g.

changing H_2O amounts, cloud cover, atmopsheric temperature, surface albedo) could affect the magnitude of both methane's SW and LW forcing. Section 5.4 demonstrates the highly sensitive nature of the SW tropopause IRF to surface albedo specification, a parameter which inevitably is affected by human-induced changes in land cover, which can alter the roughness, reflectivity and emissivity of surfaces. As discussed in Section 5.4.2, estimates of methane's SW tropopause IRF also exhibit sensitvity to cloud radative effects, which differ considerably between the SOCRATES-RF estimate, Etminan *et al.* (2016) and Collins *et al.* (2018). Long-term changes in cloud cover could therefore alter the magntiude of methane's SW IRF.

- **A more systematic evaluation of uncertainty related to methane's SW forcing**. Calculating methane's SW radiative effect using a range of background climatologies from other re-analysis and observational datasets would allow for a more comprehensive evaluation of how interannual variations in the background atmospheric state impact the forcing. This would also allow for an evaluation of how different H_2O fields impact the calculation of CH_4 SW IRF. Currently, atmospheric temperature, clouds and H_2O fields are assessed to contribute an uncertainty of 3%, 5% and 4% each to methane's SW radiative effect. Additional sensitivity tests could also be conducted using alternate datasets of α_s and a more sophisticated parameterisation of ocean α_s. CH_4 mixing ratios from other satellite-derived datasets could also be used to calculate forcing estimates to compare against the MIPAS-derived estimates presented in Chapter 6 (alternative CH_4 datasets could also be use to explore the reality of the tropical upper-troposphere maxima observed in MIPAS CH_4 VMRs). Furthermore, uncetainty related to the specification of tropopause height could be investigated in detail, whereby a range of different tropopause definitions (respresenting both climatological and seasonally-evolving tropopause heights) are used in SOCRATES-RF calculations to estimate CH_4 SW IRF and CH_4 SARF.

- **The SW RF of other GHGs.** This analysis could be expanded to other gases beyond CH_4, to advance scientific understanding of SW radiative effects of N_2O and halogenated gases.

Bibliography

Allen, M. R., and W. J. Ingram (2002), Constraints on future changes in climate and the hydrologic cycle, *Nature*, *419*(6903), 228-232, doi:10.1038/nature01092.

Anderson, D. E., and R. F. Cahalan (2005), The Solar Radiation and Climate Experiment (SORCE) mission for the NASA Earth Observing System (EOS), *Sol. Phys.*, *230*(1-2), 3-6, doi:10.1007/s11207-005-1592-6.

Anderson, G., S. Clough, F. Kneizys, J. Chetwynd, and E. Shettle (1986), AFGL Atmospheric Constituent Profiles (0.120km), 46. Bibcode: https://ui.adsabs.harvard.edu/abs/1986afgl.rept....A/abstract

Andrews, T., and M. A. Ringer (2014), Cloud feedbacks, rapid adjustments, and the forcing–response relationship in a transient CO2 reversibility scenario, *J. Clim.*, *27*(4), 1799-1818, doi:10.1175/jcli-d-13-00421.1.

Andrews, T., J. M. Gregory, and M. J. Webb (2015), The dependence of radiative forcing and feedback on evolving patterns of surface temperature change in climate models, *J. Clim.*, *28*(4), 1630-1648, doi:10.1175/jcli-d-14-00545.1.

Andrews, T., C. J. Smith, G. Myhre, P. M. Forster, R. Chadwick, and D. Ackerley (2021), Effective radiative forcing in a GCM with fixed surface temperatures, *Journal of Geophysical Research: Atmospheres*, *126*(4), e2020JD033880, doi:https://doi.org/10.1029/2020JD033880.

Arvesen, J. C., R. N. Griffin, and B. D. Pearson (1969), Determination of extraterrestrial solar spectral irradiance from a research aircraft, *Appl. Opt.*, *8*(11), 2215-2232, doi:10.1364/AO.8.002215.

Baldridge, A. M., S. J. Hook, C. I. Grove, and G. Rivera (2009), The ASTER spectral library version 2.0, *Remote Sensing of Environment*, *113*(4), 711-715, doi:https://doi.org/10.1016/j.rse.2008.11.007.

Ball, W. T., N. A. Krivova, Y. C. Unruh, J. D. Haigh, and S. K. Solanki (2014), A new SATIRE-S spectral solar irradiance reconstruction for solar cycles 21-23 and its implications for stratospheric ozone, *J. Atmos. Sci.*, *71*(11), 4086-4101, doi:10.1175/jas-d-13-0241.1.

Barkstrom, B. R. (1984), The Earth Radiation Budget Experiment (ERBE), *Bull. Amer. Meteorol. Soc.*, *65*(11), 1170-1185, doi:10.1175/1520-0477(1984)065<1170:Terbe>2.0.Co;2.

Bharmal, N. (2009), Documentation for RFMDISORT. Available online: http://www.met.rdg.ac.uk/~jp902366/rad/rfmdisort_doc_Ali.pdf. (Accessed on 22/12/20).

Bolsée, D., et al. (2014), Accurate determination of the TOA solar spectral NIR irradiance using a primary standard source and the Bouguer–Langley technique, *Sol. Phys.*, *289*(7), 2433-2457, doi:10.1007/s11207-014-0474-1.

Boucher, O., and J. Haywood (2001), On summing the components of radiative forcing of climate change, *Clim. Dyn.*, *18*, 297-302, doi:10.1007/s003820100185.

Boucher, O., et al. (2013), Clouds and Aerosols. In: Climate Change 2013: The Physical Science Basis. Contribution of Working Group I to the Fifth Assessment Report of the Intergovernmental Panel on Climate Change *Rep.*, Cambridge, United Kingdom and New York, NY, USA.

Briegleb, B., and V. Ramanathan (1982), Spectral and diurnal variations in clear sky planetary albedo, *Journal of Applied Meteorology (1962-1982)*, *21*(8), 1160-1171.

Burlov Vasiljev, K. A., E. A. Gurtovenko, and Y. B. Matvejev (1995), New absolute measurements of the solar spectrum 310-685 nm, *Sol. Phys.*, *157*(1-2), 51-73, doi:10.1007/bf00680609.

Chance, K., and R. L. Kurucz (2010), An improved high-resolution solar reference spectrum for earth's atmosphere measurements in the ultraviolet, visible, and near infrared, *Journal of Quantitative Spectroscopy and Radiative Transfer*, *111*(9), 1289-1295.

Checa-Garcia, R., M. I. Hegglin, D. Kinnison, D. A. Plummer, and K. P. Shine (2018), Historical tropospheric and stratospheric ozone radiative forcing using the CMIP6 database, *Geophysical Research Letters*, *45*(7), 3264-3273, doi:https://doi.org/10.1002/2017GL076770.

Choi, W. K., and J. R. Holton (1991), Transport of N2O in the stratosphere related to the equatorial semiannual oscillation, *Journal of Geophysical Research: Atmospheres*, *96*(D12), 22543-22557, doi:https://doi.org/10.1029/91JD02263.

Chung, E.-S., and B. J. Soden (2015a), An assessment of direct radiative forcing, radiative adjustments, and radiative feedbacks in coupled ocean–atmosphere models, *J. Clim.*, *28*(10), 4152-4170, doi:10.1175/jcli-d-14-00436.1.

Chung, E.-S., and B. J. Soden (2015b), An assessment of methods for computing radiative forcing in climate models, *Environmental Research Letters*, *10*(7), 074004, doi:10.1088/1748-9326/10/7/074004.

Ciais, P., et al. (2013), Carbon and Other Biogeochemical Cycles. In: Climate Change 2013: The Physical Science Basis. Contribution of Working Group I to the Fifth Assessment Report of the Intergovernmental Panel on Climate Change *Rep.*, Cambridge, United Kingdom and New York, NY, USA.

Clough, S. A., and M. J. Iacono (1995), Line-by-line calculation of atmospheric fluxes and cooling rates: 2. Application to carbon dioxide, ozone, methane, nitrous oxide and the halocarbons, *Journal of Geophysical Research: Atmospheres*, *100*(D8), 16519-16535, doi:https://doi.org/10.1029/95JD01386.

Coddington, O., E. C. Richard, D. Harber, P. Pilewskie, T. N. Woods, K. Chance, X. Liu, and K. Sun The TSIS-1 Hybrid Solar Reference Spectrum, *manuscript submitted to Geophysical Research Letters, 2021*, doi:https://doi.org/10.1002/essoar.10506142.1.

Coddington, O., J. L. Lean, P. Pilewskie, M. Snow, and D. Lindholm (2016), A solar irradiance climate data record, *Bull. Amer. Meteorol. Soc.*, *97*(7), 1265-1282, doi:10.1175/bams-d-14-00265.1.

Collins, W., P. J. Rasch, B. A. Boville, J. McCaa, D. L. Williamson, J. T. Kiehl, and Y. Dai (2004), Description of the NCAR Community Atmosphere Model (CAM 3.0) (No. NCAR/TN-464+STR)*Rep.*, University Corporation for Atmospheric Research.

Collins, W. D., J. M. Lee-Taylor, D. P. Edwards, and G. L. Francis (2006a), Effects of increased near-infrared absorption by water vapor on the climate system, *Journal of Geophysical Research: Atmospheres*, *111*(D18), doi:https://doi.org/10.1029/2005JD006796.

Collins, W. D., et al. (2006b), Radiative forcing by well-mixed greenhouse gases: estimates from climate models in the Intergovernmental Panel on Climate Change (IPCC) Fourth Assessment Report (AR4), *J. Geophys. Res.-Atmos.*, *111*(D14), doi:10.1029/2005jd006713.

Collins, W. D., D. R. Feldman, C. Kuo, and N. H. Nguyen (2018), Large regional shortwave forcing by anthropogenic methane informed by Jovian observations, *Science Advances*, *4*(9), doi:10.1126/sciadv.aas9593.

Cox, C., and W. Munk (1954), Measurement of the roughness of the sea surface from photographs of the Sun's glitter, *J. Opt. Soc. Am.*, *44*(11), 838-850, doi:10.1364/JOSA.44.000838.

DeAngelis, A. M., X. Qu, M. D. Zelinka, and A. Hall (2015), An observational radiative constraint on hydrologic cycle intensification, *Nature*, *528*(7581), 249-253, doi:10.1038/nature15770.

Dee, D. P., et al. (2011), The ERA-Interim reanalysis: Configuration and performance of the data assimilation system, *Quarterly Journal of the Royal Meteorological Society*, *137*(656), 553-597, doi:https://doi.org/10.1002/qj.828.

Dlugokencky, E. J., R. C. Myers, P. M. Lang, K. A. Masarie, A. M. Crotwell, K. W. Thoning, B. D. Hall, J. W. Elkins, and L. P. Steele (2005), Conversion of NOAA atmospheric dry air CH4 mole fractions to a gravimetrically prepared standard scale, *J. Geophys. Res.-Atmos.*, *110*(D18), doi:10.1029/2005jd006035.

Dlugokencky, E. J., E. G. Nisbet, R. Fisher, and D. Lowry (2011), Global atmospheric methane: Budget, changes and dangers, *Philosophical Transactions of the Royal Society A: Mathematical, Physical and Engineering Sciences*, *369*(1943), 2058-2072, doi:doi:10.1098/rsta.2010.0341.

Donner, L., and V. Ramanathan (1980), Methane and Nitrous Oxide: Their Effects on the Terrestrial Climate, *Journal of Atmospheric Sciences*, *37*(1), 119-124, doi:10.1175/1520-0469(1980)037<0119:Manote>2.0.Co;2.

Dudhia, A. (2017), The Reference Forward Model (RFM), *Journal of Quantitative Spectroscopy and Radiative Transfer*, *186*, 243-253, doi:https://doi.org/10.1016/j.jqsrt.2016.06.018.

Dudok de Wit, T., G. Kopp, C. Frohlich, and M. Scholl (2017), Methodology to create a new total solar irradiance record: Making a composite out of multiple data records, *Geophysical Research Letters*, *44*(3), 1196-1203, doi:10.1002/2016gl071866.

Dunn, R. J. H., et al. (2020), Global climate, *Bull. Amer. Meteorol. Soc.*, *101*(8), S9-S128, doi:10.1175/bams-d-20-0104.1.

Edwards, D. P. (1992), GENLN2: A general line-by-line atmospheric transmittance and radiance model. version 3.0 description and users guide (No. NCAR/TN-367+STR), *University Corporation for Atmospheric Research*, doi:doi:10.5065/D6W37T86.

Edwards, J. M., and A. Slingo (1996), Studies with a flexible new radiation code. I: Choosing a configuration for a large-scale model, *Quarterly Journal of the Royal Meteorological Society*, *122*(531), 689-719, doi:https://doi.org/10.1002/qj.49712253107.

Ellingson, R. G., J. Ellis, and S. Fels (1991), The intercomparison of radiation codes used in climate models: Long wave results, *Journal of Geophysical Research: Atmospheres*, *96*(D5), 8929-8953, doi:https://doi.org/10.1029/90JD01450.

Ellingson, R. G., and Y. Fouquart (1991), The intercomparison of radiation codes in climate models: An overview, *Journal of Geophysical Research: Atmospheres*, *96*(D5), 8925-8927, doi:https://doi.org/10.1029/90JD01618.

Elsey, J., M. D. Coleman, T. Gardiner, and K. P. Shine (2017), Can measurements of the near-infrared solar spectral irradiance be reconciled? A new ground-based assessment between 4,000 and 10,000 cm(-1), *Geophysical Research Letters*, *44*(19), 10071-10080, doi:10.1002/2017gl073902.

Elsey, J., and K. P. Shine (2020), SOCRATES water vapour self-continuum changelog.

Errera, Q., et al. (2016), Harmonisation and diagnostics of MIPAS ESA CH4 and N2O profiles using data assimilation, *Atmos. Meas. Tech.*, *9*(12), 5895-5909, doi:10.5194/amt-9-5895-2016.

Etheridge, D. M., L. P. Steele, R. J. Francey, and R. L. Langenfelds (1998), Atmospheric methane between 1000 AD and present: Evidence of anthropogenic emissions and climatic variability, *J. Geophys. Res.-Atmos.*, *103*(D13), 15979-15993, doi:10.1029/98jd00923.

Etminan, M., G. Myhre, E. J. Highwood, and K. P. Shine (2016), Radiative forcing of carbon dioxide, methane, and nitrous oxide: A significant revision of the methane radiative forcing, *Geophysical Research Letters*, *43*(24), 12614-12623, doi:10.1002/2016gl071930.

Eyring, V., S. Bony, G. A. Meehl, C. A. Senior, B. Stevens, R. J. Stouffer, and K. E. Taylor (2016), Overview of the Coupled Model Intercomparison Project Phase 6 (CMIP6) experimental design and organization, *Geosci. Model Dev.*, *9*(5), 1937-1958, doi:10.5194/gmd-9-1937-2016.

Feldman, D. R., W. D. Collins, P. J. Gero, M. S. Torn, E. J. Mlawer, and T. R. Shippert (2015), Observational determination of surface radiative forcing by CO2 from 2000 to 2010, *Nature*, *519*(7543), 339-343, doi:10.1038/nature14240.

Feldman, D. R., et al. (2018), Observationally derived rise in methane surface forcing mediated by water vapour trends, *Nat. Geosci.*, *11*(4), 238-243, doi:10.1038/s41561-018-0085-9.

Fels, S. B., J. D. Mahlman, M. D. Schwarzkopf, and R. W. Sinclair (1980), Stratospheric sensitivity to perturbations in ozone and carbon dioxide: Radiative and dynamical response, *Journal of Atmospheric Sciences*, *37*(10), 2265-2297, doi:10.1175/1520-0469(1980)037<2265:Sstpio>2.0.Co;2.

Flato, G., et al. (2013), Evaluation of Climate Models. In: Climate Change 2013: The Physical Science Basis. Contribution of Working Group I to the Fifth Assessment Report of the Intergovernmental Panel on Climate Change *Rep.*, Cambridge University Press, Cambridge, United Kingdom and New York, NY, USA.

Fligge, M., S. K. Solanki, J. M. Pap, C. Frohlich, and C. Wehrli (2001), Variations of solar spectral irradiance from near UV to the infrared - measurements and results, *J. Atmos. Sol.-Terr. Phys.*, *63*(14), 1479-1487, doi:10.1016/s1364-6826(01)00020-7.

Fontenla, J. M., E. Avrett, G. Thuillier, and J. Harder (2006), Semiempirical models of the solar atmosphere. I. The quiet- and active sun photosphere at moderate resolution, *Astrophys. J.*, *639*(1), 441-458, doi:10.1086/499345.

Forster, P., et al. (2007), Changes in Atmospheric Constituents and in Radiative Forcing: In Climate Change 2007: The Physical Science Basis. Contribution of Working Group I to the Fourth Assessment Report of the Intergovernmental Panel on Climate Change*Rep.*, 129-234 pp, Cambridge University Press, Cambridge, United Kingdom and New York, NY, USA.

Forster, P. M., et al. (2011), Evaluation of radiation scheme performance within chemistry climate models, *J. Geophys. Res.-Atmos.*, *116*, doi:10.1029/2010jd015361.

Forster, P. M., T. Andrews, P. Good, J. M. Gregory, L. S. Jackson, and M. Zelinka (2013), Evaluating adjusted forcing and model spread for historical and future scenarios in the CMIP5 generation of climate models, *J. Geophys. Res.-Atmos.*, *118*(3), 1139-1150, doi:10.1002/jgrd.50174.

Forster, P. M., T. Richardson, A. C. Maycock, C. J. Smith, B. H. Samset, G. Myhre, T. Andrews, R. Pincus, and M. Schulz (2016), Recommendations for diagnosing effective radiative forcing from climate models for CMIP6, *Journal of Geophysical Research: Atmospheres*, *121*(20), 12,460-412,475, doi:https://doi.org/10.1002/2016JD025320.

Forster, P. M. d. F., and K. P. Shine (2002), Assessing the climate impact of trends in stratospheric water vapor, *Geophysical Research Letters*, *29*(6), 10-11-10-14, doi:https://doi.org/10.1029/2001GL013909.

Forster, P. M. d. F., et al. (2005), Resolution of the uncertainties in the radiative forcing of HFC-134a, *Journal of Quantitative Spectroscopy and Radiative Transfer*, *93*(4), 447-460, doi:https://doi.org/10.1016/j.jqsrt.2004.08.038.

Forster, P. M. F., R. S. Freckleton, and K. P. Shine (1997), On aspects of the concept of radiative forcing, *Clim. Dyn.*, *13*(7), 547-560, doi:10.1007/s003820050182.

Fouquart, Y., B. Bonnel, and V. Ramaswamy (1991), Intercomparing shortwave radiation codes for climate studies, *Journal of Geophysical Research: Atmospheres*, *96*(D5), 8955-8968, doi:https://doi.org/10.1029/90JD00290.

Freckleton, R. S., E. J. Highwood, K. P. Shine, O. Wild, K. S. Law, and M. G. Sanderson (1998), Greenhouse gas radiative forcing: Effects of averaging and inhomogeneities in trace gas distribution, *Quarterly Journal of the Royal Meteorological Society*, *124*(550), 2099-2127, doi:https://doi.org/10.1002/qj.49712455014.

Gilgen, H., M. Wild, and A. Ohmura (1998), Means and trends of shortwave irradiance at the surface estimated from global energy balance archive data, *J. Clim.*, *11*(8), 2042-2061, doi:10.1175/1520-0442(1998)011<2042:Matosi>2.0.Co;2.

Gordon, I. E., et al. (2017), The HITRAN2016 molecular spectroscopic database, *Journal of Quantitative Spectroscopy & Radiative Transfer*, *203*, 3-69, doi:10.1016/j.jqsrt.2017.06.038.

Gregory, J. M., W. J. Ingram, M. A. Palmer, G. S. Jones, P. A. Stott, R. B. Thorpe, J. A. Lowe, T. C. Johns, and K. D. Williams (2004), A new method for diagnosing radiative forcing and climate sensitivity, *Geophysical Research Letters*, *31*(3), doi:https://doi.org/10.1029/2003GL018747.

Haigh, J. D. (1994), The role of stratospheric ozone in modulating the solar radiative forcing of climate, *Nature*, *370*(6490), 544-546, doi:10.1038/370544a0.

Hale, G. M., and M. R. Querry (1973), Optical constants of water in the 200-nm to 200-µm wavelength region, *Appl. Opt.*, *12*(3), 555-563, doi:10.1364/AO.12.000555.

Halthore, R. N., et al. (2005), Intercomparison of shortwave radiative transfer codes and measurements, *Journal of Geophysical Research: Atmospheres*, *110*(D11), doi:https://doi.org/10.1029/2004JD005293.

Hansen, J., D. Johnson, A. Lacis, S. Lebedeff, P. Lee, D. Rind, and G. Russell (1981), Climate impact of increasing carbon dioxide, *Science*, *213*(4511), 957-966, doi:10.1126/science.213.4511.957.

Hansen, J., I. Fung, A. Lacis, D. Rind, S. Lebedeff, R. Ruedy, G. Russell, and P. Stone (1988), Global climate changes as forecast by Goddard Institute for Space Studies three-dimensional model, *Journal of Geophysical Research: Atmospheres*, *93*(D8), 9341-9364, doi:https://doi.org/10.1029/JD093iD08p09341.

Hansen, J., M. Sato, and R. Ruedy (1997a), Radiative forcing and climate response, *Journal of Geophysical Research: Atmospheres*, *102*(D6), 6831-6864, doi:https://doi.org/10.1029/96JD03436.

Hansen, J., et al. (1997b), Forcings and chaos in interannual to decadal climate change, *Journal of Geophysical Research: Atmospheres*, *102*(D22), 25679-25720, doi:https://doi.org/10.1029/97JD01495.

Hansen, J., et al. (2005), Efficacy of climate forcings, *Journal of Geophysical Research: Atmospheres*, *110*(D18), doi:https://doi.org/10.1029/2005JD005776.

Hansen, J., M. Sato, P. Kharecha, and K. von Schuckmann (2011), Earth's energy imbalance and implications, *Atmospheric Chemistry and Physics*, *11*(24), 13421-13449, doi:10.5194/acp-11-13421-2011.

Harries, J. E., H. E. Brindley, P. J. Sagoo, and R. J. Bantges (2001), Increases in greenhouse forcing inferred from the outgoing longwave radiation spectra of the Earth in 1970 and 1997, *Nature*, *410*(6826), 355-357, doi:10.1038/35066553.

Hausmann, P., R. Sussmann, and D. Smale (2016), Contribution of oil and natural gas production to renewed increase in atmospheric methane (2007–2014): top–down estimate from ethane and methane column observations, *Atmos. Chem. Phys.*, *16*(5), 3227-3244, doi:10.5194/acp-16-3227-2016.

Hegglin, M., D. Kinnison, J.-F. Lamarque, and D. Plummer (2016), CCMI ozone in support of CMIP6 - version 1.0, edited, Earth System Grid Federation, doi:10.22033/ESGF/input4MIPs.1115.

Hegglin, M. I., et al. (2021), Overview and update of the SPARC Data Initiative: Comparison of stratospheric composition measurements from satellite limb sounders, *Earth Syst. Sci. Data*, *13*(5), 1855-1903, doi:10.5194/essd-13-1855-2021.

Held, I. M., and B. J. Soden (2000), Water vapor feedback and global warming, *Annual Review of Energy and the Environment*, *25*(1), 441-475, doi:10.1146/annurev.energy.25.1.441.

Hodnebrog, Ø., M. Etminan, J. S. Fuglestvedt, G. Marston, G. Myhre, C. J. Nielsen, K. P. Shine, and T. J. Wallington (2013), Global warming potentials and radiative efficiencies of halocarbons and related compounds: A comprehensive review, *Reviews of Geophysics*, *51*(2), 300-378, doi:https://doi.org/10.1002/rog.20013.

Hodnebrog, Ø., et al. (2020), The effect of rapid adjustments to halocarbons and N2O on radiative forcing, *npj Climate and Atmospheric Science*, *3*(1), 43, doi:10.1038/s41612-020-00150-x.

Hogan, R. J., and M. Matricardi (2020), Evaluating and improving the treatment of gases in radiation schemes: the Correlated K-Distribution Model Intercomparison Project (CKDMIP), *Geosci. Model Dev.*, *13*(12), 6501-6521, doi:10.5194/gmd-13-6501-2020.

Huang, X., X. Chen, M. Flanner, P. Yang, D. Feldman, and C. Kuo (2018), Improved representation of surface spectral emissivity in a global climate model and its impact on simulated climate, *J. Clim.*, *31*(9), 3711-3727, doi:10.1175/jcli-d-17-0125.1.

Iacono, M. J., J. S. Delamere, E. J. Mlawer, M. W. Shephard, S. A. Clough, and W. D. Collins (2008), Radiative forcing by long-lived greenhouse gases: Calculations with the AER radiative transfer models, *Journal of Geophysical Research: Atmospheres*, *113*(D13), doi:https://doi.org/10.1029/2008JD009944.

IFS Documentation CY47R1 (2020), Part IV: Physical Processes, in *IFS Documentation CY47R1*, edited, ECMWF, doi:10.21957/cpmkqvhja.

IPCC (2001), Climate Change 2001: The Scientific Basis. Contribution of Working Group I to the Third Assessment Report of the Intergovernmental Panel on Climate Change *Rep.*, 881 pp, Cambridge, United Kingdom and New York, NY, USA.

Ito, A., and M. Inatomi (2012), Use of a process-based model for assessing the methane budgets of global terrestrial ecosystems and evaluation of uncertainty, *Biogeosciences*, *9*(2), 759-773, doi: 10.5194/bg-9-759-2012.

Jain, A. K., B. P. Briegleb, K. Minschwaner, and D. J. Wuebbles (2000), Radiative forcings and global warming potentials of 39 greenhouse gases, *Journal of Geophysical Research: Atmospheres*, *105*(D16), 20773-20790, doi:https://doi.org/10.1029/2000JD900241.

Jerlov, N. G. (1976), *Marine Optics*, 2 ed., 231 pp., Elsevier Scientific Pub. Co., Amsterdam, New York. ISBN: 9780080870502.

Kiehl, J. T., and B. A. Boville (1988), The radiative-dynamical response of a stratospheric-tropospheric general circulation model to changes in ozone, *Journal of Atmospheric Sciences*, *45*(12), 1798-1817, doi:10.1175/1520-0469(1988)045<1798:Trdroa>2.0.Co;2.

Kiehl, J. T., and K. E. Trenberth (1997), Earth's annual global mean energy budget, *Bull. Amer. Meteorol. Soc.*, *78*(2), 197-208, doi:10.1175/1520-0477(1997)078<0197:Eagmeb>2.0.Co;2.

Kim, D., and V. Ramanathan (2008), Solar radiation budget and radiative forcing due to aerosols and clouds, *Journal of Geophysical Research: Atmospheres*, *113*(D2), doi:https://doi.org/10.1029/2007JD008434.

Kleipool, Q. L., M. R. Dobber, J. F. de Haan, and P. F. Levelt (2008), Earth surface reflectance climatology from 3 years of OMI data, *Journal of Geophysical Research: Atmospheres*, *113*(D18), doi:https://doi.org/10.1029/2008JD010290.

Koo, J.-H., K. A. Walker, A. Jones, P. E. Sheese, C. D. Boone, P. F. Bernath, and G. L. Manney (2017), Global climatology based on the ACE-FTS version 3.5 dataset: Addition of mesospheric levels and carbon-containing species in the UTLS, *Journal of Quantitative Spectroscopy and Radiative Transfer*, *186*, 52-62, doi:https://doi.org/10.1016/j.jqsrt.2016.07.003.

Kopp, G., K. Heuerman, D. Harber, and G. Drake (2007), The TSI Radiometer Facility - absolute calibrations for total solar irradiance instruments - art. no. 667709, in *Earth Observing Systems Xii*, edited by J. J. Butler and J. Xiong, pp. 67709-67709, Spie-Int Soc Optical Engineering, Bellingham, doi:10.1117/12.734553.

Kopp, G., and J. L. Lean (2011), A new, lower value of total solar irradiance: Evidence and climate significance, *Geophysical Research Letters*, *38*, doi:10.1029/2010gl045777.

Kopp, G. (2016), Magnitudes and timescales of total solar irradiance variability, *J. Space Weather Space Clim.*, *6*, doi:10.1051/swsc/2016025.

Kopp, G., N. Krivova, C. J. Wu, and J. Lean (2016), The impact of the revised sunspot record on solar irradiance reconstructions, *Sol. Phys.*, *291*(9-10), 2951-2965, doi:10.1007/s11207-016-0853-x.

Kratz, D. P. (2008), The sensitivity of radiative transfer calculations to the changes in the HITRAN database from 1982 to 2004, *Journal of Quantitative Spectroscopy and Radiative Transfer*, *109*(6), 1060-1080, doi:https://doi.org/10.1016/j.jqsrt.2007.10.010.

Kurucz, R., and B. Bell (1995), Atomic line data, *Kurucz CD-ROM No. 23. Cambridge, Mass.: Smithsonian Astrophysical Observatory.*

L'Ecuyer, T. S., et al. (2015), The observed state of the energy budget in the early twenty-first century, *J. Clim.*, *28*(21), 8319-8346, doi:10.1175/jcli-d-14-00556.1.

Laeng, A., et al. (2015), Validation of MIPAS IMK/IAA methane profiles, *Atmos. Meas. Tech.*, *8*(12), 5251-5261, doi:10.5194/amt-8-5251-2015.

Lelieveld, J., P. J. Crutzen, and F. J. Dentener (1998), Changing concentration, lifetime and climate forcing of atmospheric methane, *Tellus B: Chemical and Physical Meteorology*, *50*(2), 128-150, doi:10.3402/tellusb.v50i2.16030.

Levitus, S., et al. (2012), World ocean heat content and thermosteric sea level change (0-2000 m), 1955-2010, *Geophysical Research Letters*, *39*, doi:10.1029/2012gl051106.

Li, J., C. L. Curry, Z. Sun, and F. Zhang (2010), Overlap of solar and infrared spectra and the shortwave radiative effect of methane, *J. Atmos. Sci.*, *67*(7), 2372-2389, doi:10.1175/2010jas3282.1.

Liou, K.-N. (2002), *An introduction to atmospheric radiation*, 2 ed., 598 pp., Elsevier Science & Technology, Amsterdam, Boston. ISBN: 9780124514515.

Loeb, N. G., B. A. Wielicki, D. R. Doelling, G. L. Smith, D. F. Keyes, S. Kato, N. Manalo-Smith, and T. Wong (2009), Toward optimal closure of the earth's top-of-atmosphere radiation budget, *J. Clim.*, *22*(3), 748-766, doi:10.1175/2008jcli2637.1.

Loeb, N. G., J. M. Lyman, G. C. Johnson, R. P. Allan, D. R. Doelling, T. Wong, B. J. Soden, and G. L. Stephens (2012), Observed changes in top-of-the-atmosphere radiation and upper-ocean heating consistent within uncertainty, *Nat. Geosci.*, *5*(2), 110-113, doi:10.1038/ngeo1375.

Loeb, N. G., D. R. Doelling, H. L. Wang, W. Y. Su, C. Nguyen, J. G. Corbett, L. S. Liang, C. Mitrescu, F. G. Rose, and S. Kato (2018), Clouds and the Earth's Radiant Energy System (CERES) Energy Balanced and Filled (EBAF) Top-of-Atmosphere (TOA) edition-4.0 data product, *J. Clim.*, *31*(2), 895-918, doi:10.1175/jcli-d-17-0208.1.

Lyman, J. M., S. A. Good, V. V. Gouretski, M. Ishii, G. C. Johnson, M. D. Palmer, D. M. Smith, and J. K. Willis (2010), Robust warming of the global upper ocean, *Nature*, *465*(7296), 334-337, doi: 10.1038/nature09043.

Manabe, S., and R. F. Strickler (1964), Thermal equilibrium of the atmosphere with a convective adjustment, *J. Atmos. Sci.*, *21*, 361-385.

Manabe, S., and R. T. Wetherald (1967), Thermal equilibrium of the atmosphere with a given distribution of relative humidity, *J. Atmos. Sci.*, *24*(3), 241-259.

Manners, J., J. M. Edwards, P. Hill, and J.-C. Thelen (2015), SOCRATES technical guide Suite Of Community RAdiative Transfer codes based on Edwards and Slingo*Rep.*, 1-85 pp, Met Office, FitzRoy Rd, Exeter.

Marvel, K., G. A. Schmidt, R. L. Miller, and L. S. Nazarenko (2016), Implications for climate sensitivity from the response to individual forcings, *Nature Climate Change*, *6*(4), 386-389, doi:10 .1038/nclimate2888.

Maycock, A. C., and K. P. Shine (2012), Stratospheric water vapor and climate: Sensitivity to the representation in radiation codes, *Journal of Geophysical Research: Atmospheres*, *117*(D13), doi:https://doi.org/10.1029/2012JD017484.

Maycock, A. C., M. M. Joshi, K. P. Shine, and A. A. Scaife (2013), The circulation response to idealized changes in stratospheric water vapor, *J. Clim.*, *26*(2), 545-561, doi:10.1175/jcli-d-12-00155.1.

Maycock, A. C., et al. (2018), Revisiting the mystery of recent stratospheric temperature trends, *Geophysical Research Letters*, *45*(18), 9919-9933, doi:https://doi.org/10.1029/2018GL078035.

Meerdink, S. K., S. J. Hook, D. A. Roberts, and E. A. Abbott (2019), The ECOSTRESS spectral library version 1.0, *Remote Sensing of Environment*, *230*, 111196, doi:https://doi.org/10.1016/j.rse.2019.05.015.

Meftah, M., et al. (2020), A new version of the SOLAR-ISS spectrum covering the 165 – 3000 nm spectral region, *Sol. Phys.*, *295*(2), 14, doi:10.1007/s11207-019-1571-y.

Menang, K. P., M. D. Coleman, T. D. Gardiner, I. V. Ptashnik, and K. P. Shine (2013), A high-resolution near-infrared extraterrestrial solar spectrum derived from ground-based Fourier transform spectrometer measurements, *J. Geophys. Res.-Atmos.*, *118*(11), 5319-5331, doi:10.1002/jgrd.50425.

Migeotte, M. V. (1948), Spectroscopic Evidence of Methane in the Earth's Atmosphere, *Physical Review*, *73*(5), 519-520, doi:10.1103/PhysRev.73.519.2.

Mlawer, E. J., S. J. Taubman, P. D. Brown, M. J. Iacono, and S. A. Clough (1997), Radiative transfer for inhomogeneous atmospheres: RRTM, a validated correlated-k model for the longwave, *Journal of Geophysical Research: Atmospheres*, *102*(D14), 16663-16682, doi:https://doi.org/10.1029/97JD00237.

Mlawer, E. J., V. H. Payne, J.-L. Moncet, J. S. Delamere, M. J. Alvarado, and D. C. Tobin (2012), Development and recent evaluation of the MT_CKD model of continuum absorption, *Philosophical Transactions of the Royal Society A: Mathematical, Physical and Engineering Sciences*, *370*(1968), 2520-2556, doi:doi:10.1098/rsta.2011.0295.

Mlawer, E. J., et al. (2019), Analysis of water vapor absorption in the far-infrared and submillimeter regions using surface radiometric measurements from extremely dry locations, *Journal of Geophysical Research: Atmospheres*, *124*(14), 8134-8160, doi:https://doi.org/10.1029/2018JD029508.

Mlynczak, M. G., et al. (2016), The spectroscopic foundation of radiative forcing of climate by carbon dioxide, *Geophysical Research Letters*, *43*(10), 5318-5325, doi:https://doi.org/10.1002/2016GL068837.

Modak, A., G. Bala, K. Caldeira, and L. Cao (2018), Does shortwave absorption by methane influence its effectiveness?, *Clim. Dyn.*, *51*(9), 3653-3672, doi:10.1007/s00382-018-4102-x.

Moorhead, J. G. (1932), The Near Infrared Absorption Spectrum of Methane, *Physical Review*, *39*(1), 83-88, doi:10.1103/PhysRev.39.83.

Morgenstern, O., et al. (2017), Review of the global models used within phase 1 of the Chemistry–Climate Model Initiative (CCMI), *Geosci. Model Dev.*, *10*(2), 639-671, doi:10.5194/gmd-10-639-2017.

Myhre, G., and F. Stordal (1997), Role of spatial and temporal variations in the computation of radiative forcing and GWP, *Journal of Geophysical Research*, *102*, 11,181, doi:10.1029/97jd00148.

Myhre, G., E. J. Highwood, K. P. Shine, and F. Stordal (1998), New estimates of radiative forcing due to well mixed greenhouse gases, *Geophysical Research Letters*, *25*(14), 2715-2718, doi:https://doi.org/10.1029/98GL01908.

Myhre, G., F. Stordal, I. Gausemel, C. J. Nielsen, and E. Mahieu (2006), Line-by-line calculations of thermal infrared radiation representative for global condition: CFC-12 as an example, *Journal of Quantitative Spectroscopy & Radiative Transfer*, *97*(3), 317-331, doi:10.1016/j.jqsrt.2005.04.015.

Myhre, G., et al. (2013a), Anthropogenic and Natural Radiative Forcing. In Climate Change 2013: The Physical Science Basis. Contribution of Working Group I to the Fifth Assessment Report of the Intergovernmental Panel on Climate Change*Rep.*, 659-740 pp, Cambridge University Press, Cambridge, United Kingdom and New York, NY, USA.

Myhre, G., et al. (2013b), Radiative forcing of the direct aerosol effect from AeroCom Phase II simulations, *Atmospheric Chemistry and Physics*, *13*(4), 1853-1877, doi:10.5194/acp-13-1853-2013.

Myhre, G., et al. (2018), Sensible heat has significantly affected the global hydrological cycle over the historical period, *Nature Communications*, *9*(1), 1922, doi:10.1038/s41467-018-04307-4.

Neef, L., M. van Weele, and P. van Velthoven (2010), Optimal estimation of the present-day global methane budget, *Global Biogeochemical Cycles*, *24*, doi:10.1029/2009gb003661.

Nisbet, E. G., et al. (2016), Rising atmospheric methane: 2007–2014 growth and isotopic shift, *Global Biogeochemical Cycles*, *30*(9), 1356-1370, doi:https://doi.org/10.1002/2016GB005406.

Nisbet, E. G., et al. (2019), Very strong atmospheric methane growth in the 4 years 2014-2017: Implications for the paris agreement, *Global Biogeochemical Cycles*, *33*(3), 318-342, doi:10.102 9/2018gb006009.

O'Gorman, P. A., R. P. Allan, M. P. Byrne, and M. Previdi (2012), Energetic constraints on precipitation under climate change, *Surveys in Geophysics*, *33*(3), 585-608, doi:10.1007/s10712-011-9159-6.

Ohmura, A., et al. (1998), Baseline Surface Radiation Network (BSRN/WCRP): New precision radiometry for climate research, *Bull. Amer. Meteorol. Soc.*, *79*(10), 2115-2136, doi:10.1175/1520-0477(1998)079<2115:Bsrnbw>2.0.Co;2.

Oreopoulos, L., et al. (2012), The Continual Intercomparison of Radiation Codes: Results from phase I, *Journal of Geophysical Research: Atmospheres*, *117*(D6), doi:https://doi.org/10.1029/2011JD016821.

Paynter, D. (2008), Measurements and interpretations of the water vapour continuum at near infrared wavelengths, PhD thesis, University of Reading.

Pereira, N., D. Bolsée, P. Sperfeld, S. Pape, D. Sluse, and G. Cessateur (2018), Metrology of solar spectral irradiance at the top of the atmosphere in the near infrared measured at Mauna Loa Observatory: the PYR-ILIOS campaign, *Atmos. Meas. Tech.*, *11*(12), 6605-6615, doi:10.5194/amt-11-6605-2018.

Petty, G. W. (2006), *A first course in atmospheric radiation*, Second edition ed., Sundog Publishing, Madison, Wisconsin,. ISBN: 978-0-9729033-1-8.

Pincus, R., et al. (2015), Radiative flux and forcing parameterization error in aerosol-free clear skies, *Geophysical Research Letters*, *42*(13), 5485-5492, doi:https://doi.org/10.1002/2015GL064291.

Pincus, R., P. M. Forster, and B. Stevens (2016), The Radiative Forcing Model Intercomparison Project (RFMIP): experimental protocol for CMIP6, *Geosci. Model Dev.*, *9*(9), 3447-3460, doi:10.5194/gmd-9-3447-2016.

Pincus, R., et al. (2020), Benchmark calculations of radiative forcing by greenhouse gases, *Journal of Geophysical Research: Atmospheres*, *125*(23), e2020JD033483, doi:https://doi.org/10.1029/2020JD033483.

Pinnock, S., M. D. Hurley, K. P. Shine, T. J. Wallington, and T. J. Smyth (1995), Radiative forcing of climate by hydrochlorofluorocarbons and hydrofluorocarbons, *Journal of Geophysical Research: Atmospheres*, *100*(D11), 23227-23238, doi:https://doi.org/10.1029/95JD02323.

Plieninger, J., et al. (2016), Validation of revised methane and nitrous oxide profiles from MIPAS–ENVISAT, *Atmos. Meas. Tech.*, *9*(2), 765-779, doi:10.5194/amt-9-765-2016.

Prather, M. J., C. D. Holmes, and J. Hsu (2012), Reactive greenhouse gas scenarios: Systematic exploration of uncertainties and the role of atmospheric chemistry, *Geophysical Research Letters*, *39*, doi:10.1029/2012gl051440.

Ptashnik, I. V., R. A. McPheat, K. P. Shine, K. M. Smith, and R. G. Williams (2011), Water vapor self-continuum absorption in near-infrared windows derived from laboratory measurements, *Journal of Geophysical Research: Atmospheres*, *116*(D16), doi:https://doi.org/10.1029/2011JD015603.

Ptashnik, I. V., R. A. McPheat, K. P. Shine, K. M. Smith, and R. G. Williams (2012), Water vapour foreign-continuum absorption in near-infrared windows from laboratory measurements, *Philosophical Transactions of the Royal Society A: Mathematical, Physical and Engineering Sciences*, *370*(1968), 2557-2577, doi:doi:10.1098/rsta.2011.0218.

Rädel, G., K. P. Shine, and I. V. Ptashnik (2015), Global radiative and climate effect of the water vapour continuum at visible and near-infrared wavelengths, *Quarterly Journal of the Royal Meteorological Society*, *141*(688), 727-738, doi:https://doi.org/10.1002/qj.2385.

Ramanathan, V. (1975), Greenhouse effect due to chlorofluorocarbons - climatic implications, *Science*, *190*(4209), 50-51, doi:10.1126/science.190.4209.50.

Ramanathan, V., and R. E. Dickinson (1979), The role of stratospheric ozone in the zonal and seasonal radiative energy balance of the earth-troposphere system, *Journal of Atmospheric Sciences*, *36*(6), 1084-1104, doi:10.1175/1520-0469(1979)036<1084:Trosoi>2.0.Co;2.

Ramanathan, V., M. S. Lian, and R. D. Cess (1979), Increased atmospheric CO2 - zonal and seasonal estimates of the effect on the radiation energy balance and surface temperature, *Journal of Geophysical Research-Oceans*, *84*(NC8), 4949-4958, doi:10.1029/JC084iC08p04949.

Ramaswamy, V., et al. (2001), Radiative Forcing of Climate Change In: Climate Change 2001: The Scientific Basis. Contribution of Working Group I to the Third Assessment Report of the Intergovernmental Panel on Climate Change*Rep.*, 881 pp, Cambridge, United Kingdom and New York, NY, USA.

Ramaswamy, V., et al. (2018), Radiative forcing of climate: The historical evolution of the radiative forcing concept, the forcing agents and their quantification, and applications, *Meteorological Monographs*, *59*, 14.11-14.101, doi:10.1175/amsmonographs-d-19-0001.1.

Remsberg, E. E. (2015), Methane as a diagnostic tracer of changes in the Brewer–Dobson circulation of the stratosphere, *Atmos. Chem. Phys.*, *15*(7), 3739-3754, doi:10.5194/acp-15-3739-2015.

Rhein, M., et al. (2013), Observations: Ocean, in *Climate Change 2013: The Physical Science Basis*, edited by T. F. Stocker, D. Qin, G. K. Plattner, M. M. B. Tignor, S. K. Allen, J. Boschung, A. Nauels, Y. Xia, V. Bex and P. M. Midgley, pp. 255-315, Cambridge Univ Press, Cambridge.

Ricaud, P., et al. (2014), Impact of the Asian monsoon anticyclone on the variability of mid-to-upper tropospheric methane above the Mediterranean Basin, *Atmos. Chem. Phys.*, *14*(20), 11427-11446, doi:10.5194/acp-14-11427-2014.

Richard, E. C., P. Pilewskie, G. Kopp, O. Coddington, T. N. Woods, and D. L. Wu (2016), Continuing the solar irradiance data record with TSIS, edited, pp. A11I-0133.

Richard, E. C., D. Harber, O. Coddington, S. Beland, M. Chambliss, S. Mauceri, and P. Pilewskie (2018), Implementation of solar spectral irradiance measurements from the International Space Station: The TSIS-1 first light and early mission results, edited, pp. SH32B-07.

Richardson, T. B., et al. (2019), Efficacy of climate forcings in PDRMIP models, *Journal of Geophysical Research: Atmospheres*, *124*(23), 12824-12844, doi:https://doi.org/10.1029/2019JD030581.

Rigby, M., et al. (2017), Role of atmospheric oxidation in recent methane growth, *Proceedings of the National Academy of Sciences*, *114*(21), 5373-5377, doi:10.1073/pnas.1616426114.

Roesch, A., M. Wild, R. Pinker, and A. Ohmura (2002), Comparison of spectral surface albedos and their impact on the general circulation model simulated surface climate, *Journal of Geophysical Research: Atmospheres*, *107*(D14), ACL 13-11-ACL 13-18, doi:https://doi.org/10.1029/2001JD000809.

Rothman, L. S., et al. (1987), The HITRAN database: 1986 edition, *Appl. Opt.*, *26*(19), 4058-4097, doi:10.1364/AO.26.004058.

Rothman, L. S., et al. (1992), The HITRAN molecular database: Editions of 1991 and 1992, *Journal of Quantitative Spectroscopy and Radiative Transfer*, *48*(5), 469-507, doi:https://doi.org/10.1016/0022-4073(92)90115-K.

Rothman, L. S., et al. (1998), The HITRAN molecular spectroscopic database and HAWKS (HITRAN Atmospheric Workstation): 1996 edition, *Journal of Quantitative Spectroscopy and Radiative Transfer*, *60*(5), 665-710, doi:https://doi.org/10.1016/S0022-4073(98)00078-8.

Rothman, L. S., et al. (2005), The HITRAN 2004 molecular spectroscopic database, *Journal of Quantitative Spectroscopy and Radiative Transfer*, *96*(2), 139-204, doi:https://doi.org/10.1016/j.jqsrt.2004.10.008.

Rothman, L. S., et al. (2009), The HITRAN 2008 molecular spectroscopic database, *Journal of Quantitative Spectroscopy and Radiative Transfer*, *110*(9), 533-572, doi:https://doi.org/10.1016/j.jqsrt.2009.02.013.

Rothman, L. S., et al. (2013), The HITRAN2012 molecular spectroscopic database, *Journal of Quantitative Spectroscopy and Radiative Transfer*, *130*, 4-50, doi:https://doi.org/10.1016/j.jqsrt.2013.07.002.

Rotstayn, L. D., S. J. Jeffrey, M. A. Collier, S. M. Dravitzki, A. C. Hirst, J. I. Syktus, and K. K. Wong (2012), Aerosol- and greenhouse gas-induced changes in summer rainfall and circulation in the Australasian region: A study using single-forcing climate simulations, *Atmospheric Chemistry and Physics*, *12*(14), 6377-6404, doi:10.5194/acp-12-6377-2012.

Saunois, M., R. B. Jackson, P. Bousquet, B. Poulter, and J. G. Canadell (2016), The growing role of methane in anthropogenic climate change, *Environmental Research Letters*, *11*(12), 120207, doi:10.1088/1748-9326/11/12/120207.

Saunois, M., et al. (2020), The global methane budget 2000–2017, *Earth Syst. Sci. Data*, *12*(3), 1561-1623, doi:10.5194/essd-12-1561-2020.

Séférian, R., S. Baek, O. Boucher, J. L. Dufresne, B. Decharme, D. Saint-Martin, and R. Roehrig (2018), An interactive ocean surface albedo scheme (OSAv1.0): Formulation and evaluation in ARPEGE-Climat (V6.1) and LMDZ (V5A), *Geosci. Model Dev.*, *11*(1), 321-338, doi:10.5194/gmd-11-321-2018.

Senior, C. A., and J. F. B. Mitchell (2000), The time-dependence of climate sensitivity, *Geophysical Research Letters*, *27*(17), 2685-2688, doi:https://doi.org/10.1029/2000GL011373.

Sherwood, S. C., S. Bony, O. Boucher, C. Bretherton, P. M. Forster, J. M. Gregory, and B. Stevens (2015), Adjustments in the forcing-feedback framework for understanding climate change *Bull. Amer. Meteorol. Soc.*, *96*(2), 217-228.

Sherwood, S. C., et al. (2020), An assessment of Earth's climate sensitivity using multiple lines of evidence, *Reviews of Geophysics*, *58*(4), e2019RG000678, doi:https://doi.org/10.1029/2019RG000678.

Shindell, D., and G. Faluvegi (2009), Climate response to regional radiative forcing during the twentieth century, *Nat. Geosci.*, *2*(4), 294-300, doi:10.1038/ngeo473.

Shindell, D., M. Schulz, Y. Ming, T. Takemura, G. Faluvegi, and V. Ramaswamy (2010), Spatial scales of climate response to inhomogeneous radiative forcing, *Journal of Geophysical Research: Atmospheres*, *115*(D19), doi:https://doi.org/10.1029/2010JD014108.

Shine, K. P., and P. M. D. Forster (1999), The effect of human activity on radiative forcing of climate change: A review of recent developments, *Global and Planetary Change*, *20*(4), 205-225, doi:10.1016/s0921-8181(99)00017-x.

Shine, K. P., I. V. Ptashnik, and G. Rädel (2012), The water vapour continuum: Brief history and recent developments, *Surveys in Geophysics*, *33*(3), 535-555, doi:10.1007/s10712-011-9170-y.

Shine, K. P., and G. Myhre (2020), The spectral nature of stratospheric temperature adjustment and its application to halocarbon radiative forcing, *Journal of Advances in Modeling Earth Systems*, *12*(3), e2019MS001951, doi:https://doi.org/10.1029/2019MS001951.

Shine, K. P., R. E. Byrom, and R. Checa-Garcia (*In prep.*), Conceptual understanding of shortwave radiative forcing by greenhouse gases.

Shuai, Y., C. B. Schaaf, A. H. Strahler, J. Liu, and Z. Jiao (2008), Quality assessment of BRDF/albedo retrievals in MODIS operational system, *Geophysical Research Letters*, *35*(5), doi:https://doi.org/10.1029/2007GL032568.

Smith, C. J., et al. (2018), Understanding rapid adjustments to diverse forcing agents, *Geophysical Research Letters*, *45*(21), 12,023-012,031, doi:https://doi.org/10.1029/2018GL079826.

Smith, C. J., et al. (2020), Effective radiative forcing and adjustments in CMIP6 models, *Atmospheric Chemistry and Physics*, *20*(16), 9591-9618, doi:10.5194/acp-20-9591-2020.

Soden, B., W. Collins, and D. Feldman (2018), Reducing uncertainties in climate models, *Science*, *361*, 326-327, doi:10.1126/science.aau1864.

SPARC (2017), SPARC, 2017: The SPARC Data Initiative: Assessment of stratospheric trace gas and aerosol climatologies from satellite limb sounders. By M. I. Hegglin and S. Tegtmeier (eds.), SPARC Report No. 8, WCRP-5/2017, available at www.sparc-climate.org/publications/sparcreports/sparc-report-no-8/ (last access: 11 March 2021)*Rep.*

Stammes, P., P. Wang, and J. F. de Haan (2012), Update of the Doubling-Adding KNMI (DAK) radiative transfer model, in *International Radiation Symposium 2012*, edited, Dahlem Cube, Berlin, Germany.

Stamnes, K., S.-C. Tsay, W. Wiscombe, and I. Laszlo (2000), DISORT, a general-purpose Fortran program for discrete-ordinate-method radiative transfer in scattering and emitting layered media: Documentation of methodology, in *International Radiation Symposium*, edited, p. 112, Saint Petersburg.

Stephens, G. L., J. L. Li, M. Wild, C. A. Clayson, N. Loeb, S. Kato, T. L'Ecuyer, P. W. Stackhouse, M. Lebsock, and T. Andrews (2012), An update on Earth's energy balance in light of the latest global observations, *Nat. Geosci.*, *5*(10), 691-696, doi:10.1038/ngeo1580.

Stevens, B., S. C. Sherwood, S. Bony, and M. J. Webb (2016), Prospects for narrowing bounds on Earth's equilibrium climate sensitivity, *Earth's Future*, *4*(11), 512-522, doi:https://doi.org/10.1002/2016EF000376.

Takahashi, K. (2009), The global hydrological cycle and atmospheric shortwave absorption in climate models under CO_2 forcing, *J. Clim.*, *22*(21), 5667-5675.

Tang, T., et al. (2019), Comparison of effective radiative forcing calculations using multiple methods, drivers, and models, *Journal of Geophysical Research: Atmospheres*, *124*(8), 4382-4394, doi: https://doi.org/10.1029/2018JD030188.

Taylor, K. E., R. J. Stouffer, and G. A. Meehl (2012), An overview of CMIP5 and the experiment design, *Bull. Amer. Meteorol. Soc.*, *93*(4), 485-498, doi:10.1175/bams-d-11-00094.1.

Thuillier, G., M. Herse, D. Labs, T. Foujols, W. Peetermans, D. Gillotay, P. C. Simon, and H. Mandel (2003), The solar spectral irradiance from 200 to 2400 nm as measured by the SOLSPEC spectrometer from the ATLAS and EURECA missions, *Sol. Phys.*, *214*(1), 1-22, doi:10.1023/a:1024048429145.

Thuillier, G., et al. (2014), The solar irradiance spectrum at solar activity minimum between solar cycles 23 and 24, *Sol. Phys.*, *289*(6), 1931-1958, doi:10.1007/s11207-013-0461-y.

Tilstra, L. G., O. N. E. Tuinder, P. Wang, and P. Stammes (2017), Surface reflectivity climatologies from UV to NIR determined from Earth observations by GOME-2 and SCIAMACHY, *Journal of Geophysical Research: Atmospheres*, *122*(7), 4084-4111, doi:https://doi.org/10.1002/2016JD025940.

Tjemkes, S. A., et al. (2003), The ISSWG line-by-line inter-comparison experiment, *Journal of Quantitative Spectroscopy and Radiative Transfer*, *77*(4), 433-453, doi:https://doi.org/10.1016/S0022-4073(02)00174-7.

Trenberth, K. E., J. T. Fasullo, and J. Kiehl (2009), Earth's global energy budget, *Bull. Amer. Meteorol. Soc.*, *90*(3), 311-323, doi:10.1175/2008bams2634.1.

Volodin, E. M., N. A. Dianskii, and A. V. Gusev (2010), Simulating present-day climate with the INMCM4.0 coupled model of the atmospheric and oceanic general circulations, *Izvestiya Atmospheric and Oceanic Physics*, *46*(4), 414-431, doi:10.1134/s000143381004002x.

von Clarmann, T., et al. (2009), Retrieval of temperature, H2O, O3, HNO, CH4, N2O, ClONO2 and ClO from MIPAS reduced resolution nominal mode limb emission measurements, *Atmos. Meas. Tech.*, *2*(1), 159-175, doi:10.5194/amt-2-159-2009.

Walters, D., et al. (2019), The Met Office Unified Model Global Atmosphere 7.0/7.1 and JULES Global Land 7.0 configurations, *Geosci. Model Dev.*, *12*(5), 1909-1963, doi:10.5194/gmd-12-1909-2019.

Wang, W. C., Y. L. Yung, A. A. Lacis, T. Mo, and J. E. Hansen (1976), Greenhouse Effects due to Man-Made Perturbations of Trace Gases, *Science*, *194*(4266), 685-690, doi:doi:10.1126/science.194.4266.685.

Whitburn, S., L. Clarisse, S. Bauduin, M. George, D. Hurtmans, S. Safieddine, P. F. Coheur, and C. Clerbaux (2020), Spectrally resolved fluxes from IASI data: Retrieval algorithm for clear-sky measurements, *J. Clim.*, *33*(16), 6971-6988, doi:10.1175/jcli-d-19-0523.1.

Whitlock, C. H., D. S. Bartlett, and E. A. Gurganus (1982), Sea foam reflectance and influence on optimum wavelength for remote sensing of ocean aerosols, *Geophysical Research Letters*, *9*(6), 719-722, doi:https://doi.org/10.1029/GL009i006p00719.

Wielicki, B. A., B. R. Barkstrom, E. F. Harrison, R. B. Lee, G. L. Smith, and J. E. Cooper (1996), Clouds and the Earth's Radiant Energy System (CERES): An Earth Observing System experiment, *Bull. Amer. Meteorol. Soc.*, *77*(5), 853-868, doi:https://doi.org/10.1175/1520-0477(1996)077<0853:CATERE>2.0.CO;2.

Wild, M., D. Folini, C. Schar, N. Loeb, E. G. Dutton, and G. Konig-Langlo (2013a), The global energy balance from a surface perspective, *Clim. Dyn.*, *40*(11-12), 3107-3134, doi:10.1007/s00382-012-1569-8.

Wild, M., D. Folini, C. Schär, N. Loeb, E. G. Dutton, and G. König-Langlo (2013b), A new diagram of the global energy balance, *AIP Conference Proceedings*, *1531*(1), 628-631, doi:10.1063/1.4804848.

Wild, M., D. Folini, M. Z. Hakuba, C. Schar, S. I. Seneviratne, S. Kato, D. Rutan, C. Ammann, E. F. Wood, and G. Konig-Langlo (2015), The energy balance over land and oceans: an assessment based on direct observations and CMIP5 climate models, *Clim. Dyn.*, *44*(11-12), 3393-3429, doi:10.1007/s00382-014-2430-z.

Wild, M. (2017), Towards global estimates of the surface energy budget, *Curr. Clim. Chang. Rep.*, *3*(1), 87-97, doi:10.1007/s40641-017-0058-x.

Wild, M., M. Z. Hakuba, D. Folini, P. Dorig-Ott, C. Schar, S. Kato, and C. N. Long (2019), The cloud-free global energy balance and inferred cloud radiative effects: An assessment based on direct observations and climate models, *Clim. Dyn.*, *52*(7-8), 4787-4812, doi:10.1007/s00382-018-4413-y.

Wild, M. (2020), The global energy balance as represented in CMIP6 climate models, *Clim. Dyn.*, *55*(3-4), 553-577, doi:10.1007/s00382-020-05282-7.

Williams, K. D., W. J. Ingram, and J. M. Gregory (2008), Time variation of effective climate sensitivity in GCMs, *J. Clim.*, *21*(19), 5076-5090, doi:10.1175/2008jcli2371.1.

World Meteorological Organization (1986), Atmospheric ozone 1985, WMO Global Ozone Res. and Monit. Proj. Rep. 20*Rep.*, Geneva, Switzerland.

Xiong, X., S. Houweling, J. Wei, E. Maddy, F. Sun, and C. Barnet (2009), Methane plume over south Asia during the monsoon season: Satellite observation and model simulation, *Atmos. Chem. Phys.*, *9*(3), 783-794, doi:10.5194/acp-9-783-2009.

Zelinka, M. D., T. Andrews, P. M. Forster, and K. E. Taylor (2014), Quantifying components of aerosol-cloud-radiation interactions in climate models, *J. Geophys. Res.-Atmos.*, *119*(12), 7599-7615, doi:10.1002/2014jd021710.

Zelinka, M. D., T. A. Myers, D. T. McCoy, S. Po-Chedley, P. M. Caldwell, P. Ceppi, S. A. Klein, and K. E. Taylor (2020), Causes of higher climate sensitivity in CMIP6 models, *Geophysical Research Letters*, *47*(1), e2019GL085782, doi:https://doi.org/10.1029/2019GL085782.

Zhang, H., G. Y. Shi, and Y. Liu (2005), A comparison between the two line-by-line integration algorithms, .*Chin. J. Atmos. Sci.*(29), 581–593, doi:10.3878/j.issn.1006-9895.2005.04.09.

Zhong, W. Y., S. M. Osprey, L. J. Gray, and J. D. Haigh (2008), Influence of the prescribed solar spectrum on calculations of atmospheric temperature, *Geophysical Research Letters*, *35*(22), doi:10.1029/2008gl035993.